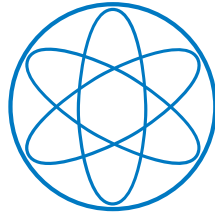


PHYSIK - DEPARTMENT



**High-Purity CaWO_4 Single Crystals
for Direct Dark Matter Search with
the CRESST Experiment**

DISSERTATION

VON

ANDREA RUTH MÜNSTER



TECHNISCHE UNIVERSITÄT MÜNCHEN

TECHNISCHE UNIVERSITÄT MÜNCHEN
Physik-Department
Lehrstuhl für Experimentalphysik und Astroteilchenphysik

High-Purity CaWO_4 Single Crystals for Direct Dark Matter Search with the CRESST Experiment

Andrea Ruth Münster

Vollständiger Abdruck der von der Fakultät für Physik der Technischen Universität München zur Erlangung des akademischen Grades eines

Doktors der Naturwissenschaften (Dr. rer. nat.)

genehmigten Dissertation.

Vorsitzende/-r: apl. Prof. Dr. Norbert Kaiser

Prüfende/-r der Dissertation:

1. Prof. Dr. Stefan Schönert

2. Prof. Dr. Shawn Bishop

Die Dissertation wurde am 09.10.2017 bei der Technischen Universität München eingereicht und durch die Fakultät für Physik am 09.11.2017 angenommen.

Abstract

One of today's great scientific mysteries is the nature of dark matter (DM). Striking evidence for its existence has been found on different length and time scales of the Universe. However, a detection of the corresponding particle has not been achieved so far. One approach are experiments directly searching for DM particles via their elastic scattering off nuclei. The CRESST (cryogenic rare event search with superconducting thermometers) experiment located in the Gran Sasso underground laboratory LNGS operates scintillating CaWO_4 single crystals as cryogenic detectors. A particle interaction in such a crystal produces a heat (phonon) signal which is detected in a superconducting phase transition thermometer directly connected to the crystal. This signal provides precise information on the energy deposited. Simultaneously, scintillation light emitted by the crystal is detected by a separate light absorber. The light signal depends on the type of interacting particle and can, therefore, be used to discriminate background events from potential recoils of DM particles. The optical quality of CaWO_4 crystals is of importance to strengthen this discrimination ability. To achieve further background reduction, a high radiopurity is required for all materials in the vicinity of the detectors as well as for the CaWO_4 target crystals. Improving the quality of CaWO_4 crystals, in particular their radiopurity, is the main topic of the present thesis.

In the past, CaWO_4 crystals operated in the CRESST experiment were supplied by external companies. To be able to improve the various production steps with respect to the radiopurity and the optical quality of the crystals, a crystal growth facility was installed at the Technische Universität München (TUM) in 2007. For several years, CaWO_4 crystals have now successfully been produced at TUM. This includes the production of CaWO_4 powder from the raw materials CaCO_3 and WO_3 , the crystal growth in a Czochralski furnace, as well as post-growth treatments like annealing in pure oxygen atmosphere, cutting, and polishing. During the annealing procedure, the number of oxygen-related defects is reduced. Adding an extra annealing step leads to a 1.5-3 times larger attenuation length at 430 nm, the wavelength of the maximal intensity of the scintillation light.

CRESST-II Phase 2 (2013-2015) used TUM-grown crystals for the first time for a DM search. The much better radiopurity of these crystals compared to commercial crystals motivated the collaboration to involve TUM-grown crystals in the majority of the detectors installed in CRESST-III Phase 1 which started data taking in summer 2016. Most of these crystals were produced as part of the present work.

For the upcoming CRESST-III Phase 2 the collaboration aims at a further improvement of the radiopurity. The main part of the present work focuses on the development of methods to reduce the intrinsic contamination level of CaWO_4 crystals as well as on the measurement of trace impurities. A careful selection of the raw materials and a handling in a clean environment were ensured as the starting point for all further measures. One method intensely studied is the chemical purification of the raw materials. In a first version (2015), uranium and thorium isotopes were removed from the dissolved CaCO_3 powder via liquid-liquid extraction. Measurements show a reduction of the thorium and

uranium contamination in the CaCO_3 powder by at least a factor of ~ 7 and ~ 35 , respectively. In the second version (2016), the liquid-liquid extraction was improved and a new method to produce CaWO_4 powder via a precipitation reaction was developed. This procedure allows a further reduction of the contamination level via additional purification steps based on coprecipitation and on washing the final CaWO_4 powder in alkaline solution. Measurements by means of inductively coupled plasma mass spectrometry (ICP-MS) and high-purity germanium (HPGe) spectroscopy at LNGS and at the Canfranc underground laboratory LSC show a successful application of all purification steps as well as a significantly improved radiopurity of the final CaWO_4 powder. The contamination level is reduced by at least a factor of 2-4 for ^{228}Th and improvement factors of at least 3 and 5.5 are achieved for the activities of ^{238}U and ^{226}Ra , respectively. As Czochralski crystal growth is – due to segregation – a cleaning process itself, the radiopurity of CaWO_4 crystals can also be improved via (multiple) recrystallization. In the present work, a feasibility study was performed for measuring the segregation coefficients of various isotopes via the gradient of contamination within one raw crystal. The study suggests that a correct determination of the segregation coefficient can be achieved when the initial activity is high (order of 10 mBq/kg) or when the segregation coefficient is larger than 0.5. Lower values can only be reliably determined when the initial activity is known.

TUM73, a crystal grown from the raw materials to which the first version of CaCO_3 purification was applied, is currently operated in CRESST-III Phase 1. A radiopurity analysis of a partial data set with an exposure of ~ 2.5 kg days per detector was performed for two TUM73 detector crystals in comparison to two detector crystals produced from a different, non-purified powder batch (TUM56). The analysis includes an investigation of background rates mainly caused by β -decays and γ -radiation occurring in the detectors and their surroundings as well as the determination of activities originating from α -interactions within the crystals. In the energy range (10-40) keV, the averaged rates were determined to be (3.85 ± 0.16) counts/(kg keV day) and (4.13 ± 0.16) counts/(kg keV day) for TUM56 and TUM73 detector crystals, respectively. In case of TUM73, an internal ^{210}Pb contamination with a total activity of ~ 0.76 mBq/kg contributes ~ 0.2 counts/(kg keV day) to the background rate in the mentioned energy window. The total α -activities calculated between 4 MeV and 7 MeV are ~ 3.5 mBq/kg (TUM73) and ~ 2.0 mBq/kg (TUM56). The contamination level in TUM73 crystals is slightly higher than in TUM56 detector crystals which can be attributed to the different batches of raw materials the two crystals were produced from. Despite of this higher total level of impurities, a lower activity of ^{232}Th - and ^{238}U -decays is measured for a TUM73 detector compared to a TUM56 detector. This indicates a successful reduction of uranium and thorium during the purification of version 1 applied to the raw materials of TUM73.

Zusammenfassung

Eine der größten Forschungsfragen der heutigen Physik betrifft die Zusammensetzung von dunkler Materie (DM). Obwohl klare Indizien für die Existenz von dunkler Materie auf verschiedenen Größenskalen des Universums zu finden sind, konnte das zugehörige Teilchen bisher noch nicht nachgewiesen werden. Ein experimenteller Ansatz ist die direkte Suche nach Kernrückstößen von DM-Teilchen. Das CRESST-Experiment befindet sich im Gran Sasso Untergrundlabor LNGS und betreibt szintillierende CaWO_4 -Einkristalle als Tieftemperatur-Detektoren. Eine Teilchenwechselwirkung in einem solchen Kristall produziert ein Wärmesignal, welches mit Hilfe eines supraleitenden Phasenübergangsthermometers ausgelesen wird und präzise Informationen über die deponierte Energie liefert. Gleichzeitig emittiert der Kristall Szintillationslicht, das von einem separaten Lichtabsorber detektiert wird. Das Lichtsignal hängt von der Art des wechselwirkenden Teilchens ab und kann daher für die Unterscheidung zwischen Untergrundeignissen und potentiellen Rückstößen von DM-Teilchen verwendet werden. Die optische Qualität von CaWO_4 -Kristallen spielt hierbei eine große Rolle. Um eine weitere Reduzierung von Untergrundeignissen zu erzielen, ist außerdem für alle Materialien, die sich in der Umgebung der Detektoren befinden, sowie für die CaWO_4 -Kristalle selbst, eine hohe Radioisotopen-Reinheit erforderlich. Eine Verbesserung der Qualität von CaWO_4 -Kristallen, insbesondere bezüglich ihrer Reinheit, ist das Hauptthema dieser Arbeit.

In der Vergangenheit wurden CaWO_4 -Kristalle von externen Firmen bezogen. Um eine Verbesserung der verschiedenen Produktionsschritte hinsichtlich der Reinheit und der optischen Qualität der Kristalle zu ermöglichen, wurde 2007 eine Czochralski-Anlage zur Kristallzucht an der Technischen Universität München (TUM) installiert. Die Herstellung der Kristalle an der TUM beinhaltet die Synthese von CaWO_4 -Pulver aus den Rohmaterialien CaCO_3 und WO_3 , die Kristallzucht sowie die weitere Bearbeitung, zu welcher das Tempern der gezogenen Kristalle in reiner Sauerstoff-Atmosphäre gehört. Durch die Temper-Prozedur wird die Anzahl Sauerstoff-bezogener Defekte verringert. Zusätzliches Tempern kann die Abschwächlänge bei 430 nm, der Wellenlänge des Intensitäts-Maximums des Szintillationslichts, um einen Faktor 1.5-3 steigern.

In CRESST-II Phase 2 (2013-2015) wurden TUM-Kristalle zum ersten Mal zur DM Suche verwendet. Im Vergleich zu kommerziellen Kristallen weisen sie eine verbesserte Radioisotopen-Reinheit auf, was die CRESST-Kollaboration dazu motivierte, hauptsächlich TUM-Kristalle, die im Rahmen dieser Arbeit produziert wurden, für CRESST-III Phase 1 (seit Sommer 2016) zu benutzen.

Eine weitere Verbesserung der Radioisotopen-Reinheit soll in der bevorstehenden Phase 2 von CRESST-III erreicht werden. Der Hauptteil der vorliegenden Arbeit konzentriert sich auf die Entwicklung von Methoden zur Reduzierung intrinsischer Kontaminationen in CaWO_4 -Kristallen sowie auf die Messung von Spurenverunreinigungen. Eine sorgfältige Auswahl der Rohmaterialien und deren Handhabung in einer sauberen Umgebung wurden für alle weiteren Maßnahmen als Grundvoraussetzungen umgesetzt. Eine Methode, die intensiv untersucht wurde, ist die chemische Reinigung der Rohmaterialien. In einer ersten Version (2015) wurde in Lösung gebrachtes CaCO_3 -Pulver per Extraktion

von Uran- und Thorium-Isotopen gereinigt. Messungen zeigen, dass dadurch eine Reduzierung der Thorium- und Uran-Kontamination im CaCO_3 -Pulver um Faktoren $\gtrsim 7$ beziehungsweise $\gtrsim 35$ erzielt werden kann. In Version 2 (2016) wurde die Extraktions-Prozedur verbessert und eine neue Produktionsmethode für CaWO_4 -Pulver mittels einer Fällungsreaktion entwickelt. Diese Methode ermöglicht die Anwendung weiterer Reinigungsschritte basierend auf Mitfällung und Spülen des CaWO_4 -Pulvers in basischer Lösung. Messungen mit ICP-MS-Instrumenten und hochreinen Germanium-Detektoren am LNGS und am Canfranc Untergrundlabor LSC bestätigen eine erfolgreiche Anwendung aller einzelnen Reinigungsschritte sowie eine wesentlich verbesserte Radioisotopen-Reinheit des hergestellten CaWO_4 -Pulvers. Die Kontaminationsniveaus von ^{228}Th , ^{238}U und ^{226}Ra konnten um Faktoren von mindestens 2-4, 3 und 5.5 erniedrigt werden.

Da die Kristallzucht mit der Czochralski-Methode aufgrund von Segregation eine Reinigungsprozedur ist, kann die Radioisotopen-Reinheit von CaWO_4 -Kristallen auch durch (mehrfache) Rekristallisierung verbessert werden. In der vorliegenden Arbeit wurde eine Machbarkeitsstudie für die Bestimmung von Verteilungskoeffizienten durchgeführt, die auf dem Konzentrations-Gradienten im Rohkristall basiert. Laut dieser Studie können Verteilungskoeffizienten korrekt bestimmt werden, wenn die Anfangsaktivität größer als 10 mBq/kg ist oder wenn der Verteilungskoeffizient $\gtrsim 0.5$ ist. Niedrigere Werte können nur zuverlässig ermittelt werden, wenn die Anfangsaktivität bekannt ist.

Der Kristall TUM73, der aus gereinigtem CaCO_3 -Pulver (Version 1) hergestellt wurde, wird momentan in CRESST-III Phase 1 als Detektor betrieben. Eine Analyse der Radioisotopen-Reinheit wurde für zwei TUM73 Detektor-Kristalle im Vergleich zu zwei Detektoren des Rohkristalls TUM56, der aus einer anderen, nicht-gereinigten Pulver-Charge stammt, durchgeführt. Die Analyse (~ 2.5 kg Tage pro Detektor) beinhaltet die Untersuchung von Untergrund-Raten, die hauptsächlich von β -Zerfällen und γ -Strahlung hervorgerufen werden, welche in den Detektoren und deren Umgebung auftreten. Außerdem wurden Aktivitäten, die von α -Zerfällen im Kristall verursacht werden, bestimmt. Im Energiebereich (10 - 40) keV ergaben sich totale gemittelte Untergrund-Zählraten von (3.85 ± 0.16) Ereignissen/(kg keV Tag) und (4.13 ± 0.16) Ereignissen/(kg keV Tag) im Falle der TUM56 beziehungsweise TUM73 Detektor-Kristalle. Eine interne Kontamination mit ^{210}Pb (~ 0.76 mBq/kg), die in TUM73 Kristallen vorhanden ist, trägt mit ~ 0.2 Ereignissen/(kg keV Tag) zur Untergrund-Rate im erwähnten Energiefenster bei. Die totalen α -Aktivitäten im Energiebereich (4 - 7) MeV betragen ~ 3.5 mBq/kg (TUM73) und ~ 2.0 mBq/kg (TUM56). Das Kontaminationsniveau in TUM73 ist im Vergleich zu TUM56-Kristallen leicht erhöht, was der Reinheit der jeweiligen Charge von Rohmaterialien, aus denen die Kristalle produziert wurden, zugewiesen werden kann. Gegenläufig dazu ist die Aktivität durch ^{232}Th - und ^{238}U -Zerfälle im Falle von TUM73 Detektor-Kristallen reduziert. Dieses Ergebnis weist darauf hin, dass eine Reinigung von Uran und Thorium im ursprünglichen CaCO_3 -Pulver erzielt werden konnte.

Contents

1. Hunting Dark Matter	1
1.1. Evidences for Dark Matter	1
1.1.1. Rotation Curves	1
1.1.2. Gravitational Lensing and the Bullet Cluster	2
1.1.3. Cosmic Microwave Background	2
1.1.4. Structure Formation	3
1.2. Recent Results	3
1.2.1. Baryon-Dominated Disk Galaxies	4
1.2.2. Dark Matter Halo Boundaries	4
1.3. Dark Matter Candidates	4
1.3.1. Requirements for Dark Matter Particles	5
1.3.2. Dark Matter Particles beyond the Standard Model	5
1.4. Direct Search for Dark Matter	6
1.4.1. Dark Matter Rate	7
1.4.2. Experimental Approaches	8
1.4.3. Backgrounds	11
2. The CRESST Experiment	15
2.1. Experimental Setup	15
2.1.1. Background Shielding	15
2.1.2. Dilution Refrigerator	17
2.2. Working Principle	17
2.2.1. Cryogenic Detector	17
2.2.2. Signal Read-Out	18
2.2.3. Detector Operation and Stabilization	20
2.2.4. Data Acquisition	21
2.2.5. Detector Module	21
2.2.6. Background Discrimination and Region of Interest	23
2.3. Results of CRESST-II Phase 2	25
2.3.1. Veto for Surface Backgrounds	26
2.3.2. Integration of TUM-Grown Crystals	28
2.3.3. Low-Threshold Analysis	29
2.3.4. Detector Modules of the Crystals TUM40 and Lise	30
2.4. CRESST-III	32
2.4.1. CRESST-III Phase 1	34
2.4.2. Projected Sensitivity of CRESST-III Phase 1 and Phase 2	34

3. Production of CaWO₄ Single Crystals	37
3.1. Properties of CaWO ₄	38
3.2. Production of CaWO ₄ Powder	40
3.3. Crystal Growth via the Czochralski Method	43
3.3.1. Working Principle	43
3.3.2. Growth Preparation and Seeding	47
3.3.3. Parameter Control	49
3.3.4. After-Heater	53
3.4. Post-Growth Treatment	53
3.5. Crystals Grown in the Present Work	54
4. Optical Characterization of CaWO₄ Crystals	57
4.1. Photoelasticity	57
4.1.1. Theory and Setup	57
4.1.2. Internal Stresses of CaWO ₄ Crystals	61
4.2. Transmittance	65
4.2.1. Method and Setup	65
4.2.2. Measured Transmittances of CaWO ₄ Crystals	69
4.3. Future Developments	76
5. Improving the Radiopurity of CaWO₄ Crystals	79
5.1. Introductory Remarks	79
5.2. Handling of the Raw Materials	81
5.3. Chemical Purification of the Powders and Trace Impurity Analysis	84
5.3.1. Separation Techniques	85
5.3.2. Purification of CaCO ₃ Powder via Solvent Extraction	87
5.3.3. CaWO ₄ Production via Precipitation and Coprecipitation	93
5.3.4. Washing of the CaWO ₄ Powder	98
5.3.5. Combination of all Purification Steps	102
5.4. Segregation of Impurities during Crystal Growth	104
5.4.1. Principle of Segregation	105
5.4.2. Segregation Measurements	107
5.4.3. Feasibility Study for the Determination of Segregation Coefficients	108
6. Analysis Methods applied to Data of CRESST-III Phase 1	117
6.1. Pulse Parameters	117
6.2. Template Fit	120
6.2.1. Truncated Template Fit	120
6.2.2. Correlated Template Fit	122
6.2.3. Templates in this Work	123
6.3. Energy Calibration	123
6.3.1. ⁵⁷ Co Calibration	123
6.3.2. Test Pulse Calibration	125
6.4. Analysis Cuts	128
6.4.1. Stability Cut	128
6.4.2. Invalid Event Classes	130

6.4.3.	Data Quality Cuts	132
6.4.4.	Removing Stick-Related Events	133
6.4.5.	RMS Cut	134
6.4.6.	Muon Veto Cut	135
6.5.	Survival Probability	135
6.6.	Dedicated Methods for the α -Analysis	137
6.7.	Activity Determination	141
7.	Results of the Radiopurity Analysis of CRESST-III Phase 1	143
7.1.	Radiopurity of TUM-Grown Crystals	143
7.1.1.	Background Spectrum below 100 keV	143
7.1.2.	α -Spectrum	146
7.2.	Analyzed CRESST-III Phase 1 Detectors and Data Set	148
7.3.	e^-/γ Band	150
7.3.1.	External Radiation	150
7.3.2.	Background Rates	150
7.3.3.	Internal ^{210}Pb Contamination	152
7.3.4.	Cosmogenic Activation Lines	153
7.3.5.	Background Spectra up to 700 keV	154
7.4.	α -Events	155
7.4.1.	Total α -Activities	156
7.4.2.	Single α -Activities	159
7.5.	Discussion	161
8.	Summary and Conclusions	167
9.	Outlook	171
A.	Reflective and Scintillating Foil	175
B.	Additional Aspects of CaWO_4 Crystal Growth	179
B.1.	Seed and Seed Holder Geometry	179
B.2.	Growth Abortion	181
B.3.	Crystal Defects	182
B.4.	CaWO_4 Powder used for TUM73	183
B.5.	Grown Crystal Ingots	184
C.	Measurement Methods for Trace Impurities	189
C.1.	γ -Ray Spectroscopy with High-Purity Germanium (HPGe) Detectors	189
C.2.	Neutron Activation Analysis (NAA)	189
C.3.	Atomic Absorption Spectroscopy (AAS)	190
C.4.	Inductively Coupled Plasma Mass Spectrometry (ICP-MS)	190
C.5.	Laser Ablation Inductively Coupled Plasma Mass Spectrometry (LA-ICP-MS)	191
C.6.	Accelerator Mass Spectrometry (AMS)	191
D.	Analysis Certificates	193

E. Analysis and Cut Parameters	203
Bibliography	207
Acknowledgements	219

1. Hunting Dark Matter

The nature of the so-called dark matter (DM) is one of the biggest mysteries of today's fundamental physics. Dark matter denotes an up to now unidentified type of matter which does not emit or interact with electromagnetic radiation. It is, however, observable through gravitational effects of celestial bodies. The term "dark matter" was already mentioned in 1922 when J. Kapteyn made a first attempt for a general theory that can explain the distribution of masses, forces and velocities in the stellar system [1]. Today there are many evidences on all scales of the Universe for the existence of dark matter (see section 1.1) and more and more facts have been revealed within the most recent investigations (section 1.2). However, its composition is still unknown. Different possibilities including candidates for a DM particle are described in section 1.3. Experimental approaches to search for such particles are given in section 1.4. As the expected interaction rate with the ordinary matter of such experiments is extremely low, this section concludes with possible background sources for an experimental search.

1.1. Evidences for Dark Matter

In 1933 F. Zwicky gave a first strong indication that the density of dark matter exceeds the one of luminous matter. In his investigations of the Coma galaxy cluster he found a discrepancy between the mass estimated from the motion of galaxies and the mass calculated on the basis of the brightness and number of galaxies [2]. Although Zwicky overestimated the amount of this "missing" matter by about two orders of magnitude, his main statement still remains: the great majority of matter seems to be dark. This first observation was followed by many other evidences for the existence of dark matter. The most important ones are introduced in the following.

1.1.1. Rotation Curves

One of the first evidences for dark matter comes from the investigation of velocities of celestial bodies within spiral galaxies. According to Newtonian dynamics, their rotational velocity v_{rot} can be calculated as

$$v_{\text{rot}} = \sqrt{\frac{GM(r)}{r}} \quad (1.1)$$

with G being the gravitational constant, r the radial distance of the object from the center and $M(r)$ the total mass contained within this radius. The majority of luminous matter in a spiral galaxy is clustered in the center (bulge), thus leading to a rise of velocities there. With luminous matter alone, $M(r)$ is nearly constant outside the bulge and there

the proportionality $v_{\text{rot}} \propto 1/\sqrt{r}$ is expected to hold. However, rotational properties of spiral galaxies first investigated in 1980 resulted in the observation that the velocity is not falling beyond the optical disk [3]. Instead, the orbital velocity stays constant hinting either towards a modified gravity treated in theories like modified Newtonian dynamics (MOND) [4] or towards an additional, significant mass contribution beyond the optical image. A possible explanation is a halo consisting of dark matter surrounding the galaxies as, e.g., calculated for the galaxy M33 in [5].

1.1.2. Gravitational Lensing and the Bullet Cluster

Apart from measuring velocity distributions within galaxies, the mass of a galaxy cluster can be determined via gravitational lensing. This method is based on the fact that – in conformity with the general theory of relativity of A. Einstein – light is bent around massive objects making gravity to act as an optical lens [6]. Via the distortion of the light from a distant object, the mass density profile of a galaxy cluster lying in the line of sight between source and observer can be calculated. Mass-to-light ratios determined by gravitational lensing confirm the discrepancy between luminous and gravitational mass as obtained by velocity measurements.

Even stronger evidences for the existence of dark matter are merger of two galaxy clusters as, e.g., the so-called Bullet cluster [7]. The composite image of figure 1.1 (a) shows the different components of the clusters. Whereas collisions between galaxies and stars (optical image) are negligible, the interstellar gas clouds of both clusters concentrate in the center due to electromagnetic interactions which emit X-rays (pink). This gas is the main mass contribution to the luminous matter. However, the mass distribution obtained by gravitational lensing (blue) shows two mass centers which are not coinciding with the gas.

This evidence for dark matter is independent of details of Newtonian gravity and remains difficult to be explained by MOND-theories [4].

1.1.3. Cosmic Microwave Background

The cosmic microwave background (CMB) – the relic radiation from the era of recombination $\sim 380\,000$ years after the big bang – was predicted in the 1940s and inadvertently discovered in 1964 by A. Penzias and R. Wilson [8]. This isotropic radiation has been precisely measured by different experiments and features the best-known black body spectrum with a temperature of $T = 2.725\text{ K}$ [9]. However, imprinted on the temperature spectrum are tiny fluctuations of the order of $\frac{\Delta T}{T} \sim 10^{-5}$ as shown in the all-sky map of figure 1.1 (b) measured by ESA’s Planck satellite [10]. The anisotropies correspond to regions of slightly different density and represent the seeds of the structures observed today. From these temperature fluctuations the relevant parameters of the standard cosmological model can be derived. The most precise values are given by the Planck’s 2015 results of the full data set. Whereas only $\sim 5\%$ of the total energy density in the Universe is composed of baryonic matter, the density of cold (non-relativistic) dark matter contributes $\sim 26\%$ (depending on the analysis). The main part of $\sim 69\%$ is due to the completely unknown dark energy [11]. The value obtained for the baryonic

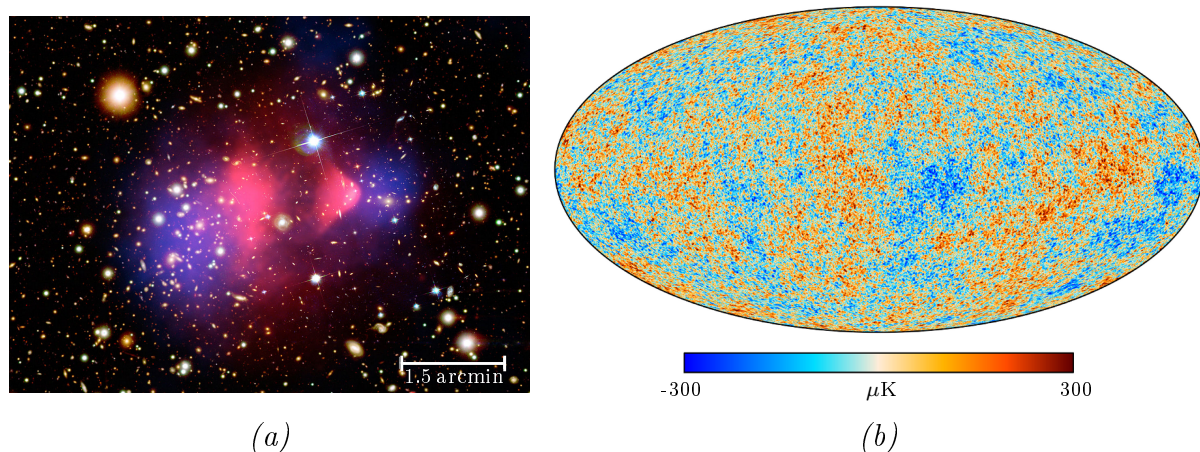


Figure 1.1.: *Evidences for the existence of dark matter: (a) shows the Bullet Cluster, a merger of two galaxy clusters [7]. The optical image of stars and galaxies was taken by the Magellan and Hubble Space telescope (credit: NASA/STScI; Magellan/U.Arizona/D.Clowe et al.). The main mass contribution of the galaxy clusters are gas clouds. Their X-ray emission as recorded by the Chandra Telescope is shown in pink (credit: NASA/CXC/CfA/ M.Markevitch et al.). Its position does, however, not coincide with the two mass centers (overlain in blue) measured by gravitational lensing (credit: NASA/STScI; ESO WFI; Magellan/U.Arizona/ D.Clowe et al.). (b) shows the cosmic microwave background radiation as detected by the Planck satellite [10]. The radiation is isotropic except for tiny temperature fluctuations of the order of $\frac{\Delta T}{T} \sim 10^{-5}$ (color-coded from blue to red). They can be used to precisely determine a cold DM density of $\sim 26\%$ [11].*

matter density is consistent with predictions from the big bang nucleosynthesis [12].

1.1.4. Structure Formation

The tiny temperature anisotropies visible in the CMB were the seeds for stars, galaxies and large-scale structures in the Universe. Computer simulations as, e.g., the MultiDark Simulation [13], are able to model the time evolution of the Universe's structures in the presence of dark matter and compare the output to sky surveys like the Sloan Digital Sky Survey [14]. These simulations confirm that baryonic matter alone is not sufficient at all to reproduce the structures visible today. Only when a certain amount of cold (and/or warm) dark matter is included in the simulation the resulting structure is comparable to our observed Universe [15].

1.2. Recent Results

Gravitational effects hinting towards the existence of dark matter have been investigated for more than 50 years. The improved methods and more sensitive instruments of today's research enable physicists to derive more accurate and detailed information about, e.g., the DM distribution in our Universe.

1.2.1. Baryon-Dominated Disk Galaxies

Flat rotation curves as explained in section 1.1.1 show that dark matter dominates the total mass of galaxies in our local Universe. Recent observations of ESO's very large telescope (VLT) in Chile revealed that galaxies of the early Universe exhibit a different behaviour. Massive, star-forming galaxies at the peak of galaxy formation about 10 billion years ago were found to rotate more slowly in their outer regions than in the regions close to the core, i.e. the corresponding rotation curves are not constant but decrease with increasing distance [16]. This suggests that these galaxies of the early Universe are dominated by baryonic matter mainly consisting of gas which efficiently condensed at the centers of the DM halos. Dark matter itself, on the other hand, is much more spread out than in the local Universe. Furthermore, large velocity distributions in early, gas-rich spiral galaxies appear to affect the rotation curves, as well.

1.2.2. Dark Matter Halo Boundaries

The shape of DM halos can be studied in more detail by investigating the distribution and colours of galaxies within galaxy clusters. Theoretically, analytical models and computer simulations predict an abrupt steepening of the halo density profiles due to a "splashback effect" [17] where matter having been accreted by the DM halo slows down and starts to orbit leading to the build-up of matter at the edge of the halo.

The density profiles of galaxy clusters were investigated with data from the Sloan Digital Sky Survey and confirm experimentally the sharp halo boundary of a cluster [18]. In addition to the distribution of galaxies, galaxy colors can be analyzed. Gas-rich blue galaxies lose gas when falling into a DM halo and appear red afterwards. An abrupt change of galaxy colors is observed right at the edge of galaxy distributions confirming the sharp drop of the DM halo.

1.3. Dark Matter Candidates

Strong indications for the existence of dark matter can be found on all scales of the Universe at any time (section 1.1). This naturally raises questions about its origin and composition. Despite of extensive searches, dark matter has so far not been detected and its nature remains still unknown. Several theories suggest modifications of Einstein's general relativity or of Newtonian dynamics [4] in order to explain the gravitational effects observed. However, these theories cannot conclusively explain all DM phenomena on different scales of the Universe and are, for example, contradicted by the observation of the Bullet cluster.

Another idea is that dark matter consists of non-luminous ordinary baryonic matter. Massive compact halo objects (MACHOs) such as black holes, neutron stars and brown dwarfs were discovered via gravitational microlensing in dedicated surveys [19]. The total mass of these objects alone, however, was found to be too small to explain the observed effects. Recently, after gravitational waves caused by two merging black holes had been detected by the LIGO experiment [20], the idea of dark matter consisting of primordial black holes (PBH) has been reconsidered and has been discussed in, e.g., [21].

Constraints on the mass of PBHs as possible DM candidate are, e.g., set by gravitational microlensing [22, 23] or by dwarf galaxy dynamics [24]. However, for certain masses and depending on the exact values of the astrophysical parameters included in the constraints, it is still possible that PBHs constitute 100 % of the existing dark matter.

1.3.1. Requirements for Dark Matter Particles

Also the investigation of the CMB and simulations of structure formation suggest an unknown form of non-baryonic matter. The particles this matter consists of have to fulfill a number of requirements:

1. As their effect is visible in the CMB as well as in the structures present today, DM particles have to be stable or at least would have to exhibit a lifetime of the order of the age of the Universe.
2. DM particles seem to be dark and, thus, do not interact electromagnetically which means that they must be neutral.
3. Since no interaction between known matter and dark matter has been observed so far, the interaction cross section has to be very small.
4. Non-relativistic (cold) DM particles are required to explain the structures observed in the Universe of today.

The only particles contained in the standard model (SM) of particle physics which fulfill at least part of these requirements are neutrinos. However, as the sum of the neutrino masses is constrained to $\Sigma m_\nu < 0.23 \text{ eV}$ [11], their energy density is limited to a value much too small to account for the whole DM density [25]. Furthermore, neutrinos are hot dark matter due to their relativistic nature and cannot have formed the observed structures of the Universe.

1.3.2. Dark Matter Particles beyond the Standard Model

All observations hint towards the existence of new particles beyond the standard model. Different theories and suggestions for DM particles such as axions, or sterile neutrinos are explained in detail in [12, 25]. The present work concentrates on a few well-motivated particle candidates which will shortly be introduced in the following.

Weakly Interacting Massive Particles

A weakly interacting massive particle (WIMP) is a particle with a mass of $\mathcal{O}(10 \text{ GeV}/c^2 - \text{TeV}/c^2)$ and an interaction cross section that is on the scale of the electroweak interaction [25]. WIMPs could have been produced through thermal freeze-out in the early Universe. Initially, the Universe was dense and hot so that all particles were in thermal equilibrium. When the temperature of the expanding Universe dropped below the mass of the WIMPs, generation was suppressed but annihilation was still possible leading to an exponential decrease of the abundance. Due to the further expansion of the Universe, the density

became so small that the WIMPs could not find each other to annihilate any more. In this status, their number density approached a constant – the thermal relic density. If WIMPs exist and are stable, this thermal relic density is consistent with the one required for dark matter – a fact that is often referred to as “WIMP miracle” [25]. A possible WIMP candidate is the lightest supersymmetric particle (LSP) predicted in supersymmetric extension theories of the standard model [26]. The so-called Lee-Weinberg bound excludes WIMP masses below $\sim 2 \text{ GeV}/c^2$ as the resulting relic density would lead to such a high total density that the Universe could never have reached its present age [27].

Light Dark Matter Particles

Recently also light dark matter with masses of $\mathcal{O}(1 \text{ GeV}/c^2)$ down to $\mathcal{O}(1 \text{ keV}/c^2)$ gained more and more interest. There exists a number of alternative models which are compatible with the observed relic density. Asymmetric dark matter (ADM) models suggest that – similarly to the baryonic sector – the present DM density might originate from a DM particle-antiparticle asymmetry. In order to obtain the observed DM abundance, such theories predict DM particle masses of $\mathcal{O}(1 \text{ GeV}/c^2)$ [28].

DM particles might also reside in a hidden sector [29, 30], where they do not feel any electroweak forces. Apart from gravitational interaction, communication with the visible sector is possible via so-called portals or connector sectors containing particles which are charged under both, the visible and the hidden sector. These DM candidates have masses in the range $10 \text{ MeV}/c^2$ - $10 \text{ GeV}/c^2$.

So-called Forbidden DM theories suggest thermal relic particles, which are naturally light and annihilate into heavier states in the early Universe. Such annihilations, for example into dark photons, vanish at zero temperature. These theories accommodate a wide range of DM masses from the electroweak scale down to a few keV/c^2 [31].

In cases where a two-body DM annihilation is kinematically forbidden during thermal freeze-out, a $3 \rightarrow 2$ annihilation channel might still be allowed [32]. In order to achieve the necessary cross section for the correct thermal relic density, light DM particles with possible masses extending down to the sub-GeV range are required. $3 \rightarrow 2$ processes can, e.g., play a role in scenarios of strongly interacting massive particles (SIMPs) [33].

For all described DM candidates (and also for further particle models not listed here), (weak) interactions with standard model particles are possible, in some cases via an additional mediator. In this way, DM particles can be detected in experimental searches.

1.4. Direct Search for Dark Matter

On the experimental side, different approaches to either produce DM particles, search for secondary particles originating from dark matter or directly search for DM particles are realized.

Production at Colliders

Highly energetic collisions of SM particles as generated, e.g., at the large hadron collider (LHC) could create DM particles. However, a direct detection is not feasible due to the low interaction cross section of ordinary and dark matter. Therefore, collider-based experiments search either for missing transverse momenta or for an additional signal produced simultaneously in a second-order process. The huge variety of possible signatures in the different production channels makes a search for dark matter rather complicated. Experiments like ATLAS [34] and CMS [35] set limits on DM particle mass and cross section, but their results are strongly dependent on the particular model. Though collider-based experiments have the potential to discover DM particles, they are not able to tell whether these particles have sufficiently long life times. Therefore, also other types of DM search experiments are necessary.

Indirect Detection

Indirect searches look for secondary SM particles (e.g. γ -radiation, neutrinos, positrons) created by the annihilation or decay of DM particles [36]. Target areas are, for example, the galactic center or satellite galaxies of the Milky Way where a high DM density and/or a low background originating from astrophysical sources is expected. The Fermi spacecraft containing the large area telescope (Fermi-LAT) and the IceCube experiment with the DeepCore subdetector search for γ -ray emission [37] and neutrinos [38] from DM annihilation, respectively. Both, γ -rays and neutrinos, have the advantage to not be influenced by magnetic fields making the determination of a possible source feasible. On the other hand, experiments measuring charged particles (especially anti-particles) in cosmic rays have to rely on a low background or good background suppression. An example is the alpha magnetic spectrometer (AMS-02) operated on the international space station conducting precision measurements of, e.g., the proton flux or of the positron fraction in primary cosmic rays [39, 40]. Up to now, no unambiguous evidence for a positive DM signal has been found.

Direct Detection

The class of experiments relevant for the present work are direct DM searches. The following sections will focus on such experiments aiming at the detection of a direct interaction between DM particles and ordinary matter via elastic DM particle (χ) - nucleon scattering.

1.4.1. Dark Matter Rate

Measurements of the rotation curve of the Milky Way suggest the existence of a DM halo surrounding our galaxy. The calculation of the local dark halo density ρ_χ depends on the choice of the DM halo profile. To be able to compare different experiments, a value of $(0.3 \pm 0.1) \text{ GeV}/c^2 \cdot \text{cm}^{-3}$ [41] has generally been adopted in the direct DM search community. However, also higher values can be found, e.g., in [42]. Assuming this density and a relative velocity $v \sim 220 \text{ km/s}$ between dark matter and a target on Earth [41], the

DM flux $\Phi = \frac{\rho_\chi}{m_\chi} \cdot v$ can be calculated to be of the order of $10^5 \left(100 \frac{\text{GeV}/c^2}{m_\chi}\right) \text{cm}^{-2} \text{s}^{-1}$. Thereby, m_χ denotes the mass of a DM particle.

To calculate the DM interaction rate R in an earthbound detector, the number of target nuclei defined as ratio of the total target mass M_{target} and the mass of a nucleus m_N as well as the (in general velocity dependent) cross section $\sigma(v)$ come into play:

$$R = \Phi \cdot \frac{M_{\text{target}}}{m_N} \cdot \sigma(v) \quad (1.2)$$

In order to evaluate the different factors, astrophysics as well as nuclear physics provide input for, e.g., the velocity distribution and the form factor of the element used as target material, respectively. For a detailed description see, e.g., [43]. With the parameters known today, very low total interaction rates of $R \lesssim 0.1 \text{kg}^{-1} \text{day}^{-1}$ are expected [44]. A high total target mass and long measurement times are, hereby, beneficial but not sufficient. A search for such rare events can only be successful when all possible backgrounds as described in section 1.4.3 are low enough.

The expected spectral shape dR/dE_R of the event distribution arising by χ -nucleon interactions in a detector is a featureless energy spectrum exponentially rising towards lower energies. The maximal recoil energy $E_{R,\text{max}}$ can be kinematically estimated via momentum conservation:

$$2\mu_N \cdot v = \sqrt{2m_N \cdot E_{R,\text{max}}} \quad \longrightarrow \quad E_{R,\text{max}} = \frac{2\mu_N^2 \cdot v^2}{m_N} \quad (1.3)$$

Hereby, $\mu_N = \frac{m_N \cdot m_\chi}{m_N + m_\chi}$ denotes the reduced mass (in the center-of-mass frame) of nucleus and DM particle. Assuming a DM particle mass in the order of 20 GeV leads to $E_{R,\text{max}} \sim \mathcal{O}(10 \text{keV})$. This means that the achievable energy threshold of the detector is a crucial parameter to increase the expected count rate. Figure 1.2 shows the effect of a threshold reduction from 10 keV (dashed) to 0.3 keV (solid) on the DM count rate exemplarily for the three nuclei oxygen (red), calcium (blue) and tungsten (green). For all elements, the lower threshold not only enhances the sensitivity for lighter DM particles but increases also the expected count rate at a certain mass [45]. Furthermore, the interaction cross section scales quadratically with the atomic mass number A . More energy has to be transferred to heavier elements like tungsten in order to be detectable (corresponds to a higher DM particle mass) but then the count rate dominates above lighter elements as oxygen or calcium. This means, a combined target material like CaWO_4 is able to separate between different DM particle masses when a discrimination between the nuclei it scatters off is achievable.

1.4.2. Experimental Approaches

Three signal channels listed in the blue boxes of figure 1.3 are mainly used to detect the tiny energy depositions of maximal $\mathcal{O}(10 \text{keV})$ (compare equation 1.3): heat (phonons), ionization, or scintillation. Selected experiments and their target materials are exemplarily included in figure 1.3 next to the read-out channel they use. Most of them are depicted between the blue boxes which means they exploit even two of the signal channels

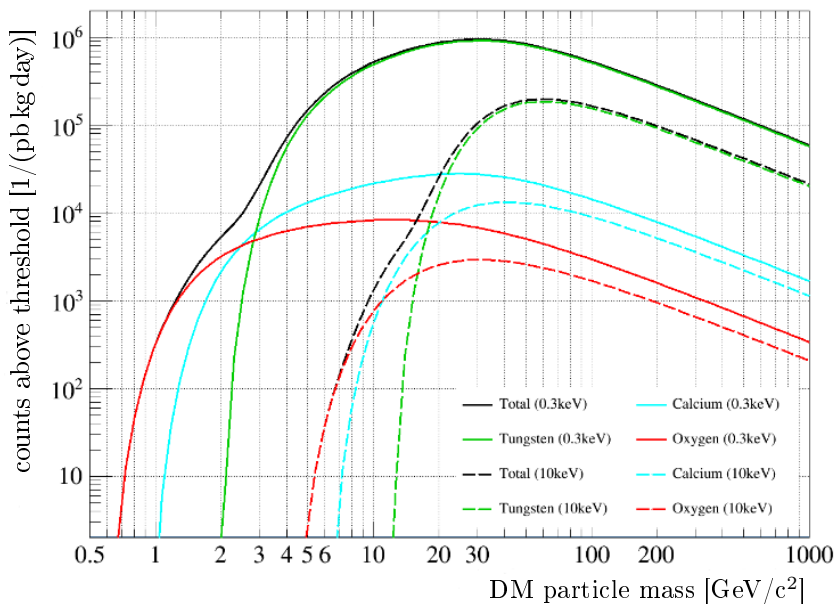


Figure 1.2.: Effect of the energy threshold on the DM count rate shown exemplarily for the three target nuclei oxygen (red), calcium (blue) and tungsten (green). For all three elements, a threshold reduction from 10 keV (dashed) to 0.3 keV (solid) increases the count rate and leads to a higher sensitivity towards lighter DM particles. The combined target material CaWO_4 is able to separate between different DM particle masses. Figure taken from [45].

to achieve a particle identification and an active background discrimination of, e.g., electron recoils (background) from nuclear recoils (potential signal) (compare section 2.2.6). One prominent class of experiments employs liquid noble gases as target material. Experiments like LUX [46], PandaX [47], or XENON [48, 49] observe particle collisions within a tank containing xenon in the two phases liquid and gaseous. Interactions within the liquid xenon produce scintillation light being measured as prompt signal. Additionally, electrons liberated by ionization are drifted to the liquid-gas interface by means of an electric field. Their extraction to the gaseous phase by another, strong, field generates also scintillation light detected additionally as delayed signal. The ratio of both scintillation signals allows to discriminate electron recoils from nuclear recoils. The lighter noble gas argon composes the detector material of, e.g., DarkSide [50] applying the same experimental technique as the xenon experiments. Only the scintillation light of liquid argon is exploited in the single-phase experiment DEAP where electron and nuclear recoils are separable due to their differing signal shapes [51, 52]. Liquid noble gas experiments have the advantage of a relatively easy scalability so that large target masses can be achieved without a drastical increase in read-out channels. In case of the XENON experiment, the target mass was recently increased from 62 kg (XENON100 [48]) to ~ 2 t (XENON1T [49, 53]).

A different approach are cryogenic detectors operating either semiconductor crystals made of germanium/silicon or dielectric crystals. Examples for mainly germanium-based experiments are EDELWEISS [54] and SuperCDMS [55]. A particle interaction in the

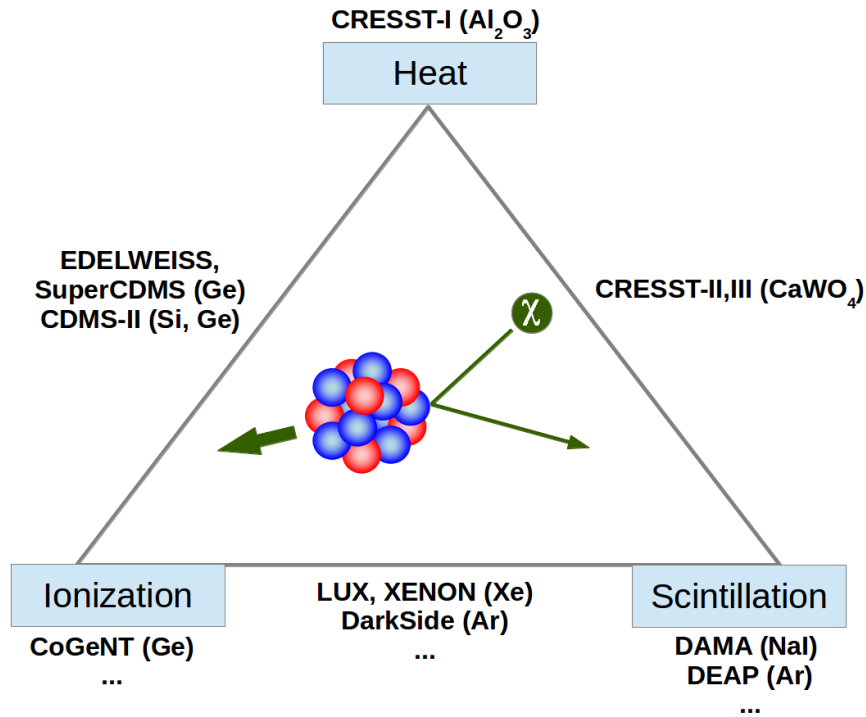


Figure 1.3.: In direct DM searches, experiments aim at the detection of a direct interaction between DM particles χ and ordinary matter via elastic DM particle-nucleon scattering (center). Three different signal channels – heat, ionization, or scintillation – are mainly used to detect energy deposited in a target. Selected experiments as well as their respective target materials are listed next to the read-out channel they use. Many of them exploit even two of these signal channels in order to achieve a discrimination between electron recoils (background) and nuclear recoils (possible signal).

germanium target creates heat which can be detected by a thermometer. Additionally, the surfaces of the absorber crystal are covered with electrodes in order to collect charge carriers created within the crystal and, thus, read out the corresponding charge signal. The ratio of both signals enables – similarly to the liquid noble gas experiments – a discrimination between different types of particles. This thesis deals with the CRESST experiment exploiting the heat and scintillation-light signal of CaWO_4 crystals. The working principle is explained in detail in chapter 2. Cryogenic detectors can achieve very low energy thresholds and are, therefore, especially suitable to search for DM particles with low masses $\mathcal{O}(1 \text{ GeV}/c^2)$ (compare figure 1.2).

As an exponentially increasing energy spectrum alone is not sufficient to provide evidence for dark matter, several experiments aim at the detection of additional signatures. An example is the seasonal variation of the signal rate. As the DM halo itself is expected to be stationary but as the solar system is revolving with a velocity of $\sim 220 \text{ km/s}$ [41] around the galactic center of the Milky Way, a so-called WIMP-wind arises. This effect is strengthened (weakened) when the Earth moves within the solar system into the same (opposite) direction like the sun. The DAMA experiment has observed a seasonal modulation of the signal rate in NaI crystals on a high confidence level [56]. This oscillation

signal could be explained by a WIMP interaction with respective parameters which is, however, in strong contradiction to the results of other direct search experiments.

1.4.3. Backgrounds

Due to the low DM rates expected (see section 1.4.1), all backgrounds originating from radioactivity and radiation have to be considered and, if possible, suppressed. Different sources are listed in the following.

Terrestrial Radiation

Within the Earth, a temperature gradient of 30° C per 1 km depth is observed [57]. This is caused by the energy-release of radioactive decays mainly in the Earth's crust and mantle. Long-lived radionuclides of uranium and thorium that exist since the beginning of the Earth are the starting points for series of α - and β -decays accompanied by γ -radiation. The three still existing natural decay chains starting from ^{238}U , ^{235}U and ^{232}Th are shown in figure 1.4 including the Q-values and half-lives (values taken from [58]) of the respective α - (red) or β -decay (blue). They contain in total 49 radioactive isotopes with different lead isotopes as stable end products. In nature, the uranium-actinium (^{235}U) chain is suppressed compared to the uranium-radium (^{238}U) chain due to the low natural ^{235}U abundance of less than 1%. Isotopes with long-lived mother isotopes form an equilibrium after a time of several half-lives has passed [57]. All isotopes which are in equilibrium feature the same activities. However, the equilibrium can also be broken, e.g. via the extraction of certain radionuclides (as done in the powder purification explained in section 5.3).

Isotopes of the natural decay chains can be found in all materials on Earth. As the only gaseous element included, radon is able to spread the radioactive decay products. For direct DM search experiments a careful selection of materials with low levels of natural radioactivity is mandatory and a radon contamination has to be prevented.

Apart from heavy nuclides, also several lighter primordial isotopes like ^{40}K exist. As potassium is important for the human body, also this radioactive isotope is incorporated and can, thus, be found in perspiration. All materials connected to the detectors of DM searches should, therefore, only be handled in a clean environment using gloves.

Cosmic Radiation

When high-energy cosmic radiation like protons, ^4He -nuclei or electrons hit the Earth's atmosphere, various reactions can occur as illustrated in figure 1.5. Via spallation of, e.g., the isotope ^{14}N , cosmic rays are responsible for the production of a number of unstable isotopes in the atmosphere like ^{14}C , ^{10}Be or ^3H (nuclei remaining after spallation are denoted as N in figure 1.5) as well as of neutrons n, protons p and pions $\pi^{\pm,0}$. This hadronic component is shown in the right part of figure 1.5. The produced pions can either create electromagnetic showers including e^+e^- pairs and γ -radiation in the case of π^0 (left part) or decay further into muons μ^{\pm} and the corresponding (anti)neutrinos $\nu_{\mu}/\bar{\nu}_{\mu}$ in the case of charged pions (central part). Because of their ultra-relativistic nature, part of the muons can permeate the Earth's surface for hundreds of meters before

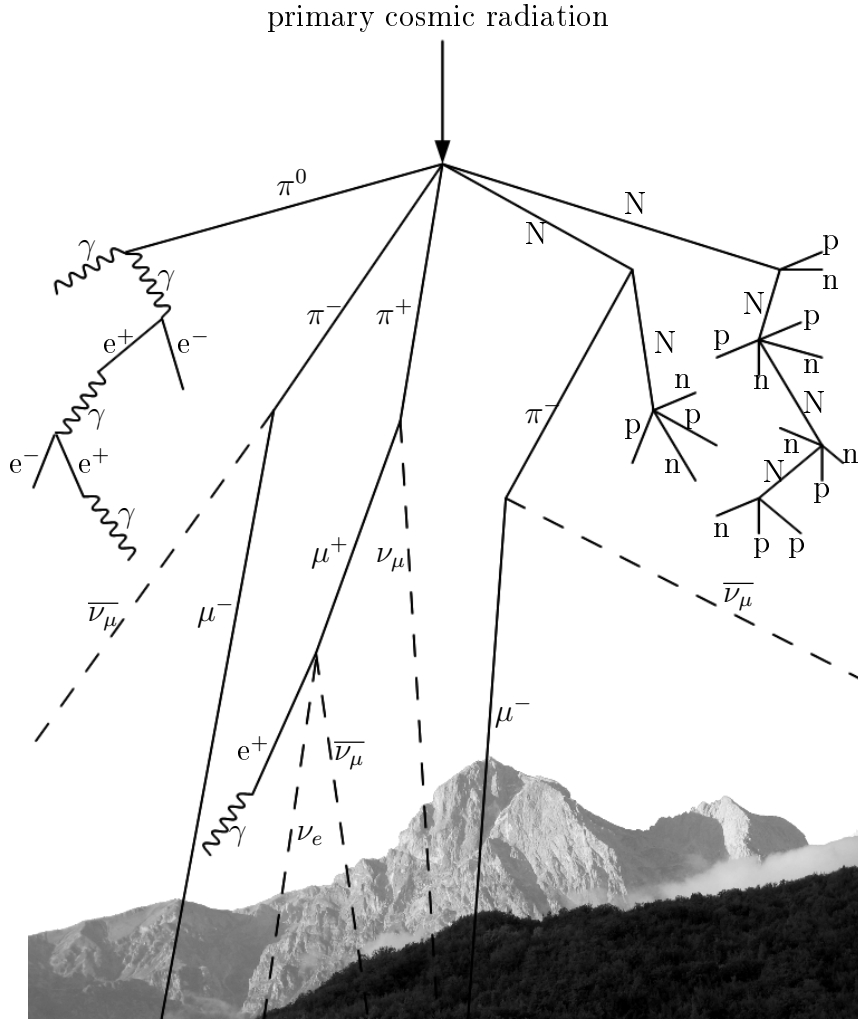


Figure 1.5.: Schematic drawing of particles created by cosmic radiation hitting the Earth's atmosphere. Spallation of nitrogen or oxygen atoms leads to electromagnetic showers ($e^+ e^-$ pairs, γ -radiation), a hadronic component including spallation products denoted generally as N as well as neutrons n , protons p and pions $\pi^{\pm,0}$. Especially muons μ^{\pm} as decay products of π^{\pm} can reach the Earth and generate a background for rare event searches that has to be considered.

decaying into e^{\pm} and the respective (anti)neutrinos [59].

Already in 1912, V. F. Hess discovered that the ionization rate of the atmosphere is increasing with altitude [60]. To minimize cosmogenic activation of detector materials via, e.g., proton capture, all transportation should be carried out on sea level avoiding any flights.

On the surface of the Earth the muon flux is about $1 \text{ cm}^{-2} \text{ min}^{-1}$. Muons themselves are not a background for DM searches as they induce high-energy signals easily discriminable. However, they can produce secondary particles via spallation of atoms in the surroundings of detectors creating a serious background source. In addition to the hadronic component of the air showers also part of these muons can be shielded by the Earth

itself when experiments are operated in underground laboratories. Still, muon-induced neutrons belong also in underground facilities to the main background components for DM search.

Anthropogenic Radiation

Apart from natural radioactivity, artificially produced radiation and radioactive isotopes cannot be neglected. Medical applications like X-ray diagnostics or nuclear medical examinations contribute just as the radioactive fall-out of nuclear bombs, nuclear installations or reactor accidents. Traces of, e.g., ^{60}Co , ^{137}Cs or plutonium isotopes can enter the atmosphere and be further spread.

2. The CRESST Experiment

This chapter deals with the CRESST (cryogenic rare event search with superconducting thermometers) experiment located in the Laboratori Nazionali del Gran Sasso (LNGS) in central Italy [61] with a limestone coverage of ~ 1300 m corresponding to ~ 3800 m water equivalent (m.w.e.). The experimental setup is described in section 2.1 and the working principle of the CRESST detectors is explained in section 2.2. Latest results for DM search of an extended physics run between 2013 and 2015 as well as the current status are presented in sections 2.3 and 2.4, respectively.

2.1. Experimental Setup

Figure 2.1 shows a schematic drawing of the whole setup. The different parts starting from outside are explained in the following.

2.1.1. Background Shielding

As introduced in section 1.4, the interaction rate expected for DM particles is with less than 0.1 counts/(kg day) very low, making it crucial to suppress potential background sources. Due to the underground location at LNGS (~ 3800 m.w.e.), various components of the cosmic radiation are shielded and the muon flux is reduced to a value of $\sim 3 \cdot 10^{-4} \text{ m}^{-2} \text{ s}^{-1}$ [62]. In addition, the experiment is surrounded by several layers of shielding material against various background sources.

To tag the remaining muons passing through the experimental setup, plastic scintillator panels with a thickness of 5 cm acting as muon veto (dark blue in figure 2.1) are installed. The veto covers 98.7% of the solid angle around the detectors, only on the top a small feedthrough for the cryostat (see section 2.1.2) is necessary.

A dangerous background source are neutrons as they also produce a nuclear recoil signal – similar to that expected for a DM particle. Neutrons with energies below ~ 10 MeV can be produced in nuclear reactions such as (α, n) reactions on light elements or fissions of heavy nuclei. Additionally, substantially harder neutrons with energies extending up to the GeV range are generated when muons or muon-induced particles interact with the surrounding rock or other materials [63]. In hall A of LNGS, a total neutron flux in the order of $10^{-6} \text{ cm}^{-2} \text{ s}^{-1}$ was measured [64] which is in agreement with simulations [65]. The contributing rate of fast muon-induced neutrons is, hereby, about $10^{-9} \text{ cm}^{-2} \text{ s}^{-1}$ [63]. In CRESST, a layer of polyethylene (PE, yellow) with a thickness of ~ 50 cm moderates external neutrons to energies $\mathcal{O}(\text{meV})$ well below the threshold of the detectors. As neutrons could also be produced in the innermost materials of the direct surroundings of the detectors, an inner polyethylene shield (dark yellow) was added in 2013.

A gas-tight box constantly flushed with nitrogen gas prevents radon gas from adsorbing

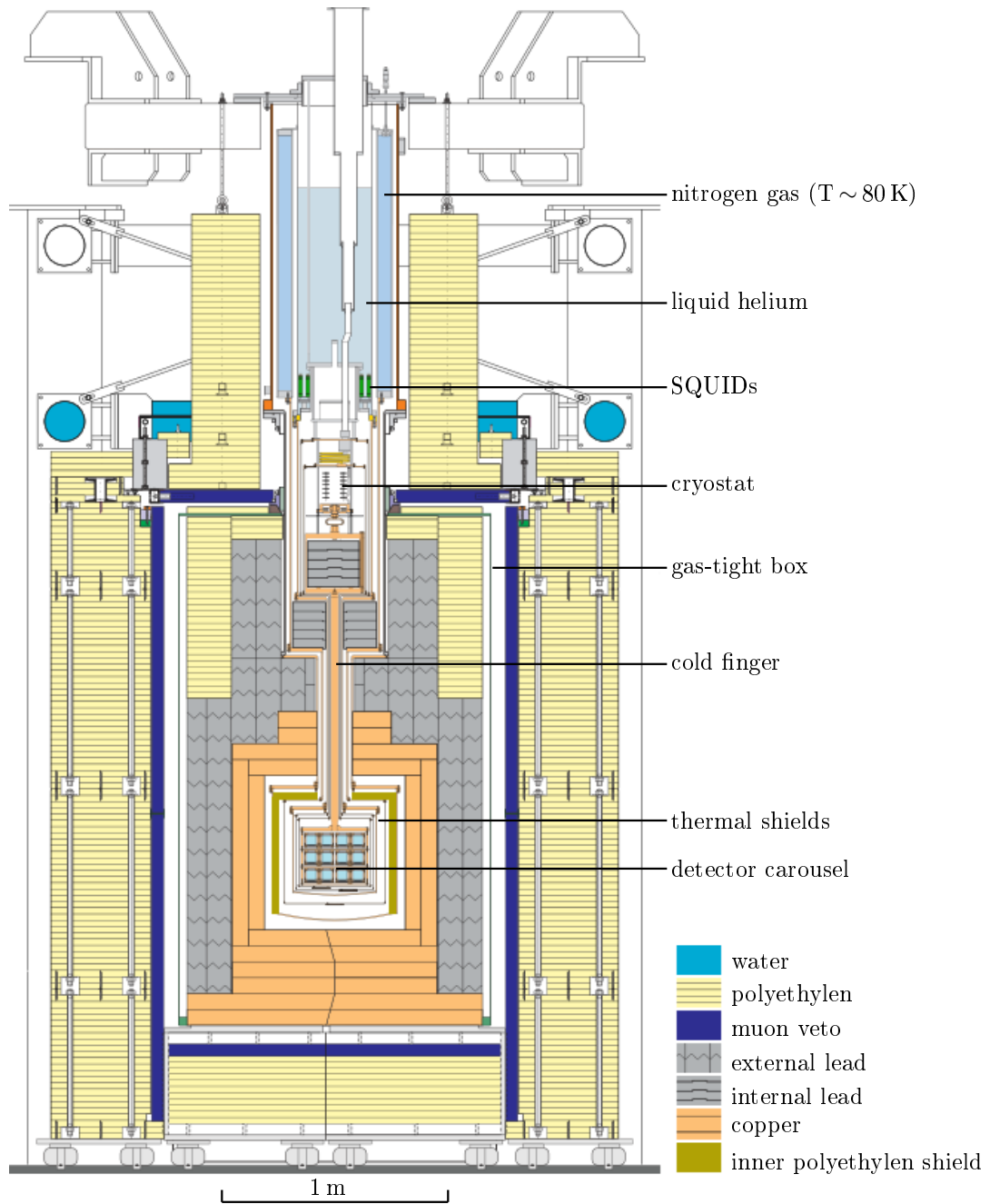


Figure 2.1.: Schematic drawing of the setup of the CRESST experiment. The experiment is located deep underground (~ 3800 m.w.e. [62]) and is surrounded by several layers of shielding to suppress various kinds of backgrounds. In the center of the drawing the detector carousel can be found. It houses the cryogenic detectors operated at mK temperatures. The temperature is provided by a $^3\text{He}/^4\text{He}$ dilution refrigerator and is transferred to the detectors via a cold finger made of copper. For more details see main text.

to the surfaces of materials in the vicinity of the detectors. The gaseous radon isotopes are produced in the natural decay chains – the isotopes of which are omnipresent in the rock of the underground laboratory – and decay further via a series of α - and β -emissions (compare section 1.4.3). However, the main background contributions are due to electrons and γ -radiation with an integral γ -flux of $\sim 0.3 \text{ cm}^{-2} \text{ s}^{-1}$ [66]. Lead (grey) provides an efficient shielding but has the disadvantage to contain the β -decaying isotope ^{210}Pb . To prevent the penetration of this radiation, as well, a layer of radiopure copper (orange) constitutes the inner shielding.

2.1.2. Dilution Refrigerator

The detector carousel housing the detectors is located in the heart of the experiment, surrounded by all the shielding layers. CRESST operates cryogenic detectors at a temperature of $\sim 10 \text{ mK}$. This low temperature is provided by a commercial $^3\text{He}/^4\text{He}$ dilution refrigerator (cryostat). The cooling power to achieve the base temperature of $\sim 5 \text{ mK}$ is provided by the heat of mixing of ^3He and ^4He isotopes. For more detailed information see, e.g., [67].

Only radiopure materials are brought into the direct surroundings of the detector carousel to avoid any unwanted irradiation of the detectors. The lower part of the setup (including the shielding and the detector carousel) is located in a class 100 clean room to allow a detector installation in a clean environment. Furthermore, the detectors are well separated from the non-radiopure commercial cryostat via a cold finger with a length of 1.5 m. It is made of radiopure copper and acts as a thermal link to the mixing chamber of the cryostat in order to transfer the low temperatures to the detector carousel. To enable a detector operation at a temperature of a few mK, external heat radiation has to be shielded. This is realized by five concentric radiation shields at different temperature levels surrounding the detector carousel and the cold finger.

The whole setup shown in figure 2.1 is installed in a Faraday cage to prevent electromagnetic radiation created by external sources from interfering with the sensitive read-out electronics. Since the detectors are highly sensitive to external mechanical vibrations produced by the cryogenic facility, the cryostat hangs on a 20 cm thick wooden plate resting on air dampers. To reduce also internal vibrations originating from, e.g., boiling of the cryogenic liquids, the detectors are mounted on a spring-loaded support.

2.2. Working Principle

This section deals with the working principle of a cryogenic detector as well as with the special features of CRESST detectors.

2.2.1. Cryogenic Detector

As illustrated in figure 2.2, a cryogenic detector consists of an absorber coupled to a sensitive thermometer which can measure the temperature rise induced by a particle interaction in the absorber [68]. The temperature can relax back to equilibrium via a thermal coupling to a heat bath. In the case of CRESST, the heat bath corresponds to

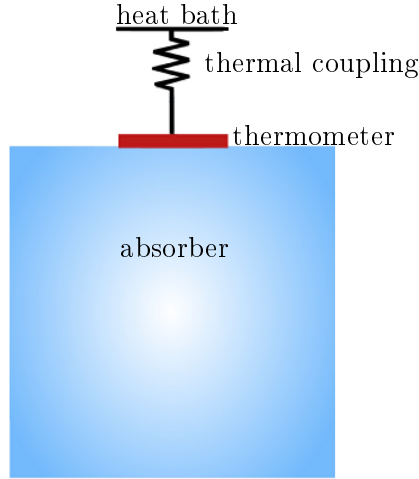


Figure 2.2.: Schematic drawing of a cryogenic detector operated at mK temperatures. It consists of an absorber and a sensitive thermometer that is coupled to the absorber and thermally linked to a heat bath. A particle interaction in the absorber produces heat in the form of phonons which is detected by the thermometer. The (weak) thermal link to the heat bath reestablishes the thermal equilibrium after such a particle interaction.

the temperature of the mixing chamber of the cryostat.

In a simplified calorimetric model, a relation between the temperature rise ΔT and the energy deposited by a particle interaction ΔE is given via the heat capacity C of the absorber:

$$\Delta T = \frac{\Delta E}{C} \quad (2.1)$$

To be able to measure small energies and to achieve a temperature rise as large as possible, it is crucial to reduce the heat capacity. In dielectric and semiconductor materials the relation

$$C \propto \left(\frac{T}{\Theta_D} \right)^3 \quad (2.2)$$

is valid at low temperatures with Θ_D being the Debye temperature of the absorber material [67]. This means that a best possible reduction of the heat capacity can be achieved via operating the detectors at low (mK) temperatures [69]. However, also a very sensitive thermometer is necessary for measuring the temperature increase of small energy depositions.

2.2.2. Signal Read-Out

The CRESST experiment operates transition edge sensors (TES) as sensitive phase transition thermometers. Such a TES consists of a thin superconducting film (e.g. made of tungsten) that is brought into the transition between normal-conducting and superconducting phase. The dependence of the TES resistance R_{TES} on the temperature can be seen in an exemplary transition curve shown in figure 2.3 (a). A typical operation point (OP) in the transition is marked as blue dot at ~ 18 mK. A small temperature rise ΔT , e.g. induced by a particle interaction in the absorber, leads to a measurable change in

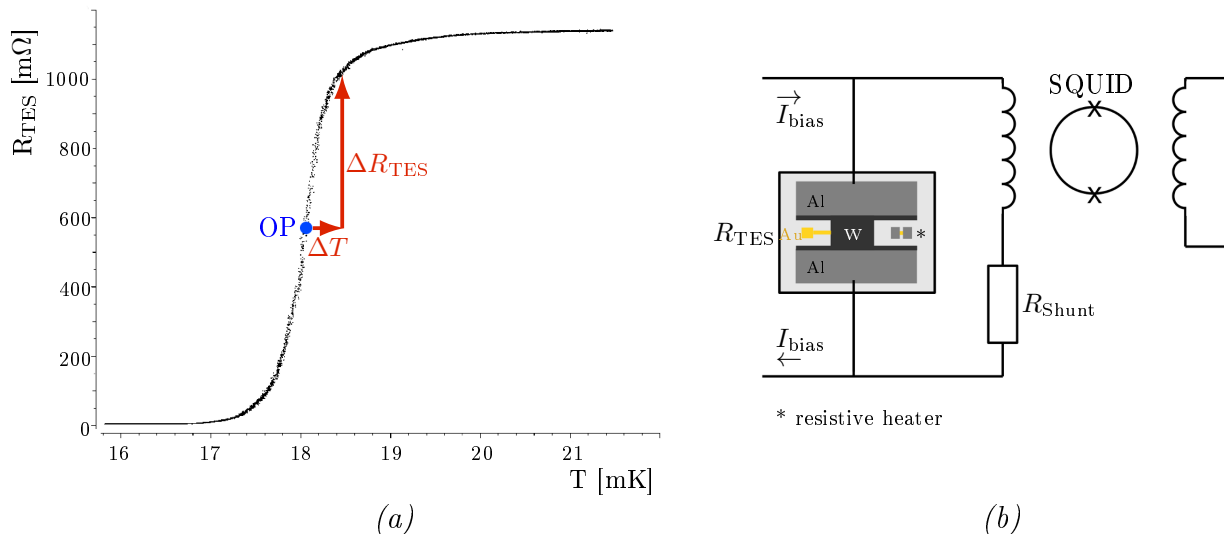


Figure 2.3.: (a) Exemplary transition curve of a tungsten TES. The operation point (OP, marked as blue dot) lies in the transition between normal-conducting and superconducting phase, in this case at a temperature of ~ 18 mK. A small temperature change ΔT leads to a measurable change of the TES resistance ΔR_{TES} . (b) ΔR_{TES} is read out with a SQUID. A constant bias current I_{bias} is applied to the parallel circuit consisting of the TES on one branch and of the input coil of the SQUID and a shunt resistor R_{Shunt} on the other branch. A change in the resistance of the TES leads to a variation of the current in the input coil inducing a change of the magnetic flux in the SQUID. The output of the SQUID is then a voltage signal proportional to the current in the input coil. For details on the TES structure see main text.

the resistance ΔR_{TES} (indicated by red arrows). A SQUID (superconducting quantum interference device) read-out scheme transforming the resistance change into a voltage signal is depicted in figure 2.3 (b). A constant bias current I_{bias} is applied to a parallel circuit consisting of two branches. One branch includes the TES, whereas the other branch consists of a serial connection of the input coil of the SQUID and of a constant reference (shunt) resistor R_{Shunt} . A change of R_{TES} modifies also the branching of I_{bias} and, therefore, the current running through the input coil of the SQUID. This causes a variation of the magnetic flux in the SQUID. Via a separate feedback coil, a voltage signal proportional to the current in the input coil is generated.

An exemplary TES structure as implemented in CRESST-III Phase 1 [70] (see section 2.4) can also be seen in the read-out circuit of figure 2.3 (b). Apart from the superconducting tungsten film (black), additional structures are needed for a successful operation of CRESST detectors. As explained in section 2.2.1, the heat capacity has to be as low as possible. This applies not only to the absorber – also decreasing the heat capacity of the thermometer can increase the sensitivity of the detectors. In case of TESs used in CRESST, aluminum films (light grey) are evaporated on top of the tungsten films. As they are superconducting at mK temperatures, they can collect phonons and transfer the absorbed energy into the thermometer without contributing to the heat capacity. For more details see, e.g., [71].

The bias current needed for the SQUID read-out is applied via two aluminum bonds connected to the two sides of the aluminum collector areas.

For an efficient heat transfer, the thermometer is linked to the heat bath via a normal-conducting structure made of a gold film (yellow) connected to the tungsten film. A gold bond thermally couples this film with the holding structure. Additionally, a second normal-conducting structure separated from the thermometer is visible in the TES of figure 2.3 (b) (marked with a *). This structure consists of aluminum films with an underlying gold film and allows to inject a heater current as explained in the following section.

The complete TES structure can either be directly evaporated onto the absorber crystal (as also applied in CRESST-III Phase 1) or be evaporated onto a carrier crystal which is then glued to the detector crystal.

2.2.3. Detector Operation and Stabilization

The heater current that is injected into the film heater structure of the TES consists of two components. A continual current enables a stabilization of each detector in its respective optimized operation point. Furthermore, heater pulses with a signal shape similar to that of particle-induced pulses are injected in regular time steps. Two different types of heater pulses are applied:

Control Pulses

Control pulses are large heater pulses which drive the thermometer completely out of the transition to the normal-conducting phase (compare figure 2.3 (a)). As the resulting signal pulses are saturated, their pulse height is a measure for the distance of the current operation point to the top of the transition. Before a measurement is started, the operation point is optimized for each detector leading to a certain (optimized) value of the control pulse height called set point. If the pulse height is too small compared to this set point, the current operation point is too high in the transition meaning that the temperature is too high and vice versa. Via a proportional-integral-derivative (PID) control loop, the continual heater current is adapted until the set operation point with its corresponding control pulse signal height is reached again. This active stabilization is necessary because already a small non-linearity in the slope of the transition can lead to a different shape and height of a pulse with the same energy deposition. For a precise monitoring, control pulses are injected about every 10 s.

Test Pulses

The second type of heater pulses are low-energy test pulses with several different pulse heights. They are injected in time intervals of ~ 100 s to monitor time dependencies of the detector response. These time dependencies in the pulse height of a certain energy injected have to be corrected during energy calibration in the analysis of the data (see chapter 6). Furthermore, test pulses with very low energies down to the detector threshold can also be used to directly measure the trigger efficiency (see, e.g., [43]).

2.2.4. Data Acquisition

Figure 2.4 shows a simplified diagram of all electronic components required for the operation and read-out of a single CRESST detector. Drawn are the heater electronics in red, the bias circuit in black as well as the SQUID read-out in blue at different temperature stages ranging from room temperature down to 4 K (liquid helium) and ~ 10 mK. A continual heating current as well as heater pulses are fed into the TES. For that purpose an adjustable voltage (U_{DAC}) given by a digital-to-analog-converter (DAC) as well as a voltage signal U_{P} created in an arbitrary waveform generator (pulser) are summed up in the heater electronics. The sum of both signals is then sent through a square rooter and converted into the total heating current $I = \sqrt{U_{\text{DAC}} + U_{\text{P}}} \cdot R^{-1}$ by a pair of resistors. The current is filtered at 4 K and finally fed into the gold film of the TES heater at ~ 10 mK. Thereby, the purpose of the square rooter is to decouple the continual heating current and the heater pulses from each other. The total heating power P in the detector is proportional to the square of the total heating current. This means, with the square rooter it can be divided into the power deposited by the continual and by the pulsed heater part: $P = (U_{\text{DAC}} + U_{\text{P}}) \cdot R^{-2} \cdot R_{\text{TES}} = P_{\text{DAC}} + P_{\text{P}}$. In this way, the power injected via a heater pulse into the TES remains the same even when the continual heating current changes.

The bias current applied to the parallel circuit of TES and SQUID input coil (plus shunt resistor) is provided by a controllable current source located at room temperature.

The SQUIDs are operated at 4 K and are connected to the SQUID electronics providing the output voltage at room temperature. The signal is split into two branches: the first branch goes directly into the digitizer whereas the second branch is responsible for the creation of a trigger signal. When the signal level after filtering and amplifying (i.e. shaping) is above a certain (adjustable) threshold, the trigger unit sends a pulse to the digitizer¹. In this case the digitizer saves the samples which are read out and written to hard disk by the DAQ software. Within the recorded signal, a pre-trigger region (first quarter) contains information about the baseline before triggering. The actual signal information can be found in the post-trigger region of the last three quarters. The trigger is blocked for the time needed for read-out and, in addition, for a full pre-trigger region (see chapter 6).

In summer 2016, a new continuous data read-out was installed in parallel to the explained DAQ. A permanent data stream is written to disk without losing non-triggered data. For the evaluation of recorded pulses and their parameters, a software trigger can be applied and optimized for each detector in the subsequent analysis [72].

2.2.5. Detector Module

CRESST uses CaWO_4 single crystals as absorber material. As these crystals are scintillating (see figure 2.5) also at mK temperatures, not only the temperature rise in the crystal (phonon signal) but also the scintillation light produced by a particle interaction is measured. Phonon and light signal are both read out separately by two different cryogenic detectors with the read-out and operation features explained above. These

¹Each digitizer unit can handle eight detectors simultaneously. All detectors of this digitizer unit are read out together, also when only one detector has triggered.

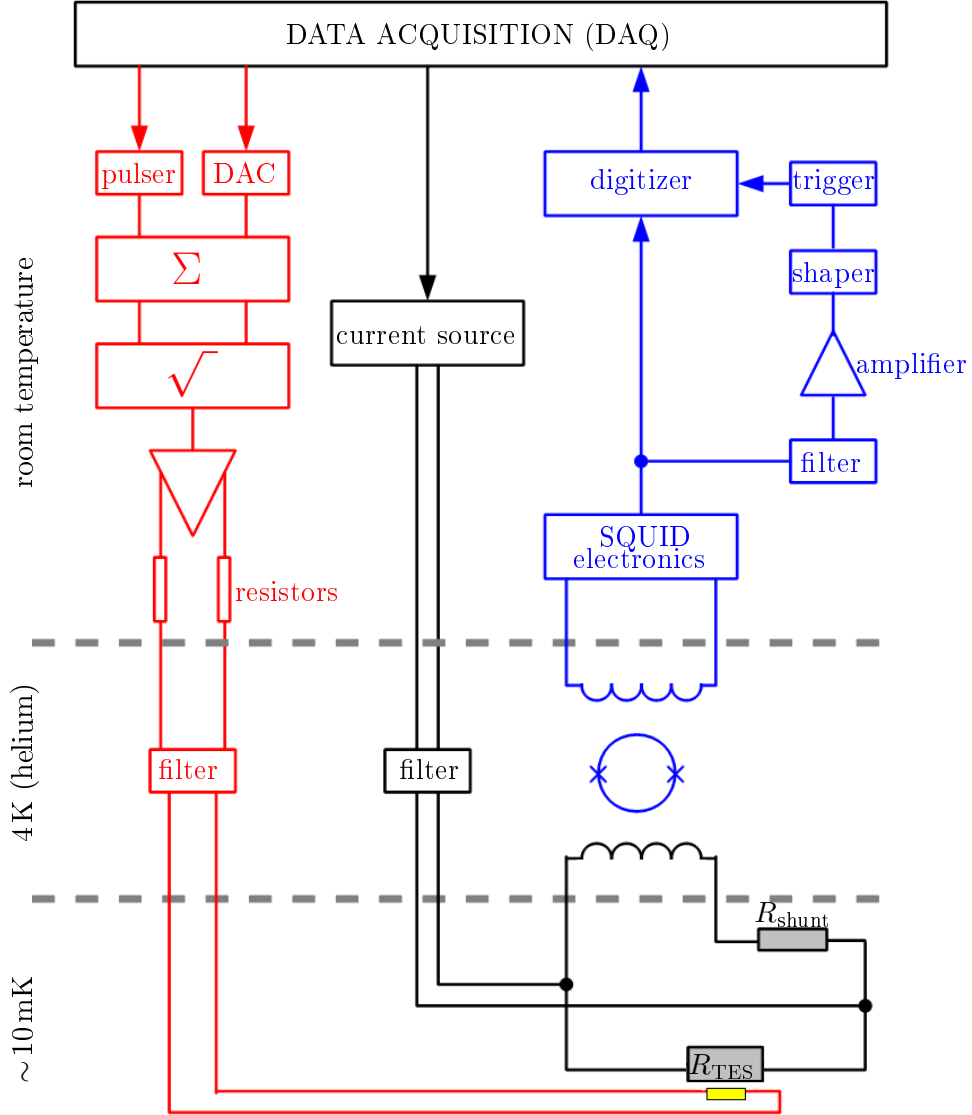


Figure 2.4.: Simplified diagram of the electronic components required for the operation and read-out of a single CRESST detector. The heater electronics (red) provide via a DAC and a pulser a continual heating voltage and a pulsed voltage signal, respectively. After summing up and square rooting, the total heater current is defined by a pair of resistors and fed into the heating structure of the TES at ~ 10 mK. The bias current applied to the SQUID parallel circuit is provided by a current source at room temperature (black). The SQUID electronics (blue) outputs a voltage that is saved by the digitizer when the trigger fired. Figure adapted from [44].

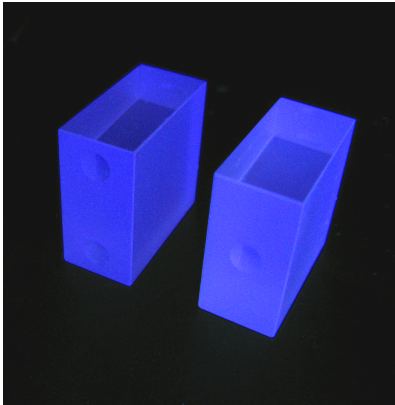


Figure 2.5.: Two block-shaped CaWO_4 detector crystals scintillating while being excited by UV light. The maximum of the emission spectrum is at a wavelength of (420 - 430) nm.

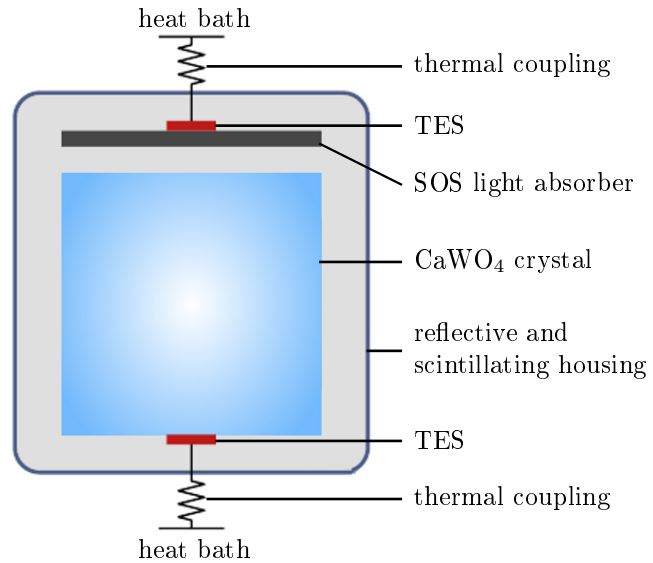


Figure 2.6.: Schematic drawing of a CRESST detector module. The CaWO_4 target crystal is equipped with a TES forming a cryogenic detector. The scintillation light emitted by the crystal after a particle interaction is detected by a second cryogenic detector consisting of a SOS light absorber linked to another TES. Both TESs are thermally coupled to the heat bath. All detectors components are enclosed in a reflective and scintillating housing in order to maximize the light reaching the light detector as well as to veto surface events.

two detectors together form a so-called detector module which is schematically drawn in figure 2.6. The phonon detector consists of a CaWO_4 absorber crystal (in the following denoted as detector crystal) equipped with a TES. In the light detector, the scintillation light is absorbed by a silicon-on-sapphire (SOS) disk and transformed into phonons that are detected with another TES coupled to the SOS absorber. Both TESs are thermally coupled to the heat bath. Phonon and light detector are surrounded by a reflective and scintillating foil to maximize the light reaching the light detector and to veto surface events (see section 2.3.1 and appendix A).

2.2.6. Background Discrimination and Region of Interest

More than 90 % of the total energy deposited by a particle interaction is visible as phonon signal which can, therefore, be used for gaining precise energy information. The amount of scintillation light produced in the crystal, however, is less than 10 % and depends on the type of interacting particle. Introducing the parameter light yield LY defined as

$$LY = \frac{E_L}{E_{Ph}} \quad (2.3)$$

allows a particle discrimination on an event-by-event basis. E_{Ph} is, hereby, the energy measured in the phonon detector and E_L is the associated light energy as measured in

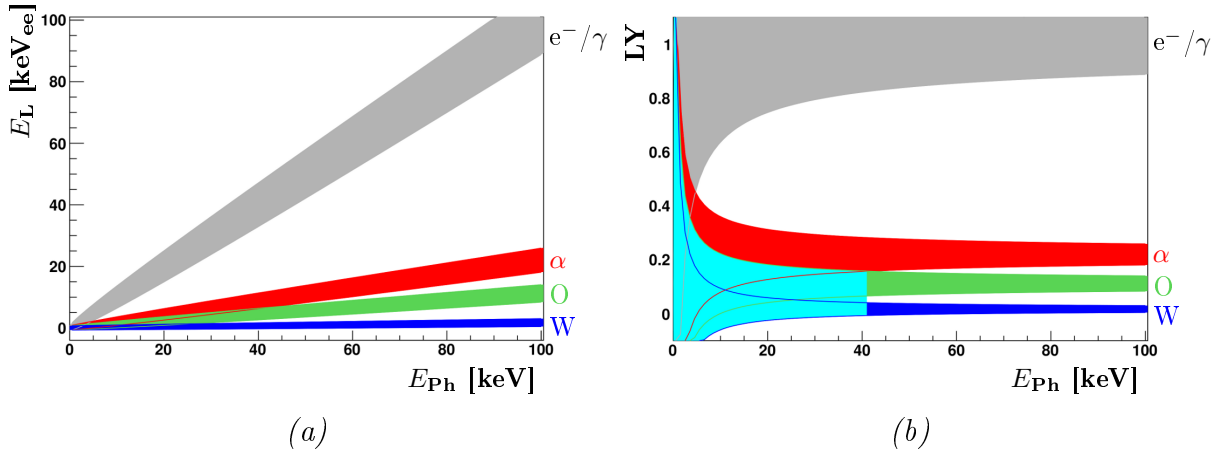


Figure 2.7.: Schematic drawing concerning the particle identification as applied in CRESST. The amount of light produced by a CaWO_4 detector crystal depends on the type of interacting particle. In (a) the light energy E_L is plotted against the phonon energy E_{Ph} which results in different bands containing a certain type of particles each. Plotting the ratio E_L/E_{Ph} denoted as light yield LY on the y-axis leads to horizontal bands (b). Electron recoils (grey) are the main background and are normalized to have a slope (a) or LY (b) equal to 1. α -particles (red) as well as nuclear recoils induced by particles scattering off oxygen (green), calcium (not shown here for reasons of clarity) or tungsten (dark blue) can be found in bands with lower slopes or LY values (see table 2.1). Highlighted in light blue is the region of interest (ROI) for possible recoils of DM particles.

the light detector. In figure 2.7, E_L (a) and LY (b) are plotted versus E_{Ph} . As E_{Ph} is – due to energy conservation – also slightly particle dependent, it is usually converted into the event type independent recoil energy (see, e.g., [43]) which will be simply denoted as energy E in later plots. It is shown schematically in figure 2.7, how different types of particles result in bands with different slopes (a) or light yield values (b). The bands are usually drawn with their 90 % upper and lower boundary meaning that 80 % of events due to a certain particle type are located within the respective band. Electron recoils in the e^-/γ -band (grey) form the main background, but also produce the most light. Typically, their light yield LY is normalized to 1 using a γ -line created by a calibration source (e.g. 122 keV of a ^{57}Co source, see section 6.3). By this calibration, E_L is assigned with the unit keV_{ee}, where the subscript “ee” stands for electron-equivalent. α -particles (red) generate only 22 % of the light of γ -radiation and can, therefore, be found in a band with a LY of 0.22 [73]. This value was derived directly from CRESST data, whereas the light yields for nuclear recoils were determined in a dedicated experiment by irradiating a cryogenic detector with a fast neutron beam. It was found that nuclear recoils induced by particles scattering off oxygen (green), calcium (would appear between oxygen and tungsten but is not shown here) or tungsten (dark blue) produce even less light leading to LY s of ~ 0.11 , ~ 0.059 and ~ 0.017 , respectively [74]. The light yields of the different bands are summarized in table 2.1.

In figure 2.7 (b), the region of interest (ROI) for direct DM search is marked in light

band	LY
e^-/γ	~ 1 (norm.)
α	~ 0.22 [73]
O	0.112 ± 0.005 [74]
Ca	0.0594 ± 0.0049 [74]
W	0.0172 ± 0.0021 [74]

Table 2.1.: Light yields LY for the different bands as shown in figure 2.7. A γ -line created by a calibration source (e.g. the 122 keV-line of ^{57}Co) is used to normalize the e^-/γ -band to a light yield of 1. Compared to that, a light yield of ~ 0.22 for α -events could be derived directly from CRESST data. The nuclear recoil bands include the three elements contained in CaWO_4 . The light yields of particles scattering off oxygen, calcium or tungsten were determined in a dedicated experiment and are at ~ 0.1 and below.

blue. It covers the nuclear recoil bands and extends from detector threshold to 40 keV in energy. Above this upper energy limit of ~ 40 keV, DM recoils become unlikely due to the nuclear form factor of tungsten (see, e.g., [44]).

To be able to identify possible recoils of DM particles, the ROI is defined in a way that the ratio of expected signal to expected background is high. It can, however, clearly be seen in the schematic drawing of figure 2.7 that the different bands are overlapping. At low energies, even the e^-/γ -band leaks into the ROI. As the energy resolution of the light detector is worse compared to that of the phonon detector, the width of the bands and, therefore, the degree of the overlap depends on the light output and on the resolution of the light detector – a higher light output or a better resolution results in more narrow bands. Additional effects, e.g., the so-called non-proportionality describing the non-linearity of the detector response at low energies, lead to a downward-bending of the e^-/γ -band at low energies (investigated in [75, 76]) and even increase the leakage into the ROI. Therefore, it is highly important to operate detector crystals with a high light output and good optical properties. Furthermore, a high crystal radiopurity is crucial to avoid any possible backgrounds for DM search. The investigation of the radiopurity of the CaWO_4 crystals as well as ways for its improvement are the major topic of this thesis (see chapters 5 and 7).

2.3. Results of CRESST-II Phase 2

CRESST-II Phase 2 was an extended physics run taking data for more than two years between 2013 and 2015. 18 detector modules (36 detectors and read-out channels) with a total CaWO_4 target mass of ~ 5 kg were operated. 12 of these detector modules were designed conventionally as in the previous phase, CRESST-II Phase 1 [73]. Additionally, three new module designs (two modules of each design) with a fully scintillating or active detector housing were implemented.

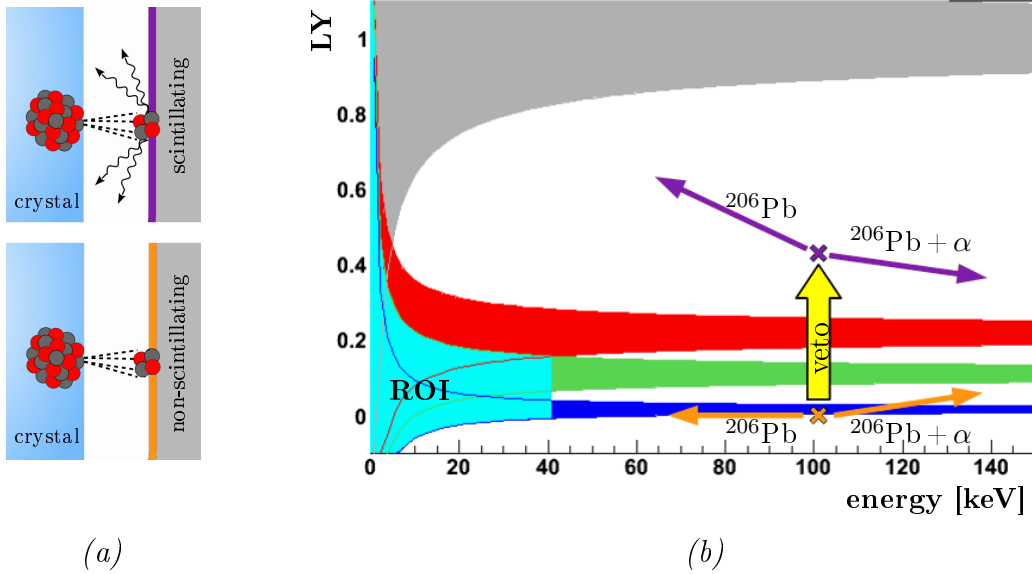


Figure 2.8.: Veto for α -decays on surfaces surrounding the CaWO_4 detector crystal. The daughter nucleus of such a decay (here ^{206}Pb) can be detected in the crystal whereas the α -particle is absorbed by the scintillating or non-scintillating surrounding material (a). If this material is non-scintillating (e.g. clamps in the conventional module design) the resulting signal of the ^{206}Pb nucleus has an energy of 103 keV and almost no light [73]. In the light yield-energy plane (b) the location of such events is marked by the orange cross. In case the ^{206}Pb nucleus loses part of its energy before hitting the crystal, a leakage into the ROI is possible (left orange arrow). By using only scintillating materials in the housing of the detectors, the α -particle creates a simultaneous light signal which shifts this event class to higher light yields (yellow and violet arrows).

2.3.1. Veto for Surface Backgrounds

To discriminate backgrounds due to events from the surfaces of the detector crystals or of the holding materials, the foil surrounding each detector module is not only reflective but also scintillating. Figure 2.8 illustrates the veto function using the example of a surface α -decay of the radon daughter ^{210}Po . Discussed in this figure is the scenario that the daughter nucleus of the decay (here ^{206}Pb) is detected by the crystal whereas the α -particle is absorbed by surrounding material. In case this material is non-scintillating (figure 2.8 (a) bottom), the resulting signal only includes the ^{206}Pb -recoil with an energy of 103 keV and almost no light production [73]. In figure 2.8 (b) the position of such events in the light yield-energy plane is marked by the orange cross. If part of the α -energy is deposited in the crystal before being absorbed by the holding material, the signal can be found at a slightly higher energy and light yield (approximating that of α -events). On the other hand, if the daughter nucleus even loses part of its energy before entering the crystal, a leakage into the ROI is possible (indicated by orange arrows). A discrimination of this background is only feasible when the α -particle is absorbed by a scintillating surface (figure 2.8 (a) top). Due to the additional simultaneous light pro-

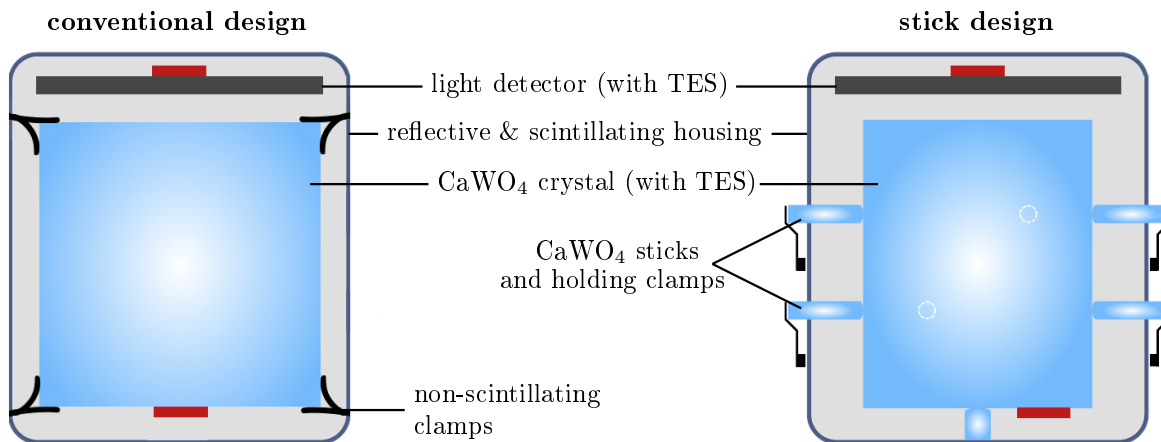


Figure 2.9.: Schematic drawings of two different module designs implemented in CRESST-II Phase 2. In the conventional module design (left), the CaWO_4 crystal is held by non-scintillating bronze clamps. The stick design (right) avoids such non-scintillating surfaces within the detector housing by holding the crystal with CaWO_4 sticks which are fixed by clamps from outside.

duction, such events are shifted out of the ROI towards higher light yields as indicated by the yellow arrow in figure 2.8 (b). As ^{206}Pb itself does almost not contribute to the light production and as the α -particle creates a constant amount of scintillation light in the foil, the distribution of these events is proportional to $1/E$ in the LY -energy-plane (violet arrows). A further investigation is performed in appendix A.

In the conventional module design (see figure 2.9 (left)), the CaWO_4 detector crystal is held by non-scintillating bronze clamps² covered with a silver (CRESST-II Phase 1) or an aluminum layer (CRESST-II Phase 2) to enhance their reflectivity [77]. In CRESST-II Phase 1, a ^{210}Po contamination in the non-scintillating clamps caused a severe background event class leaking into the ROI [73]. This leakage originating from ^{206}Pb recoils was estimated to be about constant in the ROI and was included in the results. Nevertheless, a signal excess was observed [73]. Simulations, however, suggest an additional background contribution at low energies originating from cascades of secondary nuclear recoils [78]. ^{206}Pb nuclei scattering off the non-scintillating clamps could sputter, e.g., silver atoms which create a signal in the ROI. In this way, the dominating part of the excess signal observed in CRESST-II Phase 1 could be explained.

To suppress the ^{206}Pb related backgrounds, various measures were undertaken in CRESST-II Phase 2. As the observed surface backgrounds are assumed to have mainly been radon-induced, the assembling and mounting of the detectors took place in radon-depleted atmosphere provided by the neighbouring experiment CUORE [79]. All parts were stored in nitrogen-flushed containers. For holding the crystals in the conventional design, new bronze clamps were manufactured from carefully selected radioclean material [77].

Furthermore, three alternative module designs providing a fully scintillating or fully active detector housing were installed. Consequently, surface decays hit the scintillating

²Attempts to cover the metal clamps with a plastic scintillator led to thermal stress relaxation events, i.e. events without a corresponding light signal, which induce also a background in the ROI [77].

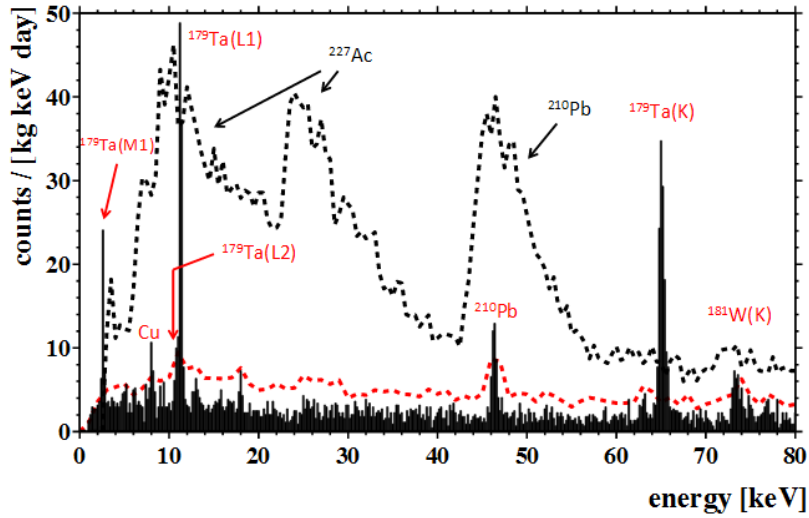


Figure 2.10.: Energy spectra below 80 keV of the TUM-grown crystal TUM40 (black) and of the two commercial crystals Daisy (red dashed) and VK31 (black dashed). With a background level of only 3.51 counts/(kg keV day) (calculated in the interval (1 - 40) keV), the radiopurity of TUM40 is significantly improved by a factor of ~ 2 -10 compared to the commercial crystals. Whereas the characteristic β -spectra of ^{227}Ac and ^{210}Pb clearly dominate especially in VK31, they are not at all or only weakly present in the spectrum of TUM40. Instead, lines originating from cosmogenic activation of the isotopes ^{182}W and ^{183}W are visible. Figure taken from [82].

surroundings and produce additional light as explained in figure 2.8. For this thesis only one of these new designs, the so-called stick design, is relevant. Figure 2.9 (right) shows schematically, how the CaWO_4 detector crystal is held by CaWO_4 sticks. The successful rejection of all surface events was confirmed in [80] for one detector module with this new fully scintillating stick-design. For further information on the different module designs included see, e.g., [43, 45, 81].

2.3.2. Integration of TUM-Grown Crystals

In CRESST-II Phase 2, four crystals grown at the Technische Universität München (TUM) (see chapter 3) were included for the first time. They feature an improved radiopurity compared to commercially available crystals. Figure 2.10 compares the energy spectra below 80 keV of the TUM-grown crystal TUM40 (black spectrum) and of the two commercial crystals Daisy (red dashed) and VK31 (black dashed). The background rate of TUM40 is 3.51 counts/(kg keV day) [82] (calculated in the energy range (1 - 40) keV) which is a significant reduction by a factor 2-10 compared to the commercial crystals. Daisy is, hereby, with ~ 6 counts/(kg keV day) the commercial crystal with the lowest background rate in CRESST-II Phase 1 and Phase 2 whereas VK31 shows a typical contamination of ~ 30 counts/(kg keV day). The characteristic β -spectra of ^{227}Ac and ^{210}Pb , which especially dominate in VK31, are not (or only weakly) present in the spectrum of TUM40. Instead, ^{179}Ta - and ^{181}W -lines originating from the cosmogenic activation of

the tungsten isotopes ^{182}W and ^{183}W are visible (for details see section 7.1).

Activities of α -decays occurring at energies in the MeV range are also a good measure for the intrinsic radiopurity of the crystals. Also here, the improved radiopurity of TUM-grown crystals is observable. In [83] total α -activities were calculated for commercial crystals analyzing data of CRESST-II Phase 1 where no TUM-grown crystals had been included. It was found that the activities in typical commercial crystals range between 10 mBq/kg and 30 mBq/kg. The crystal Daisy, which was also operated in this run of the experiment, was the best (commercial) crystal with a total α -activity of (3.05 ± 0.02) mBq/kg. In comparison, measurements of first TUM-grown crystals at the CRESST test facility (also located underground at LNGS) [77] resulted in total α -activities of only (1.23 ± 0.06) mBq/kg (TUM27) and (3.07 ± 0.11) mBq/kg (TUM40) [83]. This α -activity of TUM40 was confirmed by the data of CRESST-II Phase 2 where a value of (3.08 ± 0.04) mBq/kg was determined [82].

2.3.3. Low-Threshold Analysis

As explained in section 1.4, the energy threshold of the phonon detector is an important parameter in CRESST. Figure 1.2 shows that a low threshold can significantly increase the count rate at a certain DM particle mass and can also extend the sensitivity towards lighter DM particles. For several detector modules installed in CRESST-II Phase 2, a phonon detector threshold of less than 1 keV could be reached. In these detectors, a low-threshold analysis was performed allowing to make use of all data down to the threshold of the respective detector.

The analysis applied to this data is the so-called Yellin optimum interval method [84] which allows the calculation of an upper limit in the presence of unknown backgrounds if the signal is non-existent or below the experiment's sensitivity. Inputs for this method are the background distribution as well as the expected signal distribution. In case of CRESST data, the energy spectrum in the region of interest is the distribution to be investigated. The anticipated DM energy spectrum is expected to rise exponentially towards low energies whereas the background spectrum seems to stay flat according to the background model of [82].

The data of one detector module (including the detector crystal TUM40 [85]) is shown in the light yield-energy plane in figure 2.11 (a). The main population of events (blue dots) lies in the e^-/γ -band. The nuclear recoil bands and especially the acceptance region³ for possible DM recoils (highlighted in yellow) feature only few events. The event distribution in this region is highlighted in red in the energy spectrum of figure 2.11 (b). An exclusion limit for the DM particle mass and the scattering cross section can be calculated when this accepted spectrum is compared to the expected exponential spectrum of a potential signal. For more information see, e.g., [43, 45].

³In this case, the acceptance region extends from detector threshold (0.6 keV) to 40 keV in energy. In light yield, the upper limit of the acceptance region is the 50 % line of the oxygen nuclear recoil band.

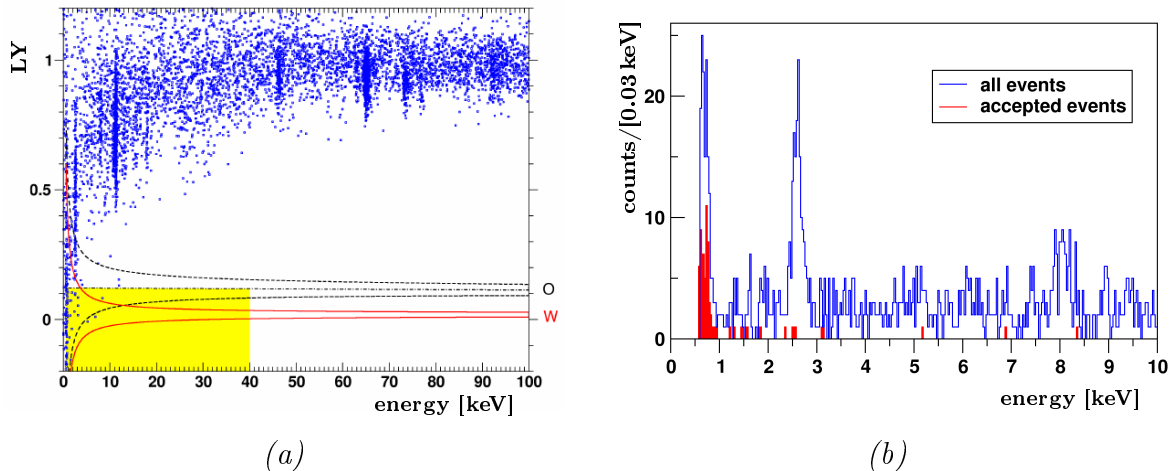


Figure 2.11.: (a) Data of the detector module including the detector crystal TUM40 (CRESST-II Phase 2) in the light yield- energy plane (blue dots). The acceptance region for a potential DM particle signal (yellow) is defined to extend from the energy threshold (0.6 keV) to 40 keV in energy. In LY its upper limit is the 50 % line of the oxygen recoil band. All events within the acceptance region are conservatively considered as possible DM recoils for the low-threshold analysis. (b) Corresponding energy spectrum with the spectrum of the events lying in the acceptance region marked in red. In the low-threshold analysis, the accepted spectrum is compared to an exponential energy spectrum as expected for DM particles. Plots adopted from [85].

2.3.4. Detector Modules of the Crystals TUM40 and Lise

Results of the low-threshold analysis described before were published for two single detector modules, namely for a module of the stick design (compare figure 2.9 (right)) including the TUM-grown detector crystal TUM40 as well as for a conventional module (figure 2.9 (left)) with the commercial detector crystal Lise. TUM40 is a block-shaped crystal (volume $V = (32 \times 32 \times 40) \text{ mm}^3$) with a mass of 249 g measured for 29.35 kg live days exposure (before cuts) [85]. The cylindrical crystal Lise, on the other hand, achieved with a diameter \varnothing and height h of 40 mm as well as with a mass of 306 g an exposure of 52.2 kg days [86]. Table 2.2 summarizes the information on these two detector modules. The TUM40-module features the best overall performance with a relatively low threshold of $(603 \pm 2) \text{ eV}$, a good radiopurity with rate of only 3.51 counts/(kg keV day) in the energy range (1-40) keV, a total α -activity of $(3.08 \pm 0.04) \text{ mBq/kg}$ and an excellent energy resolution (at threshold) of $\sigma = (107 \pm 3) \text{ eV}$ [82, 85]. Lise, on the other hand, features the lowest threshold of all detectors operated in CRESST-II Phase 2 with a value of only $(307.3 \pm 3.6) \text{ eV}$. The 1σ resolution at threshold was determined to be $(82.0 \pm 4.2) \text{ eV}$ [86]. However, Lise has a worse background level of 13 counts/(kg keV day) in the interval (1-40) keV⁴.

The DM landscape of direct search experiments after publication of the results of TUM40

⁴The detector crystal Lise was accidentally illuminated with an ^{55}Fe source. If the events around 6 keV originating from this source are excluded, the background rate in the interval (1-40) keV is reduced to a value of 8.5 counts/(kg keV day).

detector	TUM40	Lise
supplier	TUM	commercial
design	stick	conventional
crystal geometry	block-shaped	cylindric
crystal mass [g]	249	306
crystal dimensions	(32 x 32 x 40) mm ³	$\varnothing = h = 40$ mm
threshold [eV]	603 ± 2	307.3 ± 3.6
resolution [eV]	107 ± 3	82.0 ± 4.2
e^-/γ -background [(kg keV day) ⁻¹]	3.51	13 (8.5)

Table 2.2.: Summary of information on the two detector modules including the detector crystals TUM40 and Lise that were analyzed via the low-threshold method. The TUM40-module showed the best overall performance with a low threshold of 603 eV and a good radiopurity of 3.51 counts/(kg keV day) [85] whereas Lise had the lowest threshold (307.3 eV) of all detectors installed in CRESST-II Phase 2 but a higher e^-/γ -background of 13 counts/(kg keV day). Excluding two lines at ~ 6 keV originating from an accidental illumination with a ⁵⁵Fe source decreases the background rate to 8.5 counts/(kg keV day) which is, however, still well above the level of TUM40 [86].

and Lise (status of 2016) can be seen in figure 2.12 where the cross section for elastic DM particle - nucleon scattering is plotted versus the DM particle mass. The parameter space above a certain line (exclusion limit) is excluded by the respective experiment on a 90 % confidence level (C.L.). In case of a signal excess that could be compatible with dark matter a colored region is drawn. For DM particle masses above ~ 6 GeV/c², experiments using liquid noble gases as target material (e.g. XENON [48], LUX [87]) feature the best sensitivity (blue lines). The green lines representing limits of experiments operating germanium (and silicon) detectors (e.g. SuperCDMS [55]) reach down to lower DM particle masses of ~ 2 GeV/c². At the lowest masses, however, the two CRESST low-threshold detectors are most sensitive. Whereas TUM40 (dashed red line) had a leading role below ~ 4 GeV/c² in 2014, it was surpassed by the exclusion limit of Lise (solid red line). The light red band is the sensitivity expected for Lise from a data-driven sensitivity study assuming only e^-/γ -background (1σ C.L.). The excess signal stated by CRESST-II Phase 1 [73] (brownish islands) can almost completely be excluded by the TUM40 result. Marked in grey is the limit for a background-free CaWO₄ experiment arising from coherent neutrino-nucleus scattering (CNNS). The dominant component is, hereby, due to solar neutrinos [96].

Apart from the results presented here, further analyses of CRESST-II Phase 2 data were performed in, e.g., [45, 97, 98].

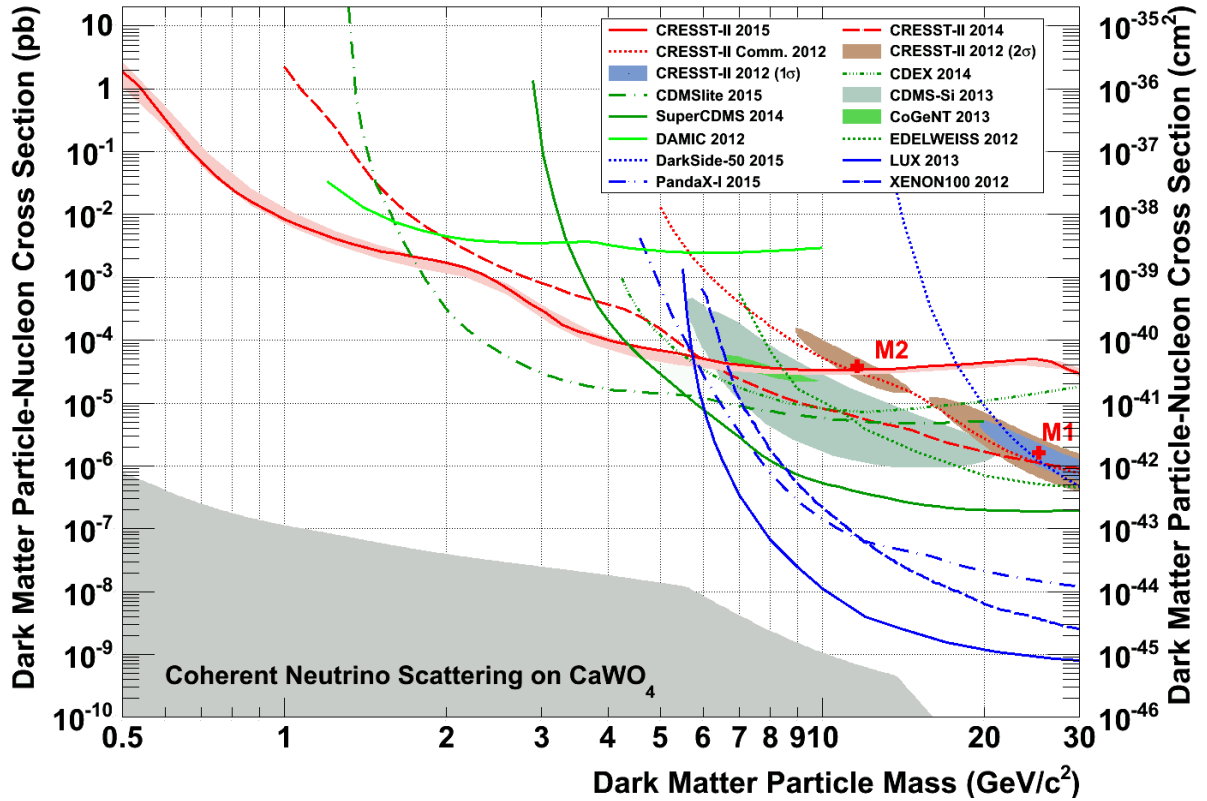


Figure 2.12.: DM landscape of direct search experiments adopted from [45] (status of 2016). Dark matter particles and cross sections above the lines are excluded by the respective experiment. Positive signals that could be compatible with dark matter are marked as colored regions. Liquid noble gas experiments [48, 50, 87, 88] (blue) feature the best sensitivities at high DM particle masses. Germanium- (and silicon-) based experiments [55, 89–94] (green) are leading between $2\text{ GeV}/c^2$ and $6\text{ GeV}/c^2$. The low-threshold detectors of CRESST-II Phase 2 – Lise [86] (solid red, CRESST-II 2015) and TUM40 [85] (dashed red, CRESST-II 2014) – have a leading role for even lighter DM particles. Also drawn is a re-analysis of the CRESST-II commissioning run (CRESST-II Comm. 2012) [95] and the signal excess of CRESST-II Phase 1 (CRESST-II 2012) [73] which can, however, almost completely be excluded by TUM40. The grey area shows the parameter region where coherent neutrino nucleus scattering is expected [96].

2.4. CRESST-III

The success of the low-threshold analysis performed for data of CRESST-II Phase 2 motivated the CRESST collaboration to further optimize the detectors with respect to very low energy thresholds. To explore the low-mass DM region, the goal of CRESST-III is to achieve energy thresholds below 100 eV at least [99]. By scaling down the size of the detector crystals by a factor of ~ 10 an improvement in the signal-to-noise ratio of up to a factor of 10 is expected due to basic phonon physics [69]. A detailed investigation has been performed in [71].

Figure 2.13 shows a schematic drawing (left) as well as a realized (opened) detector module (right) developed for CRESST-III. The block-shaped CaWO_4 detector crystal

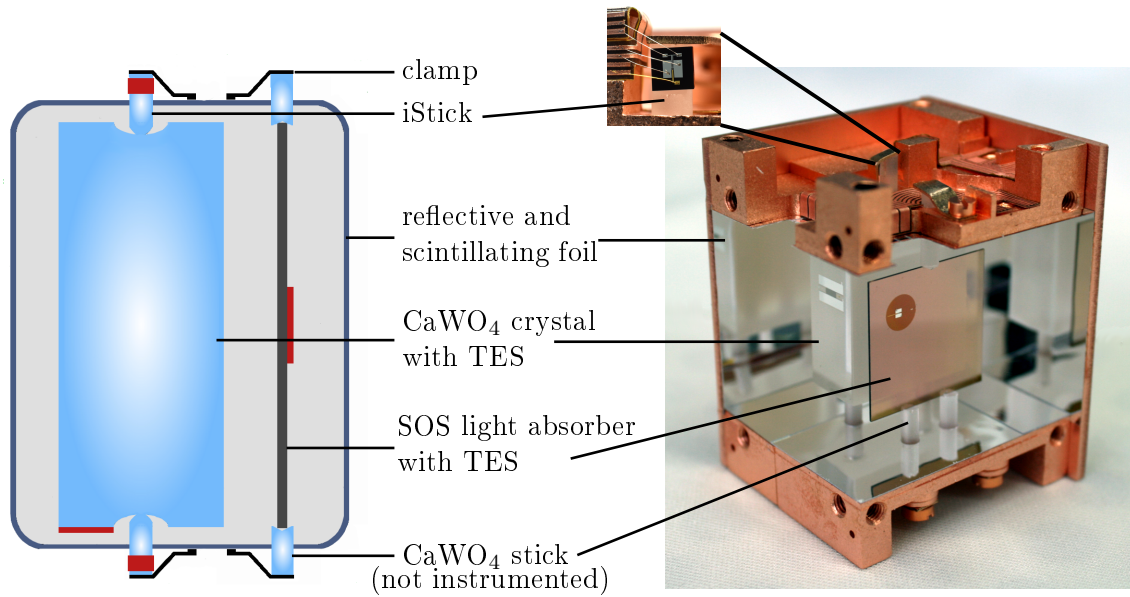


Figure 2.13.: Schematic drawing of a CRESST-III detector module (left) and picture of an opened module (right). The block-shaped CaWO_4 detector crystal has a mass of ~ 24 g and is facing a light detector which is also reduced in size compared to CRESST-II. To avoid any non-active or non-scintillating surfaces within the housing, both detectors are held by CaWO_4 sticks and surrounded by a reflective and scintillating foil. In addition, the sticks holding the crystal are equipped with a TES each ("iStick") to be able to veto possibly dangerous events that happen in the stick but have a crosstalk to the detector crystal. The zoomed picture shows the upper part of one of these iSticks together with the bonds coupling its TES to the cable.

has a mass of ~ 24 g and dimensions of $(20 \times 20 \times 10) \text{ mm}^3$. The size of the accompanying SOS light detector is with $(20 \times 20 \times 0.4) \text{ mm}^3$ adapted to the size of the detector crystal. As two stick-modules providing a fully scintillating detector housing were successfully operated in CRESST-II Phase 2, this holding scheme is also applied for the CRESST-III modules. Each detector is held by three CaWO_4 sticks (in the projection of figure 2.13 (left) only two are depicted) with a diameter of 2.5 mm and a length of ~ 12 mm each⁵. A small longitudinal recession in the light detector sticks provides a stable holding of the SOS light absorbers. Three dips are milled into the detector crystal enabling a point-like contact to the sticks. The dips are optically polished to avoid any stresses at the contact point. From outside the housing all sticks are fixed with bronze clamps.

Together with the reflective and scintillating foil surrounding the detectors a fully scintillating housing is realized. However, after a particle interaction in one of the phonon detector sticks a certain fraction of energy is transmitted to the detector crystal via the point-like interface between stick and main crystal. This can result in a degraded signal. Especially in the case of nuclear recoils or stress relaxation, such events could cause background in the ROI of detectors with low energy thresholds. For an efficient rejection of these event classes, the phonon detector is equipped with instrumented sticks referred

⁵In contrast to CRESST-II Phase 2, also the light detector is held by CaWO_4 sticks in CRESST-III Phase 1.

to as iSticks. A small silicon carrier with dimensions of $(3 \times 3.5 \times 0.4) \text{ mm}^3$ and with an evaporated TES is glued to each iStick (see zoomed picture of figure 2.13 (right)). The three iSticks of each detector module are connected in parallel and read out using one SQUID only [71, 100]. In the analysis, the ratio of the signal in the iStick and in the detector crystal can be used to discriminate stick-related events.

A prototype CRESST-III detector module was successfully operated at mK temperatures in a cryostat above ground at the Max-Planck Institute for Physics (MPP) in Munich. A 5σ energy threshold of $(192.8 \pm 5.5) \text{ eV}$ was achieved in this measurement [70]. From this result, an expected threshold of $\sim 50 \text{ eV}$ could be derived for an operation of the module in the CRESST setup where a significantly lower event rate and much better noise conditions are present.

2.4.1. CRESST-III Phase 1

For CRESST-III Phase 1, we assembled ten such detector modules (named from A to J) in a clean room facility at MPP and installed them later in the detector carousel, also under clean room conditions. A picture taken during installation is shown in figure 2.14. The ten modules on their support structure are mounted in the detector carousel. The cables coming from the inside of the modules are coupled to the so-called detector wings at the outside of the carousel where the connectors to the cryostat wiring are located.

Table 2.3 summarizes the installed modules⁶. Eight of the ten detector crystals included were grown at TUM in the frame of the present work. Details on the different TUM-grown crystals are given in chapter 3. The three detector crystals cut from TUM73 as well as TUM26 have an additional number indicating their position in the raw crystal (this information is not available for the other crystals in CRESST-III Phase 1⁷). Two detector crystals were cut from the commercial crystal Frederika (also installed in CRESST-II Phase 2) provided by the General Physics Institute (GPI) in Moscow [102].

CRESST-III Phase 1 started data taking in summer 2016.

2.4.2. Projected Sensitivity of CRESST-III Phase 1 and Phase 2

The enhanced sensitivity of the CRESST-III detector modules will allow to further explore the regime of low-mass DM particles. The projected sensitivities of CRESST-III Phase 1 and Phase 2 – conservatively assuming phonon detector thresholds of 0.1 keV – are drawn in figure 2.15 [99]. Supposing that detector crystals have a quality comparable to that of TUM40 and an exposure of 50 kg days (six 24 g detector crystals operated for $\sim 1 \text{ year}$) results in the green band ($1\sigma \text{ C.L.}$). At low DM particle masses an improvement of about two orders of magnitude compared to the Lise-result (solid red line) can be achieved. A first DM analysis is currently ongoing and will be published in the near future.

The goal for CRESST-III Phase 2 is an improvement of the total background (including

⁶In addition to the ten small modules, also three R&D modules of an improved version of the so-called beaker design [81, 101] are installed. They are, however, not treated within this thesis.

⁷For these crystals, shoulder and tail were cut and only the cylindrical part was stored before being further processed to detector crystals. This means, the information on the top/bottom orientation was lost.

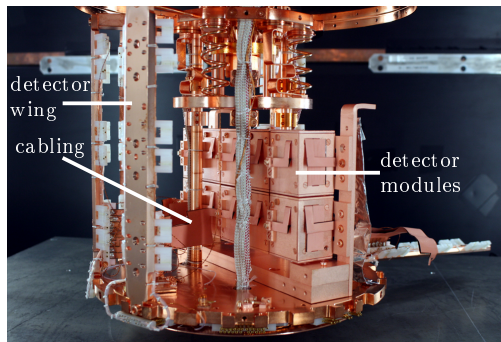


Figure 2.14.: Ten CRESST-III Phase 1 detector modules during their installation in the detector carousel. The copper-capped copper cables coming out of the modules are connected to the wings of the detector carousel. Wires inside these wings link the modules to the electronics.

module	crystal	supplier
A	TUM56	TUM
B	TUM73-1	TUM
C	TUM73-2	TUM
D	TUM56	TUM
E	TUM73-4	TUM
F	TUM68	TUM
G	TUM26-2	TUM
H	Frederika	commercial
I	Frederika	commercial
J	TUM56	TUM

Table 2.3.: List of the ten detector modules named from A to J installed in CRESST-III Phase 1. In total, eight crystals are provided by TUM, whereas two were cut from the commercial crystal Frederika already installed in CRESST-II Phase 2. In case of TUM26 and of the three crystals cut from the ingot TUM73, an additional number indicates their position in the raw crystal. This information is not available for the other crystals.

the intrinsic background of the crystals themselves as well as external radioactive contamination of the surrounding material) by a factor of 100 compared to TUM40. Based on this requirement, the present work focuses on the development of methods to improve the radiopurity of CaWO_4 crystals. Together with an increased exposure of 1000 kg days (corresponding to the operation of 100 detector modules with 24 g detector crystals for ~ 2 years), the improved radiopurity leads to the projection of the pink sensitivity band in figure 2.15. With the additional gain in performance of CRESST-III Phase 2, even the coherent neutrino scattering limit [96] marked in grey in figure 2.15 is in reach⁸.

⁸Coherent neutrino nucleus scattering was recently, for the first time, experimentally observed [103]. The development of CRESST-like detectors optimized for the investigation of coherent neutrino nucleus scattering is topic of further research projects [104,105].

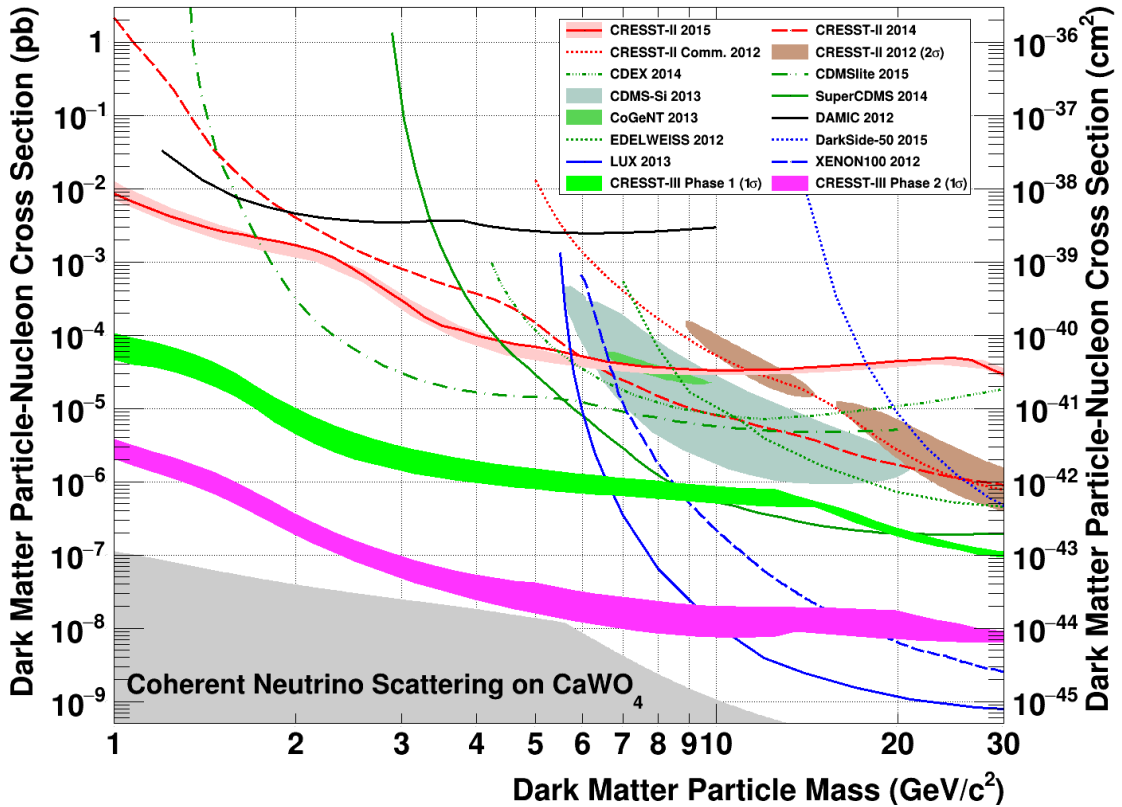


Figure 2.15.: 1σ projection bands for CRESST-III Phase 1 and Phase 2 [99]. Operating six CRESST-III detectors with a threshold of 0.1 keV and with TUM40 quality for 1 year (50 kg days) is expected to result in the sensitivity shown in light green (1σ C.L.). Assuming a background reduction by a factor of 100 as well as a higher exposure of 1000 kg days as planned for CRESST-III Phase 2 leads to the pink 1σ sensitivity band. Compared to the result of the detector crystal Lise (solid red line), the sensitivity at low DM particle masses can be increased by ~ 2 (~ 4) orders of magnitude in Phase 1 (Phase 2). With CRESST-III the chance is given to detect coherent neutrino-nucleus scattering [96].

3. Production of CaWO_4 Single Crystals

The production of CaWO_4 single crystals as described in this chapter is a major topic of the present work. Before 2013, CaWO_4 crystals installed in the CRESST experiment were obtained from commercial suppliers in Russia [102] and the Ukraine [106]. However, in this way no possibility was given to control the production process and to guarantee a clean environment and handling of the materials. Therefore, a Czochralski furnace solely dedicated to the production of CaWO_4 crystals was installed in the crystal laboratory of TUM in 2007 (in the frame of the Excellence Initiative) and a procedure to reliably produce CaWO_4 crystals was developed [107]. Now all the production steps illustrated in figure 3.1 are performed at TUM and can constantly be improved and adapted to the experimental requirements. The whole process includes the CaWO_4 powder production (b) from the raw materials CaCO_3 and WO_3 (a), the CaWO_4 crystal growth (c) as well as post-growth treatments (d). First TUM-grown crystals were installed in CRESST-II Phase 2.

This chapter deals with the standard procedures of all crystal production steps. The newly developed methods to improve especially the radiopurity of detector crystals are presented in chapter 5.

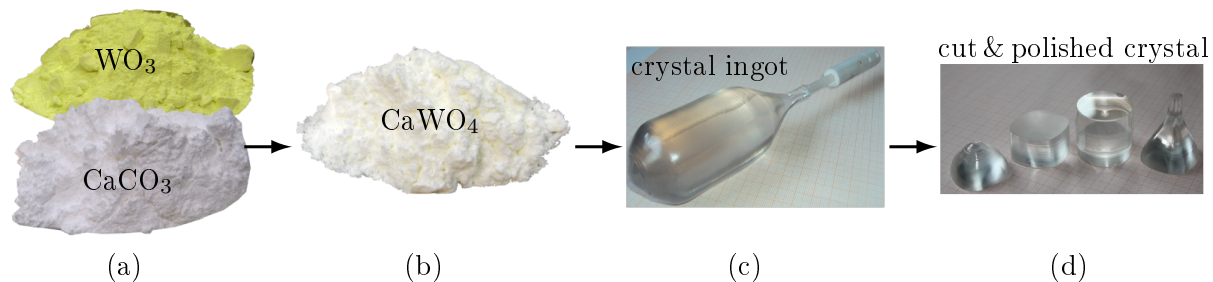


Figure 3.1.: Overview of all steps of the CaWO_4 crystal production performed at TUM within the frame of the present work. First, the two raw materials CaCO_3 and WO_3 (a) chemically react to produce CaWO_4 powder (b) which is the starting material for CaWO_4 crystal growth. Post-growth treatments of the grown raw crystal (c) involve, e.g., cutting and polishing (d).

First, section 3.1 gives an overview of CaWO_4 material parameters which influence the production and/or the characterization of the single crystals. The steps performed during the production of the CaWO_4 powder from the raw materials to the growth of the final crystal are explained in sections 3.2 and 3.3. The post-growth treatment is described in section 3.4. Section 3.5 concludes with a summary of the CaWO_4 crystals produced in the frame of the present work.

crystal system	tetragonal dipyramidal
unit cell parameters	$a = b = 5.24 \text{ \AA}$, $c = 11.37 \text{ \AA}$ [108]
space group	$I4_1/a$ [108]
cleavage planes	101, 110 [107]
molecular mass	287.92 u [111]
density	6.06 g/cm^3 [111]
melting point	$1620 \text{ }^\circ\text{C}$ [111]
hardness	(4.5 - 5) Mohs [108]
solubility	only soluble in hot acids [111]
ordinary refractive index	~ 1.92 [108]
extraordinary refractive index	~ 1.94 [108]
max. birefringence	0.017 [108]
light yield	(16 000 - 20 000) ph/MeV [112, 113]
scintillation decay time	(1 - 10) μs [114, 115]
emission maximum	$\sim 420 \text{ nm}$ [114]

Table 3.1.: Physical properties of CaWO_4 which are relevant for the production and characterization of single crystals. Included is information on the crystal structure as well as on the molecular and optical properties. All optical values refer to room temperature (RT). Especially the scintillation properties like light yield and decay time can deviate at low temperatures in the mK range [115, 116].

3.1. Properties of CaWO_4

In nature, the CaWO_4 mineral also known as scheelite (named after the Swedish chemist C.W. Scheele) is an important ore of tungsten. The crystal properties are summarized in table 3.1. Within the tetragonal crystal structure depicted in figure 3.2 (a), Ca^{2+} - ions (blue circles) are surrounded by tetrahedra of $[\text{WO}_4]^{2-}$ - ions (green and red dots) forming a cuboid-shaped unit cell with $a = b = 5.24 \text{ \AA}$ and $c = 11.37 \text{ \AA}$ [108]. As a pronounced natural cleavage tendency can be observed in the (101)- and (110)-planes¹ [107], mechanical or thermal stresses have to be minimized. Therefore, at TUM crystals are usually grown along the c-axis. The orientation of a crystal can be determined via the Laue method which is based on X-rays diffracted by certain groups of parallel atomic planes within a crystal [109]. By using a white spectrum of X-rays, all planes can satisfy the Bragg law and produce X-ray spots. A typical Laue pattern of a c-oriented TUM-grown CaWO_4 crystal (TUM73) was recorded with a real-time back reflection Laue camera with an accuracy better than 0.2° [110]. The different diffraction spots are visible as black dots in figure 3.2 (b). The pattern is highly symmetric which confirms the c-orientation of the crystal.

Due to the heavy component tungsten, CaWO_4 has a high molecular mass of 287.92 u and a density of 6.06 g/cm^3 (see table 3.1). It is a congruently melting compound (i.e.

¹In the crystallographic notation system formed by the Miller indices, (hkl) means a plane that intercepts the three points \vec{a}/h , \vec{b}/k , and \vec{c}/l .

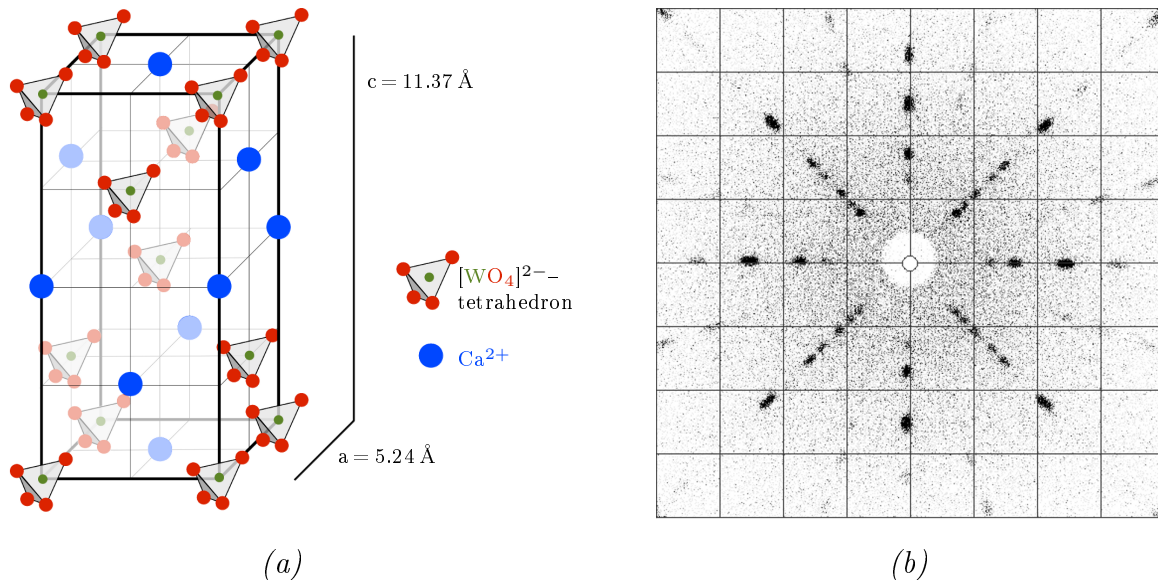


Figure 3.2.: (a) Tetragonal crystal structure of CaWO_4 . The unit cell is cuboid-shaped with $a = b = 5.24 \text{ \AA}$ and $c = 11.37 \text{ \AA}$ and includes Ca^{2+} -ions (blue) surrounded by tetrahedra of $[\text{WO}_4]^{2-}$ -ions (green and red) [108]. (b) Laue pattern of a CaWO_4 crystal (TUM73). The array of dark spots is formed by diffracted X-ray beams with certain wavelengths. The high symmetry of the pattern reveals the c -orientation (looking on (001) -planes, compare (a)) of the crystal.

the composition of the liquid that forms is the same as the composition of the solid) with a high melting point of $\sim 1620 \text{ }^\circ\text{C}$ [111]. As the material has to be melted for crystal growth, a method suitable for these high temperatures had to be found (see section 3.3). For the further treatment of the CaWO_4 crystals after growth, the hardness plays an important role. On the Mohs scale of mineral hardness, CaWO_4 lies in the middle of the scale with a value between 4.5 Mohs and 5 Mohs [108] meaning that harder materials with higher values are able to scratch CaWO_4 (e.g. diamond with a maximal hardness of 10 Mohs [108]).

The solubility of CaWO_4 in water is relatively low – at a temperature of $18 \text{ }^\circ\text{C}$ only an amount of 0.2 g of CaWO_4 material dissolves in 100 g of water. CaWO_4 is only soluble in (hot) acid (e.g. hydrofluoric acid) [111] which makes, e.g., a chemical treatment difficult. As CaWO_4 is used as scintillator in the CRESST experiment, the optical properties of CaWO_4 are of high importance. The high refractive index of $\gtrsim 1.91$ could lead to large trapping of scintillation light due to total internal reflections [117]. Additionally, CaWO_4 is slightly birefringent with a maximum difference of 0.017 between ordinary and extraordinary refractive index [108]. Light yields typically range between (16 000–20 000) photons per MeV deposited energy [112, 113] with an emission maximum at $\sim 420 \text{ nm}$ [114]. Scintillation decay times are in the order of a few μs . All optical values given here refer to measurements at room temperature. Especially the light yield and the scintillation decay time can, however, change at temperatures around 1 K or in the mK range as was previously investigated, e.g., in [115, 116].

On the one hand, defects in the crystal structure can have a negative influence on the

optical properties as they can cause scattering or absorption of photons. Apart from solid or gaseous inclusions as well as dislocations due to dielectric inhomogeneities, the main intrinsic defects in CaWO₄ crystals are oxygen vacancies [112]. On the other hand, deliberately inserting foreign atoms via doping can have a positive effect on the scintillation. Doping CaWO₄ crystals with lanthanum leads to an improved transmittance for wavelengths below 450 nm [118]. A similar improvement in the short wavelength region (330 nm - 450 nm) was observed for PbWO₄ crystals after having been doped with trivalent ions like La³⁺, Lu³⁺, Gd³⁺ or Y³⁺ [119].

However, such doping also increases the risk of unwanted radioactive contaminations that could lead to potential backgrounds in the region of interest for DM search. In the case of CRESST, a good radiopurity is the most crucial property for the produced CaWO₄ crystals. Therefore, the present work focuses on methods how the radiopurity can be improved (see chapter 5).

3.2. Production of CaWO₄ Powder

For an improvement of the quality of CaWO₄ crystals, a control of all production steps is required. Since CaWO₄ can neither be chemically treated in the form of powder nor in the form of a crystal to achieve, e.g., an enhanced radiopurity, at TUM, CaWO₄ powder is produced from the two raw materials CaCO₃ and WO₃. A high initial radiopurity is required for these powders. Thus, a suitable supplier was selected only after having investigated analysis certificates and after having screened samples of various powder batches [120]. For the crystals produced in the scope of the present work, powders from the American company MV laboratories, Inc. [121] were used. To minimize cosmogenic activation, particularly of tungsten in the WO₃ powder, the materials were delivered seaborne and overland avoiding flights and the associated higher exposure to cosmic radiation. In addition, all powders as well as crystals and other materials are usually stored in a nitrogen cabinet in the shallow underground laboratory in Garching (~ 10 m.w.e. [122]) until they are further processed.

The production of CaWO₄ powder requires an efficient transformation to the end product without creation of by-products. Any contamination with external impurities has to be avoided. Two approaches, which were both tested in the present work, are presented in the following.

Solid State Reaction

At the beginnings of CaWO₄ crystal production at TUM, a method was developed to synthesize CaWO₄ powder via a solid state reaction at high temperatures:



The upward pointing arrow implies that CO₂ gas volatilizes during the reaction. To preserve the proper stoichiometry, 2.316 g WO₃ per 1.000 g CaCO₃ have to be mixed. At TUM, the mixing of the two powders is performed within a rotating container with the help of two grinding balls. Afterwards, the mixture is filled into an Al₂O₃ crucible and put into a dedicated chamber furnace where it is heated up to 1100 °C with a rate of

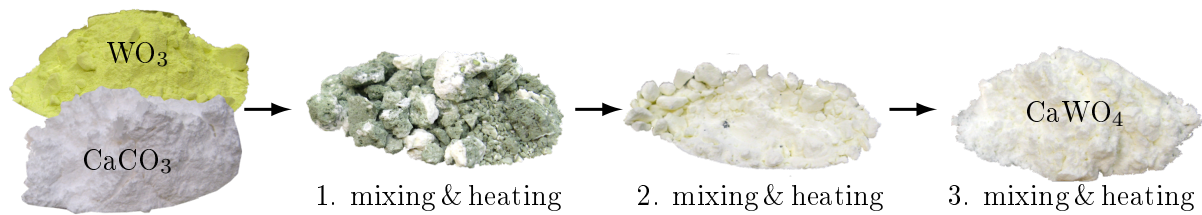


Figure 3.3.: CaWO_4 powder production via a solid state reaction (equation 3.1) as performed at TUM in the frame of the present work. The raw materials WO_3 and CaCO_3 are mixed in the right stoichiometry. Afterwards, the mixture is heated up to 1100°C in a dedicated chamber furnace. As the reaction is not yet completed after this step (greenish powder mixture due to WO_3 remainings), the procedure is repeated until the outcome is homogeneously white. In this picture, greenish speckles can still be found in the powder after the second time mixing and heating up to 1100°C . Only after the third time (heating up to 1200°C) the reaction is completed.

$275^\circ\text{C}/\text{h}$. This temperature is kept for 10 h before the chamber furnace is cooled down again. Empirical observations have shown that the mixing and baking has to be repeated at least once (usually two repetitions are applied). The reaction is not completed after the first cycle because not every molecule of one of the powders has been close enough to a reaction partner from the respective other raw powder. The resulting product is not completely white but still interfused by greenish speckles originating from WO_3 powder which has not reacted. After the first step of mixing and heating, the greenish color is still dominating while only a few speckles remain after the second mixing and heating (see figure 3.3). In the method optimized at TUM, the maximal temperature in the first two cycles is 1100°C . Only in the third (i.e. last) cycle, the powder is heated up to 1200°C which is beneficial for the reaction to complete. However, at the same time, the higher temperature increases the hardness of the powder which complicates its removal out of the crucible. To check if the reaction is completed, the weight loss of the powder due to released CO_2 gas (13.25% of the initial total powder mass) is taken as a control value. The resulting CaWO_4 powder, after the complete reaction has taken place, is homogeneously white without any observable speckles as shown in the rightmost picture of figure 3.3 (third cycle of mixing and heating).

The disadvantages of this method are the contacts of the raw materials with the crucible, the grinding balls and container, as well as the manual removal of the hard powder after baking. In connection with the high temperatures in the chamber furnace and the mechanical forces during grinding, a contamination with impurities originating from the non-high-purity components (e.g., the crucible or the grinding balls) cannot be excluded. Improvements achieved in the frame of the present work are described in section 5.2.

Precipitation Reaction

In the present work, we developed a second method for the production of CaWO_4 powder via a precipitation reaction. To enable such a reaction, the raw materials first have to be transformed into aqueous solutions. At TUM, this is achieved by dissolving the CaCO_3

3. Production of CaWO_4 Single Crystals

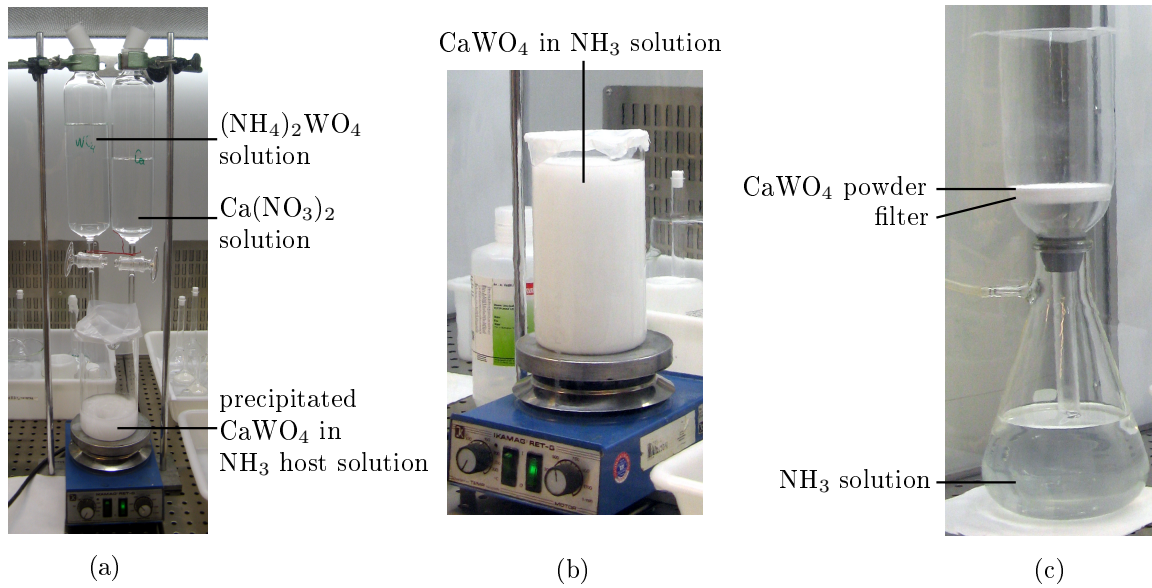
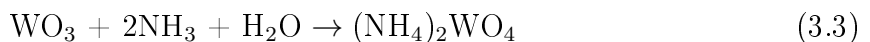
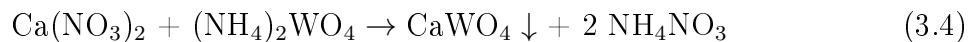


Figure 3.4.: Different steps of the production of CaWO_4 powder via the precipitation reaction (see equation 3.4). The two raw materials CaCO_3 and WO_3 are dissolved in HNO_3 and NH_3 solutions, respectively, according to equations 3.2 and 3.3. Both solutions are – under continuous stirring – slowly dropped into a 5% NH_3 host solution (a). As soon as CaWO_4 precipitates, the solution turns milky. Stirring is continued after both solutions have completely dripped into the host solutions (b) in order to ensure a complete reaction. The produced CaWO_4 powder is filtered (c) and dried.

and WO_3 powders in aqueous solutions of nitric acid (HNO_3) and of ammonia (NH_3), respectively. The chemical reaction equations are:



A limiting factor for mass production is, hereby, the slow reaction of WO_3 powder and its solubility: dissolving the powder with a concentration of ~ 0.4 mol/l lasts about three days. The corresponding equation of the actual precipitation reaction is



The downwards facing arrow indicates the precipitation of CaWO_4 powder. At TUM, this reaction is realized via dropping both solutions of $\text{Ca}(\text{NO}_3)_2$ and $(\text{NH}_4)_2\text{WO}_4$ in the proper stoichiometry into a 5% NH_3 host solution (see figure 3.4 (a)). This solution is constantly stirred and is aimed at solving impurities such as sodium and potassium. The reaction has to be performed slowly with low concentrations in order to have a clean CaWO_4 product avoiding any by-products.

When both solutions have completely dripped into the host solution, stirring is continued for (3-4) h to ensure a complete reaction. The precipitated white CaWO_4 powder stirred in the NH_3 solution is shown in figure 3.4 (b). After sedimentation, the solution is decanted and the produced CaWO_4 powder is washed with fresh NH_3 solution and

water. Finally, it is filtrated (figure 3.4 (c)) and calcinated, i.e. heated up so that the remaining moisture as well as volatile impurities and water are removed. To check if the precipitation reaction happened completely, the mass of the produced powder is controlled. In the procedure applied at TUM, 46.4 g of WO_3 powder dissolved in 500 ml solution as well as 20.0 g of CaCO_3 powder dissolved in 300 ml solution are necessary to produce one batch of CaWO_4 powder with a mass of 57.6 g.

Although this process is slower than the powder production via solid state reaction, it has the advantage that the materials are only in contact with the clean quartz glass equipment used for the reactions. Furthermore, additional cleaning steps (see section 5.3) can be applied since the raw materials are processed as solutions.

3.3. Crystal Growth via the Czochralski Method

In order to grow a single crystal, the produced CaWO_4 powder has to be melted in a suitable furnace withstanding high temperatures in the region of the melting point of CaWO_4 of $\sim 1620^\circ\text{C}$. As CaWO_4 is an oxide, a certain amount of oxygen is beneficial to be present in the growth atmosphere. Otherwise, a high amount of oxygen vacancies would arise in the crystal resulting in a worse transparency and in worse scintillation properties. The transparency to visible light as well as to infrared radiation excludes a containerless crystal growth in an optical furnace. Furthermore, CaWO_4 is an insulating material making a direct inductive heating as applied in the floating zone method (e.g. used for the production of high-purity silicon single crystals) impossible.

Already in the 1960s the Czochralski method was found to be suitable for the growth of CaWO_4 crystals [123, 124]. The basic principle as well as its realization at TUM are explained in the following.

3.3.1. Working Principle

A schematic drawing showing the principle of the Czochralski method is depicted in figure 3.5. The material to be crystallized is heated up in a crucible until a homogeneous melt has developed. A seed crystal (from the same material) with a specific crystallographic orientation is slowly lowered into the melt and moved upwards again under rotation². At the contact area a crystal with the same crystallographic orientation as the seed crystal grows from the melt. Hereafter, in the present work, the completely grown crystal is denoted as raw crystal or crystal ingot to avoid any confusion with detector crystals.

Crucible

In case of CaWO_4 , a crucible with a melting point which is at least $\sim 200^\circ\text{C}$ higher than that of CaWO_4 has to be chosen to minimize the risk of locally melting the crucible. Furthermore, a high chemical inertness and resistance against oxygen is required for the

²The rotation of the seed crystal is necessary for a homogeneous growth. Without rotation, a crystal disk would develop on the cooler melt surface.

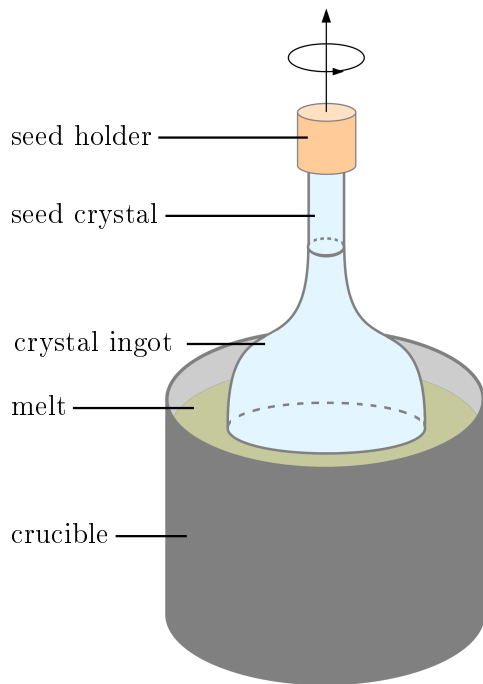


Figure 3.5.: Principle of the Czochralski method. The material to be used for crystal growth is melted in a crucible. A seed crystal from the same material is lowered into the melt and drawn up again under rotation. In this way, a cylindrically shaped raw crystal is formed featuring the same crystallographic orientation as the seed crystal.



Figure 3.6.: CaWO_4 crystal ingot hanging down from its seed crystal and holder after growth in the Czochralski furnace (here without after-heater, shown in figure 3.7). The remaining melt is solidified at the bottom of the crucible which is surrounded by insulation to minimize heat losses during growth.

crucible material. A suitable material fulfilling these requirements is rhodium³ with a melting point of 1964°C [111]. Thus, a rhodium crucible with an inner diameter and height of 80 mm, a wall thickness of 2 mm and a mass of ~ 710 g is used for CaWO_4 crystal growth at TUM⁴. It can hold up to ~ 1.6 kg of melted CaWO_4 material.

Seed Crystal and Holder

In order to obtain a nearly cylindrical shape of the raw crystal, the growth is performed in c-direction at TUM⁵. This c-orientation of the crystal ingot can only be achieved

³Another suitable material with an even higher melting point of 2446°C is iridium [111]. However, an iridium crucible would not allow any oxygen in the growth atmosphere due to oxidation.

⁴In the past, also a larger rhodium crucible ($\varnothing = 120$ mm) allowing the growth of larger crystals was used.

⁵Since the other two dimensions a and b of the crystal lattice equal each other (compare section 3.1), only slight growth anisotropies occur perpendicular to the c-axis which implies that the crystal ingot grown with c-orientation is approximately cylindrical. In general, such anisotropies in the growth rates of different directions result in facets of the grown raw crystal – weakly pronounced they are

when the CaWO_4 seed crystal is perfectly c-oriented. Already a small deviation of a few degrees can lead to an asymmetric raw crystal tending to break due to internal stresses (see appendix B.1). Conical seed crystals with a typical diameter of (7-8) mm are usually obtained via cutting them from a raw crystal with small diameter produced in a dedicated growth. In the furnace, the seed crystal is fixed to a likewise conical Al_2O_3 holder attached to the pulling head of the furnace (see figure 3.6). Unsuccessful attempts to use a differently shaped seed holder are described in appendix B.1, as well. After a successful growth, the seed crystal can be recovered by cutting the raw crystal off. It can even be slightly elongated when the raw crystal's upper part is left on the seed. This allows a higher number of seeding attempts (see section 3.3.2) or the production of a new seed crystal.

Crystal Ingot

A photograph of a crystal ingot hanging from its seed crystal above the rhodium crucible is shown in figure 3.6. The crucible contains the solidified remaining melt which can be reused together with fresh CaWO_4 material in a subsequent growth process. After several growth cycles, the remaining melt is completely removed.

Typically, crystal ingots with a mass of up to ~ 900 g, a diameter of up to ~ 47 mm and a length of up to ~ 150 mm (see, e.g., crystal ingot in figure 3.6) can be grown from the 80 mm rhodium crucible [107]. Adapting to the requirements of the smaller detector crystals used in CRESST-III (compare section 2.4), however, smaller raw crystals with a diameter of 30 mm, a mass of ~ 400 g and a length of ~ 125 mm were also produced.

Heating and Insulation

The crucible is surrounded by several insulation layers made of porous ZrO_2 stabilized by Y_2O_3 and of Al_2O_3 to minimize heat losses during growth (see figure 3.6). The temperature of the melt is provided by induction heating of the crucible. Therefore, water-cooled induction heating coils fed by a high-frequency (HF) generator (operating at ~ 7 kHz) surround the crucible and its insulation as can be seen in figure 3.7 (right). A quartz glass cylinder is integrated in order to avoid electrical discharges between the coils and the crucible. On top of the crucible, an after-heater is located which allows a slow and controlled cooling of the crystal ingot after growth. The after-heater is explained in more detail in section 3.3.4.

Furnace

The Czochralski furnace operated at TUM is a Cyberstar oxypuller 20-04 [125] which is shown in the left picture of figure 3.7. The housing of the pulling head, to the bottom of which the seed crystal is connected, can be seen on top of the furnace. It contains a precision balance which is able to measure weights up to 8.2 kg with a resolution of 1 mg [107]. In this way, the mass of the growing crystal ingot can constantly be displayed during growth.

The top of the crucible, i.e. the upper region of the initial melt as well as the seed crystal

also visible in, e.g., figure 3.6.

3. Production of CaWO_4 Single Crystals

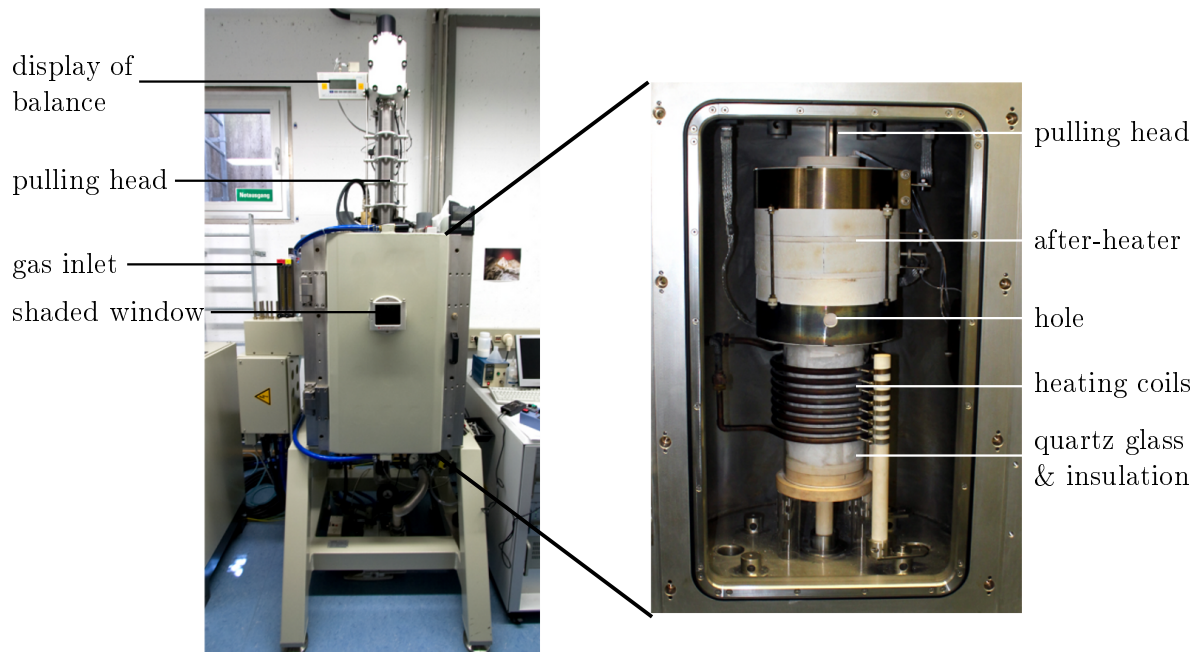


Figure 3.7.: Czochralski furnace installed at TUM, views from the outside (left) and inside (right). The pulling head is connected to the seed crystal and contains a precision balance constantly measuring the weight of the grown part of the raw crystal. The growth atmosphere can be regulated via a gas inlet. The water-cooled induction heating coils as well as several layers of insulation are installed around the crucible. Additionally, a quartz glass cylinder is integrated in order to avoid electrical discharges. After growth, the crystal ingot stays in an after-heater located on top of the crucible for several hours. There, it is afterwards slowly cooled down during a period of one day. The shaded window and the hole in the after-heater allow a view of the crystal ingot growing from the melt.

and later a part of the grown crystal ingot can be observed through a shaded window in the furnace and a hole in the after-heater (see figure 3.7). In this way, the melting of the material, the seeding as well as the shape of the growing crystal ingot can be controlled by eye, as well.

Growth Atmosphere

The crystal growth is performed in an atmosphere containing 99% of the noble gas argon not reacting with any of the components within the furnace. 1% of oxygen is added to the growth atmosphere in order to produce an equilibrium in such a way that not too much oxygen is evaporated from the CaWO_4 melt. In this way, the amount of oxygen vacancies in the raw crystals, which have a negative influence on the optical quality of the CaWO_4 detector crystal, is minimized. A higher percentage of oxygen in the atmosphere is not favorable as it would lead to the formation of volatile rhodium oxide. The flow of the 99% Ar/1% O mixture can be regulated via a gas inlet and is usually set to a value of $\sim 10\text{l/h}$.

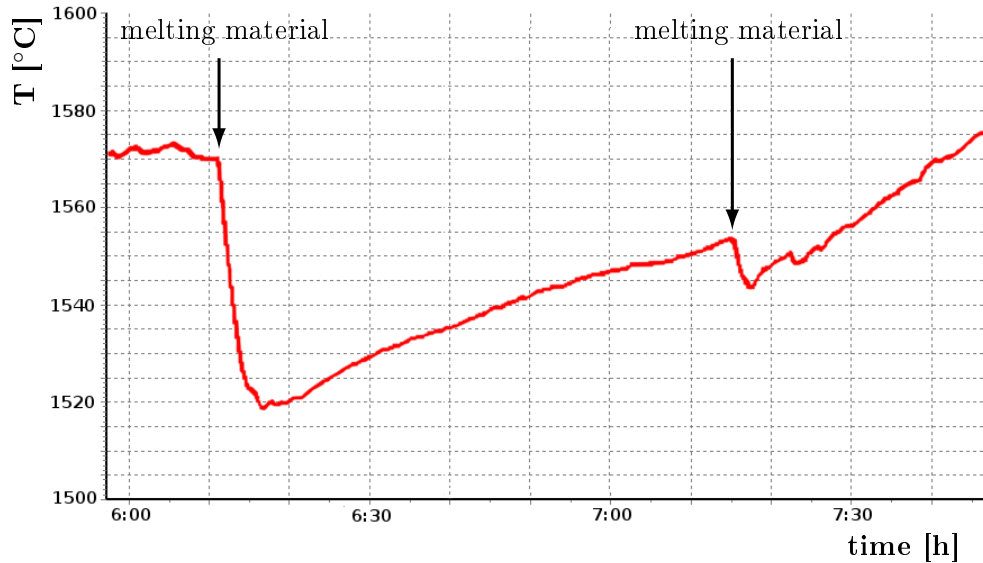


Figure 3.8.: Exemplary temperature curve of the crucible during heating-up (via increasing the power of the HF generator). The enthalpy of fusion necessary to melt the CaWO_4 material leads to a drop in temperature every time a certain part of the CaWO_4 material is melting (indicated by arrows). The degree of the temperature drop depends upon which part of the CaWO_4 material is melted – melting a crust on top, e.g., leads to a loss in heat isolation and a large temperature drop. In this case the material can solidify again before it is melted another time more homogeneously. The temperature is given by a thermocouple placed outside the crucible. As this measured temperature depends on the position and coupling of the thermocouple, it can deviate from the physical temperature (with a linear shift of $\sim 50^\circ$ on the y-axis).

3.3.2. Growth Preparation and Seeding

Before starting the growth process, various preparation steps have to be performed. If necessary, new CaWO_4 material is filled into the crucible. All required components explained before are installed. Several thermocouples are connected to control the temperature at different positions within the furnace. Afterwards, the furnace is closed, evacuated to a pressure in the order of 10^{-2} mbar and flushed with the 99% Ar/1% O mixture. The crucible is slowly (during several hours) heated up to the melting point of CaWO_4 by increasing the power of the high-frequency generator. For the generator operated at TUM, (20-25) % of the maximal power correspond to the temperatures required for CaWO_4 crystal growth. High temperature gradients which could result in local thermal stresses have to be avoided to extend the lifetime of the crucible and of the other components within the furnace. An exemplary temperature variation with time as registered by the thermocouple placed at the outside of the crucible can be found in figure 3.8 showing the last part of the heating phase⁶.

The temperature increases with increasing power until the first melting occurs. At that

⁶It has to be mentioned that the temperature measured by the thermocouple depends on its exact position and on its coupling to the crucible. Therefore, the measured temperature can deviate from the physical temperature within the melt resulting in a linear shift of $\sim 50^\circ$ on the y-axis in figure 3.8.

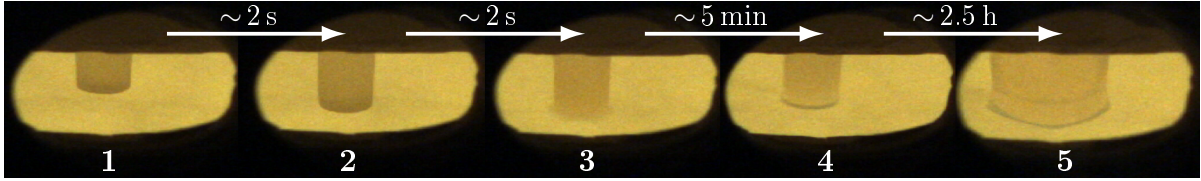


Figure 3.9.: Seeding observable through a window in the furnace. Starting from 1, the CaWO_4 seed crystal is slowly lowered towards the melt (2). When it touches the CaWO_4 melt (3) a slight light flash is visible. By slowly drawing it upwards again under rotation, CaWO_4 crystallizes at the interface and a single crystal starts growing. Only a small disk of crystallized material can be seen about 5 min after seeding (4), whereas the diameter and length are already increased after ~ 2.5 h (5).

point all the energy flows into the enthalpy of fusion of CaWO_4 leading to a temperature drop every time a part of the CaWO_4 material has melted (indicated by arrows in figure 3.8). Usually, a melt starts to develop inside while there is still a crust of CaWO_4 at the top providing a heat isolation. When this crust melts, the sudden loss of heat isolation leads to a further decrease of the temperature. In the case shown, a temperature drop of $\sim 50^\circ\text{C}$ can be seen at $\sim 6:12$. This is typical and can lead to a new freeze-out of the CaWO_4 material. In the following it is melted another time more homogeneously with only smaller temperature drops.

Before starting the crystal growth, it has to be guaranteed that all the CaWO_4 material within the crucible has completely melted. Solid CaWO_4 remnants that could act as a seed for growing another crystal directly in the melt (see, e.g., appendix B.2) have to be avoided. Therefore, the melt is overheated by about 100°C until the temperature increases steadily and no drops pointing to another solid remnant are observed any more. Only then the power of the HF generator can be decreased again in order to cool the melt down back to the melting point of CaWO_4 for seeding.

Figure 3.9 shows a sequence of pictures taken through the shaded window of the furnace during seeding. Using the pulling head of the furnace, the seed crystal is slowly lowered (1,2) within a few seconds until it touches the melt causing the seed to slightly light up (3). By slowly pulling it up again under rotation, CaWO_4 crystallizes at the interface between seed and melt. The first small disk of crystallized material can be seen after ~ 5 min in 4, whereas the diameter and length are already increased in 5 (about 2.5 h after seeding).

Only a narrow temperature window of a few degrees allows a successful seeding. If the temperature is too high, the lower part of the seed crystal simply melts and loses contact to the melt. On the other hand, a melt that is too cold leads to a fast and sudden crystallization with too large a gain of mass and diameter. It was found that melting a small portion at the lower end of the seed crystal is beneficial to achieve a good contact to the melt and a stable seeding without inclusions or defects as well as to guarantee a good adoption of the crystal lattice [126].

3.3.3. Parameter Control

After the seeding and when an equilibrium state is reached, the growth control is handed over to a dedicated software program. There, all parameters such as the crystal geometry, rotation and translation speed as well as the parameters for the proportional-integral (PI) regulation of the generator power (see below) have been defined before the start of the growth.

The geometry of a typical crystal is shown in figure 3.10 (a). The seed crystal is elongated by a short seed part of the raw crystal with constant diameter. In this way, dislocations which are potentially contained in the seed crystal can vanish [126]. The seed part is followed by the shoulder where the diameter is constantly increased. The curvature in the shoulder part is determined via the angle Θ as well as via the ratio of the two radii R_1 and R_2 . In the cylinder, the diameter stays constant before it is decreased again to zero in the tail.

If the diameter of the shoulder is changed too rapidly, radial mechanical forces originating from the weight of the crystal can appear leading to cleaving of the crystal. To avoid such cleaving, crystals at TUM are grown with long shoulders minimizing these radial forces. A raw crystal (TUM73) grown with the geometry of figure 3.10 (a) can be seen in figure 3.10 (b).

Changing the diameter in the different parts of the growing crystal ingot is achieved by adapting the temperature of the melt. This happens via the PI regulation of the power of the HF generator. A schematic drawing of the radial temperature gradient⁷ in the melt with top view onto the crucible is depicted in figure 3.11. The temperature gradient starting from the edge to the innermost part of the crucible is visualized by the color scale. Thereby, red regions are hotter compared to blue regions. As the melt is heated via the crucible, the temperature is higher in the outer regions than in the center of the crucible. Isothermal lines are, therefore, ideally concentric circles inside the crucible. The isothermal line where the temperature T equals the melting temperature T_{melt} of CaWO_4 marks the border between solid and liquid material and corresponds to the diameter of the growing raw crystal (green circle in figure 3.11). When heating up (cooling down) the crucible, this isothermal line shifts closer to (away from) the center decreasing (increasing) the diameter as indicated by the green arrows.

During growth it is necessary to have a good knowledge of the current crystal size in order to be able to correct deviations. Therefore, the mass of the grown part of the crystal ingot is constantly recorded via the precision balance connected to the pulling head of the furnace. Using the mass and the set geometry (see, e.g., table 3.2 in section 3.5), the current growth rate, its deviation from the nominal value (denoted as (growth rate) error) as well as the diameter can be calculated. Is the growth rate and, thus, the diameter too high (resulting in a positive error), the crucible has to be slightly heated up via increasing the power of the HF generator to move the crystallization border inwards. In the opposite case that the growth rate and the diameter are too low (i.e. a negative growth-rate error), the HF generator adapts the power to lower values in order to reduce the temperature.

⁷A temperature gradient also exists in z-direction which is not shown here. For possible consequences on crystal growth see appendix B.2.

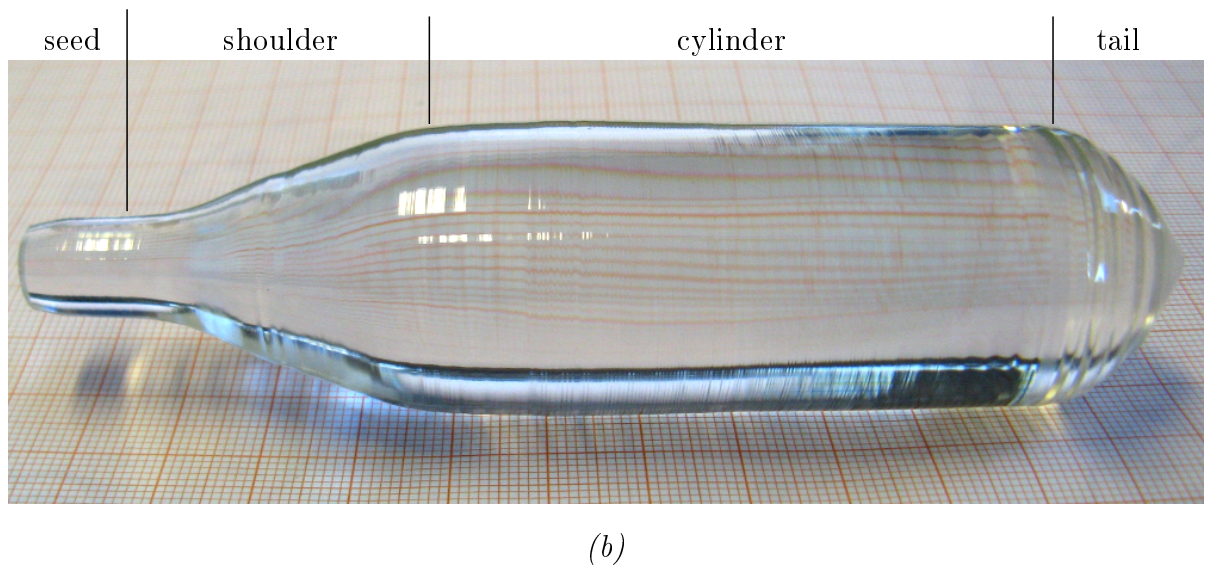
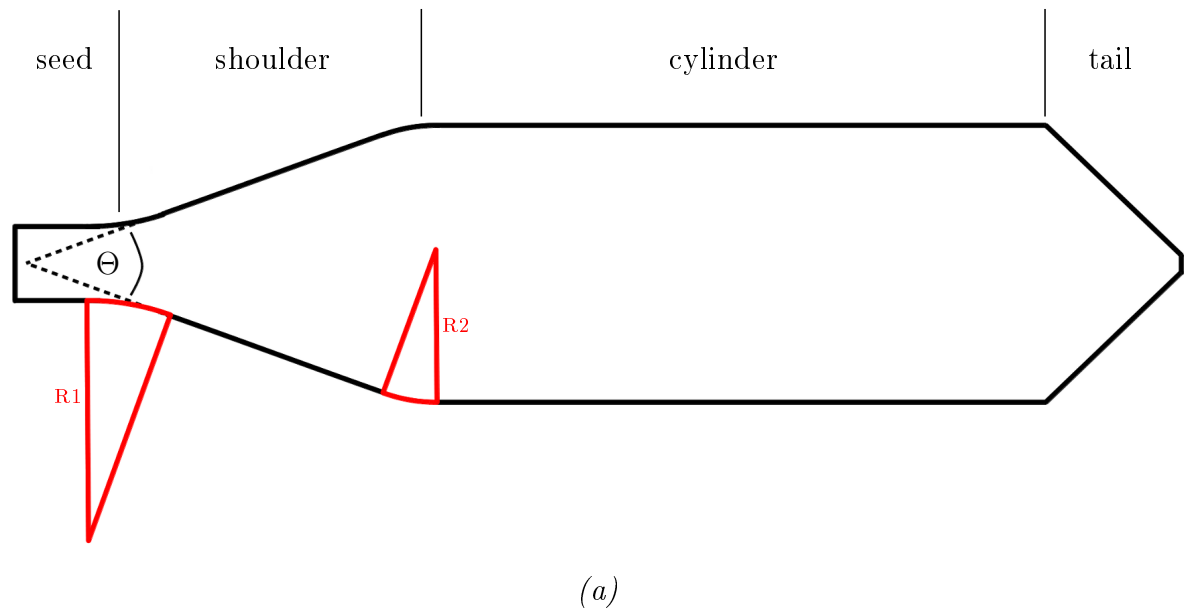


Figure 3.10.: (a) Schematic drawing of a crystal-ingot geometry programmed into the growth software. Starting from the seed, the diameter is slowly increased in the shoulder part until the cylindrical part is reached. The diameter stays constant until it is reduced to zero in the tail. The ratio of the two radii $R1$ and $R2$ as well as the angle Θ determine – as additional input parameters – the curvature in the shoulder part. (b) CaWO_4 crystal ingot TUM73 grown with the geometry of (a). All growth parameters are listed in table 3.2.

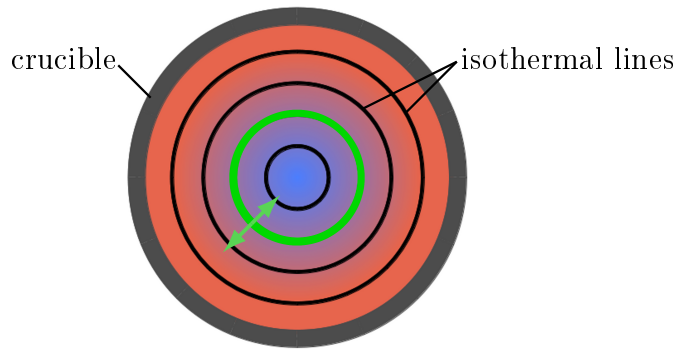


Figure 3.11.: Schematic drawing of the radial temperature gradient of the melt with top view onto the crucible. As the melt is heated by the crucible, the hottest regions (red) can be found directly next to it. The melt temperature decreases (\rightarrow blue) when approaching the center of the crucible. The isothermal lines are marked as black circles. For one of those the temperature equals the melting point of CaWO_4 (green) which determines the crystal diameter. Via increasing (decreasing) the heating power of the HF generator and, thus, the temperature, the crystal diameter can be reduced (enlarged) as indicated by the green arrows.

The values of the four parameters mass, growth-rate error, diameter and heating power are recorded for the whole growth process (lasting ~ 10 h) as exemplarily shown for the growth of TUM73 in figure 3.12 (a)-(d), respectively. The borders between the different crystal parts are drawn as green lines. The seeding (marked by the red line) happened at a time of ~ 10.5 h (after having started to heat the crucible). It can be seen that the diameter drops twice to 0 on the left side of the red line indicating that two seeding attempts failed, i.e. the seed crystal melted and lost contact to the melt. By decreasing the power by hand a suitable temperature had to be found and the third seeding attempt was successful. The growth rate stays constantly a bit too high in the seed part of the raw crystal (before ~ 11.5 h). In the shoulder part (between ~ 11.5 h and ~ 14 h) the diameter is increased up to 30 mm leading to a larger gain in mass. The diameter stays constant at ~ 30 mm in the cylindrical part (between ~ 14 h and ~ 19.2 h) resulting in a linearly increasing mass.

As is plotted in figure 3.12 (d), the heating power increases constantly over almost the whole growth process. This increase is not related to a change in diameter but due to increased radiation losses from the walls of the crucible itself when the melt level is dropping. In addition, small deviations in diameter and growth-rate error from the nominal value force the HF generator to react in order to regulate the temperature. The PI-controlled regulation of the heating power results in oscillations in growth-rate error, diameter, and power that are most pronounced in the tail (time $\gtrsim 19.2$ h) where the diameter is reduced relatively fast to zero⁸. Only in the case of unforeseen events where the growth rate becomes larger than 500 g/h, the growth process is automatically aborted

⁸The oscillation amplitudes seem to be quite high in the order of 10%. However, the grown crystal ingot does not feature diameter oscillations up to a few mm as one could expect from the recorded diameter value in figure 3.12 (c). This hints towards errors in the measurement of the actual crystal mass during growth.

3. Production of CaWO_4 Single Crystals

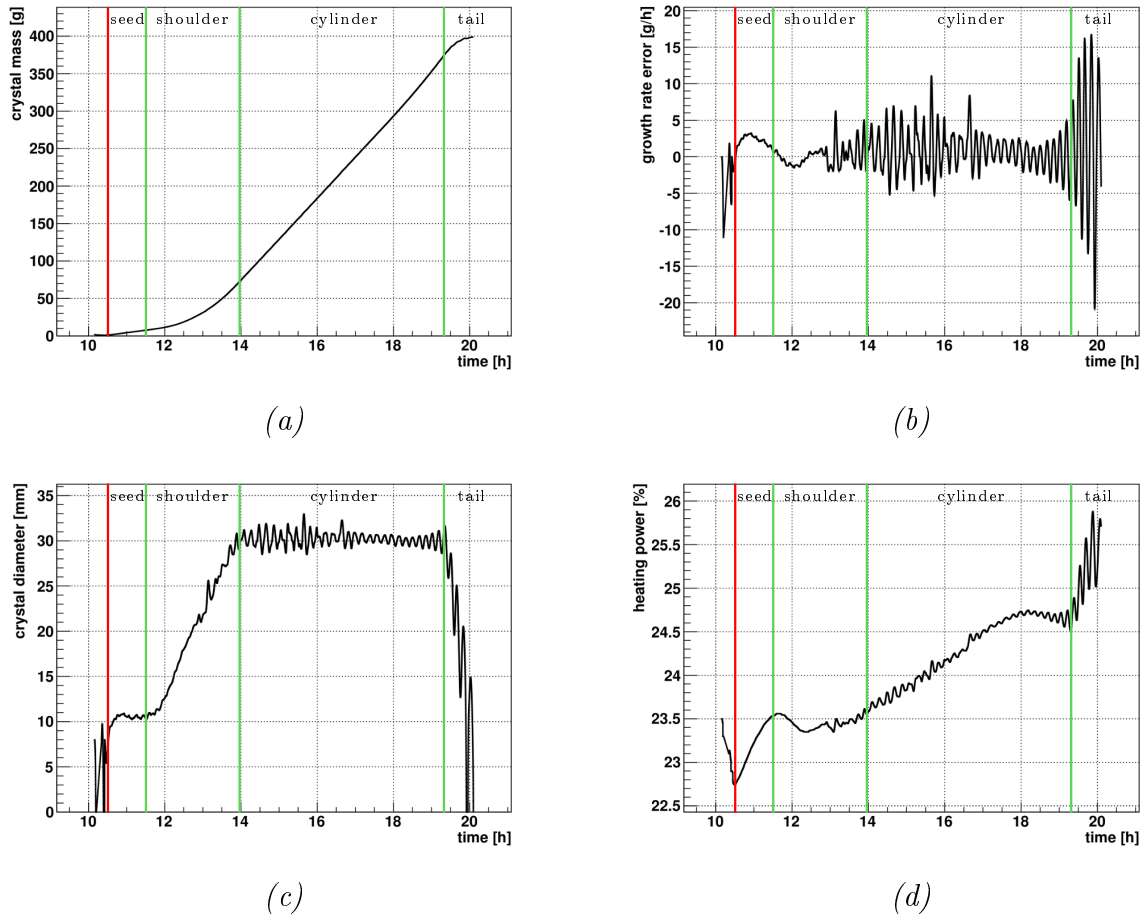


Figure 3.12.: The values of the four parameters crystal mass (a), growth-rate error (b), crystal diameter (c) and heating power (d) as recorded over time during the growth of TUM73. The seeding is marked in red, the borders between the different crystal parts are drawn as green lines. The crystal mass is constantly measured with a precision balance connected to the pulling head of the furnace. It is used to determine the current values of the diameter and of the growth rate. The growth-rate error is the deviation of this current growth rate from the desired growth rate as calculated from the geometry and growth parameters inserted (see, e.g., table 3.2 in section 3.5). The heating power is a PI-controlled parameter which reacts to this error and, thus, regulates the temperature. The PI regulation results in oscillations in error, diameter and power which are most pronounced in the tail ($t \gtrsim 19.2$ h) where a relatively large diameter change is required in a short time.

and the grown crystal ingot is prematurely extracted (for details see appendix B.2).

3.3.4. After-Heater

During crystal growth, the pulling head of the furnace moves the grown part of the crystal ingot slowly into the after-heater located on top of the crucible (see figure 3.7 (right)). Due to the heat radiation originating from the crucible and the melt and due to the insulating ceramics of the after-heater, the temperature within the after-heater stays, during growth, homogeneously constant at high values of ~ 1200 °C. In this way, the crystal is not affected by thermal stresses and the after-heater itself can remain switched-off during growth. After the growth has been finished, the raw crystal is completely extracted into the central part of the after-heater. The crucible is cooled down by reducing the power of the HF generator to zero during a period of a few hours (usually 3 h). This implies that no radiation from below keeps the crystal ingot at a high temperature any more. Therefore, the after-heater is switched on when the crystal ingot is extracted. Inside the after-heater, the raw crystal is kept at a constant temperature of 1200 °C for a time of 24 hours. Afterwards, the after-heater is slowly cooled down to room temperature with a rate of 50 °C/h. In this way, internal stresses in the raw crystal are minimized and the danger of cleavage due to temperature gradients or rapid cooling is reduced. In addition, the slow cooling rate also allows oxygenation of the crystal ingot. After the furnace has reached room temperature, it can be opened to remove the crystal ingot.

3.4. Post-Growth Treatment

As already explained in section 3.3.1, the atmosphere during crystal growth contains only 1 % of oxygen to avoid oxidation of the rhodium crucible which could damage the crucible or introduce impurities into the melt. The presence of this small fraction of oxygen precludes that too much oxygen of the CaWO_4 material is evaporated in the furnace. However, oxygen vacancies still remain in the grown CaWO_4 crystal ingot which is visible as a greyish color. These oxygen vacancies can be filled by annealing the raw crystal in a dedicated furnace in a pure oxygen atmosphere at high temperatures. The important quantity for the annealing process is the diffusion coefficient D [m^2/s] which is a measure for the mobility of particles within the crystal lattice. In the case of solids, D increases exponentially with increasing temperature T [127]:

$$D = D_0 \cdot \exp\left(-\frac{\Delta H}{k_B T}\right) \quad (3.5)$$

Hereby, ΔH denotes the activation enthalpy and k_B the Boltzmann constant. The parameter D_0 is also called frequency factor and depends amongst others on various lattice parameters and on the so-called attempt frequency which is of the order of the Debye frequency of the lattice.

To fill oxygen vacancies via diffusion, the temperature has to be high enough but still well below the melting point. In [120] different annealing procedures with varying temperatures and time periods were tested. The optimized procedure applied to all raw

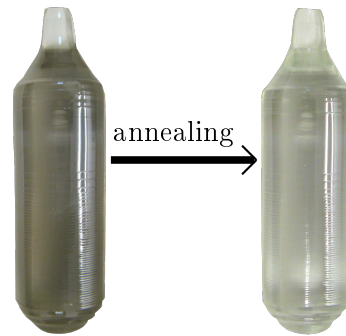


Figure 3.13.: Grown CaWO_4 crystal ingot before (left) and after (right) annealing at 1400°C in a pure oxygen atmosphere. It can clearly be seen that the greyish color originating from oxygen vacancies vanishes.

crystals produced in the scope of the present work requires to heat the crystal within 7 h to 1400°C and to keep this temperature for 20 h. In order to avoid stresses inside the crystal and to achieve the best possible oxygenation, the cooling rate is limited to $5^\circ\text{C}/\text{h}$ down to 1200°C (due to the mobility of atoms in the lattice, oxygen diffusion is only possible above this temperature) and afterwards to $50^\circ\text{C}/\text{h}$ until room temperature is reached. The effect of this annealing procedure is illustrated in figure 3.13. The greyish coloration of the CaWO_4 crystal directly after growth (left) vanishes when oxygen diffuses into the raw crystal resulting in a much higher transparency after annealing (right). For several crystals a connection between visible defects (e.g. "clouds") and the annealing procedure was investigated. The optical measurements performed as well as their results are shown in chapter 4.

After the application of the annealing procedure, mainly the cylindrical part of the raw crystals is further processed to detector crystals for the CRESST experiment. Additional works like cutting and polishing are performed in collaboration with the TUM crystal laboratory. An example is given in figure 3.14. Four small CRESST-III-like detector crystals were cut out of the cylindrical part of the crystal ingot TUM73 (compare figure 3.10 (b)). According to their position in the cylindrical part, they are given an additional number (this is also valid for other crystals where the position information could be preserved). TUM73-1 means a crystal cut from the uppermost cylindrical slice next to the shoulder whereas TUM73-2 is cut from the second slice and so on. The three detector crystals TUM73-1, TUM73-2 and TUM73-4 shown in figure 3.14 (a) are currently operated in CRESST-III Phase 1 (see section 2.4). The remaining parts of the crystal ingot TUM73 can be seen in figure 3.14 (b) and include shoulder, tail as well as TUM73-3 which was not further processed to a CRESST detector because of a small crack. TUM73-3 could, however, be used for the optical measurements performed in chapter 4 after the crack had been removed via grinding and decreasing the thickness.

3.5. Crystals Grown in the Present Work

At TUM, a consecutive number is given to every attempt to grow a crystal. The grown crystal ingot is then identified with the acronym TUM plus the corresponding number.

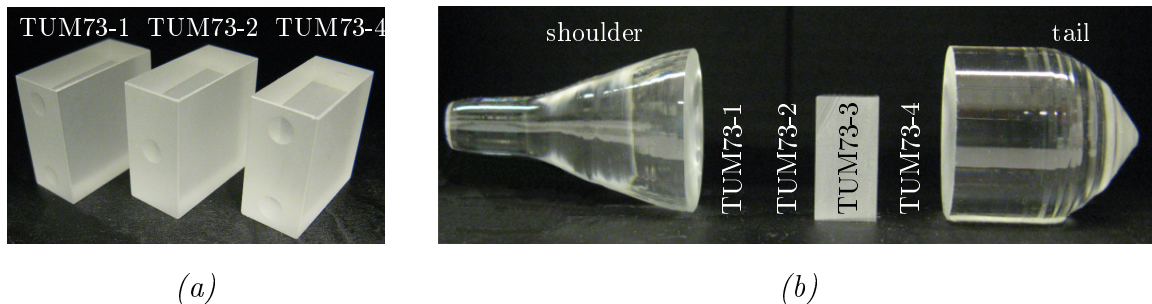


Figure 3.14.: Different parts of the raw crystal TUM73. The three small crystals TUM73-1/2/4 shown in (a) were cut from the first, second and fourth slice of the cylindrical part of the crystal ingot and are currently operated as detectors in CRESST-III Phase 1. The remaining crystal parts can be seen in (b) and include shoulder, tail and TUM73-3, which was not further processed to a detector crystal because of a small crack.

Table B.1 in appendix B summarizes all CaWO_4 crystals produced with the Czochralski method in the frame of the present work. Included are the main parameters of 35 growth processes (TUM48 - TUM82). The most crucial role for the present work play the crystal ingots TUM56 and TUM73, detector crystals of which are currently operated in CRESST-III Phase 1. TUM56 was produced from batch 1 of CaCO_3 (lot number D0712CAA3) and WO_3 powders (lot number D0113WB1) supplied by the company MV Laboratories [121]. The basis for TUM73 was a second batch of the raw materials CaCO_3 and WO_3 with the lot numbers D0812CAA2R and D0714WB1, respectively. The corresponding analysis certificates can be found in appendix D. Additionally, a chemical purification described in detail in section 5.3 was applied to the CaCO_3 powder used for the production of the raw crystal TUM73.

The growth parameters of these two crystals are listed in table 3.2. The raw crystal TUM73 was grown within 9.8 h. It has a mass of 390.3 g and a total length of 125 mm. The main part is the cylinder with a diameter \varnothing of 30 mm and a length of 65 mm. Seed ($\varnothing = 8$ mm), shoulder and tail contribute 5 mm, 40 mm and 15 mm, respectively, to the total length. The covered height (i.e. the distance that the pulling head moves) is 112.6 mm and its deviation from the crystal length (here 12.4 mm) is a measure for the change of the melt level. In comparison to these values, TUM56 features a higher mass of 737.4 g which also corresponds to a higher change of the melt level (23.4 mm) and a higher total length of 130 mm – in detail being composed of seed (5 mm), shoulder (55 mm), cylinder (45 mm) and tail (25 mm). The diameter of the seed (7 mm) is slightly lower than in case of TUM73 whereas the maximal diameter in the cylindrical part is increased to 45.5 mm. The relatively low ratio of the radii R2 and R1 of 0.5 (TUM73) and 0.3 (TUM56), as well as the low values of the opening angle Θ of 40° (TUM73) and 68° (TUM56) guarantee a long shoulder with a minimized risk for cleaving. For both crystals, the growth speed of 12 mm/h is constant over the main part of the growth process. The rotation speed starts at 15 rpm (revolutions per minute), is increased for shoulder and cylinder to a value of 25 rpm and decreased again in the tail (20 rpm)⁹. Also the values for proportional and integral term of the PI regulation are adapted for the

⁹A lower rotation speed can be applied for lower diameters.

3. Production of CaWO_4 Single Crystals

parameter	TUM73				TUM56			
crystal mass [g]	390.3				737.4			
crystal length [mm]	125				130.0			
covered height [mm]	112.6				106.6			
crucible diameter [mm]	80				80			
R2/R1	0.5				0.3			
angle [deg]	40				68			
growth duration [h]	9.8				10.3			
	seed	shoulder	cylinder	tail	seed	shoulder	cylinder	tail
length [mm]	5	40	65	15	5	55	45	25
diameter [mm]	8	8 \rightarrow 30	30	30 \rightarrow 0	7	7 \rightarrow 45.5	45.5	45.5 \rightarrow 0
growth speed [mm/h]	12	12	12	20	20	12	12	15
rotation speed [rpm]	15	25	25	20	15	25	25	20
proportional term	5	3.5	3	4	5	4	3	4
integral term	20	30	40	30	20	40	55	40

Table 3.2.: Growth parameters of the crystals TUM73 and TUM56 including mass, all geometrical values, speeds and proportional/integral terms. Global parameters are listed in the upper part, parameters changing in the different crystal parts seed, shoulder, cylinder and tail are listed below. The transitions between the values are not abrupt but are proceeding gradually.

different parts of the raw crystal. The transition between different values of a parameter are happening gradually.

The growth parameters of TUM56 (TUM73) are typical for all crystal ingots grown with a diameter of ~ 45 mm (~ 30 mm) and a mass of ~ 750 g (~ 400 g). A detailed overview for the two raw crystals TUM26 and TUM68, which are investigated with respect to their optical properties in chapter 4, is shown in table B.2 in appendix B.

4. Optical Characterization of CaWO_4 Crystals

In this chapter, several important aspects concerning the optical properties of CaWO_4 crystals are presented. After a particle interaction within a CaWO_4 detector crystal, only less than $\sim 10\%$ of the energy deposited is released as scintillation light (compare section 2.2.6). As the light signal is the discrimination parameter to identify background events in the CRESST experiment, it is crucial that as much as possible of the produced light leaves the crystal and is detected in the light detector. This implies that a high transmittance of the CaWO_4 crystals is required or, in other words, that a low amount of scattering and absorption centers exists in the crystal. In section 4.1, several basic investigations by means of photoelasticity are described which were performed for a TUM-grown and a commercial CaWO_4 crystal. This method visualizes internal stresses which are suspected to be connected to defects causing scattering or absorption of photons. The transmittance and corresponding attenuation lengths of various crystals are discussed in section 4.2. Ideas for future developments and approaches are presented in section 4.3. The light output of a CaWO_4 crystal and its scintillation properties are not treated in the present thesis. Detailed studies can be found in, e.g., [120, 128].

4.1. Photoelasticity

Before the introduction of numerical methods such as finite element simulations, photoelasticity was a standard experimental method in engineering applications to determine the stress distribution within a transparent sample. The method is based on a sample's birefringence which appears in optically anisotropic materials due to the symmetry of the crystal structure. Additionally, so-called stress birefringence can be generated when external mechanical forces are applied to a material or when a photoelastic sample exhibits internal stresses [129]. The present work restricts the discussion to plane-stress systems which means that only stresses acting parallel to the surface (with two principal stress directions¹) can be observed.

4.1.1. Theory and Setup

Light with a defined polarization passing through a birefringent material is divided into two wave components along the principal axes with different refractive indices n_1 and n_2 . In case of stress birefringence, the two resulting components are parallel to the principal

¹In a stress condition at equilibrium, perpendicular directions where no shear stresses occur are called principal stress directions.

stress axes. Due to the two different refractive indices, the two waves propagate with different phase velocities inside a sample of thickness d . This leads to a phase shift between the two wave components upon exiting the sample. Optical interference changes the polarization of the initial light with wavelength λ_0 depending on the difference δ of the wavelength numbers $\frac{d}{\lambda_0} \cdot n_{i \in \{1,2\}}$:

$$\delta = \frac{d}{\lambda_0}(n_1 - n_2) \quad (4.1)$$

Introducing the relation

$$n_1 = n_0 + \alpha \cdot \sigma_1 + \beta \cdot \sigma_2 \quad n_2 = n_0 + \alpha \cdot \sigma_2 + \beta \cdot \sigma_1 \quad (4.2)$$

between the refractive indices and the two principal stresses $\sigma_{i \in \{1,2\}}$ converts equation 4.1 into the stress-optical law [129, 130]

$$\delta = \frac{d}{S}(\sigma_1 - \sigma_2) \quad (4.3)$$

Thereby, $S = \lambda_0 \cdot (\alpha - \beta)^{-1}$ is the stress-optical coefficient, which depends on the material constants α and β , whereas δ describes the relative retardation of the light rays and is also known as isochromatic fringe order. An integral value of δ does not change the polarization direction of the light, whereas it is reflected by the principal stress axes for half-integral values. Any other value of δ creates elliptically polarized light always involving a component of both directions [131].

Figure 4.1 shows the schematic setup of a plane polariscope used for displaying the stresses inside a sample, i.e. inside CaWO_4 single crystals in the present work. Light originating from a diffuse light source² is linearly polarized by passing through a polarization filter (denoted as polarizer). A sample can be positioned in between the first and a second polarization filter (denoted as analyzer) whose polarizing axis is crossed with respect to that of the polarizer. The chosen filter setup implies that without a sample, no light is able to traverse the analyzer to be detected in a camera. The (realized) setup shown from above and as seen from the position of the camera is displayed in figure 4.2 (a) and (b), respectively. No sample is installed in the sample holder between polarizer and analyzer which means that no light from the light source can pass through the two polarization filters (their polarization directions are indicated by the white arrows in (b)). Only in the upper part of the picture shown in (b), a part of the light source is visible through the analyzer due to the larger size of the light source compared to that of the polarizer and depending on the exact position and angle of the camera. The observed dark picture of (b) does not change when a sample is installed which does not exhibit birefringence. A naturally (homogeneously) birefringent sample, however, changes the polarization in a way that a certain component of the light can get through the analyzer. Depending on the angle Φ between polarization and the principal axes of the split-up wave components, no light ($\Phi = 0, \pi/2, \pi, 3/2\pi, 2\pi, \dots$) or a maximum amount of light ($\Phi = \pi/4, 3/4\pi, 5/4\pi, \dots$) passes through the analyzer. The transitions between these two extreme cases are smooth, i.e. each angle in between corresponds to a certain fraction of light which can be recorded by the camera.

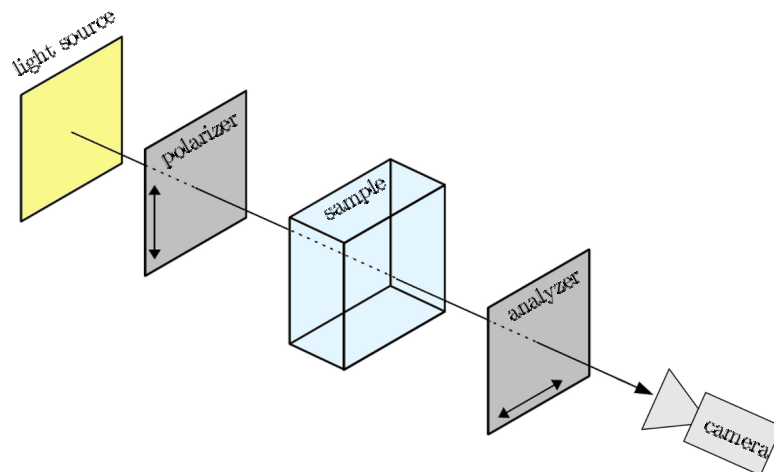


Figure 4.1.: Schematic setup of a plane polariscope used for visualizing stresses in a sample via photoelasticity. Light originating from a monochromatic or white light source is linearly polarized by a polarization filter (polarizer) before it passes through the sample and arrives at a second filter (analyzer). The polarizations of the filters are perpendicular to each other. In the case that the sample material is birefringent, the direction of polarization is changed and a certain amount of light can pass through the analyzer and be recorded by a camera.

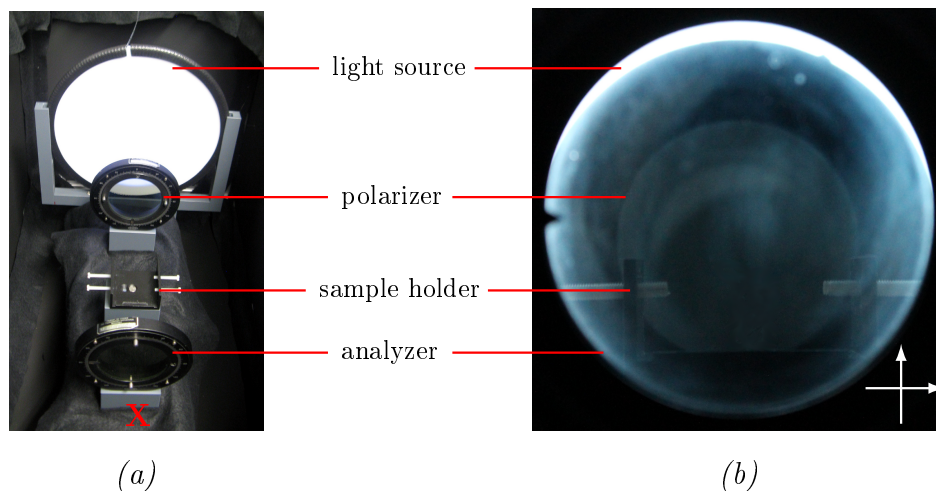


Figure 4.2.: Plane polariscope realized according to figure 4.1. (a) shows the setup including light source, polarizer and analyzer from above whereas the picture as seen at the position of the camera (indicated by the red cross in (a)) is included in (b). No sample is installed in the sample holder between polarizer and analyzer. As the two polarization filters are crossed as indicated by the white arrows, no light from the light source can pass through them. Part of the light source is visible through the analyzer in the upper part of (b) due to the larger size of the light source compared to that of the polarizer and depending on the exact position and angle of the camera.

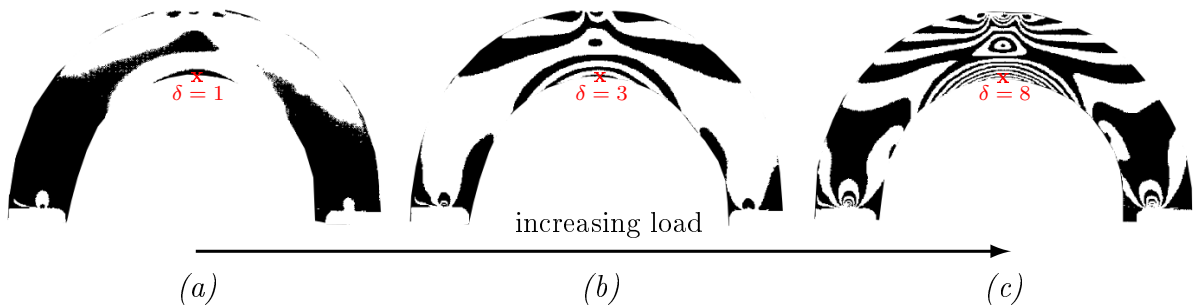


Figure 4.3.: Visualization of the relation between the amount of present stresses and the isochromatic fringe order δ . Shown is the fringe pattern of an arch with a load that is lowest in (a) and increasing towards (b) and (c). The fringe order at the position of the red cross is 1 in (a). With the increased load in (b), the black isochromatic with order 1 has moved inwards and a second and third line have appeared meaning that $\delta = 3$ at the red cross. An even higher δ of 8 reveals the further increased stress condition in (c). Figure adapted from [130].

In the presence of stresses (either internal or external), the change of the polarization in a photoelastic sample depends on the local stress condition of each sample part. This results in a fringe pattern consisting of bright and dark structures which are visible on the sample when analyzed in the described polariscope setup. Structures with a constant brightness are called isochromatics and belong to a certain δ and, therefore, to a certain difference of the principal stresses $\sigma_1 - \sigma_2$ [129, 130]. Because of the periodic behaviour, isochromatics belonging to $\delta + n$ with $n = 1, 2, 3, \dots$ result in the same brightness. Dark curves originate from integral values of δ which corresponds to the isochromatic fringe order. Hereby, higher orders occur with increasing $(\sigma_1 - \sigma_2)$ and reveal higher stresses. Figure 4.3 visualizes the relation between the amount of present stresses and the isochromatic fringe order. Shown is the fringe pattern of an arch with a load that is increasing starting from (a) via (b) to (c). The black structure marked by the red cross indicates a fringe order δ of 1 in case of (a). Increasing the external load, the black isochromatic moves further inwards and a new one occurs. In case of (b), already the third isochromatic can be observed at the position of the red cross implying a fringe order of 3. An even higher δ of 8 reveals the further increased stress condition in (c).

In the case that not a monochromatic but a white light source is used, a continuous spectrum of wavelengths is involved and the corresponding colors are split up. As a consequence, isochromatics do not appear with a certain brightness but in a defined color. Only isochromatics with order 0 are still completely dark.

Apart from isochromatics, so-called isoclinics [129, 130] are observed, as well. They are dark curves (also in the case of white light) originating from the parallelism of the direction of polarization and the principal stress axes. Therefore, they can be used to reconstruct the principal stress directions³.

²In the present work, a thin electroluminescent foil emitting evenly distributed light is used.

³Isoclinics can be suppressed when a circular polariscope is used (not in the present work). For this purpose, two quarter-wave plates with crossed principal axes (rotated by $\pm 45^\circ$ with respect to the polarizer) can be mounted behind the polarizer (for the creation of circularly polarized light) and

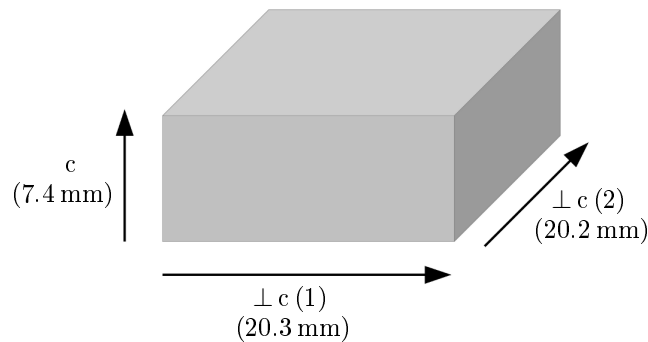


Figure 4.4.: Geometry of the crystal TUM73-3 whose optical properties were investigated with respect to internal stresses as well as to transmittance in dependence of the orientation. The crystal has a thickness of 7.4 mm in c -direction and dimensions of $(20.3 \times 20.2) \text{ mm}^2$ perpendicular to the c -axis $\perp c(1,2)$. The arrows indicate the directions of light propagation in the different measurements.

4.1.2. Internal Stresses of CaWO_4 Crystals

Internal stresses of CaWO_4 crystals have already been visualized in former works, e.g. [120, 132]. Most of the investigated CaWO_4 crystals provided by Russian or Ukrainian suppliers do not feature a photoelastic fringe pattern, whereas such a pattern is clearly visible in TUM-grown crystals revealing internal stresses there. In the present work, several basic photoelasticity measurements were applied to the TUM-grown crystal TUM73-3 as well as to the commercial Ukrainian crystal called Alexej. In both cases, a dependence of the resulting fringe pattern on the crystal orientation was studied.

Crystal Orientation

As explained in chapter 3, CaWO_4 crystal ingots are grown and then cut with an orientation along the c -axis at TUM. This implies that they can be illuminated most easily in c -direction during measurements within the photoelasticity setup. Figure 4.4 shows a schematic drawing of the cut crystal TUM73-3 (compare figure 3.14). In c -direction, the crystal has a thickness of $\sim 7 \text{ mm}$ whereas the dimensions are about 20 mm in each direction perpendicular to the c -axis $(\perp c(1,2))^4$. The crystal was integrated in three different ways in the polariscope setup explained in figure 4.2. Three photographs of the respective crystal surface in between the two polarization filters are included in figure 4.5. In each of the pictures, the contour of the crystal is highlighted in red for better clarity. In figure 4.5 (a), the line of sight is parallel to the c -axis of TUM73-3. Without intrinsic tensions, no birefringence should occur in this direction and no light is expected to be transmitted at all. However, a distinct fringe pattern indicating internal stresses

in front of the analyzer (to re-establish linear polarization). Such a setup eliminates the problem of differentiating between isochromatics and isoclinics [129, 130].

⁴Since it is not clear whether the directions perpendicular to the c -axis are a -orientated, they are denoted more generally as $\perp c(1)$ and $\perp c(2)$ in the present work.

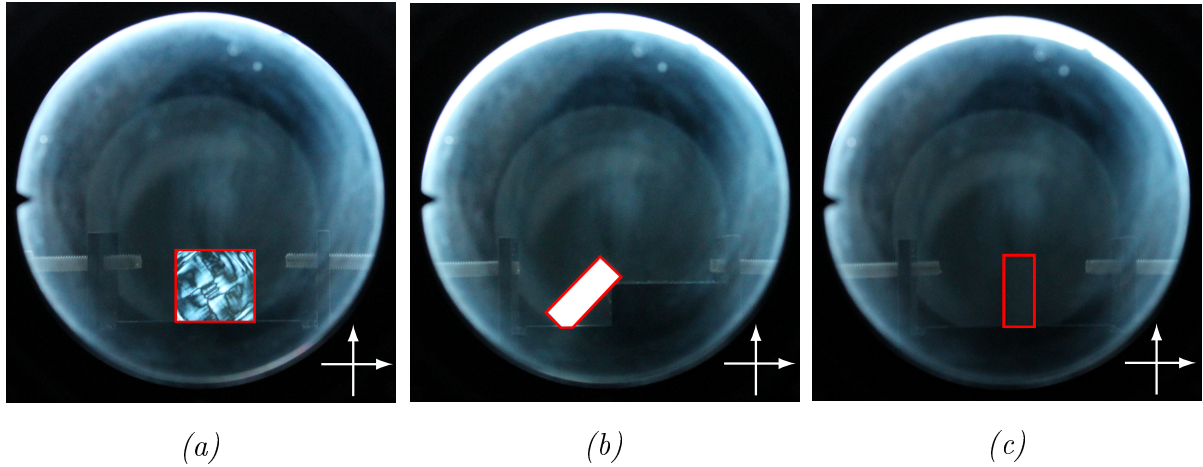


Figure 4.5.: Investigation of internal stresses within the block-shaped crystal TUM73-3 (geometry $\sim (7 \times 20 \times 20) \text{ mm}^3$, see figure 4.4). The crystal is placed in the setup of the polariscope of figures 4.1 and 4.2, the photographs were taken at the position of the camera. The polarization directions of polarizer and analyzer are indicated by white arrows. The edges of the crystal surface are highlighted in red. In (a) the c -axis of the crystal is parallel to the line of sight. A distinct fringe pattern indicating internal stresses can be observed. In case of an orientation perpendicular to the c -axis the polarization of light is changed depending on the angle between polarization and the principal axes – in the two extreme cases either a maximal amount of light (b) or no light at all (c) passes through the setup. This is due to the slight natural birefringence of CaWO_4 . No indication for further internal stresses can be observed in these directions.

is clearly visible⁵.

The situation changes when the crystal is rotated in the setup such that the direction of the light propagation, i.e. the line of sight, is perpendicular to the c -axis (figure 4.5 (b) and (c)). Due to the slight natural birefringence of CaWO_4 [108], the polarization of the light is changed depending on the angle Φ between polarization and the principal axes. In the two extreme cases, the crystal surface appears either completely bright (b) or completely dark (c). However, regardless of Φ , no additional fringe pattern due to internal stresses can be observed⁶. An explanation for the observation of figure 4.5 is that tensions within the crystal are only existing in the plane spanned by the two a -axes, perpendicular to the c -axis. Such tensions can be attributed to dislocations (slip bands) of different planes within the crystal that are caused by radial temperature gradients already during crystal growth [133].

In case of the Russian and Ukrainian suppliers, it has been observed that CaWO_4 crystals are usually not cut in an oriented way. This means it can a priori not be concluded that not c -oriented crystals which did not show a fringe pattern in, e.g., [120, 132] are completely free of internal stresses and dislocations only visible perpendicular to the

⁵It was checked that the pattern does not originate from the light source itself or from the polarization filters. Furthermore, the pattern was confirmed by a measurement in another polariscope.

⁶It was tested that no substructures suppressed by the potentially dominating effect of natural birefringence become visible when the two polarization filters are rotated with respect to each other.

c-axis. To check this hypothesis, the Ukrainian crystal Alexej was investigated. A photograph of the cylindrical crystal (with a height and diameter of 4 cm) installed in the polariscope (see figure 4.2) is shown in figure 4.6 (a). Only the natural birefringence without any additional pattern is visible. However, a measurement with a real-time back reflection Laue camera [110] revealed that the crystal is not c-orientated but that the c-axis is tilted by an angle of $\sim 25^\circ$. Therefore, a block-shaped crystal with surfaces parallel and perpendicular to the c-axis was cut from the originally cylindrical crystal as illustrated in figure 4.7. In the photoelasticity measurement of the c-oriented crystal Alexej, a photoelastic fringe pattern is observed (figure 4.6 (b)). An apparently lower order of isochromatics make the pattern much less pronounced and indicate less stresses compared to TUM73-3 (figure 4.5). Still, internal stresses are present in this crystal, as well. Although this measurement is only one exemplary crosscheck, it is probable that also other commercial crystals from the Ukraine and Russia are not completely free of intrinsic tensions. A further study of this hypothesis is, however, beyond the scope of the present work.

Additional Annealing

A detailed photograph of the pronounced fringe pattern of TUM73-3 is shown in figure 4.8 (a). As explained above, the observed bright and dark structures can be attributed to dislocations forming within the crystal during growth [133]. To exclude a connection to oxygen-related defects, an additional annealing procedure in pure oxygen atmosphere with exactly the same parameters as in the standard annealing procedure (see section 3.4) was applied to TUM73-3. The pattern observed within the photoelasticity setup after this additional annealing is shown in the photograph of figure 4.8 (b). The picture was taken with the same record settings of the camera as the photograph in (a), however, a slight deviation of position and angle of the camera cannot be excluded. The main structures of the pattern as observed before annealing remain also afterwards and no significant change or improvement is visible. A shift of the pattern (e.g. of the pronounced structure in the central part of the crystal) in (b) compared to that in (a) could be explained by a slightly deviating position and angle of the camera. Several parts of the crystal surface appear a bit darker after annealing. This might be a hint for a slightly decreased fringe order. However, more probable is also here a connection to the position of the camera. Thus, figure 4.8 confirms that the present intrinsic tensions due to dislocations forming during crystal growth can not significantly be reduced by means of annealing but potentially by an adaption of certain growth parameters (see section 4.3).

In summary, internal stresses are only visible in c-oriented crystals. They are likely caused by dislocations within the crystal structure and are much more pronounced in TUM-grown crystals than in commercial ones. Possible approaches for a more quantitative analysis as well as for an improvement of the stress conditions within TUM-grown crystals are suggested in section 4.3.

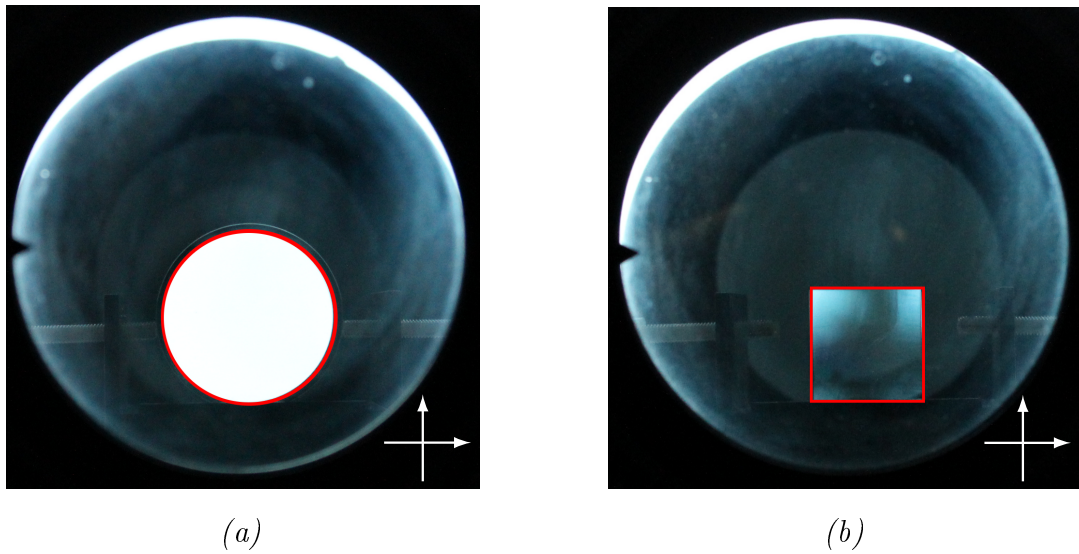


Figure 4.6.: Investigation of internal stresses in the Ukrainian crystal Alexej with the help of the photoelasticity setup. The contour of the crystal surface is highlighted in red. In the originally cylindrical crystal (with a height and diameter of 4 cm), the c -axis is tilted by $\sim 25^\circ$ and only the natural birefringence of CaWO_4 is visible (a). A c -oriented block-shaped crystal was cut from this crystal as illustrated in figure 4.7. Afterwards, an isochromatic fringe pattern is observed in c -direction (b), although it is less pronounced than in case of TUM73-3 (figure 4.5).

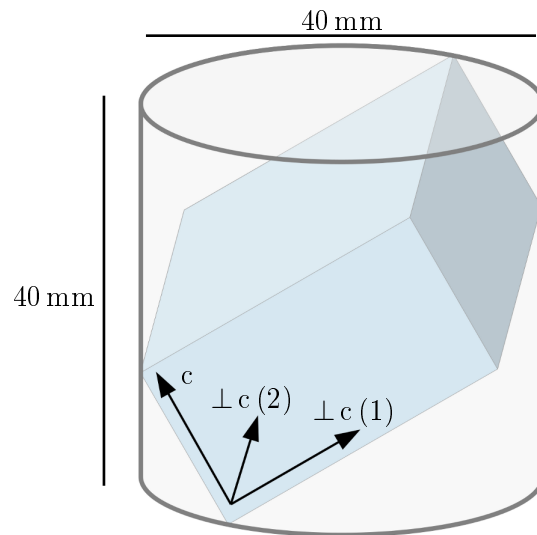


Figure 4.7.: Schematic drawing how a c -orientated block-shaped crystal was cut from the cylindrical crystal Alexej. The orientation was determined by means of a real-time back reflection Laue camera [110] before cutting.

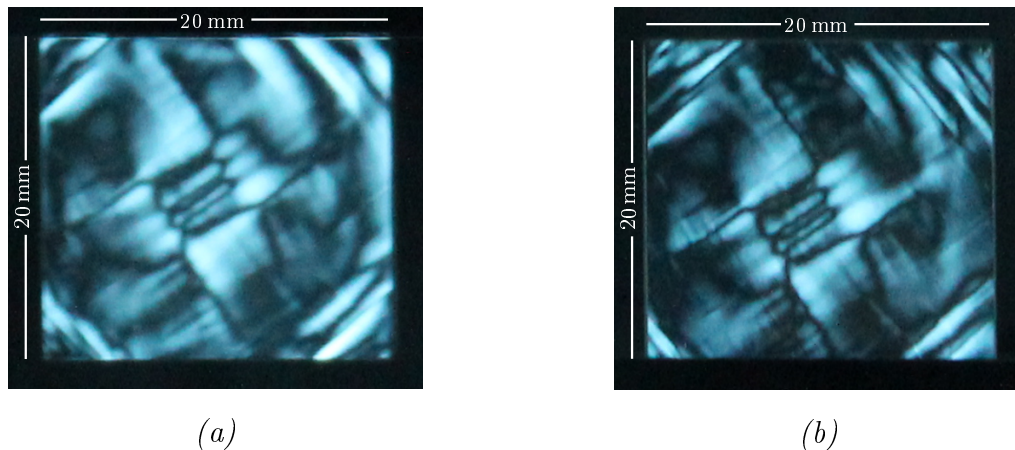


Figure 4.8.: Photographs of the photoelastic fringe pattern of the crystal TUM73-3 before (a) and after (b) an additional annealing in pure oxygen atmosphere. In total, the crystal pattern seems to be a bit darker and slightly shifted after the annealing which can be explained by a slightly deviating position and angle of the camera. The main structures remain the same which confirms the assumption that the observed internal stresses originate from dislocations having formed within the crystal already during the growth process and can not significantly be changed by annealing.

4.2. Transmittance

Potential internal scattering or absorption centers affect the transparency of a CaWO_4 crystal to light. Experimentally, the transmittance of a sample can be measured as explained in the following.

4.2.1. Method and Setup

The (total) transmittance T_{tot} of a sample is defined as the ratio between the light intensity transmitted through a sample I and the incident light intensity I_0 :

$$T_{\text{tot}} = \frac{I}{I_0} \quad (4.4)$$

In case of a solid sample, it has to be distinguished between surface transmittance T_{surf} and bulk transmittance T_{bulk} . When a light beam is sent from air into a sample with refractive index n , reflections at the surfaces occur. For light incidence perpendicular to the surface, this is described by the reflectivity R [131] via

$$R = 1 - T_{\text{surf}} = \frac{(1 - n)^2}{(1 + n)^2} \quad (4.5)$$

The bulk transmittance, on the other hand, refers to light losses by absorption or scattering inside the crystal. The quantity which characterizes the extent of these light losses is the attenuation coefficient α_{att} defined as the sum of scattering coefficient α_{scat} and absorption coefficient α_{abs} . Its reciprocal value is called attenuation length L_{att} and describes the distance after which the intensity of light travelling within the material has

dropped to a value 1/e of the initial intensity. The dependence of T_{bulk} on the attenuation coefficient is given by the Lambert-Beer-Bouguer law [109]:

$$T_{\text{bulk}} = \exp(-\alpha_{\text{att}} \cdot d) \quad (4.6)$$

with d being the thickness of the sample, i.e. the distance which the light has to travel through the sample.

A beam of light traversing a solid sample enters at the first surface, passes through the bulk and exits at the opposite surface. Including this, the total transmittance can be written as

$$T_{\text{tot}} = T_{\text{surf}} \cdot T_{\text{bulk}} \cdot T_{\text{surf}} \cdot \sum_{i \in \mathcal{N}} [(R \cdot T_{\text{bulk}})^2]^i = \frac{T_{\text{surf}}^2 \cdot T_{\text{bulk}}}{1 - (R \cdot T_{\text{bulk}})^2} \quad (4.7)$$

Here, the sum accounts for the number i of multiple reflections within the sample⁷.

The Lambert-Beer-Bouguer law of equation 4.6 deals with the intensity of a parallel light beam which means that all scattered components of the beam are considered to be lost. Furthermore, monochromatic light is required for an investigation of the dependency on the light wavelength. In the present work, an all-reflective double-monochromator Lambda 850 UV/Vis spectrometer [134] with the ability to scan wavelengths in the ultraviolet (UV) and visible (Vis) range (typically 250 nm - 800 nm) was used for transmittance measurements. The schematic setup of the spectrometer is depicted in figure 4.9. A halogen lamp and a deuterium lamp are the radiation sources for operation in the visible and UV wavelength range, respectively. During scanning of the wavelengths, the changing of the sources happens automatically. With the help of a mirror system (grey parts), the light beam (red) is guided through two monochromator systems to the sample (blue) and the detector (det). After an optical pre-filter, the radiation enters the first monochromator through a slit. The beam is collimated by another mirror and produces a spectrum when striking an UV/Vis grating. The rotational position of the grating effectively selects a narrow band of wavelengths of this spectrum which is reflected through another slit into the second monochromator. There, the procedure is repeated resulting in a radiation beam exhibiting a high spectral purity with extremely low stray radiation content. Both monochromators are slewed synchronously during the scan. The beam is split into two parts with a chopper assembly consisting of a rotating device which includes a mirror, a window and two dark elements for the creation of a dark signal. In this way, a reference beam as well as a second beam passing through the sample are created. In the detector compartment, both beams are reflected onto the detector (i.e. a photomultiplier in case of the UV/Vis range) and the transmittance of the sample is determined via a comparison to the reference beam.

For a transmittance measurement and the calculation of the attenuation length, the systematic uncertainties of the device are included⁸. Each measurement is repeated several

⁷Hereby, interference terms are neglected. Experimentally, interference within the sample can be suppressed when the beam line is not exactly perpendicular to the sample surface. It was checked, that in case of CaWO₄ the resulting transmittance does not change when the angle of the sample is slightly varied.

⁸The systematic uncertainties given by the company include an error in wavelength, the wavelength reproducibility as well as the photometric accuracy, reproducibility and linearity.

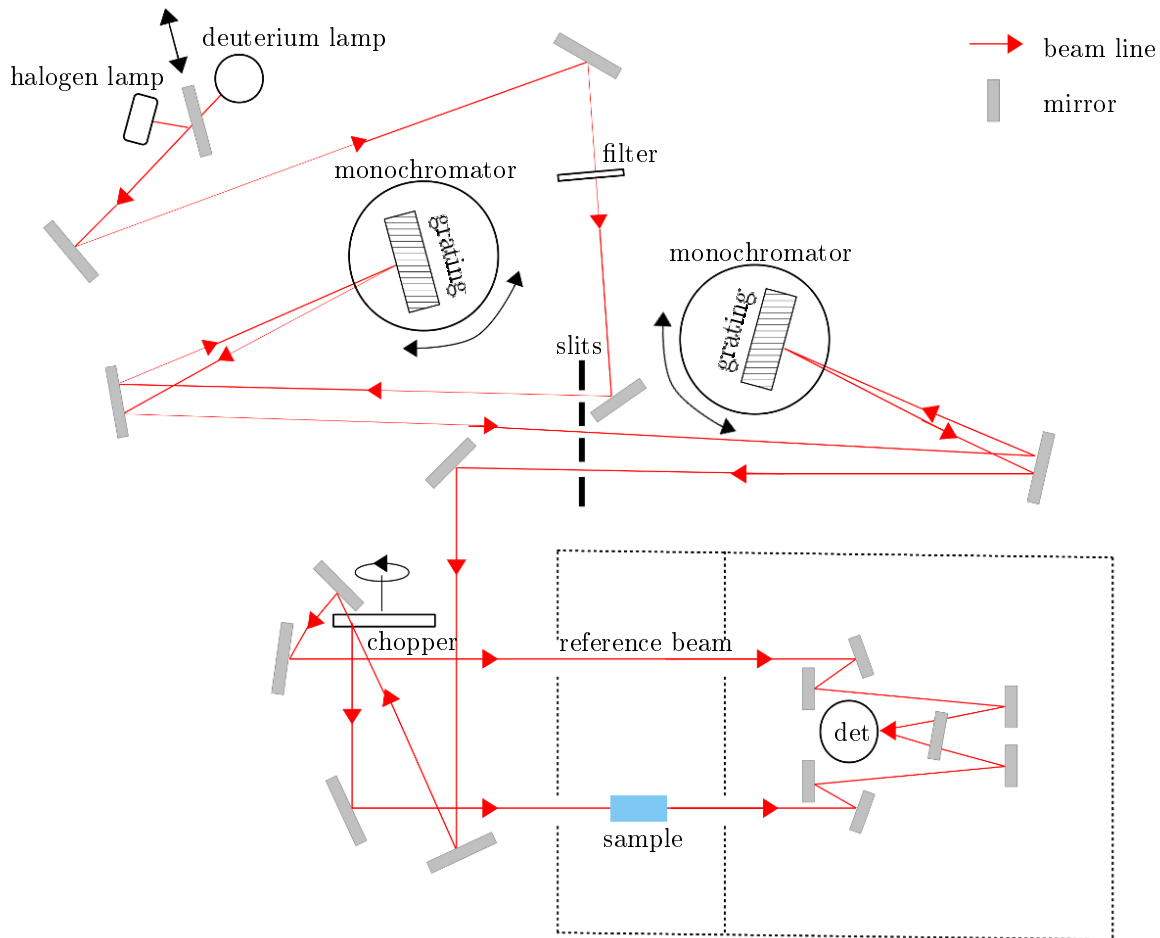


Figure 4.9.: Simplified setup of the all-reflective, double-monochromator Lambda 850 UV/Vis spectrometer [134]. A halogen lamp and a deuterium lamp are the radiation sources for operation in the visible as well as in the UV wavelength range. With the help of a mirror system (grey), the light beam (red) is guided through two monochromator systems to the sample (blue) and the detector (det). Within the monochromators a grating acts as dispersive element and a narrow band of wavelengths can be chosen via the rotational position of the two gratings. Both monochromators are synchronized and the emerging radiation exhibits a high spectral purity. The beam is split into two parts with a chopper assembly. The reference beam is directly guided into the detector whereas the second beam passes through the sample before being detected and compared to the reference beam.

times to evaluate a statistical error.

Furthermore, it has to be considered that a slight birefringence is present for CaWO_4 crystals (compare section 3.1). For crystals aligned with the light beam perpendicular to the surface and parallel to the optical axis (i.e. c-axis) this effect does not occur (except for stress-related birefringence). The reflectivity R can be calculated from equation 4.5 using the ordinary refractive index n_o according to the dispersion formula of CaWO_4

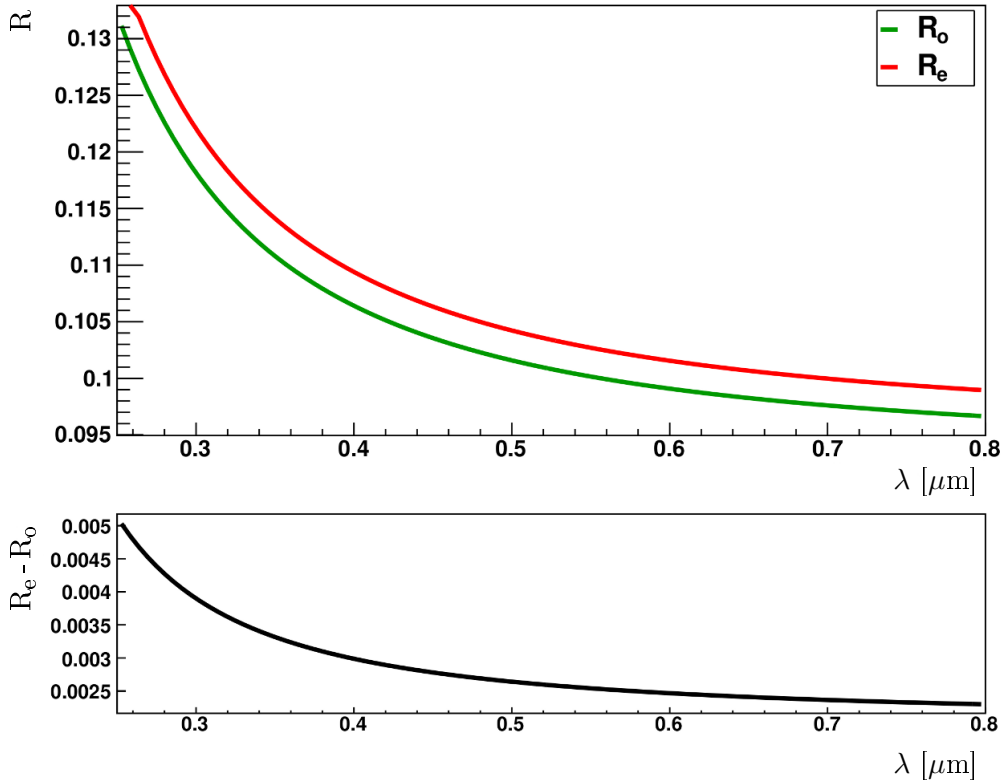


Figure 4.10.: Reflectivity R plotted for the ordinary (green) and the extraordinary (red) refractive index (taken from [136]) for wavelengths between 250 nm and 800 nm. The difference $R_e - R_o$ between extraordinary and ordinary reflectivity is smaller than 0.005 as shown in the bottom part. Including only n_e and measuring a crystal with the optical axis (i.e. c -axis) not aligned parallel to the light beam leads to a deviation of the attenuation length in the order of 1%. The effect can, however, be neglected in the following for samples not measured along c -axis. For further details see main text.

⁹ [136]:

$$n_o^2 - 1 = \frac{2.5493 \cdot (\lambda/\mu\text{m})^2}{(\lambda/\mu\text{m})^2 - 0.1347^2} + \frac{0.92 \cdot (\lambda/\mu\text{m})^2}{(\lambda/\mu\text{m})^2 - 10.815^2} \quad (4.8)$$

However, in case of a different crystal orientation also the extraordinary refractive index n_e (for formula see [136]) plays a role. The dependency of R on the wavelength λ between 250 nm and 800 nm is plotted in figure 4.10 for both refractive indices. The difference between ordinary reflectivity R_o (green) and extraordinary reflectivity R_e (red) is smaller than 0.005 in this wavelength region (see lower plot). In most cases of not c -oriented crystals it is not clear to which fraction each of the two refractive indices contributes. In an extreme case of using only R_e when measuring a crystal not aligned parallel to the optical axis, the deviation of T_{bulk} (compared to the value when using R_o only) lies below 1%. According to the exponential law of equation 4.6, this means in terms of

⁹The dispersion formula was determined based on wavelengths ranging between 0.45 μm and 4.0 μm [135]. In the present work, the formula was extrapolated down to $\sim 0.3 \mu\text{m}$. As no measurement results exist in the low-wavelength region, a small error might be introduced there.

L_{att} a deviation in the order of 1%. Furthermore, a possible small uncertainty exists for the values of the refractive indices themselves as they can be affected by, e.g., internal stresses (see section 4.1). Surface irregularities or an alignment not exactly perpendicular to the beam could cause further errors. However, it was checked that a rotation of the installed sample by a few degrees leads only to insignificant changes of the attenuation length.

In the measurement of a CaWO_4 sample where the attenuation length is determined to be much longer than the thickness of the sample, relatively large errors are observed. In other words, measuring an attenuation length, e.g., in the order of 100 mm for a CaWO_4 crystal with a thickness of ~ 10 mm only, can result in relatively large uncertainties as the light beam can probe only a distance of 1/10 of the attenuation length within the sample material. As all the deviations and uncertainties described above are smaller than this effect, only the ordinary refractive index of equation 4.8 is used for all crystal orientations. All further uncertainties connected to refractive index, reflectivity as well as crystal orientation and alignment can be neglected in the analysis performed here.

4.2.2. Measured Transmittances of CaWO_4 Crystals

In the present work, I measured the transmittance of various TUM-grown crystals with the UV-Vis spectrometer described above. It should be emphasized that – in all cases – both surfaces where the beam enters or exits the crystal have to be polished to avoid reflections and scattering due to surface roughness.

TUM26-2 is a $(20 \times 20 \times 11)$ mm³ crystal cut from a raw ingot with a diameter of 30 mm (see table B.2 in appendix B for details of the growth parameters). Its transmittance was investigated within a width of 11 mm along the c-axis. TUM68 was grown with a diameter of 45.5 mm (all growth parameters are listed in table B.2). The complete cylindrical part (TUM68-complete) with a length of 57 mm was measured along its c-axis before the crystal was further cut into six small CRESST-III-type crystals as schematically illustrated in figure 4.11. The two small crystals highlighted in red (a) and blue (b) were measured in the spectrometer. The directions where the beam passes through each of the two crystals is indicated by the arrows in figure 4.11. This means, the transmittance of the two crystals with a width of 10 mm each was probed for different orientations, perpendicular and parallel to the c-axis in case of the crystals TUM68-a and TUM68-b, respectively. The crystal TUM73-3 was cut from a 30 mm crystal ingot (see figure 3.14 and section 3.5). Its geometry is shown in figure 4.4. The arrows in the schematic drawing indicate the different orientations parallel and perpendicular to the c-axis ($\perp c$ (1,2)) that were probed in the transmittance measurement.

All crystals measured, their orientations and widths are listed in table 4.1 together with the attenuation lengths L_{att} obtained for the wavelength of the emission maximum at 430 nm. A clear tendency can be observed that the crystals cut from an ingot with a smaller diameter of 30 mm (TUM26, TUM73) have a longer attenuation length compared to that cut from a raw crystal with a diameter of 45.5 mm (TUM68). This indicates that more scattering and absorption centers are present in larger crystals. A possible reason is that oxygen-related defects can better be reduced for smaller crystals via the applied annealing procedure as the distance the oxygen has to penetrate the crystal is shorter in

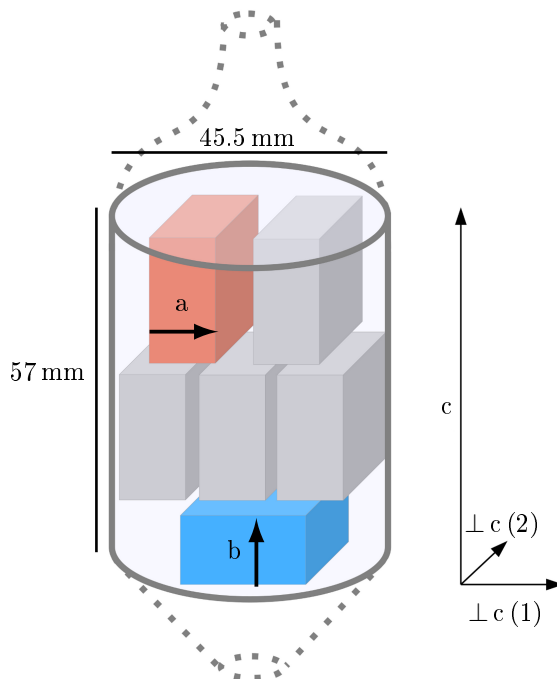


Figure 4.11.: Schematic drawing how small CRESST-III-type detector crystals with a volume of $(20 \times 20 \times 10) \text{ mm}^3$ were cut from the cylindrical part of the raw crystal TUM68 with a diameter of 45.5 mm. The transmittance of the two crystals highlighted in red (a) and blue (b) has been investigated in the UV-Vis spectrometer in the directions indicated by the arrows, i.e. with the beam being perpendicular (a) and parallel (b) to the c-axis, respectively.

these cases. The highest value of $(171.7 \pm 14.2) \text{ mm}$ for the attenuation length is achieved with TUM26-2. This value is comparable to the attenuation length of Ukrainian crystals, however, still much lower compared to several Russian crystals (e.g., the crystals Zora and Exiton I with attenuation lengths in the order of m) [120]. The reason for this large deviation is not yet clear but is being investigated.

In case of TUM68, the value of $(66.7 \pm 1.4) \text{ mm}$ obtained for the attenuation length of the complete cylinder is similar to that of the lower part TUM68-b of $(69.9 \pm 3.0) \text{ mm}$. In both cases, the beam traverses approximately the center of the cylinder where most oxygen-related defects are expected as it is the region most difficult to reach for the diffusing oxygen. In contrast, the upper part – TUM68-a – was cut from a region in the raw crystal slightly shifted from the center (compare figure 4.11) and features a slightly improved attenuation length of $\sim 100 \text{ mm}$. Apart from the radial position dependency, the transmittance in the upper part might also be better than in the lower part due to an increasing level of impurities of the melt with increasing crystallized mass (compare section 5.4) which could lead to a higher defect density. Furthermore, a connection to the orientation cannot be excluded which was, therefore, further investigated in TUM73-3. There, it can be observed that the transmittance seems to be increased in the cases the beam passes through the crystal perpendicular to the c-axis. The two values of the attenuation length at 430 nm are with $\sim 160 \text{ mm}$ the same within error bars. The atten-

crystal	orientation	width [mm]	L_{att} @ 430 nm [mm]
TUM26-2	c	11	171.7 ± 14.2
TUM68-complete	c	57	66.7 ± 1.4
TUM68-a	$\perp c$	10	100.6 ± 5.8
TUM68-b	c	10	69.9 ± 3.0
TUM73-3	c	7.4	105.8 ± 8.1
TUM73-3	$\perp c$ (1)	20.3	156.1 ± 7.6
TUM73-3	$\perp c$ (2)	20.2	162.0 ± 7.9

Table 4.1.: Various crystals investigated with respect to their transmittance in the UV-Vis spectrometer. The crystal orientation along the c -axis (c) or perpendicular to it ($\perp c$) as well as the width of the crystal the beam passes through are listed in the second and third columns, respectively. The last column contains the attenuation lengths L_{att} obtained at 430 nm. A dependency on the diameter of the raw crystal (30 mm for TUM26 and TUM73 as well as 45.5 mm in case of TUM68), on the position (compare figure 4.11) as well as on the orientation can be observed. For details see main text.

uation length of ~ 106 mm calculated from the transmittance in c -direction, on the other hand, is significantly lower. As mentioned above, only the ordinary refractive index is used for the calculation of the attenuation length although this is not exactly right in case of the measurements perpendicular to the c -axis. The difference between the three measurements of TUM73-3, however, is too large to be explained by this fact.

It can not be excluded that the observed axis-dependence originates from polarization effects which affect the setup, e.g., the sensitivity of the photomultiplier [137]. Furthermore, it is also possible that a worse transmittance is connected to a higher amount of certain internal stresses. The fringe pattern of TUM73-3 observed in figure 4.5 might imply that light propagating in c -direction is reflected or refracted to a higher extent than light propagating perpendicular to the c -axis.

For a more accurate measurement, an improved optical setup with the possibility to differentiate between scattered and absorbed light is necessary. This is, however, beyond the scope of the present work. A proposal for such a setup is shortly discussed in section 4.3.

Additional Annealing

As scattering and absorption centers within the CaWO_4 crystals can be connected to oxygen-related defects, an additional oxygen annealing with the same conditions as explained in section 3.4 was applied to the small crystals TUM68-a/b and TUM73-3. During the annealing procedure, the crystal surfaces can become slightly opaque and, therefore, have to be re-polished before the transmittance of the crystals can be re-investigated. Usually this polishment removes only $\sim 5 \mu\text{m}$ of the uppermost surface [138] and does not affect the crystal dimensions very much. Only in the case of TUM73-3 (c -orientation) the width was decreased from 7.4 mm to 6.8 mm. This is taken into account for the calculation of the attenuation length.

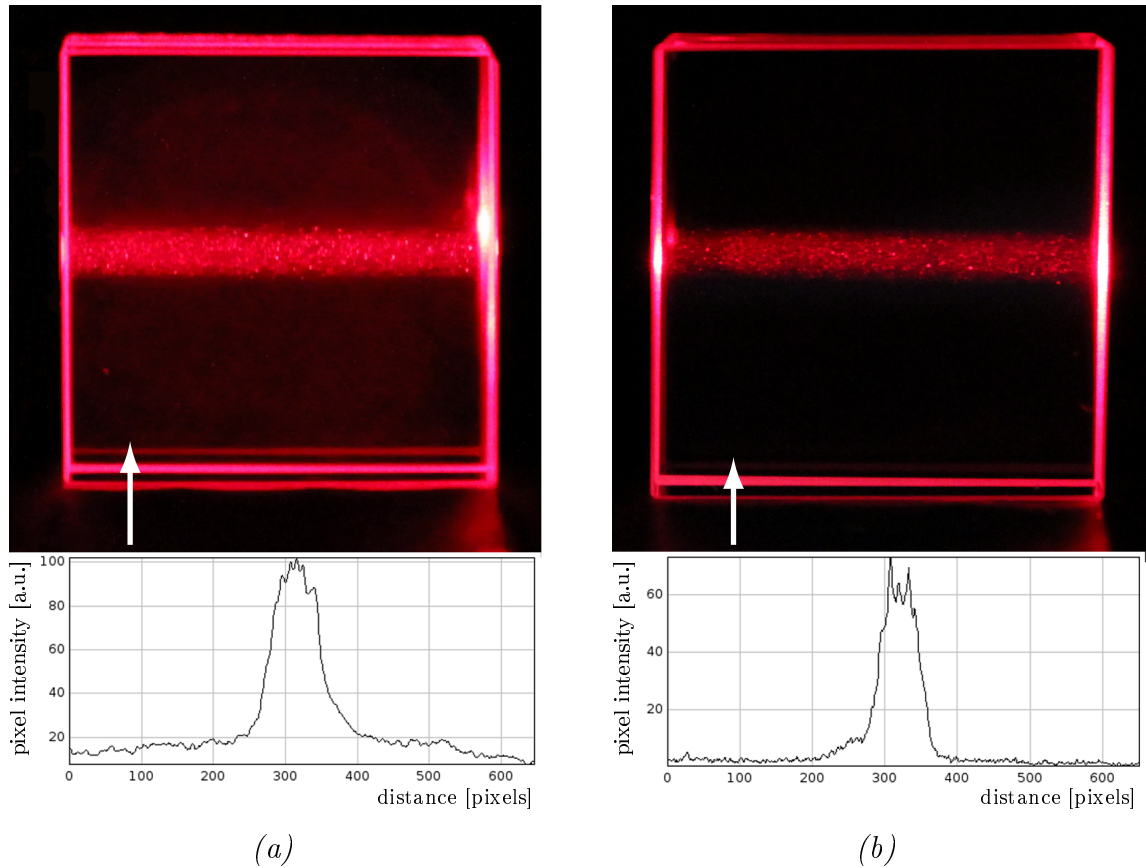


Figure 4.12.: Scattering centers within the crystal TUM73-3, visualized with the help of a laser ($\lambda = 650 \text{ nm}$). Starting at the position of the white arrow (distance = 0 pixels), an exemplary profile of the pixel intensity in the crystal bulk (excluding edges) was generated (lower plot). The intensive scattering in the direct beam line (around ~ 320 pixels) is surrounded by a slightly reddish "halo" in (a) which indicates defects dominating in the central region and diminishing towards the crystal borders. After an additional annealing (b), the amount of scattering centers within the laser beam line is significantly reduced and also the halo has almost vanished.

Figure 4.12 shows exemplary photographs of the crystal TUM73-3 before (a) and after (b) the additional annealing (with the same record settings of the camera). With the help of a laser ($\lambda = 650 \text{ nm}$), scattering centers within the crystal are visualized. Furthermore, starting at the position of the white arrow, exemplary profiles of the pixel intensity are generated in the direction of the arrow and drawn in the lower plots. The profiles only include the bulk region of the crystal neglecting the strong scattering peaks at the edges of the crystal. In (a), the pronounced scattering region within the beam line of the laser is surrounded by a slightly reddish "halo" visible in the picture as the crystal appears to be slightly brighter than the black colour of the background. In the profile plot, a pixel intensity of ~ 100 is reached in the central peak around a distance of ~ 320 pixels. Leaving the direct beam line of the laser (distance $\lesssim 250$ or $400 \lesssim$ distance), the pixel intensity is still at a value of ~ 20 but decreases to ~ 10 at a distance of 0 pixels and even to a value lower than 10 at a distance of 650 pixels (close to the upper surface

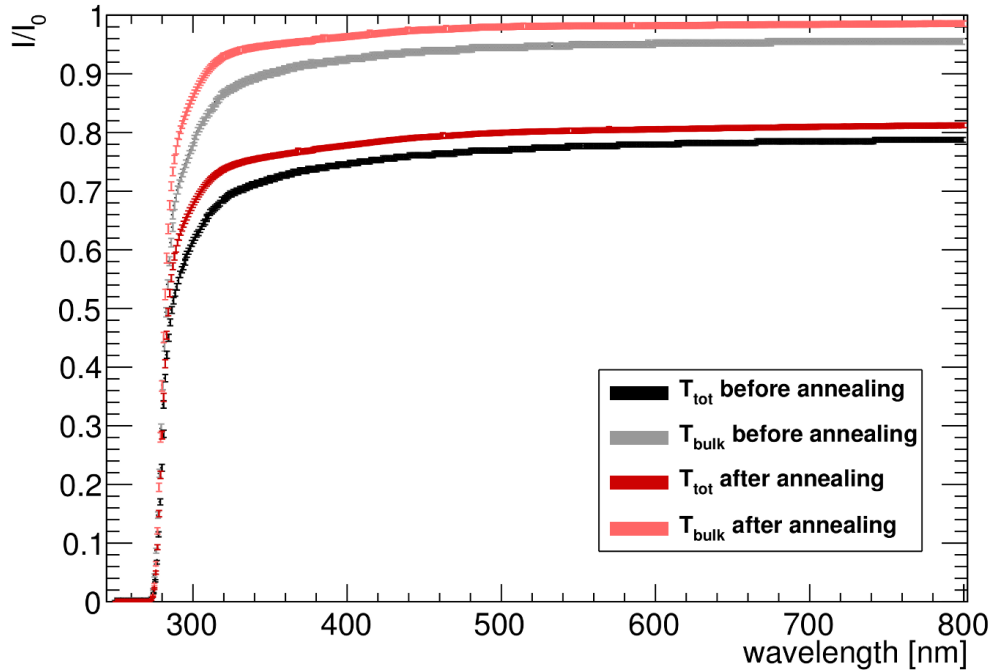


Figure 4.13.: Transmittance I/I_0 of the crystal TUM73-3 in c -orientation before (black, grey) and after (light and dark red) applying an additional annealing in pure oxygen. It is distinguished between total transmittance T_{tot} (black, dark red) and bulk transmittance T_{bulk} (grey, light red) as defined by equations 4.7 and 4.6. Both transmittance curves are increased after the annealing resulting in a significantly improved attenuation length at the wavelength of interest (~ 430 nm).

of the crystal). This behaviour indicates that defects dominate in the central region and diminish towards the crystal borders. After the annealing (figure 4.12 (b)) the amount of scattering centers within the laser beam line is significantly reduced to a pixel intensity of ~ 60 . Also the halo has almost vanished, i.e. the pixel intensity decreases to values far below 10 with increasing distance to the beam line. A few distinct peaks around the intensity maximum at ~ 320 pixels correspond to pronounced scattering centers which are still present.

A more quantitative result is delivered by a measurement with the UV-Vis spectrometer. Hereby, the crystal was mounted at the same position and in the same orientations as before. The transmittance I/I_0 in dependence of the wavelength is plotted in figure 4.13 for TUM73-3 measured in c -orientation. The black curve describes the total transmittance T_{tot} (see equation 4.7) measured before annealing. T_{tot} is approximately constant at a value of ~ 0.75 for wavelengths above ~ 400 nm and decreases below. CaWO_4 crystals are opaque for wavelengths shorter than ~ 300 nm.

Considering surface reflections, T_{tot} can be transformed to the bulk transmittance T_{bulk} according to equations 4.7 and 4.6. The resulting grey curve has the same basic shape but features higher I/I_0 values above 0.9 in the constant part. After annealing, both T_{tot} (dark red) as well as T_{bulk} (light red) are increased in the complete scanned wavelength

crystal	orientation	width [mm]	L_{att} @ 430 nm [mm]
TUM68-a	$\perp c$	10	155.5 ± 13.9
TUM68-b	c	10	217.6 ± 23.9
TUM73-3	c	6.8	231.2 ± 38.0
TUM73-3	$\perp c$ (1)	20.3	368.3 ± 35.5
TUM73-3	$\perp c$ (2)	20.2	374.0 ± 35.9

Table 4.2.: Attenuation lengths L_{att} at 430 nm of several small CaWO_4 crystals cut from the raw crystals TUM68 and TUM73 after application of an additional oxygen annealing. In comparison to the measurements before this second annealing (see table 4.1), all values could significantly be increased by a factor of ~ 1.5 (TUM68-a), of ~ 3 (TUM68-b) and of ~ 2 in case of all orientations of TUM73-3.

region (250 nm- 800 nm) compared to the respective curves before annealing. Above wavelengths of 400 nm, the total transmittance reaches values of ~ 0.8 while the bulk transmittance approximates a value of 0.99. None of the curves shown features any distinct absorption bands with reduced transmittance which can be caused when certain impurities are present. Such absorption bands were, e.g., observed for the two Russian crystals Zora and Exiton I – in these cases indicating the presence of the rare earth ions Er^{3+} and Nd^{3+} [120].

The increased transmittance after annealing confirms the optical observation of figure 4.12. The resulting attenuation lengths L_{att} at 430 nm obtained in measurements of TUM68-a/b and of TUM73-3 after the annealing are summarized in table 4.2. In comparison to the values measured before the additional annealing process (table 4.1), L_{att} could significantly be increased in all cases. With a factor of ~ 3 , the largest improvement is observed for TUM68-b whereas a factor of ~ 1.5 is found for TUM68-a. In case of the crystal TUM73-3, the attenuation length is improved by a factor of ~ 2 for all crystal directions.

It can be concluded that a large part of the scattering and absorption centers within CaWO_4 crystals is due to oxygen-related defects. The transmittance and attenuation length can significantly be improved via an additional annealing, preferably applied to small crystals allowing a more efficient oxygen diffusion. Further research is necessary in order to reach the high transmittance values measured for several Russian crystals [120]. This investigation is, however, beyond the scope of the present work. Ideas related to the crystal-growth parameters, annealing as well as doping are presented in section 4.3.

Evaporation of a Transition Edge Sensor (TES)

For the operation as cryogenic detector, each crystal has to be equipped with a TES (see section 2.2.2). Two different methods can be applied: the TES can be evaporated onto a CaWO_4 carrier which is then glued to the detector crystal in the so-called composite detector design (see, e.g., [139]). The second method is a direct evaporation of the TES onto the detector crystal as applied for all small modules in CRESST-III Phase 1. During an evaporation procedure, the crystal is put into a vacuum and heated up to different

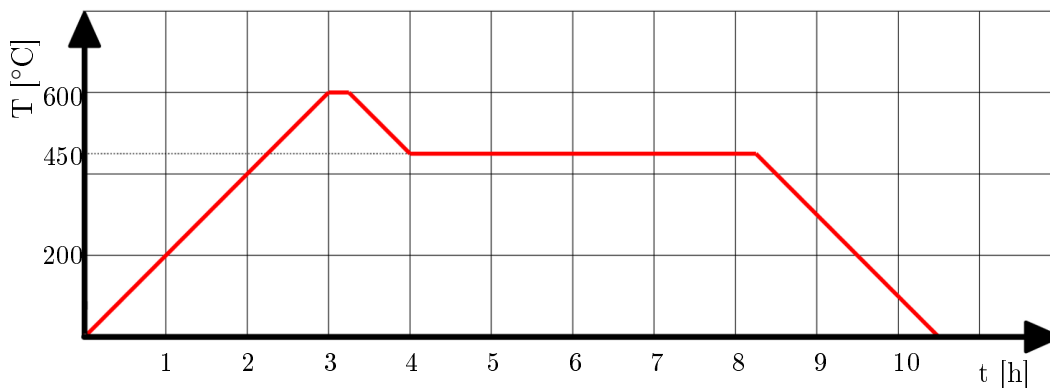


Figure 4.14.: Typical temperature curve of a TES evaporation procedure as applied (in vacuum) to CRESST-III Phase 1 detector crystals. The CaWO_4 crystal is heated up to different temperature stages, always with a rate of 200°C . The temperature of 600°C is kept for ~ 15 min and ramped back to 450°C where the actual tungsten evaporation takes place (~ 15 minutes). After an annealing at this temperature lasting for 4 h, the crystal is cooled down to room temperature.

temperature stages as illustrated in figure 4.14, always with a rate of $200^\circ\text{C}/\text{h}$. After staying at a temperature of 600°C for ~ 15 min, the temperature is reduced to 450°C where the actual evaporation of tungsten takes place (~ 15 minutes). This temperature is kept for an annealing period lasting 4 h and is then decreased back to room temperature. In the past it was observed that the light output of a CaWO_4 crystal is reduced after the evaporation procedure [132]. An explanation might be the creation of an optically "dead" layer at the crystal surface, e.g. due to oxygen evaporating at the uppermost surface layer. To investigate the effect on the transmittance, the heating procedure was applied to the crystal TUM73-3 without an evaporation. The process was performed in an evaporation device at MPP which was also used for the production of all CRESST-III Phase 1 detectors¹⁰. The upper part of table 4.3 shows the attenuation length at 430 nm obtained after the evaporation simulation for the three orientations of TUM73-3. The values are significantly decreased by a factor of ~ 2 compared to table 4.2 and are again more comparable to the initial values before additional annealing (table 4.1). It should be mentioned that defects on the large ((20 x 20) cm) surfaces of the crystal were observable by eye. It was taken care that the beam passes through a part of the crystal where optically no worsening was visible. No such damages occurred on the four small surfaces.

This measurement confirms former observations of a reduced light output after the evaporation. Regardless of the type of defects, it is expected that only the surface is affected. To investigate this hypothesis, the crystal surface was re-polished and thus, the uppermost layer with a thickness of $\sim 5\ \mu\text{m}$ was removed [138]. Afterwards, the transmission measurement was repeated another time. The results obtained for the attenuation length

¹⁰Before the simulation of the evaporation procedure at MPP, an equivalent procedure was attempted in a sputtering device at TUM. However, no change in the attenuation length was observed afterwards. Possible explanations are potentially miscalibrated thermometers or – due to the holder – a better heat coupling of the CaWO_4 crystal in the MPP device.

crystal	orientation	width [mm]	L_{att} @ 430 nm [mm]
TUM73-3	c	6.8	111.3 ± 9.6
TUM73-3	\perp c (1)	20.3	216.7 ± 16.0
TUM73-3	\perp c (2)	20.2	159.0 ± 7.8
TUM73-3	c	6.8	238.9 ± 40.6
TUM73-3	\perp c (1)	20.3	386.4 ± 37.7
TUM73-3	\perp c (2)	20.2	400.1 ± 41.4

Table 4.3.: Attenuation lengths L_{att} at 430 nm obtained for different orientations of the crystal TUM73-3 after the application of the heating procedure (in vacuum) which is necessary for the evaporation of the TES (upper part) and after re-polishing (lower part). For all orientations, L_{att} is reduced after the simulated evaporation (compare temperature curve in figure 4.14) by a factor of ~ 2 compared to table 4.2. It is expected that defects caused by the evaporation procedure occur mainly on the surfaces. This is confirmed as the values of table 4.2 are recovered after re-polishing which removes $\sim 5 \mu\text{m}$ of the uppermost surface layer [138].

at 430 nm (lower part of table 4.3) clearly confirm the expectation that defects caused by the evaporation are only present in the uppermost surface layer since the values before the simulated evaporation (table 4.2) could – within error bars – be re-established. This result also confirms the strategy we pursued during assembling the detector modules for CRESST-III Phase 1. The TES was evaporated to the only polished surface of the detector crystals, all other surfaces are roughened. After the evaporation, all crystal surfaces except for the one with the TES were re-roughened in the clean room. In this way, also for CRESST-III Phase 1 crystals the uppermost surface layer was removed together with potential defects which were contained there.

4.3. Future Developments

The previous sections 4.1 and 4.2 make clear that the optical quality achieved for TUM-grown CaWO_4 crystals has not yet reached an optimum.

Compared to CaWO_4 crystals by Russian suppliers, TUM-grown crystals feature pronounced internal stresses probably originating from dislocations frozen into the crystal structure due to radial temperature gradients during growth. Such stresses make a cutting without damaging the crystal difficult and can, furthermore, strongly influence the scintillation efficiency (not investigated here). Therefore, measures should be taken in order to remove or, at least, reduce these stresses. It appears that the observed dislocations cannot be influenced after growth any more, i.e. the growth parameters have to be adapted. According to [133], plane boundaries between the solid and the liquid phases are required. Such plane boundaries appear, however, not to be achieved during crystal growth at TUM (see appendix B.2). One possibility to reduce the observed intrinsic stress conditions might be a crystal growth with a lower growth speed.

Also concerning transmittance and light output, several Russian CaWO_4 crystals have

a significantly better quality compared to those grown at TUM. The transmittance can be connected to the stress conditions, however, also additional effects might come into play. It is shown in section 4.2 that the amount of oxygen-related scattering centers can considerably be reduced by means of an additional annealing procedure. An intense study of alternative annealing procedures with, e.g., an even further decreased cool-down rate is necessary to optimize the method.

Furthermore, in [120,132] was found that tiny amounts of rare earth elements are present in several Russian crystals. These – probably accidental – impurities can potentially explain the increased scintillation efficiency in these crystals. Specific doping tests could be performed to investigate this hypothesis. However, it has to be thought about consequences with respect to a potential contamination of the furnace or the crucible.

For all attempts to improve the optical quality, suitable analysis methods are required. Therefore, the methods introduced in this chapter should be developed further. For a more quantitative investigation by means of photoelasticity, the relation between the photoelastic fringe pattern and the stress-optical law (equation 4.3) should be found. A calibration of the amount of intrinsic tensions could be realized via applying an increasing external force to a CaWO_4 crystal while observing the behaviour of the resulting isochromatics. To achieve this goal, the option of transforming the already built plane polariscope into a circular polariscope could help to separate isochromatics from isoclinics. A CCD (charge-coupled device) camera should permanently be installed in a future upgrade of the setup in order to avoid dependencies on the viewing angle and on the position of the camera.

In order to achieve a better understanding where light can be lost in a CaWO_4 crystal, a setup being able to distinguish between scattering and absorption should be constructed. In addition to the measurement of the light which is transmitted through a crystal, a detector (array) surrounding the sample at the sides should be installed in order to measure scattered light. Comparing the amount of transmitted and scattered light would then allow a determination of the light absorbed within the crystal. Furthermore, with the help of an integrating sphere, the total scintillation light output of an excited CaWO_4 crystal could be determined.

5. Improving the Radiopurity of CaWO_4 Crystals

In order to achieve the radiopurity required for the CaWO_4 detector crystals of CRESST-III Phase 2, targeted measures have been taken within the frame of the present work as described in this chapter. Section 5.1 gives introductory remarks on the measurement of trace impurities in the materials of interest. The first approach to achieve a higher radiopurity is an improvement of the environment and of the materials used for the handling of the raw powders (see section 5.2). Secondly, a chemical purification of the raw materials was developed at TUM. Section 5.3 is dedicated to the description of the complex procedures applied during this purification. Section 5.4 concludes with the description of a cleaning effect achievable by segregation during crystal growth.

5.1. Introductory Remarks

An important component for studying the effect of the applied measures is the investigation of trace impurities in the respective samples. All measurement methods used in the present work are briefly described in appendix C. However, only a few of these methods are able to provide reliable results on the already low impurity concentrations (mostly in the ppb range) of the various powder and crystal samples. All radiopurity investigations that are presented in this chapter are performed by means of high-purity germanium (HPGe) spectroscopy, of inductively coupled plasma mass spectrometry (ICP-MS) and of laser ablation (LA-) ICP-MS. Results of HPGe spectroscopy were provided by measurements in the shallow underground laboratory (UGL) Garching [122], by Jorge Puimedón of the Laboratorio Subterráneo de Canfranc (LSC) in Spain [140, 141] as well as by Matthias Laubenstein at the LNGS [142]. Measurements with the standard ICP-MS method were conducted at LNGS [61], as well. The ICP-MS method is based on dissolving the sample before it is nebulized for the introduction into the instrument. Therefore, an (absolute) measurement of the almost insoluble CaWO_4 powder and crystal samples is not possible. An alternative also suitable for insoluble materials is LA-ICP-MS where atoms/molecules on the surface of the sample can be ablated by a pulsed UV laser before being passed into the plasma (see appendix C). LA-ICP-MS was applied to a few CaWO_4 crystal samples using an instrument of the TUM Centre for Building Materials (CBM) [143].

If not noted otherwise, the errors of HPGe measurements are given at a confidence level (C.L.) of 68 % (1σ). In the case that the contamination level is below the detector sensitivity, only the determination of limits is feasible. This is realized with a confidence level of 90 % for UGL Garching as well as for LNGS and with 95 % C.L. in case of measurements conducted at LSC. ICP-MS analyses are usually performed in semi-quantitative

mode¹ as no calibrated reference material from the same material as the sample exists. Negative values indicate that the signal of the subtracted blank measurement (without sample) is higher than the measured concentration which is equivalent to the statement that no contamination is found for the respective isotope. ICP-MS results typically have an uncertainty of 30 %.

The two raw powders (CaCO_3 and WO_3) are bought in the highest quality commercially available which is a minimum purity of 99.999 % in case of CaCO_3 and of 99.995 % for WO_3 . The corresponding analysis certificates of two different batches of CaCO_3 (lot numbers D0712CAA3, D0812CAA2R) and WO_3 (lot numbers D0113WB1, D0714WB1) supplied by the company MV Laboratories [121] and involved in the present work can be found in appendix D. Results of radiopurity measurements of the CaCO_3 powder (D0712CAA3) and of the WO_3 powder (D0113WB1) are shown in [120]. If not noted otherwise, all procedures described in this chapter were performed with the CaCO_3 and WO_3 powder batches with lot numbers D0812CAA2R and D0714WB1.

Samples of these two powder batches were measured with HPGe spectroscopy at LSC (see table 5.1). Two different batches of CaWO_4 powder (CaWO_4 (1) and CaWO_4 (2)) were produced from these two raw materials via a solid state reaction (compare section 3.2) without application of any purification treatment. They were also investigated with HPGe detectors at LSC and LNGS, respectively. The activities obtained for the different samples are listed in table 5.1 and serve as a reference for all results presented in the following.

Activities are usually given in mBq/kg. Hereby, 1 mBq/kg translates to a concentration of $8.0 \cdot 10^{-11}$ g/g (0.08 ppb) and of $2.5 \cdot 10^{-10}$ g/g (0.25 ppb) in the cases of ^{238}U and ^{232}Th , respectively. Several contaminations with isotopes of thorium, uranium, radium and actinium are found in the CaCO_3 powder of table 5.1². The highest activity of (47 ± 10) mBq/kg is observed for $^{234\text{m}}\text{Pa}$ which corresponds also to the activity of ^{238}U . As WO_3 has a compact structure where impurities cannot be incorporated as well as in CaCO_3 , it is, in general, expected to be cleaner than CaCO_3 . This expectation is confirmed by HPGe spectroscopy: only two contaminations are found whereas in all other cases the concentrations of the respective isotopes lie below the detector sensitivity resulting in an upper limit for the activity. Although the activity of ^{40}K is much higher than desired and was not observed in earlier batches [83, 120], the value of (161 ± 10) mBq/kg is compatible with the upper limit of < 5 ppm given in the analysis certificate of MV Laboratories (see figure D.2 in appendix D).

The contaminations within the two raw materials are transferred to the CaWO_4 powder. Only the activity value of ^{40}K is decreased which might hint towards a partial evaporation during CaWO_4 powder production as the boiling point of potassium (759°C [111]) is lower than the temperature in the chamber furnace ($(1100 - 1200)^\circ\text{C}$). However, potassium is also expected to be bound in molecules, e.g., in K_2WO_4 , which have a higher boiling point. Still, a certain fraction of the present potassium might evaporate during

¹A semi-quantitative assay is similar to a qualitative assay in detecting the presence or absence of a chemical substance (analyte). Additionally, a numeric representation of the amount of the analyte is provided due to the comparison to a reference.

²In general, the activity of the isotope ^{226}Ra is calculated from the activities of ^{214}Bi and ^{214}Pb . The activity of ^{228}Ra is obtained from the value of ^{228}Ac whereas the activity of ^{228}Th is derived from ^{212}Bi and ^{212}Pb . For the activity of ^{227}Ac , equilibrium is assumed.

sample		CaCO ₃	WO ₃	CaWO ₄ (1)	CaWO ₄ (2)
origin	isotope	activity [mBq/kg]			
²³² Th chain	²²⁸ Ra	< 3.2	< 3.0	< 4.5	1.9 ± 0.5
	²²⁸ Th	2.2 ± 0.6	< 1.7	3.0 ± 0.9	1.3 ± 0.4
²³⁸ U chain	^{234m} Pa	47 ± 10	< 40	< 55	48 ± 18
	²²⁶ Ra	2.5 ± 0.6	1.8 ± 0.4	4.7 ± 0.7	5.1 ± 0.5
²³⁵ U chain	²³⁵ U	2.2 ± 0.5	< 2.0	< 3	< 1.6
	²²⁷ Ac	5.2 ± 1.2	< 3.2	< 4.8	-
other	¹³⁷ Cs	< 1.0	< 0.80	< 1.1	< 0.19
	⁶⁰ Co	< 0.7	< 0.63	< 0.8	-
	⁴⁰ K	< 9.6	161 ± 10	109 ± 10	67 ± 9

Table 5.1.: Different powder samples investigated with HPGe spectroscopy at LSC (CaCO₃, WO₃ and CaWO₄ (1)) and at LNGS (CaWO₄ (2)). The two measured batches of CaWO₄ powder have been produced from the same batch of the two raw materials CaCO₃ and WO₃ via a solid state reaction without applying any cleaning procedures. Contaminations present in the raw materials are transferred to the CaWO₄ powders. Only in the case of ⁴⁰K a reduction is observed which hints towards a partial evaporation of ⁴⁰K during the reaction to CaWO₄ happening at a temperature of ~1200°C. Errors are given with a confidence level (C.L.) of 68%, limits with 95% C.L. (at LSC) and 90% C.L. (at LNGS).

the reaction in the chamber furnace. Depending on the number of cycles, the exact temperature and duration in the furnace as well as on the strength by which the powder is pressed into the crucible, the amount of evaporating potassium could differ. This could explain the deviation in ⁴⁰K contamination (see table 5.1) between the two CaWO₄ samples (1) and (2).

Measures to decrease the contaminations observed (table 5.1) and the respective results are described in the following.

5.2. Handling of the Raw Materials

Previously, the laboratory used for CaWO₄ powder production was shared with other groups where the required working conditions could not always be ensured. In the scope of this work, the CaWO₄ powder production was moved to a dedicated laboratory. If the powders are not within a closed vessel, they are only handled in a flow box to avoid any contamination, e.g., due to dust. Gloves, mouth protection and clean room coats are used to avoid particles from skin and clothes to come into contact with the materials. In the most recent development the laboratory was also equipped with a lock as well as air filters.

Not only the environment, but also all materials the powders are in contact with should be as radiopure as possible. It is differentiated between the two different production methods via a solid state reaction and precipitation (compare section 3.2).

sample		PVC cylinder	ZrO ₂ balls	steel-teflon balls
origin	isotope	activity [mBq/kg]		
²³² Th chain	²²⁸ Ra	157 ± 19	(546 ± 37) · 10 ³	58 ± 40
	²²⁸ Ac	157 ± 19	(546 ± 37) · 10 ³	58 ± 40
	²²⁸ Th	33 ± 6	(492 ± 15) · 10 ³	170 ± 93
	²¹² Pb	26 ± 8	(379 ± 46) · 10 ³	< 47 ± 5
	²¹² Bi	70 ± 32	(598 ± 80) · 10 ³	170 ± 93
	²⁰⁸ Tl	43 ± 11	(502 ± 16) · 10 ³	< 57 ± 2
²³⁸ U chain	²³⁸ U	434 ± 63	(2803 ± 367) · 10 ³	901 ± 622
	^{234m} Pa	434 ± 63	(2803 ± 367) · 10 ³	901 ± 622
	²²⁶ Ra	1 741 ± 45	(1 114 ± 22) · 10 ³	63 ± 37
	²¹⁴ Pb	1 814 ± 70	(1 024 ± 47) · 10 ³	63 ± 37
	²¹⁴ Bi	1 692 ± 57	(1 141 ± 26) · 10 ³	< 31 ± 1
	²¹⁰ Pb	4 936 ± 250	-	-
other	⁴⁰ K	-	(34 ± 6) · 10 ³	184 ± 126
	¹³⁷ Cs	32 ± 4	< (1 333 ± 1 378) · 10 ³	< 18 ± 1
	⁶⁰ Co	30 ± 3	1 096 ± 129	< 8.0 ± 0.2

Table 5.2.: The different components used for the mixing and grinding of the powders during CaWO_4 powder production via a solid state reaction were measured with the two HPGe detectors LoAx2 (PVC) and GEM (balls) in the UGL Garching. Due to huge contaminations in the PVC container and the ZrO₂ grinding balls, they were replaced by a teflon container and steel balls surrounded by a teflon layer. The (much lower) activities of the steel-teflon balls are expected to originate mainly from the steel which, however, is not in direct contact with the powders. Errors are given with a confidence level (C.L.) of 68 %, limits with 90 % C.L.

Materials used for Solid State Reaction

As explained in section 3.2, the powder production via the solid state reaction includes several mixing and grinding steps. In the past, this was performed within a PVC container utilizing grinding balls made of ZrO₂. Measuring both, the container and the grinding balls, via HPGe spectroscopy in the UGL Garching (see table 5.2) led to the discovery of a huge number of impurities which potentially can contaminate the CaWO_4 powder. In the PVC cylinder, contaminations up to a few Bq/kg are found for several isotopes. Even higher activities in the order of kBq/kg are measured for certain isotopes in the ZrO₂ balls. As a consequence, a new container made of the cleaner material teflon was manufactured and also the grinding balls were exchanged. Table 5.2 confirms that the new steel balls surrounded by a teflon layer are, in total, much less contaminated by several orders of magnitude. Furthermore, it is expected that the obtained activities mainly originate from the steel inside the balls which cannot directly get in contact with the powders.

After grinding, the powder is heated up in an Al₂O₃ crucible for the solid state reaction to take place. Two such crucibles were also measured via HPGe spectroscopy in the

sample		Al ₂ O ₃ crucible (old)	Al ₂ O ₃ crucible (new)	quartz ware
origin	isotope	activity [mBq/kg]		
²³² Th chain	²²⁸ Ra	153 ± 15	54 ± 7	144 ± 37
	²²⁸ Ac	153 ± 15	54 ± 7	144 ± 37
	²²⁸ Th	172 ± 11	48 ± 4	122 ± 22
	²¹² Pb	187 ± 25	41 ± 7	126 ± 33
	²¹² Bi	272 ± 49	99 ± 22	492 ± 188
	²⁰⁸ Tl	162 ± 12	49 ± 5	110 ± 29
²³⁸ U chain	²³⁸ U	1 063 ± 254	3 523 ± 479	1 120 ± 1 013
	^{234m} Pa	1 063 ± 254	3 523 ± 479	1 120 ± 1 013
	²²⁶ Ra	421 ± 12	70 ± 3	832 ± 47
	²¹⁴ Pb	429 ± 21	68 ± 5	813 ± 61
	²¹⁴ Bi	417 ± 16	73 ± 5	860 ± 72
other	⁴⁰ K	366 ± 59	55 ± 21	< 173 ± 22
	¹³⁷ Cs	8.0 ± 2.0	3.3 ± 1.0	< 18.4 ± 0.7
	⁶⁰ Co	5.3 ± 1.2	1.8 ± 0.6	< 13.4 ± 0.4

Table 5.3.: Al₂O₃ crucibles and quartz ware in form of two quartz-glass beakers measured with the HPGe detector GEM in the UGL Garching. The old crucible named "crucible (old)" was used for many CaWO₄ production cycles (via solid state reaction) before measurement, whereas a new crucible was measured directly after delivery. Activities observed in the old crucible are for most isotopes higher by a factor of 3-6 compared to those of the new crucible. It is, however, not clear if this deviation results from a contamination of the old crucible during usage or from a cleaner batch material in case of the new crucible. Comparable values are observed for the contamination of the two quartz-glass beakers (measured together) used for the solutions in the precipitation reaction. Errors are given with a confidence level (C.L.) of 68 %, limits with 90 % C.L.

UGL Garching (see table 5.3). One of these crucibles referred to as "crucible (old)" was, hereby, used for many production cycles before the measurement, whereas a new crucible was measured directly after delivery from the company. Both crucibles show contaminations with various isotopes. Apart from the activities obtained for ²³⁸U (which is in equilibrium with ^{234m}Pa), the activities of most isotopes listed in table 5.3 are increased by a factor of ~3-6 in the case of the old crucible. However, it is not clear, whether the observed differences in the level of impurities originate from a contamination during usage for many powder production cycles or whether the new crucible was simply produced from a cleaner batch of Al₂O₃ raw material. In any case, the Al₂O₃ crucible cannot easily be replaced by a cleaner one made from an equally suitable material that withstands temperatures of up to 1200 °C without reacting with the powders inside.

Materials used for Precipitation Reaction

In the case of CaWO₄ powder production via the precipitation method, no grinding or heating up to high temperatures is applied to the raw materials. Instead, the powders

are dissolved in aqueous ammonia (NH_3) and nitric acid (HNO_3) solutions before being further processed. These solutions get in contact with different vessels, funnels and filters as well as with magnetic stirrers. The majority of the lab ware used in this process is made from quartz glass and teflon which are the cleanest available materials. Only two suction filters still consisted of normal glass during the powder production cycles performed in the scope of the present work. For future CaWO_4 powder productions, these will be replaced by quartz-glass filters, as well. As can be seen in the last column of table 5.3, the contaminations within two quartz-glass beakers (quartz ware) are comparable to those of the Al_2O_3 crucibles. It has to be noted, that the highest activity of $\sim 1 \text{ Bq/kg}$ found for ^{238}U has an uncertainty which is in the same order of magnitude.

Before being used for the powder processing, the whole lab ware involved is soaked in an aqueous solution containing 5 % of nitric acid to clean it from radionuclides at the surfaces.

Chemical substances like ammonia solutions and nitric acid solutions are also needed in different concentrations³ for the various procedures applied to the powders. If possible, these solutions are bought in "supra quality" indicating a total metallic impurity level in the order of 10 ppb, otherwise in the best quality commercially available. A few liquids are bought even of "ultra quality" which implies that the total contamination with metallic impurities is in the order of $\sim 1 \text{ ppb}$. The respective analysis certificates can be found in appendix D.

Clean water with a conductivity of $18 \text{ M}\Omega\text{cm}$ is provided by a water purification system (TUM Physics Department, chair E22). The quality of two water samples was validated by means of ICP-MS at LNGS and the results are listed in table 5.4. Whereas the sample "water (fac.)" was taken directly out of the facility, the sample "water (PE)" was stored for approximately two months in a PE container. Apart from a few exceptions, possible impurities in both water samples are below the sensitivity of the ICP-MS instrument. The upper limits given in the table are in the ppb range or below, which indicates that the water has at least "supra quality". As no significant differences between the two samples could be observed, it can be concluded that storing the water in the PE container does not degrade the quality (i.e. radiopurity) of the water.

5.3. Chemical Purification of the Powders and Trace Impurity Analysis

Impurities within materials the raw powders get in contact with can have a negative influence on the resulting radiopurity. The other way round, the powders can also be purified by a special chemical treatment. In this section, the different methods for such a chemical purification of the raw materials as developed at TUM are presented. The principles of the applied techniques are included in section 5.3.1. Figure 5.1 summarizes two different versions that were tested in the frame of this work. In both versions, CaCO_3 powder was purified by means of a solvent extraction explained in section 5.3.2. Version 1 processes the cleaned CaCO_3 powder via a solid state reaction further to CaWO_4 powder. In version 2, coprecipitation is added as an additional purification step

³An expression like 10 % NH_3 solution means, hereby, an aqueous solution containing 10 % ammonia.

sample	water (fac.)	water (PE)	sample	water (fac.)	water (PE)
isotope	concentration [ppb]		isotope	concentration [ppb]	
⁷ Li	< 0.001	< 0.001	⁸⁸ Sr	0.03	0.02
²³ Na	< 0.1	< 0.1	⁸⁹ Y	< 0.001	< 0.001
²⁴ Mg	0.10	0.07	⁹⁵ Mo	< 0.001	< 0.001
²⁷ Al	< 0.05	< 0.05	¹⁰⁷ Ag	< 0.001	< 0.001
⁴⁴ Ca	< 2	< 2	¹¹⁰ Cd	< 0.001	< 0.001
⁵¹ V	< 0.01	< 0.01	¹¹⁶ Sn	< 0.005	0.008
⁵³ Cr	< 0.1	< 0.1	¹³⁷ Ba	< 0.002	< 0.002
⁵⁵ Mn	< 0.005	< 0.005	¹⁴⁰ Ce	< 0.001	< 0.001
⁵⁷ Fe	< 2	< 2	²⁰³ Tl	< 0.001	< 0.001
⁵⁹ Co	< 0.005	< 0.005	²⁰⁸ Pb	< 0.002	0.002
⁶⁰ Ni	< 0.005	< 0.005	²⁰⁹ Bi	< 0.001	< 0.001
⁶³ Cu	< 0.02	< 0.02	²³² Th	< 0.0001	< 0.0001
⁶⁴ Zn	< 0.005	< 0.005	²³⁸ U	< 0.0001	< 0.0001

Table 5.4.: Two water samples provided by a millipore facility with a conductivity of 18 MΩcm measured by means of ICP-MS at LNGS. The sample "water (fac.)" was directly taken out of the facility whereas the sample "water (PE)" was stored for approximately two months in a PE container. For most isotopes only upper limits in the ppb range or below are given, which indicates that the water has at least "supra quality". As no significant difference between the two samples is observed, a storage in the PE container does not degrade the quality of the water. The uncertainties of the measured concentrations are ~ 30 %.

before the final CaWO₄ powder is produced via a precipitation reaction (section 5.3.3). A washing procedure of the produced CaWO₄ powder is included again in both versions (section 5.3.4).

5.3.1. Separation Techniques

In order to separate quantitatively and effectively small amounts of (especially long-lived) radionuclides from the surrounding material, so-called separation techniques are applicable. As explained in detail in [144], electrolysis, distillation, ion exchange and chromatography are among such techniques. Most suitable for the requirements of the present work, however, appeared to be solvent extraction and coprecipitation which are explained in more detail in the following.

Solvent Extraction

The solvent extraction (also called liquid-liquid extraction) is a rather simple method to separate compounds due to their relative solubilities in two different immiscible solvents, usually water and an organic liquid. The principle is schematically shown in figure 5.2 (a). One solvent (here an aqueous solution) is enriched in certain solutes that should be

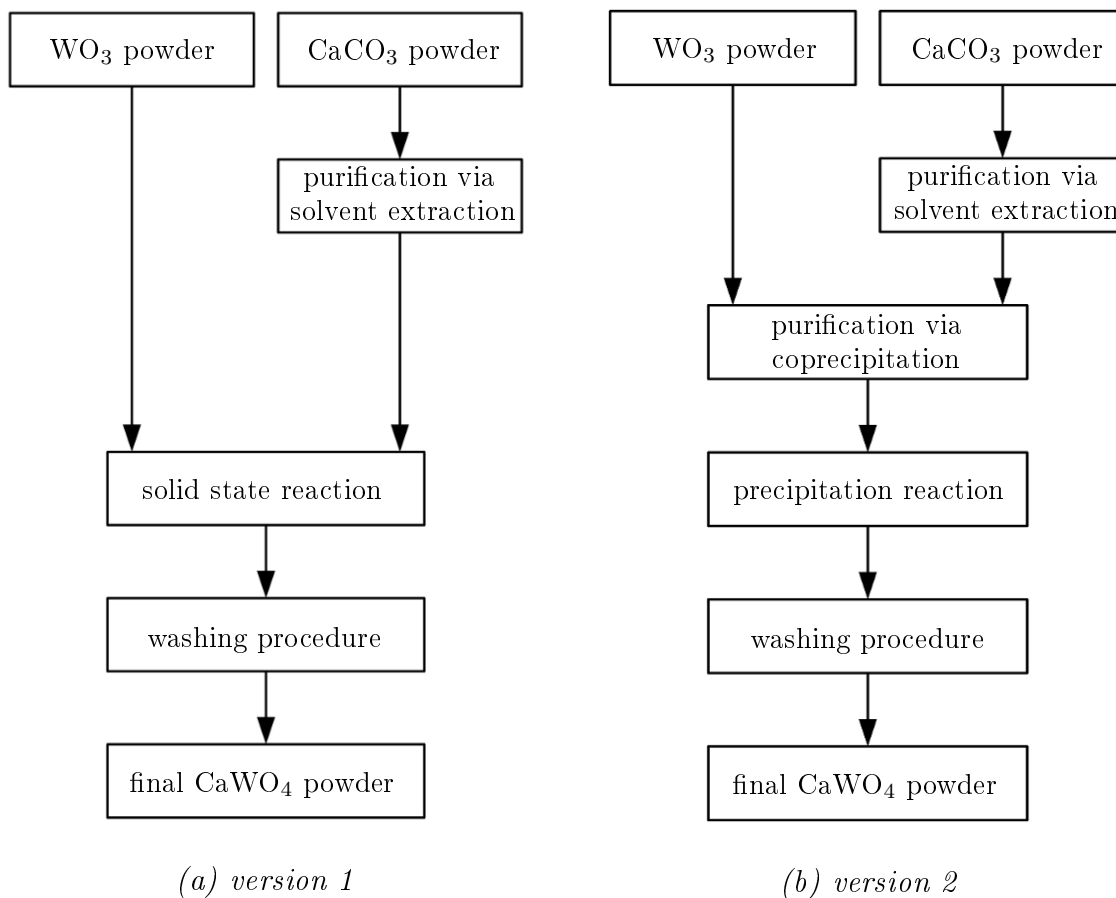


Figure 5.1.: Summary of the two versions of a chemical purification of the raw powders CaCO_3 and WO_3 and of the respective production of CaWO_4 powder developed in the present work. Both versions involve a purification of CaCO_3 powder by means of solvent extraction. The cleaned CaCO_3 powder is further processed to CaWO_4 powder via a solid state reaction in version 1 (a), whereas a precipitation reaction including an additional cleaning step via coprecipitation is applied in version 2 (b). A final washing procedure is performed in case of both versions.

removed, while the other solvent (here an organic solution) is depleted in these solutes. Both solutions are thoroughly mixed and impurities are, thereby, transferred between the two solutions – in this case they move from the aqueous to the organic liquid (indicated by the arrows). The concentrations of the solutes change in the two phases until equilibrium is reached. The two solutions can then be separated again since they are immiscible and the solution of interest can be recovered. The ratio of the total concentrations of a solute (in all forms) in the organic and aqueous phases after the liquid-liquid extraction is called distribution coefficient and is a quantitative measure for the extraction. For more detailed information see, e.g., [145, 146].

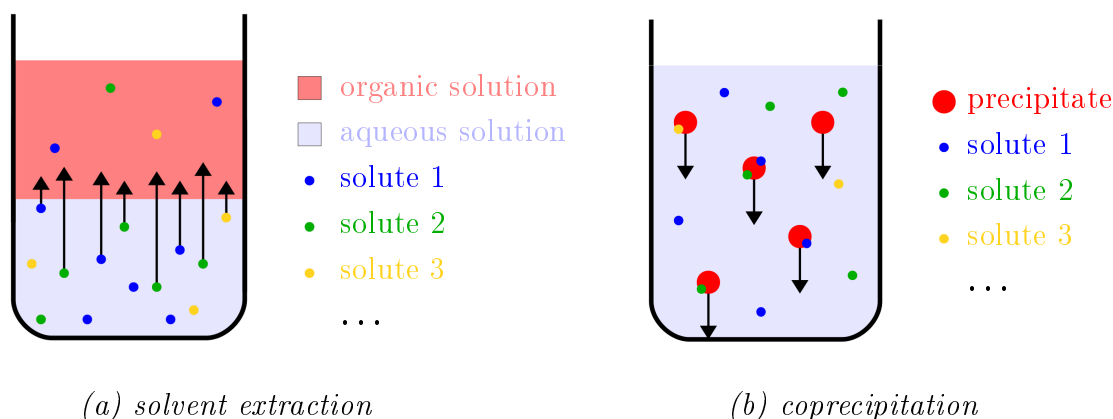


Figure 5.2.: (a) Principle of the solvent extraction technique. Two immiscible solutions containing certain solutes are thoroughly mixed. Due to different solubilities, the solutes can be transferred from the enriched (here aqueous solution) to the depleted phase (organic solution) thereby changing the concentrations of the solutes until equilibrium is reached (indicated by the arrows). As both solutions are immiscible, the cleaned solution of interest (here aqueous solution) can be separated again. (b) Principle of coprecipitation. Substances normally soluble (here solute 1,2,3) are carried down by a precipitate (indicated by the arrows), e.g., via the formation of mixed chemical compounds, surface adsorption or occlusion. After filtration of the precipitates, the remaining solution is cleaner than before.

Coprecipitation

Via this method, trace elements can be isolated via their precipitation on so-called carriers. The starting product is a solution that contains a small amount of (undesired) substances, which are normally soluble, as schematically shown in figure 5.2 (b). When a precipitation reaction is performed by adding a suitable second solution, a precipitate forms and acts as carrier. This means, it carries down also part of the contamination solutes with chemical properties similar to the ones of the precipitate. Different mechanisms for this effect are the formation of mixed crystals and mixed chemical compounds, surface adsorption as well as occlusion and mechanical inclusion of trace components into the other compound during crystal formation. An ionic (or partially charged) precipitate can, for example, attract other ions from the solution which are then adsorbed and can be trapped by subsequent layers of the precipitate.

Coprecipitation can specifically be applied as a separation technique. When the precipitates, which contain also a certain amount of carried-down contaminating substances, are separated by, e.g., filtration, the solution is cleaned. For further information on this procedure, see [145, 146].

5.3.2. Purification of CaCO_3 Powder via Solvent Extraction

At TUM, a procedure to clean CaCO_3 powder via solvent extraction was developed in 2015 (version 1) and further improved in 2016 (version 2). The steps involved in this

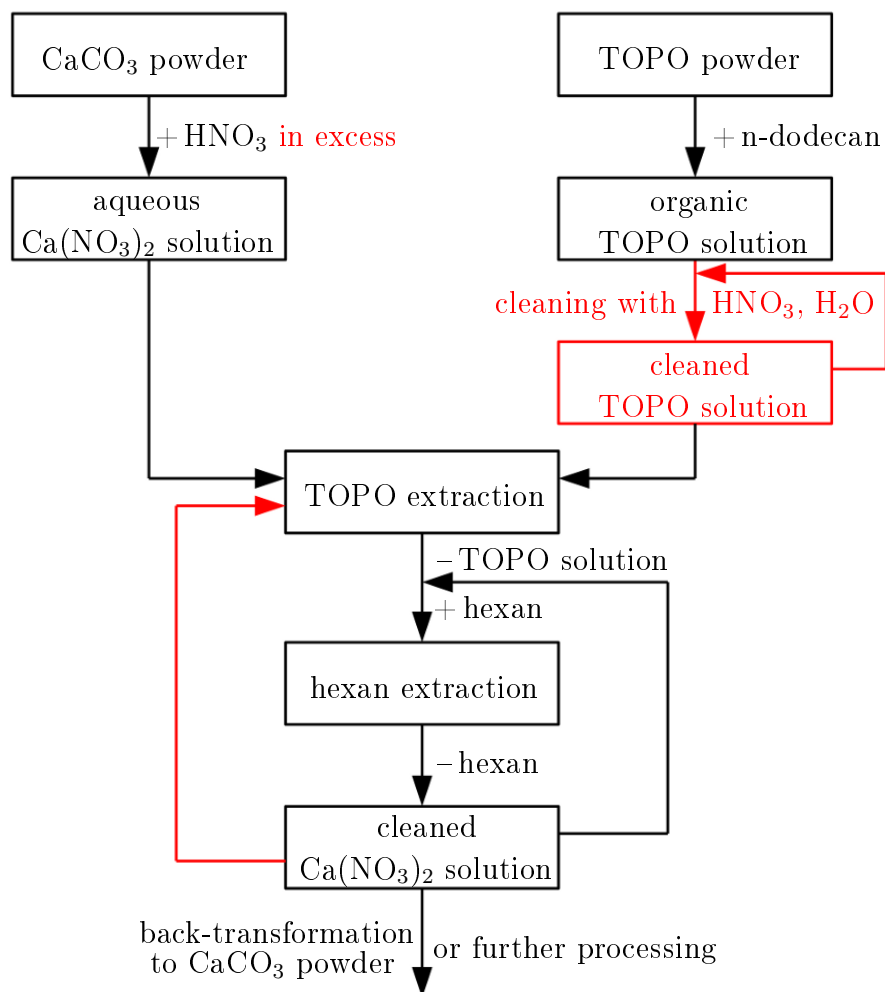


Figure 5.3.: Procedure for the chemical purification of CaCO_3 via solvent extraction with TOPO dissolved in *n*-dodecan. At TUM, a first version (named version 1) was developed in 2015 (black). CaCO_3 powder is first transformed into an aqueous solution of $\text{Ca}(\text{NO}_3)_2$. The solvent extraction is carried out with the organic TOPO solution. To remove possible remnants of *n*-dodecan, two hexan extraction cycles follow. Additional steps included in an advanced procedure 2016 (version 2) are marked in red. In this improved version 2, the whole extraction procedure is repeated with fresh (cleaned) TOPO solution to enhance the purification effect before the cleaned $\text{Ca}(\text{NO}_3)_2$ solution is further processed. For details see the main text.

procedure are illustrated in figure 5.3. The steps of version 1 are drawn in black whereas additional steps added in the improved version 2 are marked in red.

Version 1

In order to apply a liquid-liquid extraction, the CaCO_3 powder has to be transformed into a solution. In a reaction with HNO_3 , an aqueous $\text{Ca}(\text{NO}_3)_2$ solution according to equation 3.2 in section 3.2 is prepared with a $\text{Ca}(\text{NO}_3)_2$ concentration of 2 mol/l. In the

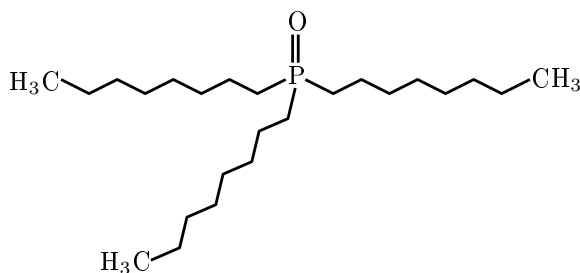
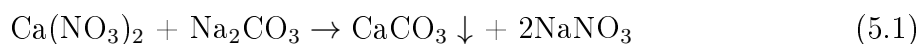


Figure 5.4.: Structural formula of trioctylphosphineoxide (TOPO) [111] used as extractant for the CaCO_3 purification. Due to its high polarity which results from the dipolar phosphorus-oxygen bond, TOPO is able to bind various metals, particularly uranium and thorium. Not drawn are the CH_2 groups located at each corner.

first tests of 2015, this solution was neutral (pH value ~ 7). Simultaneously to the preparation of the $\text{Ca}(\text{NO}_3)_2$ solution, the extractant has to be prepared. In the present work, the organophosphorus compound trioctylphosphineoxide (C_8H_{17})₃PO (TOPO) with the structural formula as shown in figure 5.4 is used for this purpose. The high polarity resulting from the dipolar phosphorus-oxygen bond allows TOPO to bind various metals, especially uranium and thorium [147]. The efficiency depends, hereby, on the chemical conditions of the involved solutions. As the octyl groups C_8H_{17} confer solubility in low-polarity solvents, TOPO is dissolved in the organic liquid n-dodecan ($\text{C}_{12}\text{H}_{26}$) with a concentration of 0.2 mol/l.

In order to perform the TOPO extraction, the aqueous $\text{Ca}(\text{NO}_3)_2$ solution and the organic TOPO solution are mixed in a volume ratio of 1:1 with a magnetic stirrer for 30 min⁴. This time suffices for stabilizing a new equilibrium for solutes such as uranium and thorium. The mixture is filled into a separatory funnel and after a time of ~ 15 min both solutions are well separated from each other as shown in figure 5.5. The originally transparent TOPO solution (upper phase) has turned slightly yellow which might be a hint for an increased concentration of impurities. The cleaned $\text{Ca}(\text{NO}_3)_2$ solution is carefully filled into an empty vessel and the contaminated TOPO solution is removed. After the separation, n-dodecan can still be present in the $\text{Ca}(\text{NO}_3)_2$ solution in the form of emulsions. These remaining traces can be bound with hexan (C_6H_{14}) by applying the same extraction procedure as in the case of the TOPO solution (i.e. 30 min mixing and separation after 15 min). In order to ensure that all n-dodecan remnants are removed from the $\text{Ca}(\text{NO}_3)_2$ solution, the solvent-extraction with hexan is repeated.

In this version, the purified $\text{Ca}(\text{NO}_3)_2$ solution was transformed back to CaCO_3 powder to be further processed to CaWO_4 via the solid state reaction. For the back-transformation, a precipitation reaction with an aqueous 2 mol/l solution of Na_2CO_3 was performed:



After completion of the back-reaction, the precipitated CaCO_3 was filtrated and rinsed with supra-pure water in order to wash out solvable remnants of, e.g., sodium. Figure 5.6 shows the white CaCO_3 powder after having dried.

⁴For the extraction of uranium and thorium only, a stirring time of ~ 10 min suffices. A longer stirring time increases the probability that also other metals, e.g., iron are extracted.

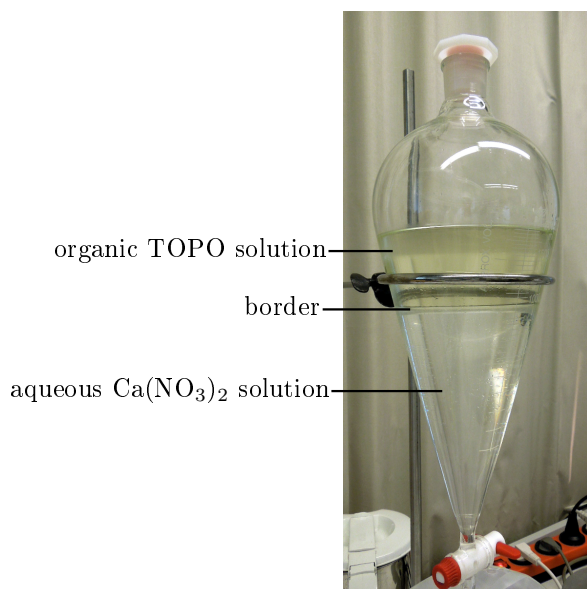


Figure 5.5.: Solvent extraction of aqueous $\text{Ca}(\text{NO}_3)_2$ solution using the extractant TOPO dissolved in *n*-dodecan. Shown are the two phases, separated again after having been mixed.



Figure 5.6.: Cleaned CaCO_3 powder after TOPO extraction and back-transformation via a precipitation reaction with the help of a Na_2CO_3 solution (compare equation 5.1).

CaCO_3 samples before and after the chemical purification via TOPO extraction were measured by means of ICP-MS at LNGS. The results in table 5.5 show a significant reduction of the contamination with thorium and uranium by a factor of $\gtrsim 7$ and $\gtrsim 35$, respectively. Simultaneously, a slight increase in the strontium and lead concentrations is observed. Although the values are still compatible within the 30 % uncertainties of the ICP-MS measurement, a contamination originating from, e.g., contact to air (and dust) or from the Na_2CO_3 powder cannot be excluded. A strontium concentration of 1000 ppb was, indeed, found in the Na_2CO_3 powder which was also measured by means of ICP-MS. No measurable contamination is present for lead, uranium and thorium. The CaCO_3 powder cleaned in the first purification tests of 2015 was transformed into CaWO_4 powder via the solid state reaction. After the reaction in the chamber furnace, the produced CaWO_4 was very hard and could only be pulverized again with special effort (see appendix B.4). A diffractometer measurement confirmed that the end product is indeed CaWO_4 . However, it was discovered that a huge amount of sodium is present in the CaCO_3 powder and, therefore, also in the CaWO_4 material. An ICP-MS measurement of the CaCO_3 powder at LNGS determined a concentration of 0.49 % with an uncertainty of 10 %. This indicates that, in the procedure applied, not all sodium remnants originating from Na_2CO_3 could be washed out. As this could, however, be a problem for the crystal growth and the purity of the resulting detector crystals, a washing method was developed and applied in order to remove the main part of the sodium contamination. This washing procedure, which was also performed in the case of version 2, is described in detail in section 5.3.4. The high sodium contamination as well as the much finer structure of the CaCO_3 powder after purification could explain

sample	CaCO ₃ before	CaCO ₃ after	Na ₂ CO ₃
element	concentration [ppb]		
Th	0.22	< 0.03	< 0.03
U	2.8	< 0.08	< 0.05
Sr	4300	5000	1000
Pb	100	150	< 5

Table 5.5.: ICP-MS measurements (at LNGS) of CaCO₃ powder samples before and after a chemical purification via TOPO extraction as well as of Na₂CO₃ powder used for the back-transformation (see equation 5.1). Whereas the concentrations of thorium and uranium are improved by a factor of $\gtrsim 7$ and $\gtrsim 35$, respectively, in the CaCO₃ sample after purification, the contamination with strontium and lead seems to be slightly increased. The Na₂CO₃ sample shows a measurable contamination only for strontium. Errors are $\sim 30\%$ of the given values.

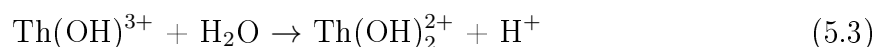
the hardness of the CaWO₄ powder after reaction. The raw crystal ultimately produced from this powder is called TUM73. From this crystal ingot, several detector crystals have been produced and are now operated in CRESST-III Phase 1 (see section 2.4). A radiopurity analysis was performed as described in chapters 6 and 7.

Furthermore, a small sample of TUM73 was investigated by means of LA-ICP-MS at CBM in comparison to a sample of the crystal TUM69 which was produced from the same raw materials but without any purification steps. The results are shown in table 5.6. Rows which are highlighted in green (red) indicate that the concentration is decreased (increased) by a factor > 2 in TUM73 compared to TUM69. Examples for elements whose concentration is significantly reduced in TUM73 are iron, tin and iodine. Also the contamination with the two main elements affected by the TOPO extraction applied to the CaCO₃ powder of TUM73 – uranium and thorium – has a lower value in TUM73. Concentrations that are slightly higher in case of TUM73 are only found for a few elements (e.g., lithium and rhodium).

Furthermore, hints for an improved quality of TUM73 compared to TUM69 were also found in [148].

Version 2

In 2016, the purification of CaCO₃ powder via solvent extraction was improved by applying several changes and additional steps (marked in red in figure 5.3). The cleaning efficiency in a neutral Ca(NO₃)₂ solution could be decreased due to the formation of hydrates of, e.g., thorium(IV) and uranium(VI) in aqueous solutions [149, 150]. In neutral aqueous solutions so-called oxocations can be formed:

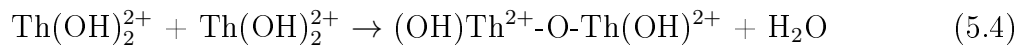


5. Improving the Radiopurity of CaWO₄ Crystals

crystal	TUM69	TUM73	crystal	TUM69	TUM73	crystal	TUM69	TUM73
element	concentration [ppb]		element	concentration [ppb]		element	concentration [ppb]	
Li	9.9	23.6	Ge	< 0.01	< 0.01	La	14.12	1.25
Be	4.0	< 0.01	As	8.8	13.2	Ce	13.4	4.1
B	< 1	< 1	Rb	1.3	< 0.01	Pr	0.2	< 0.001
Na	< 0.01	< 0.01	Sr	521	510	Nd	22.0	< 0.001
Mg	< 0.01	< 0.01	Y	13.9	11.8	Sm	< 0.001	< 0.001
Al	< 0.01	< 0.01	Zr	10.0	6.2	Eu	4.9	< 0.001
Si	< 1	< 1	Nb	466	361	Gd	< 0.001	< 0.001
K	< 0.1	< 0.1	Mo	1 219	914	Tb	2.6	< 0.001
Sc	3.9	11.2	Rh	7.0	39.4	Ta	61.0	50.8
Ti	5.8	11.7	Ag	< 0.001	< 0.001	Re	85.9	72.1
V	269	28.3	Cd	< 0.01	< 0.01	Ir	< 0.001	< 0.001
Cr	< 0.01	< 0.01	In	0.3	0.2	Pt	23.8	< 0.001
Mn	< 0.01	< 0.01	Sn	274	17.3	Au	339	217
Fe	608	< 0.01	Sb	1.6	< 0.001	Tl	< 0.001	< 0.001
Co	6.4	2.6	Te	< 0.01	< 0.01	Pb	2.6	< 0.001
Ni	< 0.01	< 0.01	I	305	< 1	Bi	3.0	1.2
Cu	< 0.01	< 0.01	Cs	< 0.001	0.2	Th	1.7	0.7
Zn	< 0.01	< 0.01	Ba	< 0.001	< 0.001	U	0.2	< 0.001

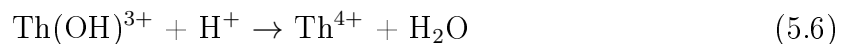
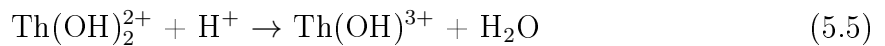
Table 5.6.: Samples of the raw crystals TUM69 and TUM73 measured by means of LA-ICP-MS at CBM. Both crystals were produced from the same batches of raw materials. In case of TUM73, a chemical purification of the CaCO₃ powder via TOPO extraction (version 1) was applied. Rows marked in green (red) indicate that the concentration of the respective element is decreased (increased) in TUM73 by a factor > 2. Strongly reduced concentration levels are, e.g., found for iron, tin, iodine, and also uranium (and thorium). Uncertainties are ~ 30 % of the given values.

Between different oxocations, oxobridges can build up leading to the formation of inorganic polymers containing many atoms of thorium or uranium:



Such oxocations and oxobridges are difficult to be extracted due to their strong covalent bonds that can not be broken by an extractant.

Hydrolysis can be suppressed by acidification of the solution. When the concentration of the acid is in excess, oxocations and compounds with oxobridges disappear:



More detailed information can be found in [150]. To achieve acidic conditions with a pH value of 2-3, HNO₃ was added to the CaCO₃ powder with an excess of 1 mol/l in the improved purification procedure of version 2.

To enhance the extraction capabilities of the organic TOPO solution, version 2 of the process contains an additional cleaning step. In four cycles, the TOPO solution is alternately mixed with a 5% HNO₃ solution and water (supra-quality) in equal proportions

and then separated again. Via liquid-liquid extraction, impurities can be removed from the TOPO solution.

Furthermore, after the first TOPO extraction followed by two cycles of hexan extraction, a second extraction cycle with a fresh TOPO solution is applied to the already once cleaned $\text{Ca}(\text{NO}_3)_2$ solution (compare figure 5.3). In this way, an enhancement of the total purification effect can be accomplished. After completion of the second extraction cycle, the cleaned $\text{Ca}(\text{NO}_3)_2$ is further processed as solution in the precipitation method. ICP-MS measurements of the $\text{Ca}(\text{NO}_3)_2$ solution before and after the extraction procedure of version 2 were performed at LNGS. However, due to the reduced concentration of CaCO_3 dissolved in diluted nitric acid, no significant changes could be observed in these measurements. The improved contamination level of the resulting CaWO_4 powder, after also the steps explained in the following sections 5.3.3 and 5.3.4 have been applied, can be found in table 5.13.

5.3.3. CaWO_4 Production via Precipitation and Coprecipitation

The CaWO_4 powder production via the precipitation method provides an additional possibility to remove contaminations from dissolved CaCO_3 and WO_3 powders via coprecipitation. The process steps of the so-called cross-cleaning developed at TUM within the scope of the present work are depicted in figure 5.7. The cleaned $\text{Ca}(\text{NO}_3)_2$ solution (end product of the procedure shown in figure 5.3) is diluted and brought into slightly alkaline conditions (pH value of ~ 9) via the addition of a 20 % NH_3 solution. Also the WO_3 powder has to be dissolved in NH_3 solution (10 %). The reaction for dissolving WO_3 with a concentration of ~ 0.4 mol/l is a very slow process which is only completed after about three days.

For precipitation, the two resulting alkaline solutions of $\text{Ca}(\text{NO}_3)_2$ and $(\text{NH}_4)_2\text{WO}_4$ have to contain the same molar amount of the substances Ca^{2+} and WO_4^{2-} . In addition, impurities such as Sr^{2+} , Pb^{2+} or Ra^{2+} are also present in the solutions and, as explained in section 5.3.1, a certain part of these impurities can be carried down by a precipitate, e.g., by CaWO_4 . To pre-precipitate a small amount of CaWO_4 in the two solutions, the so-called cross-cleaning method is applied: 2 % of each solution are taken and – under continuous stirring – added to the respective other solution. Contaminating isotopes attach themselves to the precipitated CaWO_4 molecules until a new chemical equilibrium is reached. This process is, in general, independent of the precipitate's amount in the solution [151].

Figure 5.8 shows the realization of the cross-cleaning. In the left picture, 2 % of the $(\text{NH}_4)_2\text{WO}_4$ solution (in the back) is added to the $\text{Ca}(\text{NO}_3)_2$ solution (in the front). After a short time the solution turns milky indicating the precipitation of CaWO_4 (right picture). After a stirring time of 30 min, the precipitated CaWO_4 sediments in both solutions. To retrieve both transparent solutions, the CaWO_4 and all coprecipitated by-products are removed by means of filtration. The cross-cleaning is repeated with another 2 % of each solution (compare figure 5.7). Only after the second filtration, the actual precipitation reaction as described in section 3.2 is performed.

It was observed that the CaWO_4 powder precipitated in the $\text{Ca}(\text{NO}_3)_2$ solution exhibits a finer structure than the CaWO_4 powder produced in the $(\text{NH}_4)_2\text{WO}_4$ solution. This

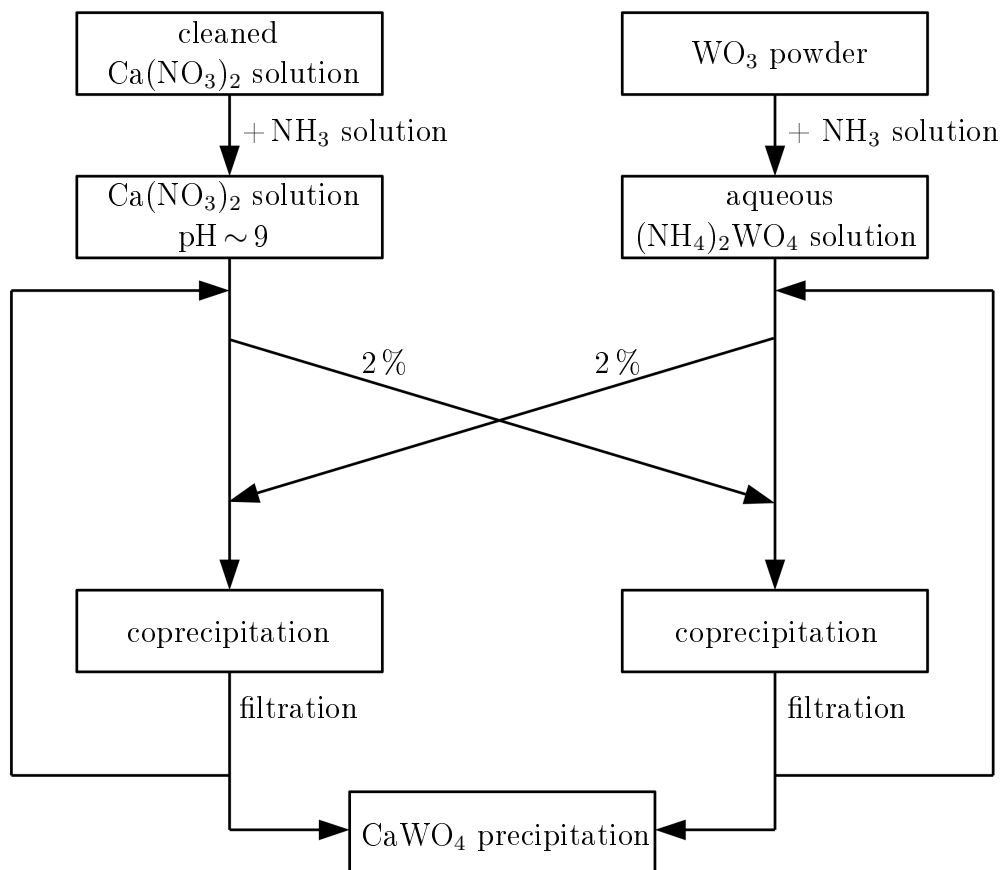


Figure 5.7.: Principle of the cross-cleaning procedure via coprecipitation as developed at TUM in the scope of the present work. 20 % NH_3 solution is added to the cleaned $\text{Ca}(\text{NO}_3)_2$ solution until slightly alkaline conditions ($\text{pH} \sim 9$) are reached. The WO_3 powder is dissolved in 10 % NH_3 solution. 2 % of each solution ($\text{Ca}(\text{NO}_3)_2$ and $(\text{NH}_4)_2\text{WO}_4$) are added to the respective other solution leading to a partial precipitation of CaWO_4 and possible coprecipitation of contaminating ions. After filtration of both components, the cross-cleaning is repeated before the actual CaWO_4 precipitation reaction is performed.

can be explained by the different conditions in the two solutions: in case of the $\text{Ca}(\text{NO}_3)_2$ solution the CaWO_4 molecules can potentially be surrounded by Ca^{2+} ions, while in case of the $(\text{NH}_4)_2\text{WO}_4$ solution by the larger WO_4^{2-} ions. This means that the structures that are formed in the $(\text{NH}_4)_2\text{WO}_4$ solution are larger than in the $\text{Ca}(\text{NO}_3)_2$ solution. Therefore, a filter with a nominal pore size of (10 - 16) μm (pore number 4) has to be used in case of the $\text{Ca}(\text{NO}_3)_2$ solution whereas for the $(\text{NH}_4)_2\text{WO}_4$ solution a filter with a nominal pore size of (16 - 40) μm (pore number 3) is – in principle – sufficient. However, in the near future also this filter will be exchanged so that only filters with pore number 4 are used during the whole procedure.

The coprecipitation method applied here has the advantages that not only the amount of metal impurities like lead or strontium can be reduced but that also mechanical impurities originating, e.g., from a potential abrasion of the magnetic stirrer are removed during filtration. Furthermore, it can be assured that no additional contaminations are

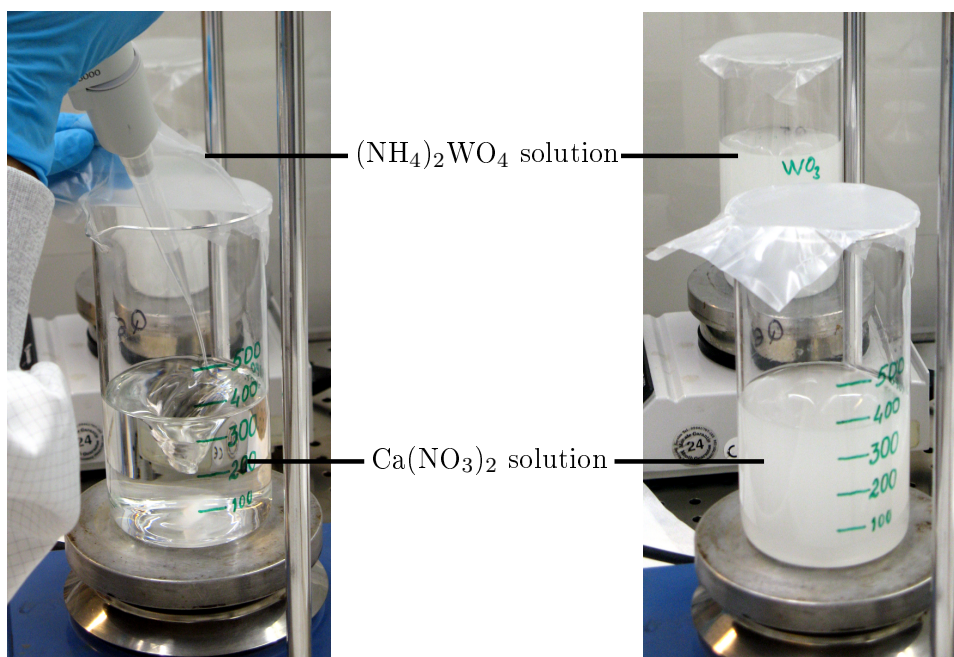


Figure 5.8.: Cross-cleaning of the two solutions of $(\text{NH}_4)_2\text{WO}_4$ (back) and $\text{Ca}(\text{NO}_3)_2$ (front). 2% of each solution are – under continuous stirring – added to the respective other solution (left picture). After a short time, the solutions turn milky indicating the precipitation of CaWO_4 (right picture). Together with the precipitate CaWO_4 , a certain amount of contaminations is expected to coprecipitate. In this way, a purification of both solutions can be achieved.

introduced since only the two solutions prepared for the main reaction and no new materials are involved. The only drawback of this method is a loss of $\sim 4\%$ of the final CaWO_4 powder.

The effect of the cross-cleaning procedure on the radiopurity of the $\text{Ca}(\text{NO}_3)_2$ and $(\text{NH}_4)_2\text{WO}_4$ solutions was investigated by means of ICP-MS. Table 5.7 shows the concentrations of the measured isotopes in the $\text{Ca}(\text{NO}_3)_2$ solution before and after the first pre-precipitation reaction and filtering. In case of a concentration value which is decreased (increased) by a factor > 2 after the coprecipitation, the row with the respective isotope is highlighted in green (red). For several isotopes such as ^{23}Na , ^{39}K , ^{53}Cr or ^{55}Mn , the contamination values are significantly reduced by a factor of up to 10 after the 2% pre-precipitation. For the majority of the isotopes no change is observed within the 30% uncertainty of the measurement. In the case of, e.g., ^{11}B or ^{208}Pb , the concentrations are increased after the cross-cleaning which hints towards an introduction of these impurities via the $(\text{NH}_4)_2\text{WO}_4$ solution. The added $(\text{NH}_4)_2\text{WO}_4$ solution is also the reason for the significant raise of the amount of ^{182}W which indicates, furthermore, that not all tungstate molecules have undergone the reaction to CaWO_4 . The apparently large contamination with ^{57}Fe is likely not due to this isotope itself, but instead originating from an interference with CaOH^+ ions which have the same mass number. In order to draw a final conclusion on the purification efficiency of the cross-cleaning procedure, additional information on contaminations within the $(\text{NH}_4)_2\text{WO}_4$ solution before and after

5. Improving the Radiopurity of CaWO_4 Crystals

sample	$\text{Ca}(\text{NO}_3)_2$ before	$\text{Ca}(\text{NO}_3)_2$ after	sample	$\text{Ca}(\text{NO}_3)_2$ before	$\text{Ca}(\text{NO}_3)_2$ after
isotope	concentration [ppb]		isotope	concentration [ppb]	
^7Li	0.95	0.9	^{95}Mo	0.72	0.5
^9Be	< 0.29	< 0.29	^{107}Ag	0.3	0.24
^{11}B	2.3	74	^{111}Cd	2.4	2.2
^{23}Na	510	41	^{115}In	0.096	< 0.065
^{24}Mg	470	370	^{118}Sn	0.8	-0.59
^{27}Al	60	-7.7	^{121}Sb	-0.75	-1
^{39}K	110	29	^{125}Te	< 2.9	< 2.9
^{45}Sc	6.8	6	^{133}Cs	0.55	0.63
^{47}Ti	6.5	8.4	^{137}Ba	32	20
^{51}V	0.16	< 0.10	^{139}La	0.2	< 0.052
^{53}Cr	6.8	0.25	^{140}Ce	-0.13	-0.061
^{55}Mn	2.8	0.88	^{146}Nd	0.28	< 0.24
^{57}Fe	$(62 \cdot 10^3)$	$(53 \cdot 10^3)$	^{182}W	75	1300
^{59}Co	19	16	^{193}Ir	< 0.082	< 0.082
^{60}Ni	120	120	^{195}Pt	< 0.18	< 0.18
^{63}Cu	6.1	7.1	^{197}Au	< 0.13	< 0.13
^{66}Zn	-4.4	-5.3	^{202}Hg	0.022	2
^{72}Ge	34	33	^{205}Tl	0.92	0.88
^{75}As	1.4	1.3	^{208}Pb	1.5	27
^{85}Rb	0.62	1.8	^{209}Bi	0.0085	-0.013
^{88}Sr	300	260	^{232}Th	< 0.059	< 0.059
^{89}Y	0.084	< 0.074	^{238}U	< 0.056	< 0.056

Table 5.7.: Results for the $\text{Ca}(\text{NO}_3)_2$ solution before and after the first pre-precipitation with 2% of the $(\text{NH}_4)_2\text{WO}_4$ solution, measured by means of ICP-MS at LNGS. Rows marked in green (red) indicate that the concentration of the respective isotope is decreased (increased) after the coprecipitation by a factor > 2 . The contamination level of ^{23}Na and ^{39}K , for example, is significantly reduced, whereas the concentration of the isotopes ^{11}B or ^{208}Pb is higher after the coprecipitation. The amount of ^{182}W is significantly raised as $(\text{NH}_4)_2\text{WO}_4$ was added during the cross-cleaning. The apparently high concentration of ^{57}Fe is probably due to an interference of CaOH^+ ions with the same mass number. Negative values mean that the signal of the subtracted blank solution is higher than the measured concentration. Uncertainties are 30% of the given values.

adding 2% of the $\text{Ca}(\text{NO}_3)_2$ solution is required. Therefore, table 5.8 lists the ICP-MS results for the pure 10% NH_3 solution used for dissolving WO_3 powder as well as for the $(\text{NH}_4)_2\text{WO}_4$ solution before and after the first and the second coprecipitation step. It has to be mentioned that the concentrations measured for the different $(\text{NH}_4)_2\text{WO}_4$ solutions are no absolute values. As the sample treatment for ICP-MS includes an acidification with HNO_3 solution, WO_3 or H_2WO_4 molecules precipitate. Only the remaining solution is analyzed and impurities that might still be present in the precipitates are, therefore, neglected. Still, the resulting concentrations can be compared to each other

5.3. Chemical Purification of the Powders and Trace Impurity Analysis

sample isotope	10 % NH ₃	(NH ₄) ₂ WO ₄ before	(NH ₄) ₂ WO ₄ after first	(NH ₄) ₂ WO ₄ after second
	concentration [ppb]			
⁷ Li	-0.34	2.7	-0.37	4.1
⁹ Be	< 0.84	< 8.5	< 8.5	< 8.5
¹¹ B	6.6	90	100	86
²³ Na	-26	590	120	130
²⁴ Mg	8.9	140	130	360
²⁷ Al	36	540	640	660
³⁹ K	67	-2 100	-450	12
⁴³ Ca	300	4 100	2 100	2 700
⁴⁵ Sc	-0.28	-0.37	-2	0.72
⁴⁷ Ti	9.8	-16	-19	160
⁵¹ V	0.29	320	230	140
⁵³ Cr	-1.2	-6.6	6.6	13
⁵⁵ Mn	0.91	19	4.4	4.1
⁵⁷ Fe	95	-3 900	-2 200	-2 000
⁵⁹ Co	< 0.22	< 2.2	< 2.2	< 2.2
⁶⁰ Ni	1.2	13	12	14
⁶³ Cu	0.46	30	31	21
⁶⁶ Zn	0.96	730	21	24
⁷² Ge	-0.67	-8.4	-5.9	-16
⁷⁵ As	< 2	33	25	23
⁸⁵ Rb	< 0.021	17	16	15
⁸⁸ Sr	0.12	24	5.3	4.5
⁸⁹ Y	< 0.17	< 1.8	< 1.8	< 1.8
⁹⁵ Mo	< 1	180	140	130
¹⁰⁷ Ag	< 0.086	< 3.2	< 3.2	6
¹¹¹ Cd	< 1.7	< 17	< 17	< 17
¹¹⁵ In	< 0.17	6.4	2.4	2.3
¹¹⁸ Sn	0.33	22	-0.95	5.7
¹²¹ Sb	< 0.62	< 6.2	< 6.2	< 6.2
¹²⁵ Te	< 7.7	< 77	< 77	< 77
¹³³ Cs	< 0.19	< 1.9	< 1.9	< 1.9
¹³⁷ Ba	< 1.6	< 15	< 15	< 15
¹³⁹ La	< 0.14	< 1.5	< 1.5	< 1.5
¹⁴⁰ Ce	-0.072	-0.520	-0.310	-3.000
¹⁴⁶ Nd	< 0.67	< 6.8	< 6.8	< 6.8
¹⁹³ Ir	< 0.2	< 2.1	< 2.1	< 2.1
¹⁹⁵ Pt	< 0.44	< 4.5	< 4.5	< 4.5
¹⁹⁷ Au	-0.16	24	23	11
²⁰² Hg	< 0.410	(14 · 10 ³)	(13 · 10 ³)	(9.5 · 10 ³)
²⁰⁵ Tl	0.59	3.3	2.3	-0.23
²⁰⁸ Pb	0.12	2.3	0.31	-0.16
²⁰⁹ Bi	-0.063	< 1.6	< 1.6	< 1.6
²³² Th	< 0.14	(4)	(3.2)	(1.7)
²³⁸ U	< 0.13	< 1.4	< 1.4	< 1.4

Table 5.8.: 10 % NH₃ solution as well as WO₃ dissolved in this solution ((NH₄)₂WO₄) before and after a first and second pre-precipitation with 2 % of the Ca(NO₃)₂ solution measured by means of ICP-MS at LNGS. As the sample treatment includes an acidification, WO₃ or H₂WO₄ molecules precipitate and the remaining solution is analyzed. Therefore, the values given for the three (NH₄)₂WO₄ solutions can be compared to each other but are no absolute concentrations. Rows marked in green (red) indicate that the concentration of the respective isotope is decreased (increased) by a factor > 2 after the second coprecipitation compared to the ((NH₄)₂WO₄) solution before the cross-cleaning. In case of several isotopes, e.g., ⁸⁸Sr or ²⁰⁸Pb the contamination level inserted by WO₃ is reduced after the two coprecipitation steps. The apparently high contamination values of ²⁰²Hg and ²³²Th are probably due to an interference of ¹⁸⁶W¹⁶O and ¹⁸⁴W¹⁶O₃ molecules, respectively, with the same mass number. Negative values mean that the signal of the subtracted blank solution is higher than the measured concentration. Uncertainties are 30 % of the given values.

in order to investigate the general trend of the impurities.

It can clearly be observed that the WO_3 powder introduces many additional impurities to the NH_3 solution. The concentrations of many isotopes such as ^{23}Na , ^{24}Mg , ^{27}Al , ^{88}Sr and ^{208}Pb are increased in the $(\text{NH}_4)_2\text{WO}_4$ solution before coprecipitation by at least a factor of 10 compared to the pure NH_3 solution. As in the case of the $\text{Ca}(\text{NO}_3)_2$ solution, several contaminations, e.g., with ^{23}Na , ^{66}Zn , ^{88}Sr , or ^{208}Pb are significantly reduced during the cross-cleaning (marked in green in table 5.8). A slight increase can only be observed for a few isotopes (highlighted in red), potentially introduced by the $\text{Ca}(\text{NO}_3)_2$ solution. The apparently high contamination values of ^{202}Hg and ^{232}Th are probably due to an interference of $^{186}\text{W}^{16}\text{O}$ and $^{184}\text{W}^{16}\text{O}_3$ molecules, respectively, with the same mass number.

In summary, the cross-cleaning works well for a number of isotopes, including the main isotopes of interest ^{23}Na , ^{39}K , ^{88}Sr and ^{208}Pb . The purification efficiency appears to be different for the various isotopes as well as for the respective solution ($\text{Ca}(\text{NO}_3)_2$ and $(\text{NH}_4)_2\text{WO}_4$), i.e. coprecipitation of a certain isotope might work better in one solution than in the other. Additional substances which could be used for coprecipitation are currently investigated in collaboration with Vasily Morgalyuk [149].

5.3.4. Washing of the CaWO_4 Powder

After the CaCO_3 powder, which was cleaned in version 1 of the TOPO extraction (compare section 5.3.2), had been further processed to CaWO_4 powder, a high sodium contamination ($\sim 0.5\%$ in the CaCO_3 powder) likely originating from the reaction with the Na_2CO_3 solution was discovered. An additional potassium contamination could not be excluded since this element has the same chemical properties as sodium. Furthermore, it can be seen in table 5.1 that already in this batch of the raw material WO_3 a comparably high activity of the isotope ^{40}K is present. As it is not clear how exactly these contaminations behave in the Czochralski-furnace during crystal growth and how they would influence the radiopurity of detector crystals, another purification procedure applicable to the CaWO_4 powder was developed at TUM. It is based on the fact that CaWO_4 powder itself is insoluble in aqueous, alkaline solutions whereas contaminations such as sodium and potassium are well solvable therein. The individual steps of this so-called washing procedure are shown in figure 5.9 (a).

The CaWO_4 powder obtained via the solid state or the precipitation reaction is mixed with suprapure 5% NH_3 solution and stirred for about 30 min. During this time, solvable impurities captured by CaWO_4 molecules are expected to escape the powder crystals and to be dissolved in the alkaline solution. After stirring has been stopped, the CaWO_4 powder is left for sedimentation (30 min). Afterwards, the majority of the NH_3 solution can be decanted and only a small remnant remains in the CaWO_4 powder (see figure 5.9 (b)). Within this first step, the removed NH_3 solution has turned milky which indicates that substances have been transferred from the CaWO_4 powder into the solution. The washing step with the NH_3 solution is repeated twice, in the last cycle with ultrapure NH_3 . After decantation, this NH_3 solution is much more transparent than in the first step which could imply that the amount of impurities is already reduced. In order to remove remnants of the NH_3 solution containing dissolved impurities, water is

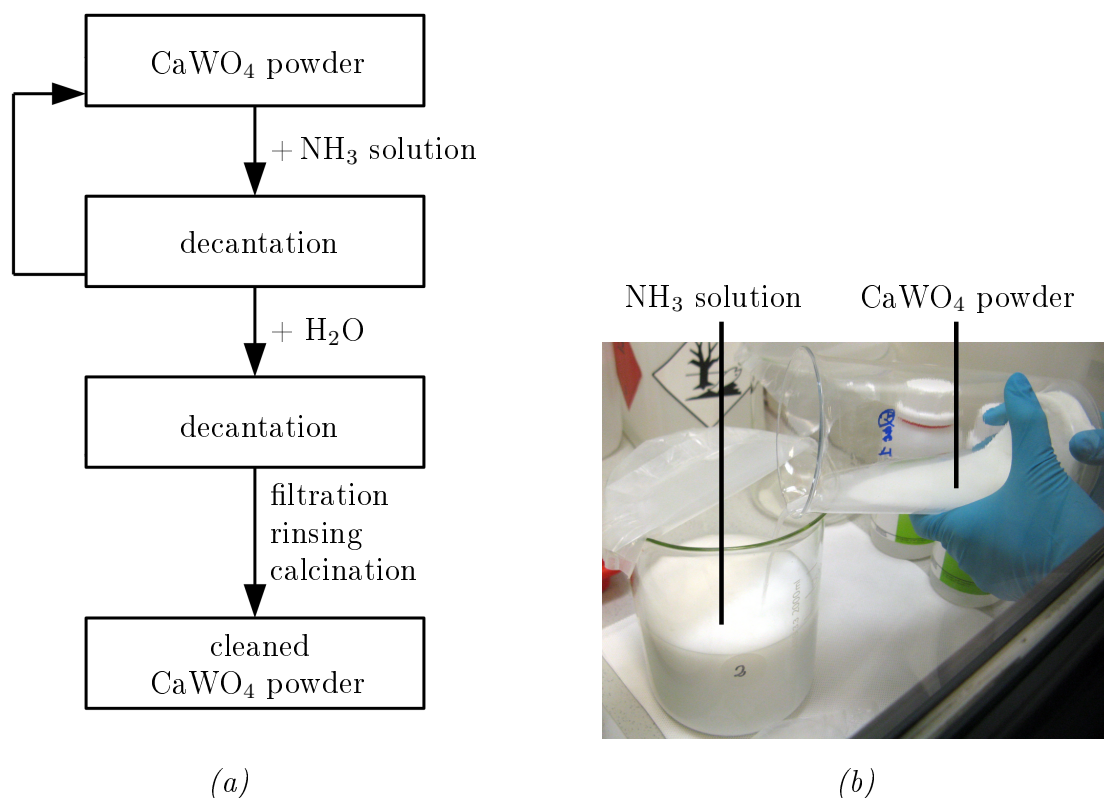


Figure 5.9.: (a) Principle of the CaWO_4 washing method developed at TUM. The goal is to remove water-soluble contaminations such as sodium and potassium from the CaWO_4 powder. In different cycles, the powder is mixed first with a NH_3 solution which is decanted after the CaWO_4 powder has sedimented again. A picture taken during decantation is shown in (b). The initially transparent NH_3 solution has turned milky indicating that it has washed out substances from the CaWO_4 powder. In order to remove NH_3 remnants which contain the dissolved contaminations, the washing is repeated with water before the CaWO_4 powder is filtrated, rinsed, and calcinated (a).

used as washing agent in the second part of the process. After mixing and decanting once, the CaWO_4 powder is filled into a suction filter and rinsed with more suprapure H_2O and even ultrapure water in the last step⁵.

For calcination (see section 3.2), the powder is dried in a furnace at different temperature stages of $\sim 90^\circ\text{C}$ and $\sim 210^\circ\text{C}$. If an excess of $(\text{NH}_4)_2\text{WO}_4$ is present (e.g., when the initial weight of WO_3 did not correspond to the exact stoichiometry), the oxidation number of tungsten is reduced from VI to IV under the creation of the brownish substance $\text{WO}(\text{OH})_2$ during drying. Therefore, the resulting brownish uppermost thin layer is removed before storing the powder for further usage.

Table 5.9 summarizes the results of HPGc spectroscopy at LSC and shows how the

⁵At present, ultrapure NH_3 solution and water are only used in the respective last washing step for financial reasons (ultra quality is a factor of ~ 5 more expensive than supra-quality). A further improvement concerning radiopurity can potentially be achieved when only ultrapure materials are involved.

5. Improving the Radiopurity of CaWO_4 Crystals

sample		CaWO_4 (1)	CaWO_4 (1) cleaned	CaWO_4 (3) cleaned
origin	isotope	activity [mBq/kg]		
^{232}Th chain	^{228}Ra	< 4.5	< 5.6	2.1 ± 0.7
	^{228}Th	3.0 ± 0.9	2.3 ± 0.9	2.3 ± 0.6
^{238}U chain	$^{234\text{m}}\text{Pa}$	< 55	< 60	59 ± 14
	^{226}Ra	4.7 ± 0.7	4.8 ± 0.7	1.8 ± 0.4
^{235}U chain	^{235}U	< 3	< 3.3	2.7 ± 0.7
	^{227}Ac	< 4.8	< 5.4	< 3.4
	^{227}Th	< 14	< 16	< 9.0
	^{223}Ra	< 7.9	< 9.4	< 5.5
	^{219}Rn	< 8	< 8.9	< 5.7
	^{211}Pb	< 15	< 18	< 10
	^{211}Bi	< 8.3	< 7.5	< 5.8
other	^{137}Cs	< 1.1	< 1	< 0.7
	^{60}Co	< 0.8	< 0.7	< 0.4
	^{40}K	109 ± 10	50 ± 8	22 ± 4

Table 5.9.: CaWO_4 samples measured via HPGe spectroscopy at LSC before and after the application of the washing procedure with NH_3 solution and water. Hereby, the sample CaWO_4 (1) corresponds to the powder already listed in table 5.1. After washing, this powder sample was measured again (CaWO_4 (1) cleaned). The ^{40}K activity is clearly reduced by a factor of ~ 2 whereas the other values stay the same within their uncertainties. Another CaWO_4 sample was measured after applying an improved washing procedure (CaWO_4 (3) cleaned), however, in this case no information on the activities before washing are available. The further reduced potassium activity could result from a cleaner starting batch or from the improved procedure applied. Errors are given with a confidence level (C.L.) of 68 %, limits with 95 % C.L.

measured activities change after the washing procedure has been applied. Hereby, the activities listed for sample CaWO_4 (1) are those already shown in table 5.1. This sample was measured again after having been washed with (only) suprapure NH_3 solution and water (CaWO_4 (1) cleaned). The ^{40}K activity is clearly decreased by a factor of ~ 2 from (109 ± 10) mBq/kg to (50 ± 8) mBq/kg whereas the contaminations measured for the other isotopes are – within their uncertainty – not influenced. An additional CaWO_4 sample was measured after an improved washing procedure has been applied under the usage of ultrapure water in the last cycle (CaWO_4 (3) cleaned). As in this case no information on the activities before washing are available, it is not clear if the further reduced potassium activity of (22 ± 4) mBq/kg as well as a lower value of (1.8 ± 0.4) mBq/kg observed for ^{226}Ra (compared to (4.8 ± 0.7) mBq/kg) results from the improved washing procedure or from a cleaner starting batch of raw powders. However, using ultrapure materials in the last cycles can only be advantageous for the final purity and is, therefore, implemented in the optimized procedure.

As explained before, ICP-MS measurements are usually based on dissolving the samples

of interest. CaWO_4 powder and crystal samples are, however, hardly solvable (compare section 3.1). At the chemistry laboratory of LNGS, a rinsing method was developed which does not deliver absolute contamination values, however, allows a comparison of different CaWO_4 samples when the applied procedure is exactly the same. In this method, the CaWO_4 powder is leached with a solution of 1 % HNO_3 which reacts with a small part of the powder and dissolves impurities contained in the sample. After ten minutes of mixing, the samples are centrifuged to remove the remaining powder which cannot be introduced into the instrument. The leaching solution containing a certain amount of impurities that were rinsed out of the CaWO_4 powder is recovered and analyzed by means of ICP-MS. Although no absolute concentration values can be measured, a comparison between the rinsing solutions of different CaWO_4 powder samples is possible⁶. The rinsing method was performed for CaWO_4 powder (denoted as CaWO_4 (4); this powder was produced from CaCO_3 powder after the extraction purification of version 1, see figure 5.1 (a)) before and after the washing procedure shown in figure 5.9. The results of the rinsing solutions are shown in table 5.10. For most isotopes, the contaminations extracted from the CaWO_4 sample after washing are significantly decreased (highlighted in green) hinting towards a successful cleaning of the CaWO_4 powder. The largest effect is observable for isotopes such as ^{23}Na , ^{24}Mg , ^{39}K , ^{60}Ni or ^{89}Y . The reduction of ^{39}K confirms, hereby, the decreased potassium contamination listed in table 5.9. For other isotopes no change of the measured concentrations within the 30 % uncertainties or even an increased value after cleaning as in the cases of ^{59}Co , ^{72}Ge , or ^{137}Ba (marked in red) can be found.

The other way around, also the NH_3 solution can be measured before and after having been used for one washing cycle of the CaWO_4 powder. The results of the corresponding ICP-MS measurement (at LNGS) are listed in table 5.11. A significant increase (by a factor > 2) of the concentration after washing is highlighted in red and can be observed for many isotopes. Especially the substances of interest, namely sodium and potassium in the form of ^{23}Na and ^{39}K , respectively, are accumulated in the solution during the washing procedure. Also a significant amount of isotopes like ^{24}Mg , ^{27}Al , ^{60}Ni or ^{63}Cu seem to have moved from the CaWO_4 powder to the NH_3 solution and even for ^{88}Sr a slight increase is visible. The results are consistent with the conclusion drawn from table 5.10. The concentration of ^{43}Ca in the NH_3 solution is naturally raised as the solution has been in contact with CaWO_4 powder.

In summary, the different purification steps including solvent extraction, coprecipitation, and washing with NH_3 solution and water were successfully applied to the raw materials. Their effect on the radiopurity was intensely studied in various HPGe, ICP-MS and LA-ICP-MS measurements. In all cases, a significant improvement is observable.

⁶The leaching and centrifuging steps are repeated with fresh 1 % HNO_3 solution and the recovered solutions after the second rinsing were also analyzed by means of ICP-MS. It was observed that all values measured after the second rinsing are significantly reduced compared to the first one. This implies that the dominant fraction of impurities is rinsed out of the CaWO_4 powder already in the first step.

5. Improving the Radiopurity of CaWO_4 Crystals

sample	CaWO_4 (4) before	CaWO_4 (4) after	sample	CaWO_4 (4) before	CaWO_4 (4) after
isotope	concentration [ppb]		isotope	concentration [ppb]	
^7Li	1.3	0.45	^{75}As	10	1.7
^9Be	0.31	0.021	^{88}Sr	2.6	0.89
^{23}Na	$58 \cdot 10^3$	980	^{89}Y	0.38	0.0046
^{24}Mg	770	120	^{111}Cd	0.097	0.051
^{27}Al	920	260	^{115}In	0.036	0.066
^{39}K	190	17	^{118}Sn	1.4	0.86
^{45}Sc	0.045	0.029	^{121}Sb	0.059	0.088
^{53}Cr	2.2	2.8	^{137}Ba	7.8	24
^{55}Mn	0.71	1.2	^{139}La	0.0097	0.0054
^{57}Fe	(120)	(89)	^{202}Hg	(250)	(39)
^{59}Co	0.19	0.59	^{205}Tl	0.01	-0.00076
^{60}Ni	12	1.4	^{208}Pb	-0.011	-0.046
^{63}Cu	1.8	2	^{209}Bi	0.0018	0.00045
^{66}Zn	-0.54	-2.8	^{232}Th	(0.05)	(< 0.0031)
^{72}Ge	0.0016	0.011	^{238}U	0.15	0.035

Table 5.10.: CaWO_4 powder before and after the application of the washing procedure with NH_3 solution and water (compare figure 5.9) measured via the ICP-MS rinsing method at LNGS (see text). The given concentrations are no absolute values and should only be used to compare samples where exactly the same procedure has been applied. For many isotopes, the contaminations extracted from the CaWO_4 sample after washing are significantly decreased by at least a factor of 2 (green) hinting towards a successful cleaning of the CaWO_4 powder. Rows highlighted in red indicate a slightly increased concentration (by a factor > 2) of, e.g., ^{137}Ba . Negative values mean that the signal of the subtracted blank solution is higher than the measured concentration. For ^{57}Fe , ^{202}Hg , and ^{232}Th an interference from molecules with the same mass (CaOH^- , $^{186}\text{W}^{16}\text{O}$, and $^{184}\text{W}^{16}\text{O}_3$, respectively) could be present. The values have an uncertainty of 30%.

5.3.5. Combination of all Purification Steps

In 2016, a CaWO_4 powder batch (denoted as CaWO_4 (5)) with a mass of ~ 550 g was produced in several cycles including all the different purification steps described in sections 5.3.2 (version 2), 5.3.3 and 5.3.4. By means of diffractometer measurements of several samples, the end product was confirmed to be 100% CaWO_4 powder (with an error of 1%). A small sample of this CaWO_4 powder was investigated with ICP-MS at LNGS applying the same rinsing method as the one described concerning the results in table 5.10. This makes a comparison of the concentrations listed in tables 5.12 and 5.10 possible. Concentration values which are decreased (increased) by a factor > 2 with respect to table 5.10 are highlighted in green (red). A significantly reduced contamination level is observed for the majority of the isotopes. Especially concerning the lighter isotopes ^{23}Na , ^{24}Mg , ^{27}Al , and ^{39}K , the powder appears to be much more radiopure. ^{137}Ba , which was increased after the washing procedure applied to the powder of table 5.10, has a strongly reduced concentration in table 5.12. This indicates a successful coprecipitation of barium which is reasonable due to the chemical similarity of barium to the calcium bound in the precipitate CaWO_4 . As the element radium is found in the same

sample	NH ₃ before	NH ₃ after	sample	NH ₃ before	NH ₃ after
isotope	concentration [ppb]		isotope	concentration [ppb]	
⁷ Li	< 1.5	1.8	⁷⁵ As	< 1.3	< 1.3
⁹ Be	< 0.45	< 0.45	⁸⁸ Sr	0.54	1.2
²³ Na	67	540	⁸⁹ Y	< 0.12	< 0.12
²⁴ Mg	7.9	73	¹¹¹ Cd	< 1.1	< 1.1
²⁷ Al	7.6	1200	¹¹⁵ In	0.13	< 0.1
³⁹ K	< 300	570	¹¹⁸ Sn	< 3	< 3
⁴³ Ca	250	43 · 10 ³	¹²¹ Sb	0.51	0.64
⁴⁵ Sc	< 0.5	< 0.5	¹³⁷ Ba	< 0.93	1.2
⁵³ Cr	0.9	2.2	¹³⁹ La	0.1	< 0.1
⁵⁵ Mn	< 1	< 1	¹⁴⁰ Ce	< 3	< 3
⁵⁷ Fe	< 100	140	²⁰² Hg	< 0.29	(0.61)
⁵⁹ Co	< 0.13	1.8	²⁰⁵ Tl	1.2	0.85
⁶⁰ Ni	0.62	8.3	²⁰⁸ Pb	0.24	0.38
⁶³ Cu	0.57	94	²³² Th	< 0.1	< 0.1
⁶⁶ Zn	1.1	9.5	²³⁸ U	< 0.098	< 0.098
⁷² Ge	0.16	0.43			

Table 5.11.: NH₃ solutions measured by means of ICP-MS at LNGS before and after having been used for one washing cycle of the CaWO₄ powder. The concentrations of many isotopes – in particular also of ²³Na and ³⁹K – are significantly increased by a factor > 2 after the washing procedure (red rows). This means impurities have been removed from the CaWO₄ powder and transferred to the NH₃ solution. The measured contamination of ²⁰²Hg can originate from an interference of ¹⁸⁶W¹⁶O molecules. Uncertainties are 30 % of the given values.

main group of the periodic table, a reduction of barium hints also towards a decreased contamination with radium isotopes.

Other isotopes that were also aimed to be removed with coprecipitation (⁸⁸Sr, ²⁰⁸Pb) seem to have higher values in this CaWO₄ sample. However, it is shown in tables 5.7 and 5.8 that the purification via coprecipitation appears to work also for these isotopes. Thus, it appears that – due to a different structure of the CaWO₄ powder – a higher amount of certain isotopes can be leached out of the powder. For the values given for ⁵⁷Fe, ²⁰²Hg and ²³²Th an interference from molecules with the same molar mass CaOH⁻, ¹⁸⁶W¹⁶O and ¹⁸⁴W¹⁶O₃, respectively, cannot be excluded.

The complete CaWO₄ batch of ~ 550 g produced according to the procedures explained in the previous sections was also sent to LSC for a HPGe measurement (see table 5.13). Except for an activity of (39 ± 3) mBq/kg in case of ⁴⁰K, all contaminations are below the sensitivity of the germanium detector making this CaWO₄ powder sample (see picture in figure 5.10) to the radiopurest one ever produced at TUM and measured with HPGe spectroscopy. Reduction factors of at least 2-3 could be achieved for the isotopes ²²⁸Th, ²³⁸U (^{234m}Pa), ²³⁵U and ²²⁶Ra compared to tables 5.1 and 5.9. Motivated by this

sample	CaWO_4 (5)	sample	CaWO_4 (5)
isotope	concentration [ppb]	isotope	concentration [ppb]
^7Li	0.12	^{75}As	0.8
^9Be	< 0.0099	^{88}Sr	6.6
^{23}Na	5	^{89}Y	< 0.0024
^{24}Mg	15	^{111}Cd	0.036
^{27}Al	0.49	^{115}In	0.003
^{39}K	1.1	^{118}Sn	0.038
^{45}Sc	0.15	^{121}Sb	0.019
^{53}Cr	0.34	^{137}Ba	0.12
^{55}Mn	0.019	^{139}La	< 0.0017
^{57}Fe	(1600)	^{202}Hg	(150)
^{59}Co	0.53	^{205}Tl	0.0097
^{60}Ni	3.2	^{208}Pb	0.52
^{63}Cu	0.083	^{209}Bi	0.0037
^{66}Zn	0.22	^{232}Th	(0.01)
^{72}Ge	0.054	^{238}U	< 0.0018

Table 5.12.: ICP-MS rinsing method applied at LNGS to a CaWO_4 powder sample produced via precipitation including all purification steps described in sections 5.3.2 (version 2), 5.3.3, and 5.3.4. Concentration values which are decreased (increased) by a factor > 2 compared to table 5.10 are highlighted in green (red). A reduced contamination level is observed for the majority of the isotopes suggesting a better total radiopurity of the powder. For the values given for ^{57}Fe , ^{202}Hg and ^{232}Th an interference from molecules with the same mass (CaOH^- , $^{186}\text{W}^{16}\text{O}$ and $^{184}\text{W}^{16}\text{O}_3$, respectively) could be present. Uncertainties are 30 % of the given values.

result, the purification and production of CaWO_4 powder via the described methods was continued in 2017. With the produced amount of in total ~ 1500 g of CaWO_4 powder, a crystal will be grown in the near future. An operation as cryogenic detector will enable an even more accurate investigation of the radiopurity.

5.4. Segregation of Impurities during Crystal Growth

Apart from the purification of the raw materials explained in section 5.3, crystal growth itself is a cleaning process as not all atoms in the melt are built into the crystal lattice. This segregation of impurities is based on their different solubilities in the solid and liquid phase. The principle of segregation as well as a simulation for a future measurement are described in this section.

sample		CaWO ₄ (5)
origin	isotope	activity [mBq/kg]
232Th chain	228Ra	< 1.4
	228Th	< 0.71
238U chain	234mPa	< 17
	226Ra	< 0.9
235U chain	235U	< 0.78
	227Ac	< 1.1
	227Th	< 2.9
	223Ra	< 1.7
	219Rn	< 2.0
	211Pb	< 4.0
	211Bi	< 2.2
other	137Cs	< 0.50
	60Co	< 0.09
	40K	39 ± 3

Table 5.13.: HPGe measurement at LSC of a CaWO₄ powder sample produced via the precipitation reaction with application of all purification steps described in sections 5.3.2 (version 2), 5.3.3 and 5.3.4. Except for a measured value of ⁴⁰K, all contaminations are below the sensitivity of the germanium detector. Errors are given with a confidence level (C.L.) of 68 %, limits with 95 % C.L.



Figure 5.10.: CaWO₄ powder produced via the precipitation reaction including all purification steps described in sections 5.3.2 (version 2), 5.3.3, and 5.3.4. The resulting product is a fine and homogeneously white powder.

5.4.1. Principle of Segregation

As explained in detail in [152], the segregation coefficient or effective partition coefficient in equilibrium conditions k is defined as

$$k = \frac{c_s}{c_l} \quad (5.7)$$

with $c_{s/l} = \frac{M_{\text{cont}}^{s/l}}{M_{s/l}}$ being the concentration of a contamination with mass $M_{\text{cont}}^{s/l}$ in the solid/liquid phase (crystal/melt) with mass $M_{s/l}$, respectively. In addition, as it takes a finite time for rejected impurities to diffuse back into the melt, the effective partition coefficient depends on the growth speed, the diffusion coefficient of the impurity species as well as on the thickness of the so-called diffusion boundary layer. This diffusion boundary layer is a liquid layer below the crystallization interface where the impurity concentration is increased for $k < 1$. For the case considered here, a constant growth speed and constant diffusion conditions as well as a constant k are assumed.

During crystal growth, the mass of a certain contamination is transferred from the melt

into the crystal when a conservative system without any material exchange with the surroundings is assumed. This means, the concentration of a contamination in the crystal changes continuously with the crystallized mass fraction $g = M_s/M$ with M being the initial (total) mass of the melt:

$$c_s = \frac{dM_{\text{cont}}^s}{dM_s} = \frac{dM_{\text{cont}}^s}{dg} \cdot \frac{1}{M} = -\frac{dM_{\text{cont}}^l}{dg} \cdot \frac{1}{M} \quad (5.8)$$

At the same time, also

$$c_s = c_l \cdot k = \frac{M_{\text{cont}}^l}{M - M_s} \cdot k = \frac{M_{\text{cont}}^l}{M(1-g)} \cdot k \quad (5.9)$$

is valid. The two equations 5.8 and 5.9 are equalized and integrated according to [152]:

$$\int_{M_{\text{cont},0}^l}^{M_{\text{cont}}^l} \frac{dM_{\text{cont}}^l}{M_{\text{cont}}^l} = \int_0^g -\frac{k}{1-g} dg \quad (5.10)$$

Relations 5.9 and 5.10 together lead then to the following expressions:

$$\frac{c_s}{c_0} = k \cdot (1-g)^{k-1} \quad (5.11)$$

$$\frac{c_l}{c_0} = (1-g)^{k-1} \quad (5.12)$$

Hereby, c_0 denotes the initial concentration of the contamination in the melt. In figure 5.11 (a), the relative concentration in the crystal $\frac{c_s}{c_0}$ is plotted as a function of the crystallized mass fraction g for different segregation coefficients k . When $k = 1$ (black curve), the relative concentration is independent of g and stays constant. In the case of $k > 1$ (red lines), impurities are rather built into the crystal lattice than remaining in the melt. This implies that, within the crystal, a high concentration can be found in the first part and only after a certain g (~ 0.33 for $k = 5$ or ~ 0.5 for $k = 2$) the crystallized material becomes cleaner than the initial concentration. A segregation coefficient smaller than 1 (green curves), on the other hand, means that the probability for an impurity to stay in the melt is higher than to be included in the crystal. The relative contamination concentration $\frac{c_s}{c_0}$ is lowest in the first part of a crystal and increases slowly during crystal growth due to the rising impurity level in the melt. After a certain mass fraction g has been exceeded, the concentration in the crystal is higher than the initial concentration. This value of g depends again on the segregation coefficient – a relatively large k of 0.5 leads to $\frac{c_s}{c_0} > 1$ for mass fractions above ~ 0.75 whereas for $k = 0.01$ this point is only reached when $g = 0.98$.

Analogously, the relative concentration in the melt (equation 5.12) is drawn in figure 5.11 (b). Also here, the concentration stays constant for $k = 1$ (black line) whereas it increases steadily starting from c_0 when the segregation coefficient is smaller than 1 (green lines). A decreasing contamination level of the melt is observed for cases where $k > 1$ (red curves) as impurities are preferably built into the crystal lattice there.

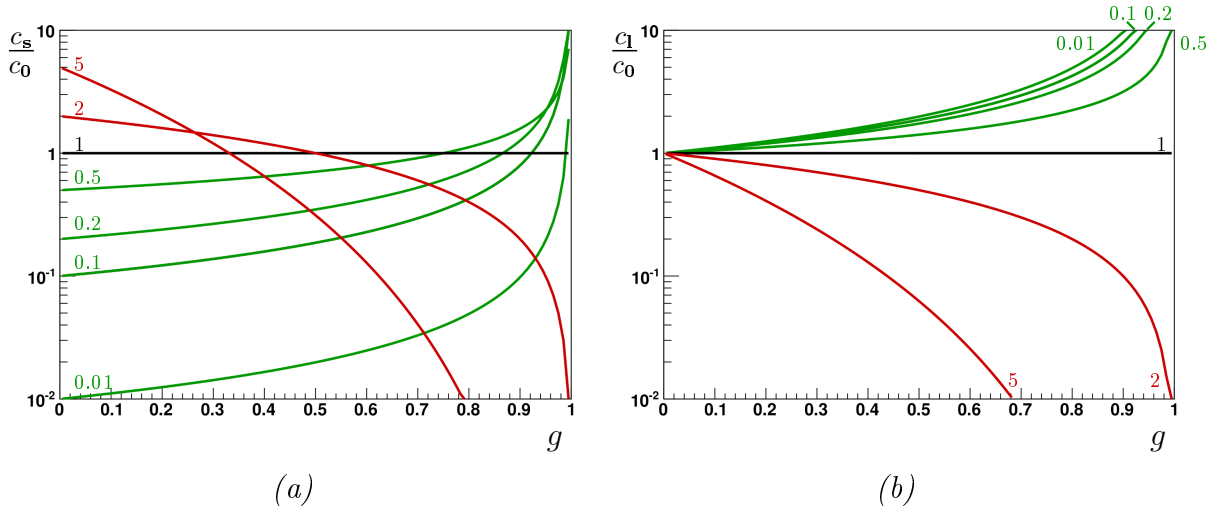


Figure 5.11.: Relative concentration of a contamination in the crystal $\frac{c_s}{c_0}$ (a) and in the melt $\frac{c_l}{c_0}$ (b) in dependence of the crystallized mass fraction g for various segregation coefficients k . If k equals 1 (black line) the concentrations in crystal and melt stay constant. In the case $k > 1$ (red lines) contaminations are preferentially built into the crystal lattice. This leads to a concentration in the melt which is declining with g throughout crystal growth (b). In the crystal, the concentration is high in the beginning before it follows the decreasing behaviour of the melt and is also reduced (a). For $k < 1$ (green lines) contaminations are accumulated in the melt leading to a strong segregation for small mass fractions. With increasing g , the concentration in the melt grows (b) resulting also in an increasing concentration in the crystal (a).

5.4.2. Segregation Measurements

An example for the segregation of ^{226}Ra during crystal growth is given in table 5.14. The purity of the WO_3 and CaCO_3 powders, of the resulting CaWO_4 powder as well as of a CaWO_4 crystal directly produced from this powder was investigated with HPGe spectroscopy at LNGS. In the CaCO_3 powder (in this case supplied by Alfa Aesar), a contamination with the isotope ^{226}Ra is present which is also transferred to the CaWO_4 powder. In the crystal grown from this powder, however, only an upper limit of 3.4 mBq/kg can be set meaning that the segregation coefficient for ^{226}Ra is $\lesssim 3.4/28 = 0.12$ (90 % CL) [83]. The segregation of impurities is not only observable in the direct comparison between powder and crystal, but can also be obtained from measurements of crystal ingots grown with subsequent growth numbers without removing the remaining melt in between. An example is plotted in figure 5.12 where four crystal samples of TUM13, TUM16, TUM20 and TUM22 were investigated with HPGe spectroscopy at LNGS [83]. For each crystal growth, the remaining melt of the preceding growth process was reused. Only after growth number 19 (red dashed line), the remaining melt was removed and the crucible was cleaned. TUM13 and TUM16 exhibit increasing values of the ^{228}Th (blue rectangle) and ^{226}Ra (green triangle) activities due to an increasing contamination within the remaining melt. In the crystals TUM20 and TUM22 grown after the cleaning, only upper limits with values below the previous activities were observed for the isotopes ^{228}Th and ^{226}Ra .

sample	WO_3 (powder)	CaCO_3 (powder)	CaWO_4 (powder)	CaWO_4 (crystal)
isotope	activity [mBq/kg]			
^{226}Ra	< 10	26 ± 6	28 ± 6	< 3.4

Table 5.14.: Example for the segregation of ^{226}Ra during CaWO_4 crystal growth. Samples of the raw materials WO_3 , CaCO_3 as well as of the CaWO_4 powder and the CaWO_4 crystal directly produced from these powders were measured with HPGe spectroscopy at LNGS. A contamination of ^{226}Ra with an activity of (26 ± 6) mBq/kg is found in the raw material CaCO_3 and transferred to the CaWO_4 powder. In the CaWO_4 crystal, however, the set upper limit is already a factor of ~ 8 below the measured value of the powders resulting in a segregation coefficient $\lesssim 3.4/28 = 0.12$ (90 % CL) [83].

An additional information, which radionuclides are rejected during crystal growth and accumulated in the melt can be obtained from a measurement of the residual melt. Also here, a clear indication for the segregation of radium and thorium isotopes with $k < 1$ can be found [120].

Reference [153] confirms the segregation of radium which can be explained by the relatively large ionic radius of Ra^{2+} precluding an accommodation of this ion at the site of calcium. Also uranium was found to be rejected by the crystal with a segregation coefficient of ~ 0.3 for ^{238}U [153]. As thorium has chemical properties comparable to those of uranium, it is expected to behave in a similar way. Lead, on the other hand, can form PbWO_4 molecules with the same structure as CaWO_4 which appears to prevent a segregation in this case. However, in total, a further improved radiopurity of the crystals can be achieved by (multiple) recrystallization. Re-melting an already grown crystal in a clean and empty crucible leads to a reduced concentration of contaminations in this melt compared to the melt this crystal was produced from. As k does not depend on c_0 , the same segregation is achieved when another crystal is grown from this melt resulting in an improved radiopurity. An improvement of the overall radiopurity of the CaWO_4 crystals by one order of magnitude was achieved by means of recrystallization in [153].

5.4.3. Feasibility Study for the Determination of Segregation Coefficients

As contamination concentrations in a CaWO_4 crystal ingot are expected to change with the crystallized mass fraction g , it should be possible to estimate the segregation coefficient k and – if not known – the initial activity A_0 of the melt via probing the radiopurity at different positions within the raw crystal. A possible approach is to cut the raw crystal into several slices of the same mass and to operate each of these slices as cryogenic detector in order to determine the respective contamination level of certain (radioactive) impurities. In a cryogenic measurement, the quantity of interest is, thereby, not the concentration of an impurity but the number of its decays $N = A_c \cdot m_c \cdot t_{\text{meas}}$ occurring in a detector crystal of mass m_c with an activity A_c [mBq/kg] in a certain measurement time t_{meas} . The relative concentration $\frac{c_c}{c_0}$ in the detector crystal is equal to $\frac{A_c}{A_0}$, the fraction of the activity within the detector crystal A_c and of the initial activity A_0 . Therefore, the

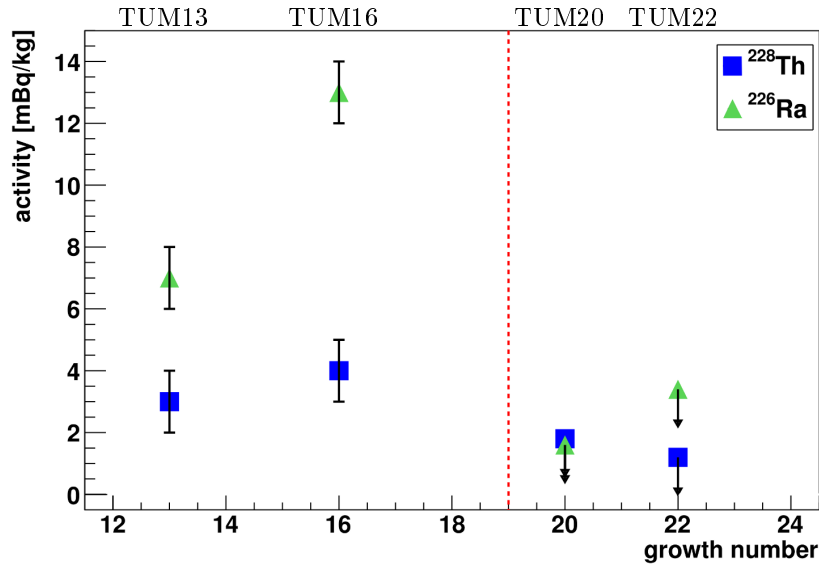


Figure 5.12.: Correlation between growth number and contamination level. Samples of the crystal ingots TUM13, TUM16, TUM20 and TUM22 were measured with HPGe spectroscopy at LNGS. For the growth of each of these crystal ingots, the remaining melt was reused. Only after growth number 19 (red dashed line), the remaining melt was removed and the crucible was cleaned. TUM13 and TUM16 exhibit increasing activity values of the isotopes ^{228}Th (blue rectangle) and ^{226}Ra (green triangle). TUM20 and TUM22 grown after the cleaning of the crucible do not have a measurable contamination with ^{228}Th and ^{226}Ra which indicates that these two isotopes have a segregation coefficient $k < 1$ [83].

number of counts can be rewritten as

$$N = \frac{c_s}{c_0} \cdot A_0 \cdot m_c \cdot t_{\text{meas}} \quad (5.13)$$

The observed number of counts can be plotted for each detector crystal, i.e. as a function of the crystallized mass fraction g , and fitted by the combination of equations 5.11 and 5.13.

In order to investigate which values of the segregation coefficient can be determined in dependence of the initial activity, a simulation was developed within the frame of the present work in collaboration with Andreas Zöller [154]. Thereby, as indicated in figure 5.13, it is assumed for reasons of simplicity that the crystallization at the crystal/melt interface happens in slices with an infinitely small thickness. Effects such as a strongly convex crystallization border as described in appendix B.2 are neglected. Furthermore, certain standard conditions are assumed in the following if not noted differently:

- The maximal crystallized mass fraction g_{max} is set to 0.5. For a typical initial mass of the melt of 1.5 kg, this is equivalent to a crystal ingot with a mass of 750 g. This mass fraction of 50% was found to be a realistic value for the amount of material that can be crystallized from the melt during one growth process (compare appendix B.2).

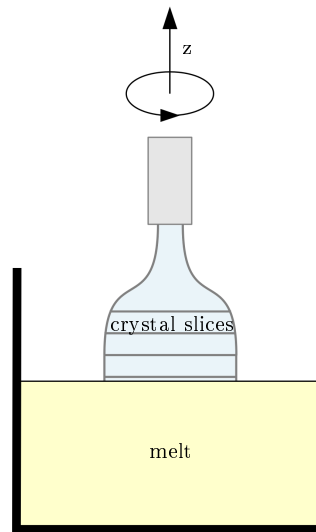


Figure 5.13.: For the estimation of the segregation coefficient, a crystallization in slices of an infinitely small thickness is assumed at the crystal/melt interface due to reasons of simplicity.

- Three crystal slices of the same mass are cut from the raw crystal, i.e. the number of detector crystals $n_{\text{crystal}} = 3$. In case of a 750 g crystal ingot, this corresponds to a mass of 250 g for each detector crystal.
- A data taking time (here also called live time, see chapter 6) of four weeks is assumed. Including dead times due to refilling of the cryostat, this translates to a total measuring time of (5-6) weeks.

Figure 5.14 visualizes the different steps of a simulation. Assuming certain values for k and A_0 (here 0.5 and 10 mBq/kg, respectively), the resulting relative concentration is shown in dependence of g as black line in (a) (analogously to figure 5.11). The mass fraction is divided into three equal parts corresponding to the three detector crystals in the ranges $0 < g < 1/6$, $1/6 < g < 2/6$ and $2/6 < g < 3/6$. The concentration curve is integrated over each range and divided by the mass fraction of the detector crystal resulting in an average relative concentration one expects to measure in each crystal slice. These averaged data points (drawn in red, green, and blue in figure 5.14 (a)) lie – due to the integration – slightly above the theoretical curve. This deviation is, however, hardly visible in figure 5.14 (a).

Based on the relative concentration, the number of expected counts N is determined according to equation 5.13. In an experiment, the measured values can deviate from the data points calculated in figure 5.14 (a) due to Poisson statistics. Therefore, the numbers of counts (including errors) are simulated with a Poisson distribution around the calculated values (blue data points in figure 5.14 (b)). The horizontal lines illustrate the mass range, i.e. the integration range, of each detector crystal. As a cross-validation, the corresponding theoretical curve is shown as dashed-dotted blue line.

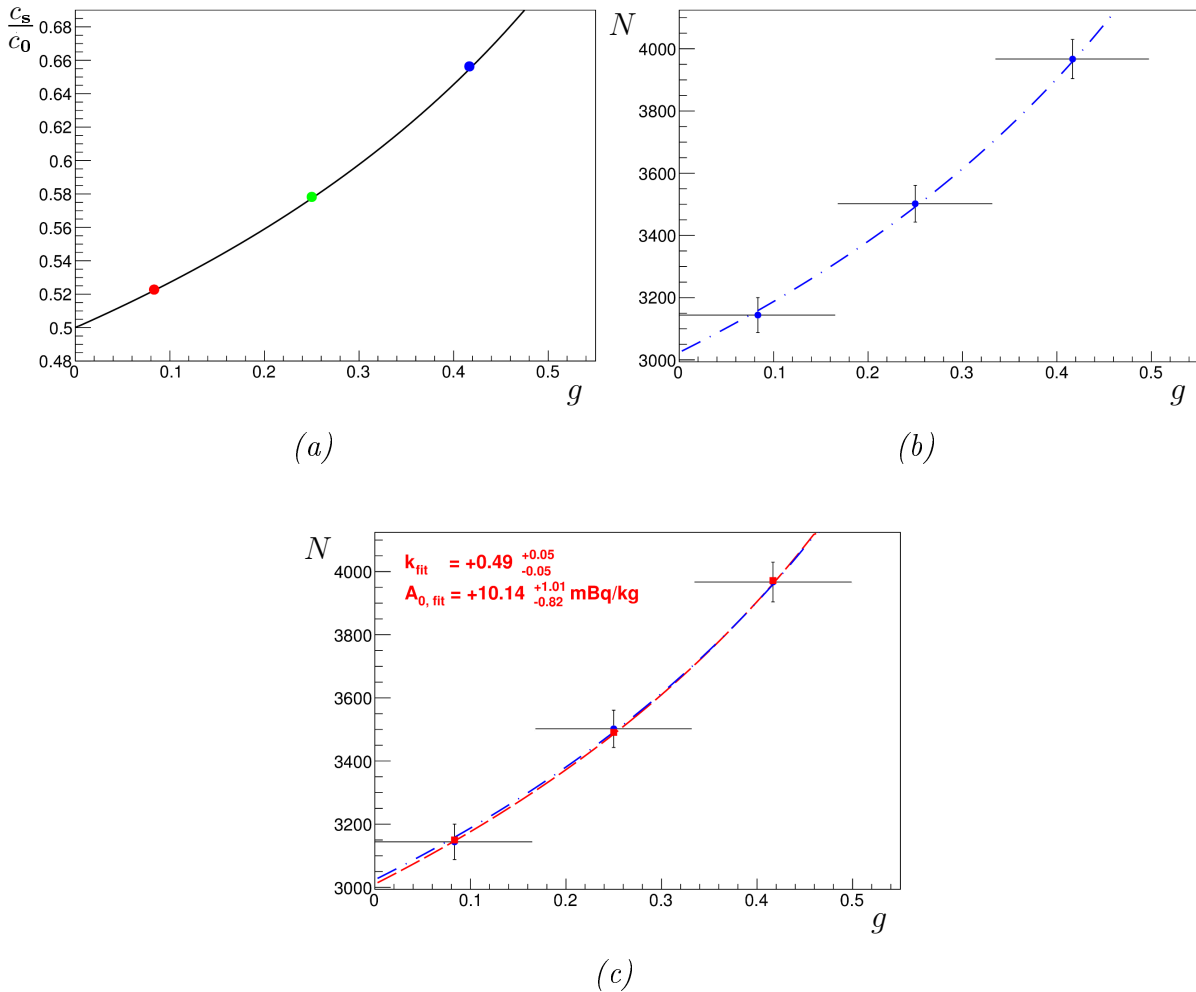


Figure 5.14.: Example for the simulation of data with input parameters $k = 0.5$ and $A_0 = 10 \text{ mBq/kg}$. It is assumed that a crystal ingot with a maximum mass fraction of 0.5 is cut into three detector crystals of the same mass. (a) shows the theoretical curve according to equation 5.11 and three data points calculated for the three crystals via integrating and averaging the curve in the respective mass range. Based on the concentration, the number of expected counts N occurring in four weeks measuring time is determined according to equation 5.13 in (b). Data points and their vertical error bars are simulated due to Poisson statistics. The horizontal lines mark, hereby, the mass (integration) range of each crystal. The corresponding theoretical curve is plotted as blue dashed-dotted line. The blue data points are fitted with the two free parameters k and A_0 according to equations 5.11 and 5.13 in (c). The best fit curve achieved with a likelihood fit and the corresponding data points calculated from this fit curve are depicted in red. The fit result agrees well with the input parameters of k and A_0 .

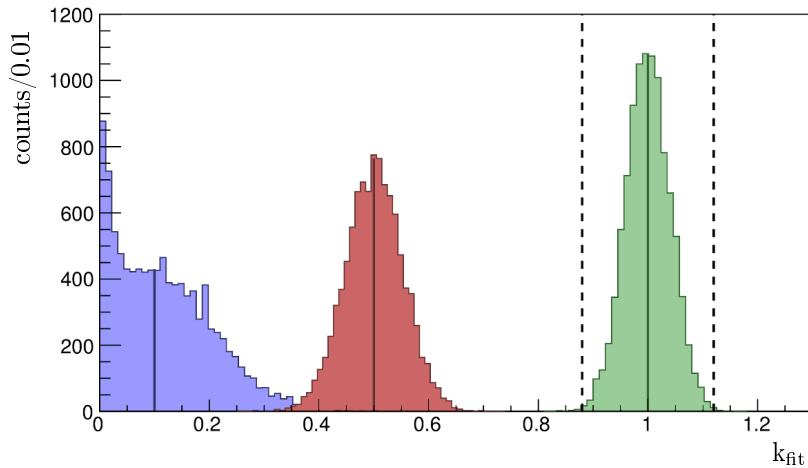


Figure 5.15.: Distributions of k_{fit} after 10 000 repetitions of the simulation and fit with input values of k being 1 (green), 0.5 (red) and 0.1 (blue). The initial activity A_0 is 10 mBq/kg and left as free parameter in the fit. Furthermore, a maximal mass fraction of 0.5, a measuring time of four weeks and a measurement of three crystal slices are assumed. The fit reproduces the input value of k well in the green and the red distributions whereas it fails in case of $k = 0.1$. The dashed black lines mark the 3σ -boundaries of the green distribution corresponding to a deviation of 12 % from the mean value of $k_{\text{fit}} = 1$.

In the last step, these (simulated) data points⁷ are fitted with the combined equations 5.11 and 5.13 (see figure 5.14 (c)). Thereby, k and A_0 are the two fit parameters. For a certain fit curve, the corresponding data points can be calculated and compared to the simulated ones. The usage of the likelihood fit method allows to minimize the difference between data and expected (fit) values. The best fit result is drawn in red in figure 5.14 (c). Furthermore, the fit exports a value k_{fit} and $A_{0,\text{fit}}$ including the respective errors. In the case shown, the input values of $k = 0.5$ and $A_0 = 10$ mBq/kg could be well reproduced.

In figure 5.14 (c), it is assumed that no prior information on the initial activity is known, i.e. A_0 is a free fit parameter. In addition to this fit, an alternative option can be applied when a measured value (involving its error) exists for A_0 , for example, via having screened the CaWO_4 powder before crystal growth. In this case, A_0 can be constrained or be completely fixed in the fit making the determination of the segregation coefficient more accurate as only one free fit parameter is left.

In order to obtain statistically relevant information on the systematic errors, the simulation of the data points as well as the corresponding fit is repeated 10 000 times for each investigated parameter set (k , A_0). The resulting distributions for k_{fit} , $A_{0,\text{fit}}$ and their errors reveal the reliability of a measurement and of the fit for a certain parameter set. As – in the present work – the main issue is the determination of segregation coefficients, only the resulting distributions of k_{fit} are treated in the following.

Figure 5.15 shows three exemplary distributions of k_{fit} with the respective input values

⁷In the present work, data points are only simulated. In principle, these data points can also originate from a measurement.

of k included as vertical solid lines. In all cases, A_0 has an input value of 10 mBq/kg and is a free parameter in the fit. The green fit distribution results from an input value of $k = 1$ and can be well described by a Gaussian function around the expected value of 1 with a width of 0.04. The two dashed black lines represent the 3σ -boundaries of a Gaussian fit corresponding to a deviation of 12% from the mean. This percental deviation serves as a reference in the following.

In case of an input value of $k = 0.5$ (red), the resulting k_{fit} is also Gaussian distributed, however, with an increased width of 0.05. Still, in $\sim 75\%$ of the cases the fit value lies within a deviation of 12% from the mean. In contrast to that, the fit fails in most cases for $k = 0.1$ (blue) resulting in a broad distribution between 0 and 0.4. Only a fraction of $\sim 10\%$ has the right fit result (within the 12% deviation), however, with large errors (not shown here).

In order to compare the results of the simulation of different sets of parameters (k, A_0), the number of fits resulting in a value k_{fit} deviating less than 12% from the input value of k is determined for each distribution. The results of the probed parameter values of k (0.1-1) and of A_0 (ranging between 0.1 mBq/kg and 100 mBq/kg) are depicted in figure 5.16. The numbers within each bin represent the percentage of fit results where the input value of k is reproduced within a deviation of 12%. On the color scale, green values imply a correctly determined segregation coefficient in more than $\sim 50\%$ of the cases. Below a probability of $\sim 50\%$, the bins are marked in yellow or red. In case of white bins, the fit failed completely and did not deliver any output, i.e. the percentage of correct fit results is zero.

The plot in figure 5.16 (a) is based on the standard assumptions $g_{\text{max}} = 0.5$, $t_{\text{meas}} = 4$ weeks, and $n_{\text{crystal}} = 3$. It can be observed that the fit works well for high values of k and A_0 . A segregation coefficient down to 0.8 is still well reproducible for an initial activity of 1 mBq/kg. Low values of k down to 0.2 are only correctly fitted for high initial activities of at least 50 mBq/kg. To achieve a correct fit with a probability of more than 50% for $k = 0.5$, an A_0 of 5 mBq/kg is required.

Compared to figure 5.16 (a), one of the standard assumptions is changed in each of the plots of (b), (c) and (d). Five crystals are measured instead of three in figure 5.16 (b). The mass of the single detector crystals is reduced compared to the three crystals of (a) leading to a decreased number of expected counts in each of them. However, due to the increased number of (mass) data points, the result within the (k, A_0)-parameter space is similar to that of (a). When the measuring time is doubled (c), the outcome of the simulation is slightly improved, i.e. the probability for a correct fit result is slightly higher for lower values of k and A_0 (compared to (a)). However, taking, e.g., the simulation of the input parameters $k = 0.1$ and $A_0 = 10$ still only a fraction of 13.45% is correctly fitted. To achieve a probability of about 50% for a correct fit of this parameter set, a measurement time of almost 3 years is required. Such a long measurement is even beyond the run time of a typical CRESST phase ($\lesssim 2$ years).

In figure 5.16 (d) a higher mass fraction of 2/3 is assumed. Also in this case, only a slight improvement can be achieved.

In all scenarios of figure 5.16, a correct determination of low values of k (~ 0.1) does not seem to be feasible. The picture changes when the initial activity is known and constrained in the fit with an error of 10%. Figure 5.17 (a) shows the resulting parameter

5. Improving the Radiopurity of CaWO_4 Crystals

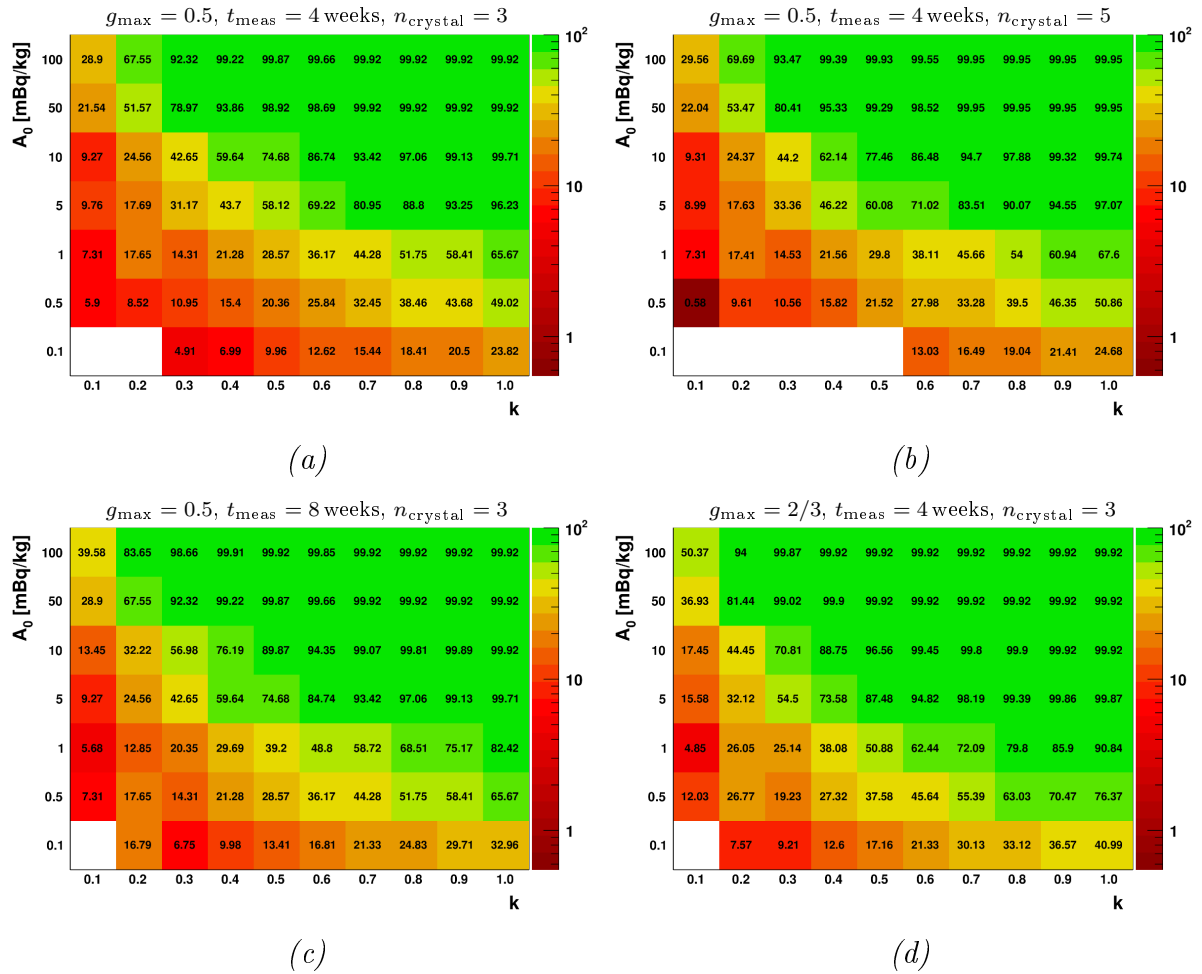


Figure 5.16.: Probabilities of a correct fit determination of the segregation coefficient k within a deviation of 12% for different input parameter sets (k, A_0). In (a) a maximal mass fraction g_{\max} of 0.5, a measuring time t_{meas} of four weeks and a slicing into three detector crystals is assumed. Compared to (a), the number of detector crystals n_{crystal} is increased to five in (b) whereas a longer measuring time of eight weeks and a larger maximal mass fraction of $2/3$ are assumed in (c) and (d), respectively. On the color scale, green values imply a correctly fitted value of k in more than 50% of the cases. Below 50%, the respective bin is marked in yellow or red. White bins imply that the fit did not deliver any output. In general, high values of k and A_0 result in a better fit. No significant difference is observed for varying n_{crystal} . Slightly higher probabilities for a correct fit result can be achieved for increased t_{meas} (c) or g_{\max} (d) which confirms expectations.

space of different (k, A_0)-sets in the same ranges as in figure 5.16. In this constellation, a large improvement is observed and almost all segregation coefficients can be reconstructed with probabilities well above 50%. Even lower input values of k and A_0 down to 0.001 and 0.01 mBq/kg, respectively, are included in figure 5.17 (b). A correct determination of k down to 0.005 is feasible when A_0 is at least 5 mBq/kg. In case of very low initial activities of 0.05 mBq/kg, only values of k above 0.5 can be fitted correctly

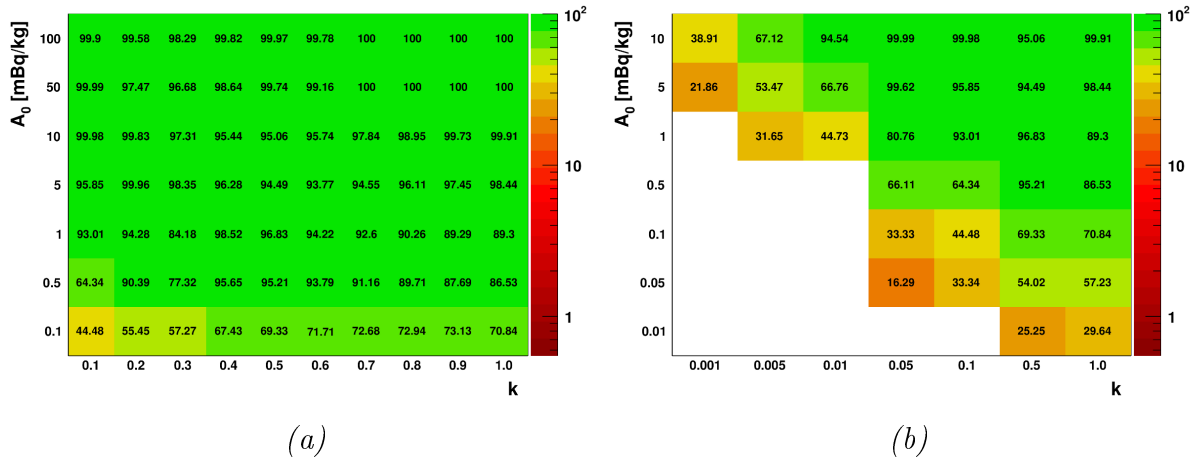


Figure 5.17.: Probabilities of a correct fit determination of the segregation coefficient k within a deviation of 12 % for different input parameter sets (k, A_0) . In the fit, a fixed value of A_0 plus/minus a deviation of 10 % is included. A maximal mass fraction of 0.5, a measuring time of four weeks and a slicing into three crystals are assumed. On the color scale, green values imply a correctly determined value of k in more than 50 % of the cases. Below 50 %, the respective bin is marked in yellow or red. White bins imply that the fit did not deliver any output. Compared to figure 5.16, a correct fit result is achieved for lower values of k and A_0 since the initial activity is known.

with a probability of more than 50 %.

It is shown in figure 5.16 that the number of measured crystal slices has almost no effect on the result of the simulation. This is also valid for the case of a known initial activity. Therefore, the easiest approach would be to measure the contamination level of the initial material, to grow a crystal from this material and to investigate the (new) radiopurity in one cryogenic measurement of the whole crystal ingot. However, it has to be mentioned that the clear determination of activities in the initial material might be challenging due to the limited sensitivity of, e.g., HPGe detectors. Raw materials with an increased impurity level could simplify such a measurement, however, have the risk of contaminating the crucible and the Czochralski furnace. Alternatively, one or two large crystals could be operated as cryogenic detectors to determine the activity of various isotopes before they are melted and recrystallized for another cryogenic measurement of a crystal grown from them.

It is concluded that a determination of k (and A_0) via a fit to the count numbers measured for different crystal slices of a raw crystal succeeds for high values of $k \gtrsim 0.5$ and $A_0 \gtrsim 5$. Slightly higher probabilities for a correct fit result can be achieved when the measuring time and/or the maximal mass fraction is increased. A correct fit for smaller values of k is only feasible when the initial activity is known. In this case, one cryogenic measurement of the whole crystal ingot suffices to determine segregation coefficients down to ~ 0.05 for initial contaminations $\gtrsim 0.5$ mBq/kg.

6. Analysis Methods applied to Data of CRESST-III Phase 1

This chapter concerns the analysis methods developed to derive information on the radiopurity of CaWO_4 crystals operated as cryogenic detectors in CRESST-III Phase 1. The radiopurity analysis includes an investigation of the e^-/γ -band up to recoil energies of several 100 keV as well as an investigation of the α -region up to ~ 10 MeV. As these energies extend to values far above the region of interest of a standard DM analysis, dedicated analyses with different preparation steps had to be developed for both energy ranges. The analysis methods applied to the data are explained in this chapter whereas the actual results are presented in chapter 7.

The software package utilized for the analysis performed in the present work is a programme called OxRop [155, 156]. It is based on the ROOT analysis framework [157] and can read, visualize and analyze all binary data produced by the CRESST DAQ system. Furthermore, it can easily be extended via the application of user-written macros and libraries. Starting from the different parameters calculated for each pulse recorded (section 6.1), sections 6.2 - 6.5 describe the treatment of the e^-/γ -band using the features and methods provided by OxRop. Modifications and peculiarities of the α -analysis are given in section 6.6. The methods used for the calculation of activities and rates are explained in section 6.7.

6.1. Pulse Parameters

A typical pulse recorded by a phonon detector operated in CRESST-III Phase 1 is shown in figure 6.1. The record window consists of 16384 samples¹. The time base is set to $40 \mu\text{s}$ which corresponds to a total record time of 655.36 ms. The first quarter (163.84 ms) is called pre-trigger region and comprises information about the baseline parameters. The remaining 491.52 ms (post-trigger region) contain the actual pulse information.

A set of basic parameters is calculated for each record to describe the main features of a pulse. For several of the pulse parameters a moving average filter for covering 50 samples is applied to reduce the influence of the noise².

Time since Start [h] This parameter stores the total measuring time since the beginning of the data set.

¹Compared to CRESST-II, the length of the record window is doubled as the TES design was optimized for low energies such that pulses have longer decay times.

²A moving average filter calculates for each sample the average of a fixed number of samples (here 50). The value of the subsequent sample is determined by shifting the samples to be averaged by one, i.e. removing the first one and adding the next one to the end.

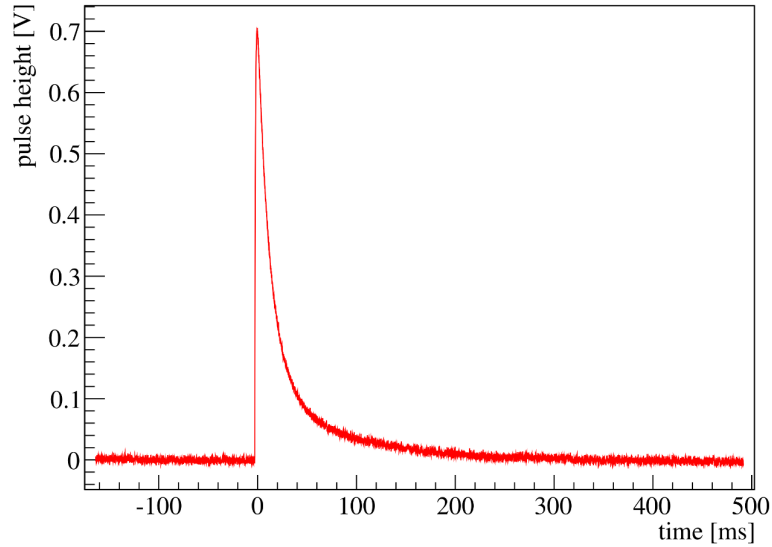


Figure 6.1.: Typical pulse with a pulse height of ~ 0.7 V recorded with a CRESST-III Phase 1 phonon detector. The record window consists in total of 16384 samples with a time base of $40 \mu\text{s}$. The first quarter of this record time of 655.36 ms is called pre-trigger region and contains information about the baseline whereas the actual pulse can be found in the post-trigger region. For an accurate description of each pulse, various parameters as, e.g., the pulse height, rise times, and decay times are calculated. For details see main text.

Live and Dead Time [h] The parameter time since start is the sum of live time and dead time. Live time means the time in which a detector was sensitive to a potential particle interaction whereas dead time accumulates periods where the data taking was interrupted. Included in the calculated dead time are the time required for reading out the signals as well as the record times of control and test pulses since during their recording, particle pulses are not recognized as signal events. Furthermore, the dead time is also increased by the time when triggering is blocked for a detector after an event has been recorded.

Trigger Delay [ms] The signal of each detector is sampled with a transient digitizer. Several digitizer channels are included in one physical digitizer module. A trigger delay of zero is assigned to the detector which triggers first. In case the signal of a detector of another detector module but within the same digitizer module rises above the trigger threshold, its trigger delay is the time difference to the first trigger. The trigger is blocked in the second half of the post-trigger region, which means that the trigger delay is set to a maximum value of 245.76 ms for detectors within the digitizer module which have not triggered at all.

Test Pulse Amplitude [V] For heater pulses, this parameter is the actual amplitude of the injected pulse. Control pulses usually have a test pulse amplitude larger than

10 V whereas particle pulses are assigned a value of 0 V. In CRESST-III Phase 1, a test pulse injected into the main absorber also leads to a crosstalk signal in the corresponding iSticks and vice versa. Therefore, heater pulses are sent alternatingly to the detector crystal and to one of the iSticks. In the analysis, real test pulses and crosstalk pulses can be differentiated.

FWHM of Baseline [V] This parameter is calculated from the standard deviation of the first samples in the pre-trigger range (in this case 95 %) under the assumption of a Gaussian sample distribution. It describes, therefore, the noise conditions during a pulse.

Pulse Height [V] The difference between the maximal sample in the moving average pulse and the baseline level is stored as pulse height. As this parameter is biased by noise, a more sophisticated method for the determination of the real pulse height is introduced in section 6.2.

Peak Position [ms] This parameter is the time within the pulse at which the maximal signal height occurred (stored as pulse height). Thereby, the triggering time is set to 0.

Peak Onset [ms] Going from the peak position backwards in time, the peak onset is defined as the time sample where the signal height is indistinguishable from the baseline noise, i.e. where it is (for the first time) smaller than the FWHM of baseline parameter.

Rise Time [ms] Two parameters are stored for the time a pulse (without moving average) requires to rise from 10 % to 50 % or to 70 % of the pulse height, respectively.

Decay Time [ms] The time between the peak position and the sample where the pulse has fallen to a value of $1/e$ of the total pulse height is stored as decay time. Like the rise time, this parameter can be an indicator for different pulse shapes.

Peak Position - Peak Onset [ms] This parameter describes the time difference between the peak position and the peak onset. In principle, it is similar to the rise time.

Right - Left Baseline [V] The difference of the baseline level in the averaged last (right) and first (left) 50 samples of the plain record is stored as right - left baseline.

Delta Voltage/RMS Delta spikes probably caused by electronic disturbances can occur. A loop over all samples of the plain record (without moving average) is performed and the largest voltage drop between two adjacent samples is calculated. The resulting value is normalized to the root mean square (RMS) deviation of the baseline to relate the quantity to the baseline noise observed during the current pulse.

6.2. Template Fit

The radiopurity analysis of the present work aims at the investigation of events up to the MeV region. This means, the analysis comprises a much wider energy range compared to a standard DM analysis. A method had to be found which is able to correctly determine the energy of a particle interaction, taking also effects like saturation of pulses into account. In principle, the (real) pulse height of a record is directly connected to the energy deposited in the respective detector. However, the previously explained pulse height parameter, which is calculated for each record, is only a rough estimator since it is biased due to noise. The maximum of the pulse is more likely to be located at a positive noise fluctuation, i.e. this parameter generally overestimates the true pulse height. Furthermore, the pulse height can only be used as indicator for the energy when pulses with the same shape are compared, a requirement which is not fulfilled for saturated pulses. The procedure applied in the present work for an accurate determination of the real pulse height (and, thus, the energy) is the so-called template fit (also called standard event fit).

The first step is the creation of a template with a pulse shape typical for a certain event class. Therefore, a number (usually in the order of 10 - 100) of non-saturated pulses from the same energy range, e.g. a mono-energetic line in background or calibration data, is averaged. A relatively narrow energy window avoids a broadening of the rising part of the template pulse due to so-called trigger walk, a dependence of the peak onset on the pulse height. A strict manual pulse selection guarantees that only proper pulses without disturbances are included. The resulting template pulse describes the pulse shape of the respective event class with a noise contribution which is reduced compared to that of a single pulse due to averaging over several pulses. As illustrated in figure 6.2 (a) this template (black) is then fitted to each recorded pulse (red) under adaption of baseline offset (1), time shift (2) and pulse amplitude (3). The best fit is determined via the minimization of the root mean square (RMS) deviation of the fitted function and the recorded data points. The fit parameters are stored for each record. Important for the present work are the fitted pulse height, in the following called (fitted) amplitude [V], and the RMS value.

6.2.1. Truncated Template Fit

The template fit works well for the determination of the real pulse height as long as the fitted pulses are small enough to stay in the linear range of the transition between normal- and superconducting state (compare section 2.2.2). As soon as pulses are saturated, their pulse shape changes. The template cannot describe this pulse form anymore which leads to a rise of the RMS parameter. In CRESST-III Phase 1, phonon pulses already start to saturate at energy depositions of a few 10 keV (depending on the detector). To be able to determine the true pulse height despite of this saturation, a modified fit is applied where the template is truncated at a certain level denoted as truncation limit. Figure 6.2 (b) shows an example for a saturated pulse (red) with a calculated pulse height of ~ 4.2 V. The fitted template (solid black line) is truncated at 2 V (dashed black line). Record samples above the truncation limit are neglected and only the first and the last part of the pulse in the linear transition range are fitted. The amplitude

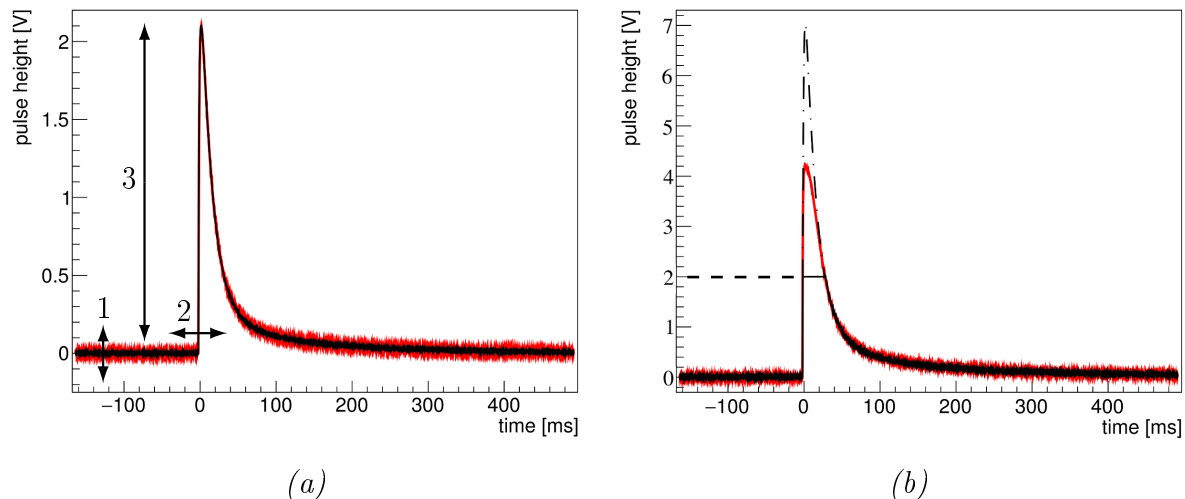


Figure 6.2.: (a) For each detector and event class, a template with a typical pulse shape (black) is created and fitted to the recorded pulses (red) under adaption of baseline offset (1), time shift (2) and pulse amplitude (3). (b) In case of saturated pulses, the part of the pulse in the non-linear region of the transition cannot be described by the shape of the template anymore. For an accurate determination of the real pulse height, a truncated template fit is applied. Only pulse samples below the so-called truncation limit (dashed line) are used for the extrapolation of the amplitude (dashed-dotted line) of the linear pulse shape.

(here ~ 7 V corresponding to ~ 40 keV) is derived by an extrapolation of the linear pulse shape to the non-linear regime (dashed-dotted black line).

For the determination of the truncation limit, two competing aspects have to be considered in the present analysis. Figure 6.3 (a) shows in black the RMS distribution after a template fit without truncation has been applied to the data set. As soon as the non-linear transition region is reached, the pulse shapes deviate from the shape of the template and the RMS starts to rise. In the case shown (of an exemplary CRESST-III Phase 1 phonon detector), pulses slightly start to saturate already at an amplitude of ~ 2 V which corresponds to an energy of ~ 10 keV. This means, a value lower than the value where the rise starts should be chosen as truncation limit in order to create a (relatively) flat RMS distribution for the truncated template fit (red data points). On the other hand, a wide energy range up to the MeV region shall be investigated in the present work. A higher energy deposition in the detector results in a higher degree of saturation and a longer pulse decay time. It is illustrated in figure 6.3 (b) that highly energetic pulses (here with a pulse height of ~ 4.5 V which corresponds to a fitted amplitude of ~ 6 V without truncation and of ~ 130 V with truncation) cannot decay back to the previous baseline level within the record window. However, a truncated template fit can only successfully be applied when also pulse information at the end of the record is included. The resulting minimum truncation limit is drawn as dotted green line. For the case shown in figure 6.3, a truncation limit of 2 V (green line) was chosen as a compromise between the two effects described.

With the truncated template fit, the detector response can be linearized up to high en-

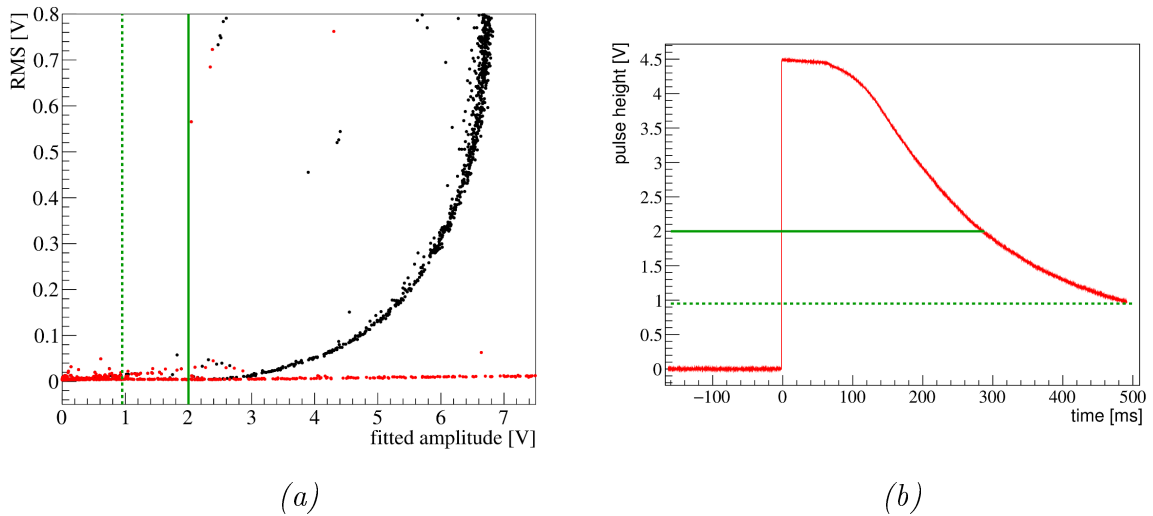


Figure 6.3.: Two competing aspects have to be considered for the determination of the truncation limit. The RMS distribution shown in (a) rises as soon as the amplitudes determined by the not-truncated template fit (black) leave the linear region of the transition as their pulse shapes start to saturate, i.e. deviate from the shape of the template. The truncation limit should be chosen below this rise to ensure a proper fit in the linear region only, resulting in a flat RMS distribution (red). Data points above the main band are due to not-physical events which can be removed via the application of analysis cuts (see section 6.4). On the other hand, in this analysis the template fit should also work for high-energy pulses with long decay times where the pulse does not reach the previous baseline level within the record window (b). As for the evaluation of the amplitude also information of the decaying pulse is needed, a minimum truncation limit (dotted green line) is necessary. The truncation limit at 2 V chosen in this case (solid green line) lies below the rise of the RMS and still well above the minimum level.

ergies. In case of CRESST-II detectors, even the α -range with energies of a few MeV could be well described for several detectors [158]. The much smaller CRESST-III Phase 1 detectors are optimized for low energies in the phonon detector down to the threshold of ~ 100 eV. Compared to CRESST-II, a much lower energy deposition suffices to reach saturation. As a consequence, the shape of phonon pulses in the MeV region is extremely distorted (see section 6.6). A reasonable truncated template fit is only feasible up to energies of (500-1000) keV, strongly depending on the detector.

6.2.2. Correlated Template Fit

In case of low-energy events another measure becomes necessary to achieve a proper determination of the amplitudes. As, e.g., only a small part of the energy deposited in a detector crystal is converted into scintillation light, low-energy events feature extremely low light pulses which hardly rise above the baseline noise. The simultaneous phonon pulse, on the other hand, has a much larger signal. In a correlated fit, phonon and light pulse are fitted simultaneously and the position of the light pulse is fixed by the

phonon pulse. In this way, the template fit can be improved especially for low-energy light pulses. In case of a correlated fit, both templates for phonon and light pulses should be created from the same set of events containing valid light and phonon signals to avoid a difference in the peak onset due to trigger walk.

6.2.3. Templates in this Work

The template fit is applied for ordinary particle pulses as well as for test pulses in both, phonon and light detector. The respective particle pulse templates are created from the γ -line at 11.27 keV originating from cosmogenic activation of tungsten (see section 7.1.1). As the light signal of this 11.27 keV-line is quite low in a few light detectors, the noise contribution can hardly be reduced via averaging. This implies that the respective template cannot be well fitted to pulses with high energies. Therefore, in these cases an additional template is created for light pulses from the 63.3 keV line of a ^{57}Co calibration source. Although this light template seems to be already slightly saturated, it leads to an improved fit result. For the test pulse template, a non-saturated test pulse line is used. Additionally, a template can also be created and fit for special event classes such as, e.g., stick events. Information about the truncation limits used for the template fits of each detector is included in table E.2 of appendix E.

6.3. Energy Calibration

After the reconstruction of the real amplitude of an event by means of the template fit, this amplitude can be converted into the energy that was deposited in the crystal. The energy scale can be set with a mono-energetic γ -line typically produced by a calibration source. The time-dependent detector response on a wider energy range is monitored using the test pulses introduced in section 2.2.3. The exact procedure is explained in the following.

6.3.1. ^{57}Co Calibration

Typically, at the beginning of each measurement campaign, a dedicated calibration run is performed in which the detectors are irradiated for a couple of days by a ^{57}Co source to set the energy scale for the recoil events. The reconstructed energy spectra of a CRESST-III Phase 1 detector module are exemplarily shown on logarithmic scale in figure 6.4. It should be mentioned that – due to the detector optimization for very low energies – the reconstructed energy scale can deviate by a few percent for energies above ~ 100 keV. The energy spectrum of the phonon detector (red) features several lines and structures whereas the electron-equivalent energy spectrum of the corresponding light detector (blue) cannot resolve all structures. The two prominent γ -lines of ^{57}Co lie at energies E_γ of 122.1 keV and 136.5 keV (see table 6.1). In most cases the γ -rays interact with the atoms of the target crystals and eject an electron from the shell. The hole is quickly filled with electrons from outer shells under the emission of Auger-electrons or X-rays with an energy E_X . If such an interaction happens close to the surface, the X-ray may escape and an escape line at the energy $E_{\text{esc}} = E_\gamma - E_X$ can be observed in the

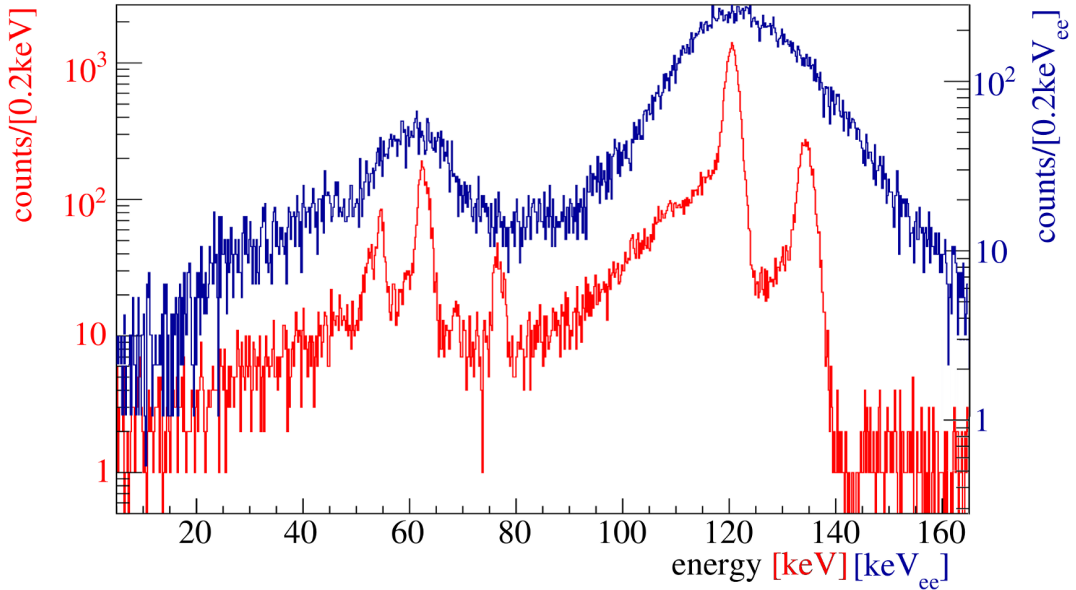


Figure 6.4.: Energy spectrum of a ^{57}Co calibration source recorded by a CRESST-III Phase 1 phonon detector (red) and by the corresponding light detector (blue). The energy scale of the light detector is denoted as electron equivalent and labelled with the subscript "ee". The two prominent γ -lines of ^{57}Co at 122.1 keV and 136.5 keV as well as a couple of lines originating from escaping tungsten X-ray lines (see table 6.1) are observed in the phonon detector. As only a small fraction of the deposited energy is emitted as scintillation light, the different structures cannot be resolved by the light detector and only two broadened peaks are observable there.

spectrum. The energy E_X would only be visible in the case that an X-ray escaping a neighbouring detector is absorbed in the crystal. However, in CRESST-III Phase 1 all detector modules are installed within a copper housing with a thickness of 2 mm which shields external X-rays to a large extent. The fraction of radiation which is able to penetrate the housing is $\sim 12\%$ at an energy of ~ 70 keV [159].

The tungsten X-ray lines with the highest intensities as well as the respective escape lines for the two γ -energies 122.1 keV and 136.5 keV are listed in table 6.1. The escape lines with the highest intensities are 122.1 keV - $K_{\alpha 1/2}$ at energies E_{esc} of 62.8 keV and 64.1 keV, respectively. They cannot be resolved in the phonon spectrum of figure 6.4 and only a combined peak at a mean energy of 63.3 keV (weighted by intensity) is observed. The same is valid for the escape peaks 136.5 keV - $K_{\alpha 1/2}$ at a mean energy of 77.7 keV. The tungsten $K_{\beta 1/2}$ X-rays escaping the 122.1 keV line result in escape lines at 53.0 and 54.9 keV. As their energy difference is slightly higher than in case of the $K_{\alpha 1/2}$ X-rays, they can at least partially be resolved by the phonon detector. The intensities of the 136.5 keV - $K_{\beta 1/2}$ escape lines are much lower, but their structure can still be guessed at an energy of ~ 68 keV in the logarithmic scale of figure 6.4.

In earlier CRESST phases, typically the 122.1 keV line of the ^{57}Co spectrum was used to set the energy scale of the detectors (see, e.g. [43, 45]). However, in case of most CRESST-III Phase 1 detectors the events from this line are already highly saturated

line type	line origin	energy [keV]	intensity
emission lines	^{57}Co	122.1	85.6
	^{57}Co	136.5	10.7
X-ray lines	W $K_{\alpha 2}$	58.0	34.8
	W $K_{\alpha 1}$	59.3	60.5
	W $K_{\beta 1}$	67.2	13.1
	W $K_{\beta 2}$	69.1	4.5
escape lines	122.1 keV - $K_{\beta 2}$	53.0	-
	122.1 keV - $K_{\beta 1}$	54.9	-
	122.1 keV - $K_{\alpha 1}$	62.8	-
	122.1 keV - $K_{\alpha 2}$	64.1	-
	136.5 keV - $K_{\beta 2}$	67.4	-
	136.5 keV - $K_{\beta 1}$	69.3	-
	136.5 keV - $K_{\alpha 1}$	77.2	-
	136.5 keV - $K_{\alpha 2}$	78.5	-

Table 6.1.: Origin of the lines observed in the ^{57}Co calibration spectrum of figure 6.4 and the corresponding literature values of their energies and intensities [58]. The two main emission lines of ^{57}Co have an energy E_{γ} of 122.1 keV and 136.5 keV, respectively. The tungsten $K_{\alpha 1/2}/K_{\beta 1/2}$ X-ray lines with energies E_X are listed in the second part of the table. When they escape the crystal, so-called escape lines appear in the spectrum at energies equal to the difference between E_{γ} and E_X (lower part).

and one has to rely on the reconstruction of the amplitude via the truncated template fit described before. To minimize the introduction of uncertainties due to the template fit, the intensity-averaged energy 63.3 keV of the 122.1 keV - $K_{\alpha 1/2}$ escape lines is used for energy calibration. In the background data, the resulting energy scale can be cross-checked and corrected with the help of the cosmogenic activation line at an energy of 11.27 keV (compare figure 2.10).

6.3.2. Test Pulse Calibration

With the ^{57}Co source, the detector response of a certain calibration line (e.g., 63.3 keV in CRESST-III Phase 1) can be determined only for the time period of the dedicated calibration run. Therefore, another measure is necessary to monitor the detector response of a wider energy range throughout the data taking period. Heater pulses with various test pulse amplitudes (typically ~ 15 amplitudes ranging between energies below 1 keV and ~ 100 keV in CRESST-III Phase 1) are injected into each detector in regular time intervals. As the test pulse amplitudes are equivalent to different, but distinct energies, they help to transfer the energy calibration down to the region of interest. In particular, it is possible to ensure a calibration down to the thresholds of the detectors. In addition to the energy information, the detector response can be probed time-dependently which

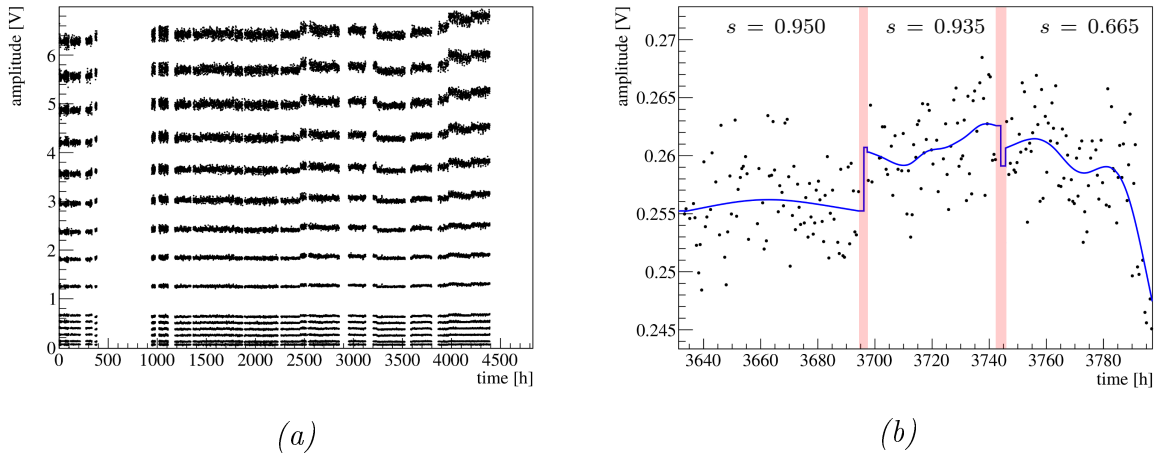


Figure 6.5.: To consider time variations of the detector response for the energy calibration, heater pulses with various test pulse amplitudes are injected into each detector in regular time intervals. The time dependency of the resulting measured amplitudes (linearized with a truncated template fit) is shown in (a). The gaps where no data is present are due to cryostat maintenance (order of 1 h) or are due to a distinct calibration campaign ($\sim (400-900)$ h). (b) shows the time dependency of the detector response to one injected amplitude throughout three measurement files in more detail. The light red areas mark the periods where data taking was interrupted. A spline fit (blue line) is applied to the data points (black). The so-called smoothing factor s is adapted automatically for each spline fit. A high value of s in the first two measurement files of (b) ($(3630-3695)$ h and $(3697-3742)$ h) indicates only a slight time dependence whereas for the third measurement ($3746-3800$) h, only a lower value of s describes the data points well.

allows a time-dependent correction. In figure 6.5 (a) the amplitudes of the test pulse response are plotted versus the measuring time exemplarily for a CRESST-III Phase 1 phonon detector. Like in the case of particle pulses, this amplitude is the result of the linearization with a truncated template fit. The gaps mean that either no background data was taken during this time period or that this data was not included in the set used for the analysis of the present work. The large gap between $\sim (400-900)$ h is the time of the ^{57}Co calibration campaign. Furthermore, after every ~ 50 h, data taking is interrupted for about three hours due to technical reasons: the cryostat has to be refilled with liquid helium which causes vibrations. This leads to a temperature increase in the detectors such that they are out of their operation point and no data taking is possible during this time. Only when all detectors are fully operational again, a new measurement file is started.

In total, 15 different test pulse amplitudes are injected and slight time variations of the detector response can clearly be observed for all amplitudes in figure 6.5 (a). In order to track such systematic time variations, a method called smoothing spline [160] is performed for the amplitudes of all test pulse events belonging to a certain injected test pulse amplitude. Whenever a new measurement is started, a new smoothing spline is applied to the corresponding time period. A so-called smoothing factor s has to be set

and determines the sensitivity of the spline fit. In the extreme case of $s = 1$, a straight line is fitted to the data points. For a smoothing factor approximating zero, on the other hand, the spline fit smoothly interpolates all the data points. In [43, 45] an adaptive method was developed for an automatic determination of the smoothing factor of each amplitude and measurement file. In this procedure, the data points are divided into a training set and a test set and s can be varied in the allowed range between 0 and 1. The smoothing is performed for the training set for distinct values of s whereby the RMS deviation of the resulting function and of the data points of the test set is calculated. A minimum value of this RMS corresponds then to the optimum value of s .

Figure 6.5 (b) shows the response of one test pulse amplitude (black data points) in a more narrow time window including three measurement files. The light red areas mark the time periods where data taking was interrupted due to the refill of the cryostat. The spline fit applied to this amplitude of each measurement file is drawn in blue. The smoothing factors determined by the adaptive method are larger than 0.9 in the first two measurement files of figure 6.5 (b) indicating only a slight time dependency of the amplitude. In case of the measurement started at ~ 3746 h, a higher time variation has to be corrected which is realized with a lower value of $s = 0.665$.

It can happen that there are invalid test pulse events, e.g. due to pile-up with a simultaneous particle interaction, which do not reflect the correct detector response (compare section 6.4). These events appear as outliers and are removed before the spline fit is performed since they could lead to a wrong energy calibration.

After a spline fit has been performed for each measurement file and test pulse amplitude, the actual energy calibration can be applied. Whenever a particle interaction occurs, the corresponding splines are evaluated at the time of this event for all amplitudes of the test pulses. This results in the black data points in figure 6.6 which are fitted by a polynomial function (black line) in order to relate the injected test pulse amplitude to the fitted amplitude at that time. With the additional help of the calibration peak (here 63.3 keV, originating from the W K_α escape-lines of the ^{57}Co source), a linear conversion factor can be calculated. This so-called CPE (convert pulse height to energy) factor [keV/V] finally connects the injected (or equivalent) test pulse amplitude to the energy scale (red lines), i.e. the fitted amplitude can now be transformed into the equivalent particle energy. In this way, each amplitude can be assigned to the corresponding energy. A pulse with a fitted amplitude of 5.65 V, for example, is equivalent to an energy deposition of 95 keV (blue lines). The calculated CPE factors of all investigated detectors are listed in table E.2 in appendix E.

A precise energy calibration with a polynomial fit of the test pulses as applied in figure 6.6 is only feasible in the energy region which is supported by test pulses. As CRESST-III Phase 1 is optimized for very low thresholds, also the injection of test pulses is adapted to amplitudes equivalent to energies below ~ 100 keV. For investigations of the e^-/γ -band above this region, an approximated energy calibration can be achieved by a linear extrapolation of the test pulses.

However, for very high energies in the MeV range, large deviations might occur also with this estimation method. An alternative is given in the presence of pronounced background lines (γ or α) which can be used instead of test pulses to correct time dependencies and to adapt the (linear) energy calibration.

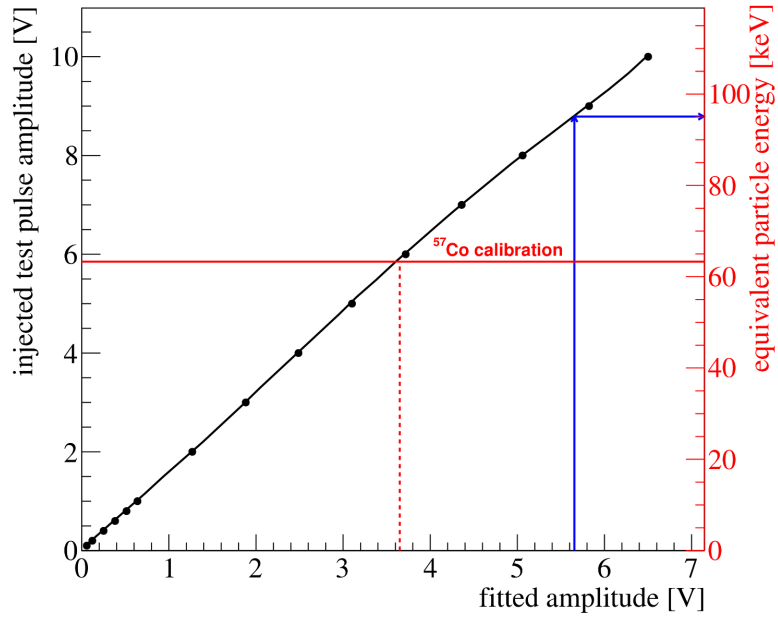


Figure 6.6.: Energy calibration in CRESST-III Phase 1. The black data points are the detector response (fitted amplitude) to test pulses with various injected test pulse amplitudes (left scale) at a certain time. They are fitted with a polynomial function (black line). In addition, the calibration peak (here 63.3 keV) of a ^{57}Co source connects the energy scale (right) with fitted and injected amplitude values (red lines). By evaluating the fit function at the amplitude of a particle pulse occurring at this time, the amplitude can be converted into an equivalent particle energy (blue). For amplitudes higher than the region supported by test pulses, the energy can be approximated with a linear fit of the test pulses.

6.4. Analysis Cuts

For each analysis it has to be ensured that only valid events are considered. Events that are not physical but, e.g., caused by the electronics or events that have wrongly determined pulse parameters (i.e., in particular, misfitted amplitudes or energies), are invalid and, thus, have to be removed. This data selection is achieved by the application of various cuts.

6.4.1. Stability Cut

As explained in section 2.2.3, control pulses are injected into each phonon and light detector to check the stability over time. Time periods where one or both detectors of a module were not in their operation point have to be removed from the data as it cannot be guaranteed that the detectors were capable of recording valid pulses.

The optimized operation point (temperature) of each detector corresponds to a certain measured pulse height of the injected control pulses. The detector cannot exactly be kept in this predefined operation point but fluctuates around the set value ($\mathcal{O}(1\ \mu\text{K})$).

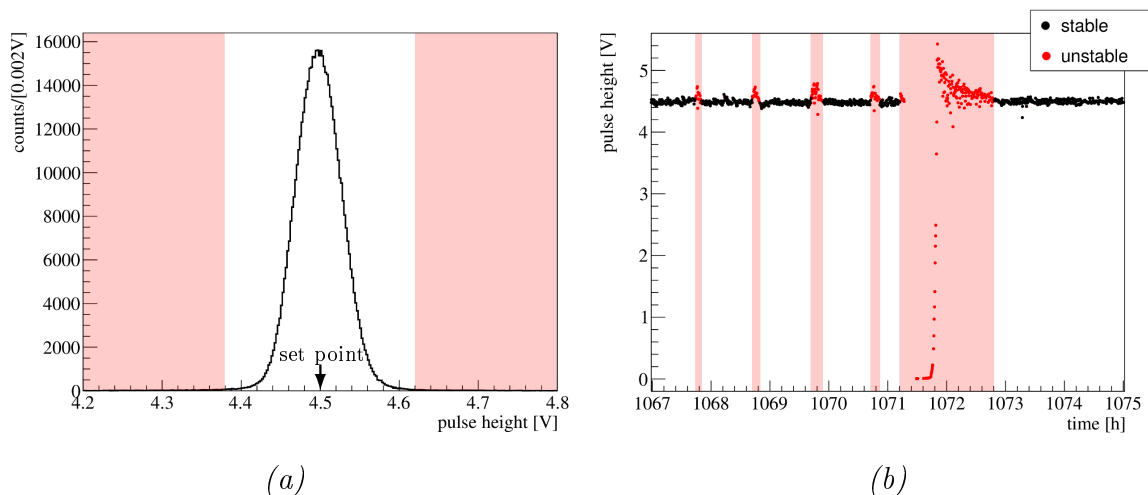


Figure 6.7.: (a) Measured pulse height spectrum of the control pulses injected into a detector. Pulse heights with a strong deviation from the mean value (set point) indicate unstable time periods which have to be removed from the data set (light red area). The stable range defined in the present work corresponds to the 5σ values of the Gaussian approximation of the distribution. (b) Measured control pulse height in dependence of the measuring time in a selected time window. Control pulses inside (outside) the stable range of (a) are plotted as black (red) data points. Unstable control pulses initiate unstable periods (light red) which are cut from the data set.

Histogramming the control pulse height as exemplarily shown in figure 6.7 (a) results in the given distribution around the set point (here 4.5 V). This distribution can be approximated by a Gaussian function. Strong deviations of the pulse height from this set point indicate unstable periods, e.g. caused by external disturbances. For the stability cut, a stable range of the control pulse height has to be defined. In the analysis of the e^-/γ -band performed in the present work, control pulses with a detector response deviating more than 5σ from the mean value of the Gaussian fit of the distribution (see table E.3 in appendix E) are assumed to be outside this stable range (light red area in figure 6.7 (a)).

At least two subsequent control pulses have to be recorded with a pulse height outside the stable range to initiate an unstable time period which starts with the time of the last stable control pulse³. The unstable period ends when a control pulse has a detector response within the stable range again. In some cases of strong disturbances (e.g. earthquakes) the detectors are very suddenly heated up to the normal-conducting state and cannot receive the injected pulses anymore. The last control pulse before such a period might still be stable – nevertheless, the time period has to be recognized as unstable. Therefore, the stability cut also sets an unstable period when ~ 5 subsequent control pulses could not be recorded in a detector.

Figure 6.7 (b) shows the control pulse height over time. Control pulses in the stable

³Time periods where only one control pulse is out of the allowed range are usually not caused by instabilities but are due to a wrong determination of the pulse height when, e.g., a pile-up with a particle pulse occurs in the record.

(unstable) range as defined in (a) are drawn in black (red). The time periods marked in light red are removed by the stability cut according to the explained conditions. This means, all particle and test pulses occurring within this region are cut from the data. The stability cut is simultaneously applied to phonon and light detectors and assures that only data with both detectors of a module running stably is used for further analysis. In the present work, the stability cut typically removes a live time of less than 5% per detector module.

6.4.2. Invalid Event Classes

Even after having selected time periods where phonon and light detector worked stably, some of the recorded pulses are invalid and have to be removed for further analysis. This includes records which are not due to real particle interactions but are created artificially, e.g., by disturbances caused electronically. If such disturbances occur during a real particle interaction, the result is also an invalid record. Figure 6.8 shows examples of the different phonon/light events belonging to such event classes. The simultaneous signals of the iSticks are not included for reasons of clarity but will be explained later in this section. Vibrations can lead to a temporarily enhanced noise level in the detectors. In case of figure 6.8 (a) the noise level was above the trigger threshold triggering the read-out of the whole module. A so-called delta spike is shown in (b) for phonon (red) and light (blue) detector. Such a sudden delta-like decrease of the pulse height value for a very short time period is most probably caused by external electronic disturbances. Two invalid event classes related to the SQUID electronics are included in figure 6.8 (c) and (d). A SQUID outputs a voltage which is periodic in the applied magnetic flux and has a periodicity equal to one so-called flux quantum. In case of very large and fast rising signals, the SQUID might not be able to follow the resulting flux change leading to a loss of an integer number of flux quanta (for a more detailed description see, e.g., [161]). An example of a phonon pulse featuring flux quantum losses is shown in figure 6.8 (c). The voltage losses in the rising part of the pulse lead to a lower baseline level in the end of the record and to a wrong amplitude determination in the template fit. In principle, a reconstruction of the real amplitude might be possible provided that the pulse returns to a constant baseline level at the end of the record window which is, however, not the case for most of these pulses. A correct amplitude determination might be achieved with the continuous read-out installed for CRESST-III Phase 1 [72] which is beyond the scope of the present work.

A flux quantum loss is often followed by a SQUID reset (see figure 6.8 (d)). The reason is that the baseline level is reset by the SQUID electronics whenever the output value reaches the boundaries of the read-out electronics. The result is a record with a step-function-like pulse.

Apart from these pathological pulses, also real particle pulses can be distorted as in the cases shown in figure 6.9 which makes a correct determination of the pulse parameters and the deposited energy challenging. After the recording of a high-energy pulse, the voltage level in the digitizer can still be above threshold when triggering is re-enabled. Thus, the decaying baseline of the previous pulse is recorded (a). In a few cases, an interaction happens simultaneously and a pulse is present on top of the decaying baseline.

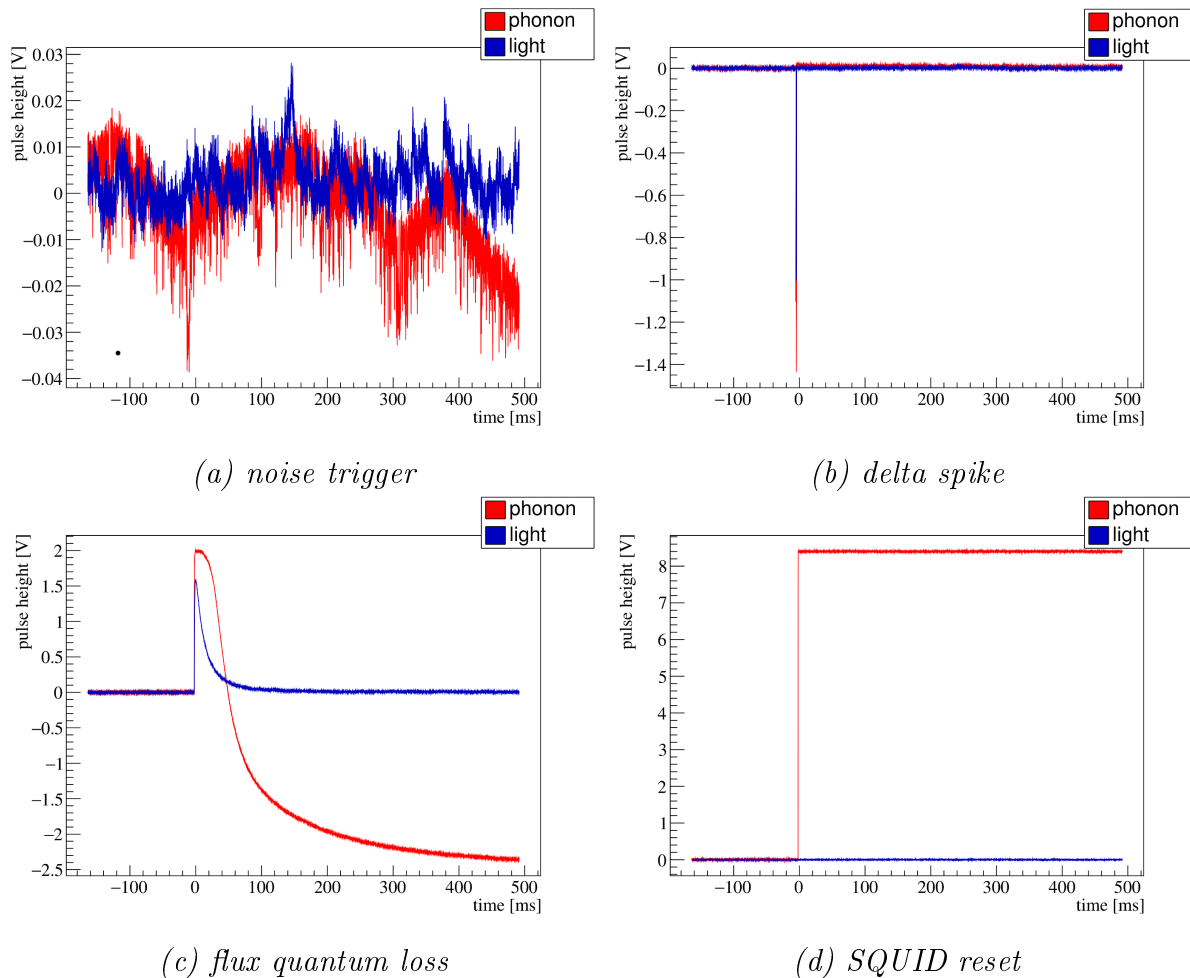


Figure 6.8.: Invalid pulses occurring in the phonon (red) or in the light (blue) channels have to be removed from the data set via application of data quality cuts. Noise triggers (a) appear when the noise level is enhanced above trigger threshold, e.g., due to external vibrations. (b) shows a so-called delta spike probably originating from electronic disturbances. Flux quantum losses (c) and SQUID resets (d) are related to the SQUID electronics and result in a shift or step of the baseline level. The signal of the *iStick* is not shown for reasons of clarity. For further details see main text.

For strongly tilted baselines, a correct pulse reconstruction is challenging. A detector can also observe two particle interactions in a very short time period resulting in a pile-up event as shown in (b). In principle, a reconstruction of both interactions might be possible. As, however, such events are very rare due to the low total trigger rate of much less than 1 Hz in each CRESST-III Phase 1 detector this is not done here. Finally, figures 6.9 (c) and (d) show pulses happening very early or late in the record window. In case of early pulses, a particle interacts during the time when triggering is blocked after a previous record. When the pulse level is still above threshold after the trigger has been reactivated, the pulse is recorded, however, with incomplete pre-trigger region, i.e. shifted towards earlier samples. Late pulses, on the other hand, occur when a detector in the digitizer module triggers and, by chance, an event in another detector of this digitizer

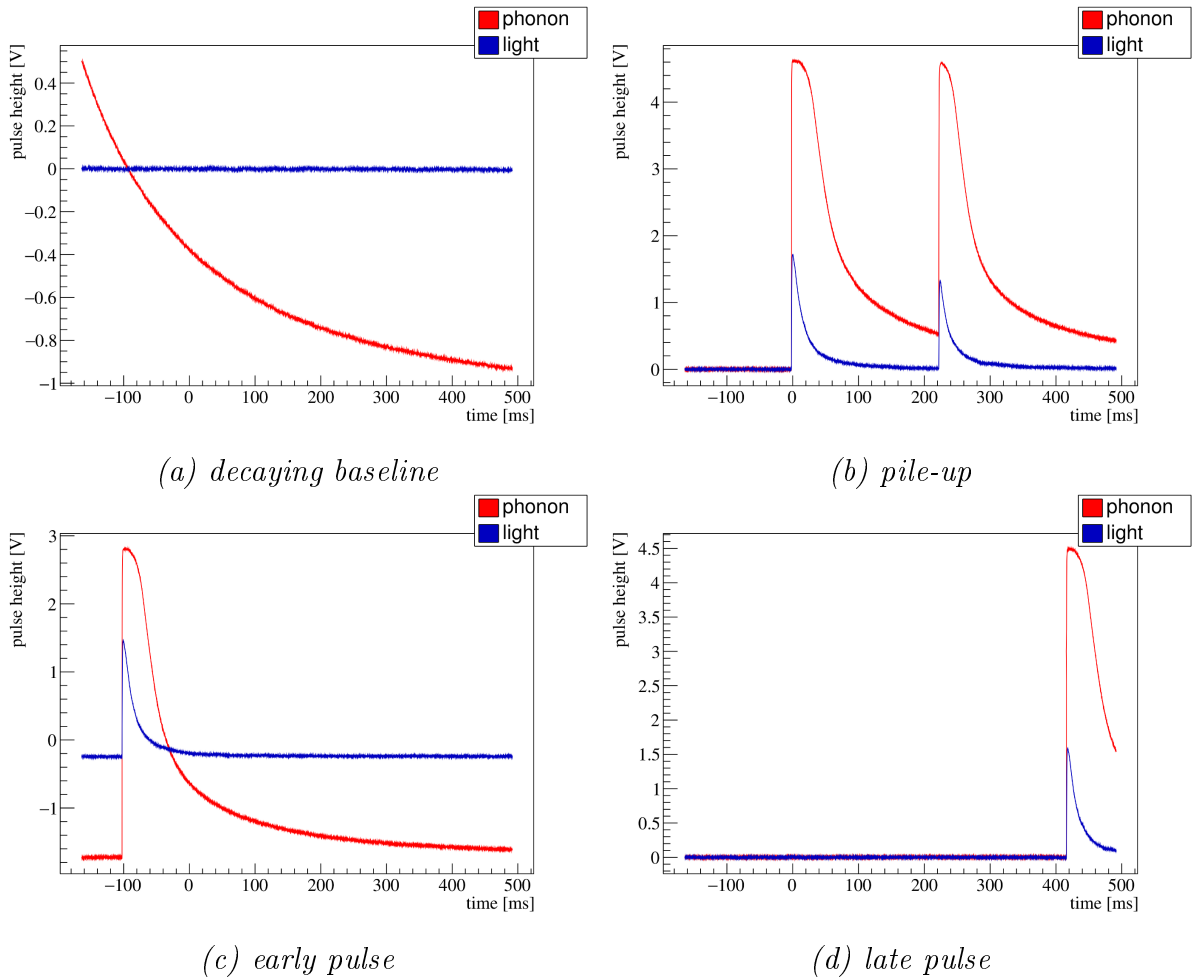


Figure 6.9.: Event classes containing incomplete or pile-up pulses in phonon (red) and light (blue) detectors (*iStick* signal is neglected for reasons of clarity). After a high-energy event the voltage signal could still be above threshold when triggering is reactivated resulting in the recording of the decaying baseline of the previous event (a). Two particle interactions observed by a detector within a short time result in a pile-up event as shown in (b). Pulses can also occur very early (c) or late (d) in the record window, when the interaction happens during the blocking of the trigger. As a correct amplitude and energy reconstruction is not guaranteed, these event classes have to be removed from the data set by means of quality cuts.

happens within the record time of the first pulse. In both cases of time-shifted pulses, either information of the baseline or of the decaying part of the pulse is missing, which is, however, necessary information for a correct amplitude and energy determination.

6.4.3. Data Quality Cuts

Regardless of type and origin, all invalid event classes as depicted in figures 6.8 and 6.9 have to be removed from the data set as they either do not contain any physical information or imply a wrong determination of the pulse parameters (in particular of the

amplitude) which could lead to a defective energy calibration. Therefore, a series of basic data quality cuts is applied in the present analysis. For decaying baselines and noise triggers, which make up $\sim 80\%$ of the triggers in the initial data set, the determination of the pulse parameter "peak position" as well as of the difference between peak onset and peak position is defective. Therefore, a cut on the "peak position" and "peak position - peak onset" parameters can be applied to efficiently remove these invalid events. Remaining decaying baselines, SQUID resets and flux quantum losses (a few percentage of the remaining events) have the common property of a deviating baseline level in the beginning and at the end of a record and can be discarded by a cut on the "right-left baseline" parameter. For the investigation of high-energy events, the cut should not be too strict as the pulse might not return to the previous baseline level within the record resulting in an increased right-left baseline value (compare figure 6.3 (b)). Delta spikes ($\lesssim 3\%$ of the remaining events) can easily be removed by cuts on the parameter "delta voltage/RMS". To discard events with a significantly enhanced noise level, a cut on the FWHM of the baseline is performed.

All cut limits applied to the different detectors analyzed in the present work are summarized in appendix E. Cuts on the phonon parameters "peak position", "peak position - peak onset", "right-left baseline", "delta voltage/RMS" as well as on the FWHM of the baseline are applied. As the light signal is – especially for nuclear recoils – much lower than the phonon signal, an accidental removing of low-energy light pulses should be avoided. Therefore, for the light detector only cuts on the parameters "right-left baseline" and "delta voltage/RMS" are applied.

6.4.4. Removing Stick-Related Events

In CRESST-III Phase 1, two types of CaWO_4 sticks can be found within the detector housing, namely the iSticks holding the crystal as well as non-instrumented sticks fixing the light detector. Interactions occurring in the iSticks can have a crosstalk to the main CaWO_4 absorber crystal and vice versa resulting in a degraded event in the phonon or in the iStick channel, respectively (see figure 6.10). Such degraded signals in the main absorber could potentially leak into the ROI in a dark matter analysis and are, therefore, also removed in this investigation of the e^-/γ -band.

For small energy depositions in the main crystal, no signal is visible in the iStick due to a low crosstalk. Only when the deposited energy is high enough ($\mathcal{O}(\text{MeV})$), a small pulse is recorded by the iStick as demonstrated in figure 6.10 (a). On the other hand, a particle interaction in the iStick with an energy that is high enough to cause a visible crosstalk signal in the main crystal, always leads to a detectable pulse in the iStick (b). This means, a simple cut on the pulse height of the iStick signal is able to discard degraded events in the main crystal. The cut limits are listed in table E.3 in appendix E.

Also events happening in the holding sticks of the light detector can cause low-energy signals in the phonon detector when the light that is produced in the stick is absorbed in the crystal. Such events have a phonon signal of only a few keV. Although their light yield is usually higher than that of electrons or γ -radiation in the main absorber, a leakage into the region of interest cannot be excluded. However, such events do not play a role in the analysis performed in the present work as they occur mainly below an

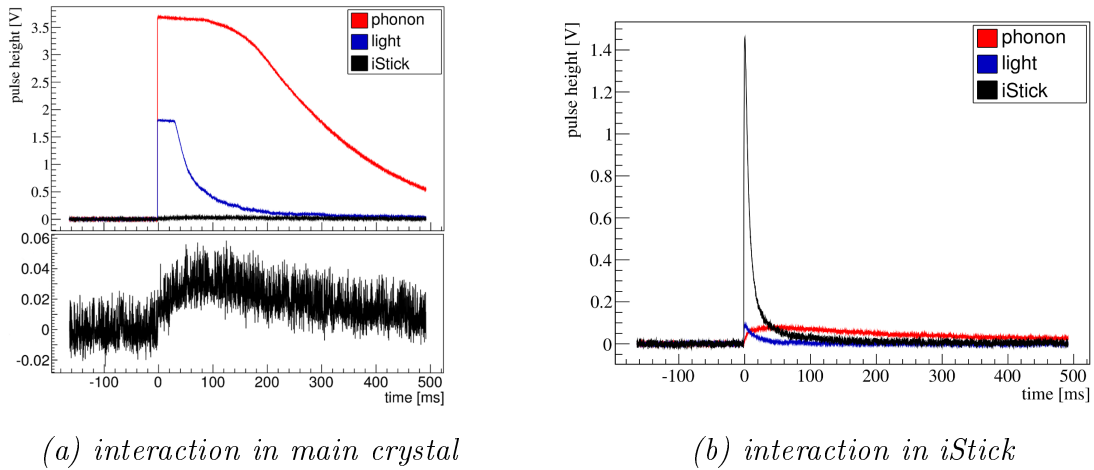


Figure 6.10.: Particle interactions occurring in the main crystal (a) or in the *iStick* (b) can result in crosstalk (phonon) signals in the respective other detector when the deposited energy is high enough. The degraded low-amplitude signal in the *iStick* (black) after a crosstalk interaction is shown in the zoomed lower plot of (a). In case of degraded crosstalk events in the phonon detector (red) as depicted in (b), a leakage into the ROI is possible. Such events can, however, easily be removed by a simple cut on the pulse height of the *iStick* signal.

energy of ~ 5 keV whereas only energies above 5 keV are investigated here⁴.

6.4.5. RMS Cut

A cut on the RMS parameter, which is calculated for each pulse during the template fit (see section 6.2), has in former CRESST phases been a powerful measure to reject pulses featuring a deviating shape with respect to the standard (template) shape (see, e.g. [43, 45]). However, in the radiopurity analysis of CRESST-III Phase 1 data of the present work, no RMS cut is performed. The reason for this approach is that all methods for the application of a reasonable RMS cut appear to be unsuitable as explained in the following.

Despite of the truncated template fit, the resulting RMS parameter still rises slightly for energies higher than the one the template was built from (~ 12 keV). This energy dependence has to be considered in a potential cut. Different approaches for the objective determination of an energy-dependent cut limit were developed in former works. The RMS distribution can be considered separately for different energy slices with a width in the order of 10 keV. A certain (constant) fraction of pulses with an increased RMS value can be defined and removed from each energy slice [158, 162]. For this method, the fraction of "bad" pulses is required to be constant over a wide energy range. This is, however, an assumption which is not necessarily true like in the case of the detectors

⁴A separation of events happening in the holding sticks of the light detector is, in principle, feasible by a cut on the trigger delay parameter. Usually, the phonon detector triggers first but in these cases of stick interactions its trigger is slightly delayed compared to the light detector. No such cut was applied in the present analysis.

analyzed in the present work.

Neglecting time dependencies, the RMS values of valid signals can usually be approximated by a Gaussian distribution in each energy slice – bad pulses distort the shape of the distribution. Therefore, a Gaussian function or an empiric model (consisting of the sum of a Gaussian function convoluted with an exponential and a linear function) can be fitted to the RMS distribution in each energy slice for the determination of the cut limit [43]. However, also this method did not work for the data set analyzed in this thesis as statistics in each energy slice are too low for a reasonable fit result.

Further possibilities based on a simulation (see section 6.5) were also found to be unsuitable. Although a linearization of the amplitudes is achieved with the truncated template fit, the RMS still rises slightly for energies above the truncation limit (which is about the energy the template is created from, i.e. ~ 10 keV). The RMS value of simulated pulses, on the other hand, stays rather flat with energy as the simulation and template fit are both performed with the same standard event. As the RMS values of simulated pulses do, thus, not reflect the real behaviour, neither a determination of the cut limit in the simulated data nor a calculation of a correct survival probability (see section 6.5) in case of a manual RMS cut is feasible.

Although no RMS cut was applied in this analysis, no pulses with distorted pulse shapes are left in the final data set which was controlled by eye.

6.4.6. Muon Veto Cut

Records in the cryogenic detectors that are in coincidence with a valid event registered by the muon veto system hint towards a muon-induced particle interaction and are discarded from the e^-/γ data set. As it has to be guaranteed that every real muon event is vetoed, all interactions triggered by the muon veto system are conservatively considered as muon events.

The interaction in the muon veto and a corresponding energy deposition in one of the cryogenic detectors happen (almost) simultaneously. However, the trigger in the cryogenic detector is usually slightly delayed due to the slow detector response and due to signal propagation delays in the electronics. On the other hand, an uncertainty in the determination of the peak onset can result in a time reconstruction seemingly slightly before the event in the muon veto. Therefore, a time window of ± 5 ms around the muon event is chosen for discarding muon-induced cryogenic events. With this value, the fraction of measuring time vetoed is in the order of 5% (see section 7.2).

6.5. Survival Probability

The cuts described before should be chosen in a way that ideally all or (in reality) at least the great majority of invalid events are removed from the data set. However, this comes at the cost of removing also part of the valid pulses by means of the cuts. For a correct calculation of, e.g., activities and rates in the e^-/γ -band, the survival probability has to be estimated. The survival probability is here defined as the probability that a signal candidate event survives the analysis cuts, or – in other words – as the fraction of valid e^-/γ -pulses surviving the cuts. For an estimation of this probability, pulses are simulated

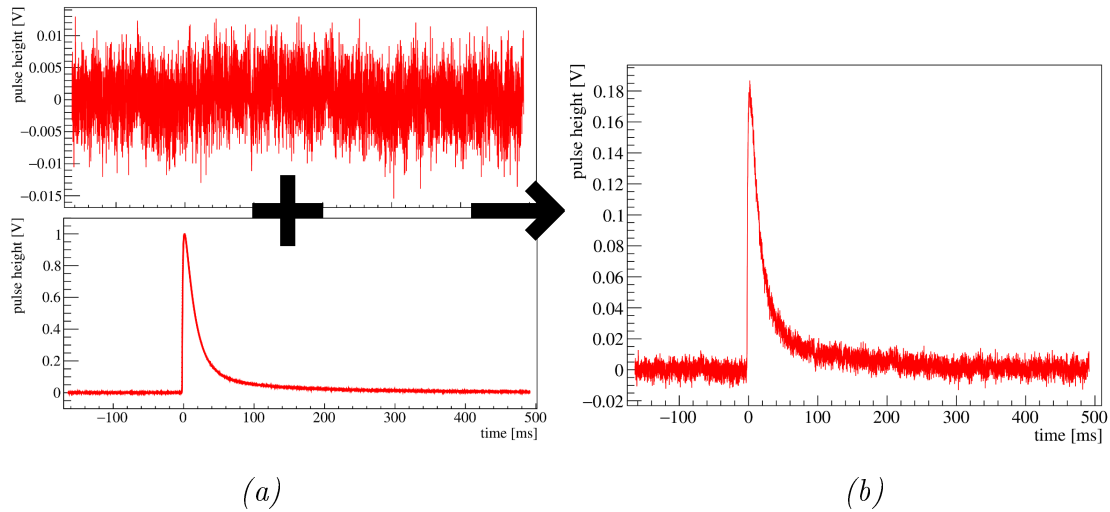


Figure 6.11.: Creation of artificial pulses. During data taking, CRESST records also empty baselines (see (a) top). For each detector, its template pulse ((a) bottom) can be scaled to different amplitudes (i.e. energies) and added to these empty baselines. An example for a pulse simulated in this way is shown in (b). When the analysis chain as applied to the real data is also applied to the simulated data set, an energy-dependent survival probability can be determined.

over the energy range of interest – in the present work for energies between 5 keV and ~ 500 keV. The artificially created pulses are saved to disk and are indistinguishable from real records for the data analysis software so that the same analysis chain as applied to the real data can be performed for the simulated data. In this way, the fraction of pulses surviving the various cuts can be calculated for each simulated energy. This results in an energy-dependent survival probability $\epsilon(E)$ which is $> 90\%$ for all detector modules investigated in this analysis (details are presented in section 7.2).

For pulse simulation, the templates of the respective detectors as well as empty baselines, which are recorded in regular time intervals during data taking, are used. As illustrated in figure 6.11 the template ((a) bottom) of each phonon detector is scaled to different amplitudes, i.e. energies, and added to the empty baselines ((a) top) recorded with this detector. An example for a pulse simulated in this way is shown in (b). In total, each simulated amplitude is added to each baseline. As e^-/γ -interactions are investigated in the present thesis, artificial pulses with the same energies (in electron equivalent) are simulated for the simultaneous light signal.

Figure 6.12 shows two exemplary distributions of cut parameters for the real data (blue) and for the simulated data (cyan) scaled to the statistics of the real data. In case of the right-left-baseline distribution (a), the position of the main peak is the same and a slight deviation is only visible around 0.1 V. The right-left baseline parameter increases with increasing energy as the pulse cannot return to the baseline level before the end of the record. Therefore, this deviation can be explained by the fraction of high-energy pulses which is much higher in case of the simulated data than in the real data. However, the lose cut between -0.5 V and 2 V (red regions) as applied to the data is not affected by

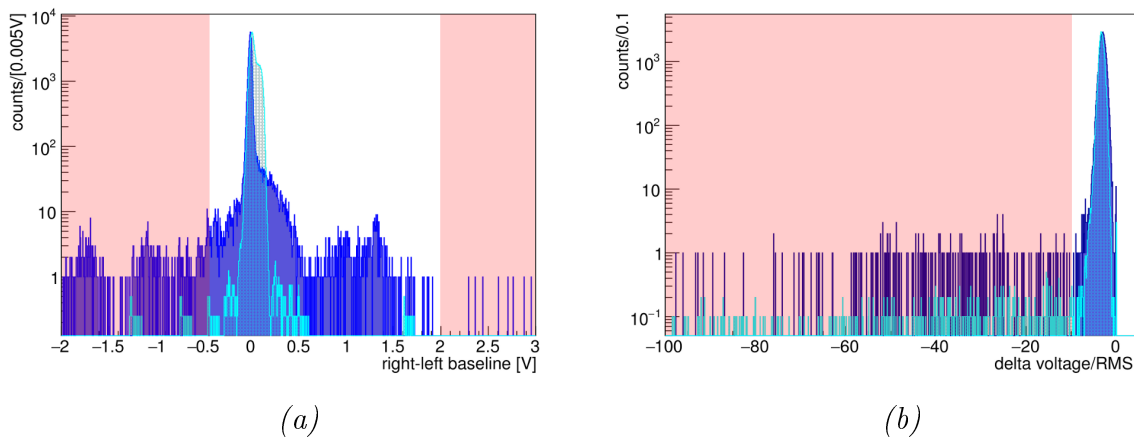


Figure 6.12.: Exemplary distributions of the cut parameters right-left baseline (a) and delta voltage/RMS (b) for the real data (blue) and for the simulated data (cyan) scaled to the statistics of the real data. The respective cut regions are marked in red. In case of the right-left-baseline distribution (a), the position of the main peak is the same and a slight deviation is only visible around 0.1 V which can be explained by the higher fraction of high-energy pulses in the simulated data set. The real distribution of the parameter delta voltage/RMS (b) can be well described by the simulated events.

the slight deviation.

The distributions of the cut parameter delta voltage/RMS is depicted in Figure 6.12 (b). The simulated pulses reflect the behaviour of the real data well. All simulated pulses in the removed (red) region are taken into account for the calculation of the survival probability.

Most of the parameter distributions of the simulated data describe also those of the real data. However, there are a few minor drawbacks of this simulation method. During the creation of artificial pulses, no time shift of the pulse within the record window can be introduced as the record lengths of the template and of the recorded empty baselines are the same. This means that the amount of valid events removed at early or late times in the record window cannot be determined⁵. Furthermore, also iStick signals in connection with crosstalk events are challenging to be simulated. Although it is safe to assume that the fraction of valid phonon/light events discarded by a cut on the pulse height of the iStick signal can be neglected, a small error might be introduced.

6.6. Dedicated Methods for the α -Analysis

The analysis procedure described in the previous sections is applicable to events in the e^-/γ -band with energies below ~ 1 MeV. An identification of different contaminating isotopes within the crystals is also feasible via investigating α -decays. In the previous CRESST runs, an analysis of these decays could be performed for several detectors where

⁵This problem does not occur in a data analysis using the continuous read-out [72] which was, however, beyond the scope of the present work.

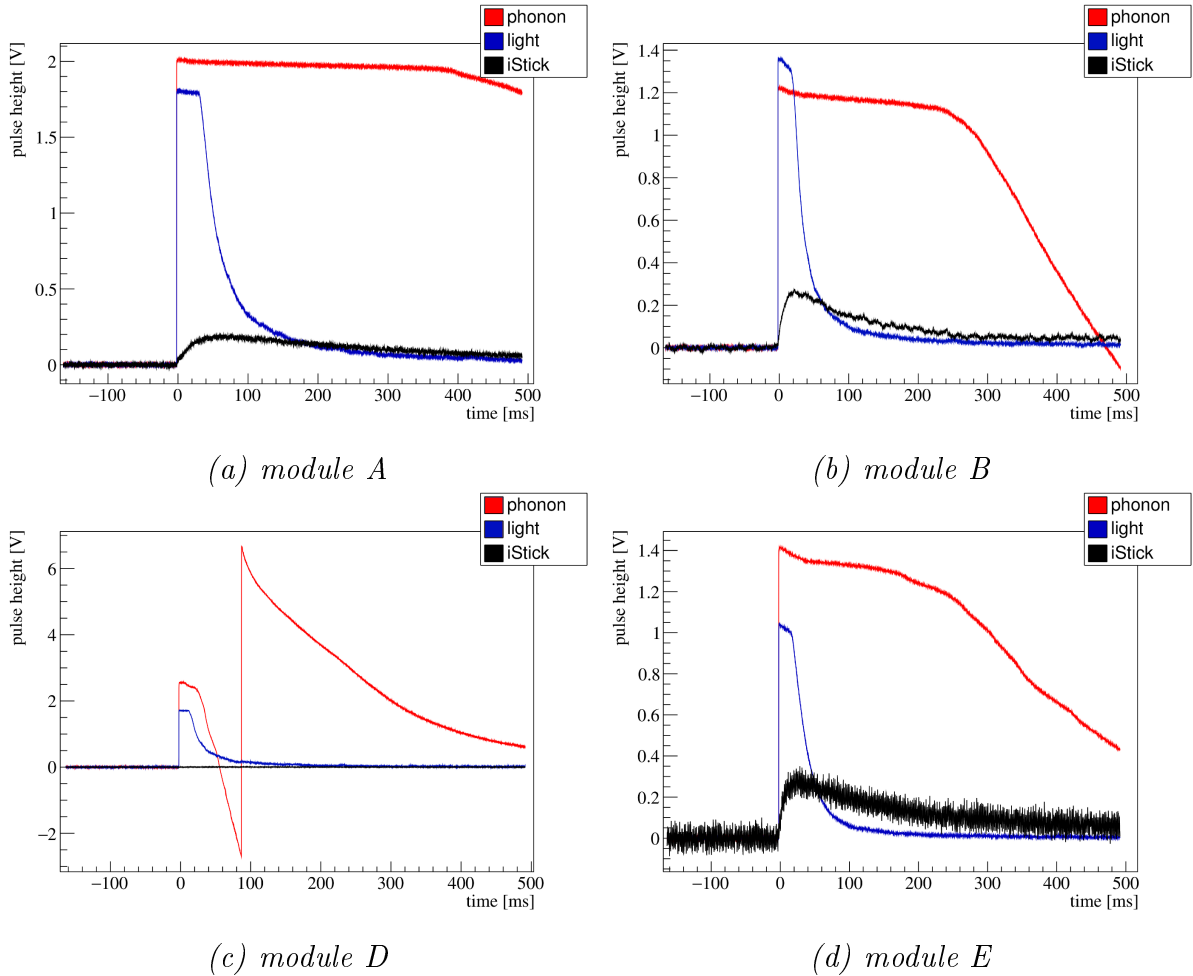


Figure 6.13.: Typical α -events in the four analyzed detector modules A (a), B (b), D (c) and E (d). The phonon signal (red) is not suitable for an energy reconstruction due to a very high degree of saturation (a), flux quantum losses (b), SQUID resets during the pulse (c) or non-linearities in the transition (d). However, the energy of the light signal (blue) can be reconstructed. Furthermore, the pulse height of the crosstalk pulses in the iStick (black) varies with the energy deposited in the main absorber and can be used for an investigation of α -decays.

an energy reconstruction up to a few MeV was achieved [158]. This, however, cannot easily be done with CRESST-III detectors and the development of new analysis methods is required. When looking at the typical α -events occurring in the four detector modules A, B, D, and E (see figure 6.13 (a), (b), (c), and (d)), it becomes clear that the actual amplitude of the phonon signal (red) cannot be reconstructed due to problems like a huge degree of saturation (a), flux quantum losses (b), SQUID resets during the pulse (c) and non-linearities within the transition (d)⁶. However, the energy deposited in the main absorber is high enough to create a degraded crosstalk signal in the iStick (black).

⁶A possibility to use the phonon signal could be a future analysis with the continuous read-out installed for CRESST-III Phase 1. However, the fitted amplitudes will be huge and problems of flux quantum losses etc. make also this approach challenging.

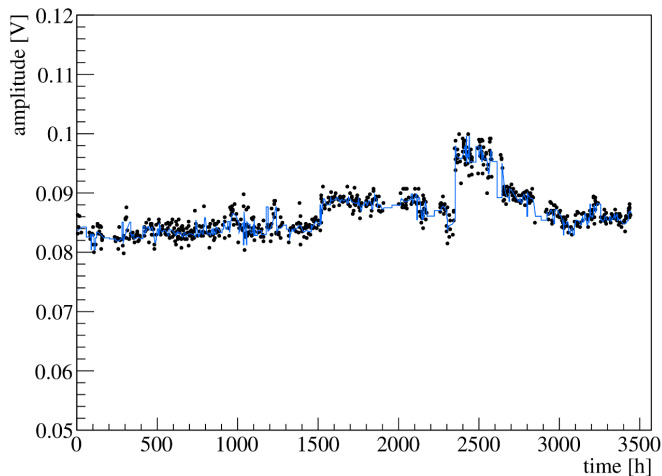


Figure 6.14.: It is shown, how a spline fit (blue) is applied to the time-dependent amplitude of a pronounced α -line in the iStick of detector module A (black data points). In this way, time variations can be corrected and an energy scale can be set when the α -line could be identified.

These crosstalk signals are easily distinguishable from direct iStick events as they feature a defined pulse shape with long rise times and decay times. The pulse height of the total iStick signal is not yet saturated in the region of degraded α -events and, therefore, varies depending on the energy⁷. Although the achieved resolution might be decreased, this offers the possibility of an α -analysis via crosstalk signals in the iStick.

For the investigation of α -decays via crosstalk signals, the preparation steps as explained in the previous sections have to be modified. An iStick template is created from a pronounced region in the α -band. As the signal-to-noise ratio is quite low in some cases of these pulses, the template is fitted in correlation with the light detector in order to find the proper pulse onsets. A truncation limit as defined before is only applied to the light template, as the degraded α -signals do not saturate the iStick channel.

An (electron equivalent) energy calibration of the light detector can be achieved by a linear extrapolation of the test pulse method explained in section 6.3.2. In case of the iStick channel, the identification of at least one α -line is necessary for setting the energy scale. Apart from the calibration, more crucial is the correction of time dependencies. Heater pulses are also sent alternately to the different iSticks. In a first approach, the time-dependent detector response to the test pulses of one iStick can be used. However, this was found not to be an accurate method. Instead, figure 6.14 shows how a spline fit (blue) is applied to the time variations of (at least) one pronounced α -line (black). With the help of this line, a readjustment of the time correction (and energy calibration) can also be applied to the light detector at high energies.

Time periods, where the detectors were not capable of recording valid pulses, should also be removed in an α -analysis. It was observed that the 5σ definition of the stable control

⁷It should be clarified that the pulse height of all three iSticks together is not saturated. This does not exclude that one of the iSticks saturates already at lower pulse heights in case of direct hits.

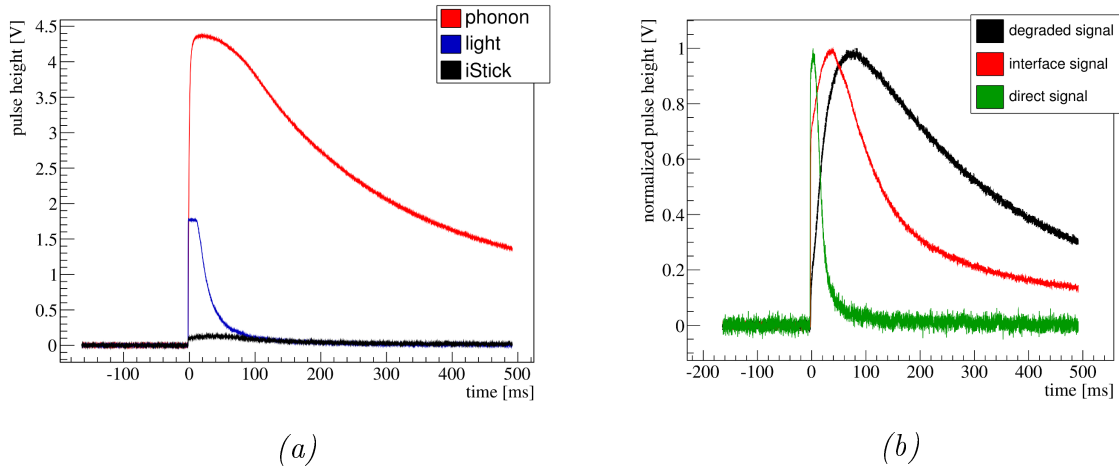


Figure 6.15.: (a) Pulses in phonon (red), light (blue) and iStick (black) channels for an a priori unknown event class occurring close to the α -region in several detectors (here module A). The pulse shapes of phonon and iStick signal are clearly deviating from that of e^-/γ - or α -events occurring in the main absorber or in one of the iSticks. (b) Comparison of the iStick pulse shapes (normalized to 1) of degraded signals (black), direct hits (green) and the new event class (red). The red pulse lies with a relatively fast rise time and a long decay time in between the two other pulses. This is a hint for a mixed event which could happen at the interface between main crystal and iStick and, thus, contains both, a direct signal part and a degraded signal part.

pulse range as applied to the e^-/γ data set is not suitable since a non-proportionally large fraction of α -events is removed in several detectors. A possible explanation is that the huge energy deposition of an α -particle can disturb the detector to such a high degree that more than one control pulse has a deviating pulse height. Therefore, a much larger stable range (compare figure 6.7) is defined for the analysis of α -decays and only obvious outliers or time periods where no control pulses could be detected are considered by the stability cut (see table E.4 in appendix E).

For a better discrimination from non-physical events and direct iStick interactions, several cuts are applied. In case of α -events, all three detectors of a module (phonon, light, iStick) show a clear signal. This implies that all events where at least one detector features no signal can be removed by cutting all records that have a negative value of the parameter "peak position - peak onset" in one of the three detectors. This cut removes only pulses with an arbitrary shape and the survival probability can be assumed to be 100%. Furthermore, the trigger delay of degraded crosstalk-signals is well above zero whereas the iStick triggers first in case of direct particle interactions. This means, direct iStick hits can be removed by cutting pulses with a trigger delay of zero. It is possible that random coincidences between an α -event in the main crystal and a simultaneous interaction in the iStick are also removed, however, the probability is very low and neglected in the following.

In several detectors, an (a priori) unknown event class was discovered close to the α -region. An example of such an event recorded by module A is shown in figure 6.15 (a).

Whereas the shape of the light signal is comparable to that of other events in the e^-/γ -band and α -region, the shape of the phonon pulse deviates – independently of the saturation effect – from normal signals occurring in the main absorber and also from crosstalk signals which have happened in one of the iSticks. The same is valid for the iStick pulse which features a fast rise time and a relatively high decay time. Figure 6.15 (b) compares the different iStick pulse shapes (normalized to 1) of direct hits in one of the iSticks (green), of degraded signals (black) and of the new event class (red). It can be observed that the red pulse lies in between the two other pulses which is a hint for a mixed event containing both, a direct signal part and a degraded part. Such events could occur at the interface between main absorber and iStick. Depending on the energy deposition and on the pulse height where the involved iStick saturates, this event class can occur as a narrow or as a broad distribution, also in the α -region. In any case, the signal shapes of the iStick and the phonon detector clearly deviate from that of α -decays happening in the bulk. A highly affective parameter for the separation of degraded α -events and interface events is the rise time of the iStick. Therefore, in the α -region, all iStick signals with fast rise times are discarded by a cut. All cut limits defined for the α -analysis can be found in table E.4 in appendix E.

Table 6.2 summarizes the differences between the two analyses applied to the e^-/γ -band and to the α -region with energies $\lesssim 500$ keV and > 2 MeV, respectively. A correlated template fit is performed for the respective main signals phonon + light (e^-/γ) and iStick + light (α). The test pulse method with a polynomial interpolation can be used to calibrate the energies deposited by e^-/γ -interactions below ~ 100 keV whereas a linear extrapolation is applied for events with higher energies. In case of α -signals in the iStick, α -lines have to be identified to apply a time correction and energy calibration. For the stability cut, a maximal deviation of 5σ from the TES set point is allowed for the control pulse height in the analysis of the e^-/γ -band. Only obvious outliers are removed in case of the α -analysis. The parameters used for analysis cuts on the phonon detector (PD), the light detector (LD), and the iStick are also adapted for the respective analysis.

6.7. Activity Determination

For an investigation of the radiopurity of the CaWO_4 crystals operated in CRESST-III Phase 1, rates and activities A of events in the e^-/γ -band and in the α -region are calculated using the equation

$$A = \frac{n_{\text{obs}}}{t_{\text{live}} \cdot m \cdot \epsilon(E)} \quad (6.1)$$

The number of events observed in a certain region or line is denoted as n_{obs} , whereas t_{live} means the live time (after stability cut) and m the mass of the involved crystal. The survival probability $\epsilon(E)$ (see section 6.5) is obtained at the mean energy E of the corresponding line or as mean value of the energy region.

To calculate an event rate in a certain energy region, all events occurring in this region are simply counted to determine n_{obs} . γ -lines are fitted by the sum of a Gaussian function with amplitude C , mean μ and width σ and a constant background. As no continuous background is expected in the α -range, lines there are fitted by the Gaussian function

6. Analysis Methods applied to Data of CRESST-III Phase 1

analysis region	e^-/γ	α
energy range	$\lesssim 500$ keV	> 2 MeV
energy reconstruction	correlated template fit phonon + light	correlated template fit iStick + light
energy calibration	test pulse method (+ ^{57}Co γ -lines)	linear extrapolation of test pulse method (light), α -lines (iStick)
control pulse heights discarded by stability cut	$> 5\sigma$ deviation from set point	obvious outliers
cut parameters PD	peak position peak position - peak onset right - left baseline delta voltage/RMS FWHM baseline	peak position - peak onset
cut parameters LD	right - left baseline delta voltage/RMS	peak position - peak onset
cut parameters iStick	pulse height	peak position - peak onset trigger delay rise time

Table 6.2.: Summary of the differences in the radiopurity analyses of the e^-/γ -band and of the α -region. Included are the respective energy regions investigated in the present work, the methods of the energy reconstruction (template fit) and energy calibration, the allowed deviation of control pulse heights from the set point defined for the stability cut as well as the various cut parameters of the phonon detector (PD), the light detector (LD), and the iStick.

only. The number of counts observed in a certain line is determined via integrating the Gaussian part:

$$n_{\text{obs}} = \int_{-\infty}^{\infty} C \cdot \exp\left(-\frac{(E - \mu)^2}{2\sigma^2}\right) dE = \sqrt{2\pi} \cdot C \cdot \sigma \quad (6.2)$$

For all calculated rates and activities, the statistical errors obtained either from the number of counts or from the fit value are included as uncertainty.

7. Results of the Radiopurity Analysis of CRESST-III Phase 1

After all preparation steps explained in chapter 6 had been applied, the radiopurity of several CRESST-III Phase 1 detector modules including TUM-grown crystals was investigated in the e^-/γ -band and in the α -region. For comparison, the radiopurity results of the crystal TUM40 (CRESST-II Phase 2) are given in section 7.1. The analyzed data sets and detectors of CRESST-III Phase 1 are described in section 7.2. The results of the radiopurity analysis of the e^-/γ -band and of the α -region are presented in sections 7.3 and 7.4, respectively, and are discussed in section 7.5.

7.1. Radiopurity of TUM-Grown Crystals

The crystal TUM40 was operated as cryogenic detector in CRESST-II Phase 2 (see section 2.3). The TUM40 background spectra serve as a benchmark for the results of the radiopurity analysis of CRESST-III Phase 1 detectors.

7.1.1. Background Spectrum below 100 keV

Figure 7.1 (a) shows the energy spectrum of TUM40 between 5 keV and 100 keV for an exposure of ~ 130 kg days corresponding to the whole CRESST-II Phase 2 data set. The total background rate in the range (1 - 40) keV was calculated to be 3.51 counts/(kg keV day) which is equivalent to 1.58 mHz/kg [82]. In the energy range starting at 10 keV and extending up to 40 keV, the value of the total e^-/γ -rate was found to be slightly reduced to (3.26 ± 0.08) counts/(kg keV day) (estimation based on the analysis of [43]). The different features visible in the spectrum are explained in the following.

Copper Fluorescence Line

The copper X-ray fluorescence (K_α) at 8.05 keV [58] is produced when γ -radiation excites copper atoms in the vicinity of the detectors, e.g., in the holders. This means that the observed copper-line is not of crystal-intrinsic origin.

Cosmogenic Activation Lines

Several γ -lines originate from the cosmogenic activation of tungsten: proton capture on ^{182}W and the successive release of an α -particle result in the isotope ^{179}Ta which then decays via electron capture (EC) to ^{179}Hf (half-life 665 days). The distinct peaks in figure 7.1 (a) correspond to the binding energies of electrons in the K-shell (65.35 keV),

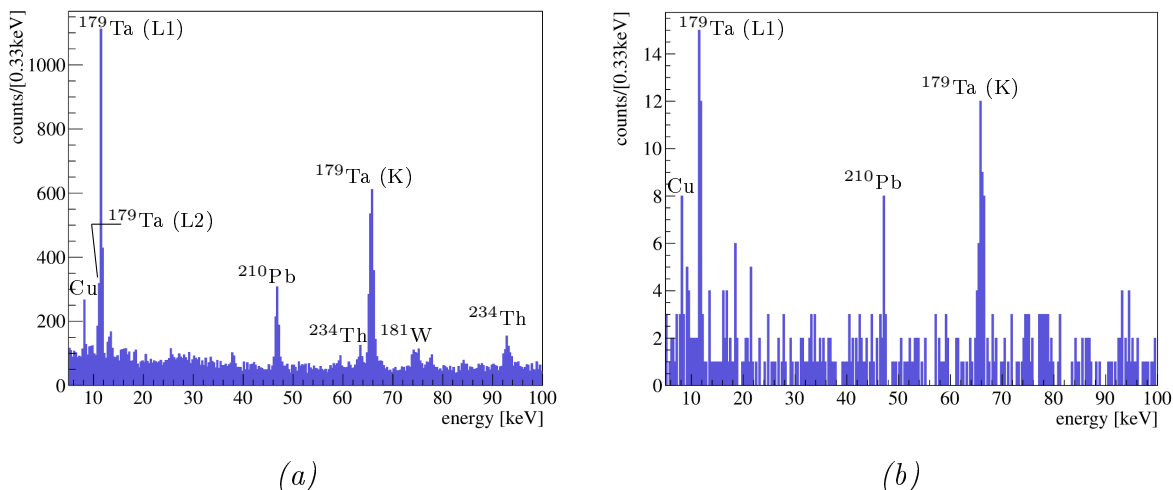


Figure 7.1.: Energy spectrum between 5 keV and 100 keV of the crystal TUM40 operated in CRESST-II Phase 2. (a) shows the spectrum of the complete data set with an exposure of ~ 130 kg days. For a better comparison to the CRESST-III detectors, the exposure is adapted to a value of ~ 2.75 kg days in (b). Several lines can clearly be identified also with the low statistics of (b). This includes the ^{179}Ta K- and L1-lines originating from cosmogenic activation, the Cu K_{α} -line at 8.05 keV as well as a γ -line at 46.5 keV caused by external radiation of ^{210}Pb . The plots are created on the basis of the analysis performed in [43].

L1-shell (11.27 keV) and L2-shell (10.74 keV) of ^{179}Hf [58]. Not shown here but visible, e.g., in figure 2.10 is the line corresponding to the binding energy of the M1-shell at an energy of 2.60 keV [58]. The activities of the two most prominent lines ^{179}Ta (L1) and ^{179}Ta (K) were calculated to be $(177.24 \pm 5.59) \mu\text{Bq/kg}$ and $(207.71 \pm 6.57) \mu\text{Bq/kg}$, respectively. For the L2-line, an activity of $(25.69 \pm 2.03) \mu\text{Bq/kg}$ was determined [43]. The resulting L/K-capture ratio is 0.98 ± 0.04 , a value which is in good agreement with the ratio of 1.4 ± 0.4 published in [163] but which differs from the value of 0.63 ± 0.06 found in [164].

Similarly, also the activation process $^{183}\text{W}(p,t)^{181}\text{W}$ is possible. The resulting isotope ^{181}W decays via EC into an excited ^{181}Ta nucleus (half-life 121 days) which de-excites under emission of γ -radiation with an energy of 6.2 keV. The released energy of ~ 74 keV is the sum of this 6.2 keV γ -radiation and of the binding energy of the Ta K-shell electron (67.4 keV) [58]. The decay of ^{181}W was found to have an activity of $(107.67 \pm 19.77) \mu\text{Bq/kg}$ [43].

^{210}Pb Line

A γ -line originating from ^{210}Pb is present at 46.54 keV. This isotope is part of the ^{238}U decay chain (see figure 1.4) and decays via emission of a β -particle to ^{210}Bi as shown in the decay scheme of figure 7.2 (a). In 84 % of the decays the endpoint of the β -spectrum is 17 keV and the daughter nucleus ^{210}Bi is in an excited state which relaxes within 3 ns to the ground state under the emission of a γ -ray with an energy of 46.54 keV [58]. When

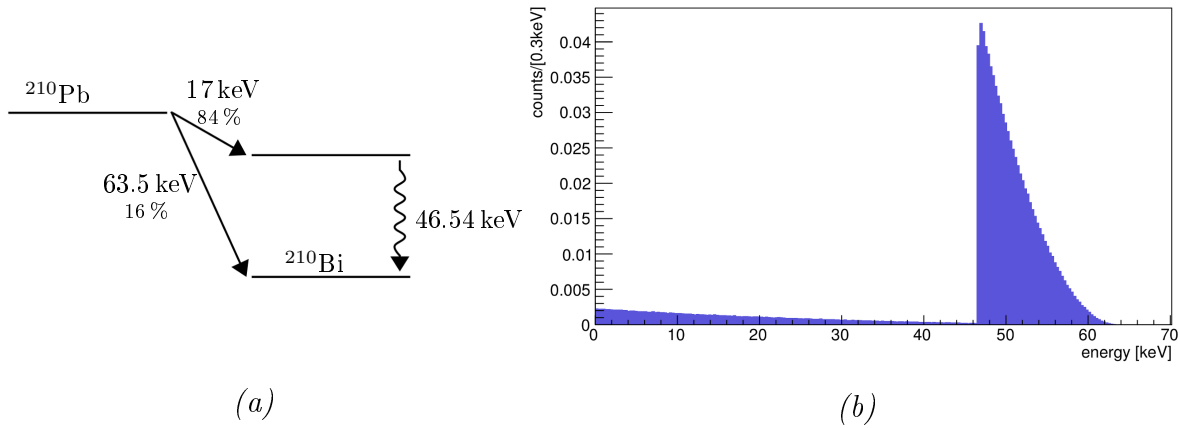


Figure 7.2.: (a) Scheme of the β -decay of the isotope ^{210}Pb . In 84 % of the decays the daughter nucleus ^{210}Bi is in an excited state which relaxes within 3 ns to the ground state under the emission of a γ -ray. (b) Simulated ^{210}Pb spectrum (integral normalized to 1) as it would be recorded by a CRESST detector in case of a crystal-intrinsic contamination. The main contribution (84 %) between 46.5 keV and 63.5 keV is the sum of the β -decay into the excited state and the subsequent 46.54 keV γ -radiation. The remaining 16 % of the decays create a β -spectrum extending from zero energy up to 63.5 keV.

this decay happens externally, only the γ -radiation is detected in the crystal resulting in a line as observed in figure 7.1 (a) (activity = $(75.26 \pm 4.73) \mu\text{Bq/kg}$ [43]). In the case of an internal contamination of ^{210}Pb within the CaWO_4 crystal, also the β -particle would be detected. In the energy spectrum, the sum of the γ -radiation and the β -decay would be visible as a β -spectrum starting at 46.5 keV and extending up to 63.5 keV. In the remaining 16 % of the decays, the β -spectrum is distributed between 0 and the Q-value of 63.5 keV. Simulating a crystal-intrinsic ^{210}Pb -contamination results in the total spectrum shown in figure 7.2 (b) (credit: H. Kluck et al. [165,166]). The integral of the complete spectrum is, hereby, normalized to 1.

^{234}Th Lines

A similar behaviour is valid for the β -decaying isotope ^{234}Th , for which the resulting daughter nucleus can be in excited states with different energy levels. Observing the discrete γ -lines at 63.3 keV, 92.4 keV and 92.8 keV in figure 7.1 (a) and no hint for related β -spectra implies that also here an external origin can be assumed in case of TUM40.

Continuous Contributions

The contribution of β -decays within the TUM40 crystal was investigated by a Monte Carlo simulation in [82]. A fraction of ~ 30 % of the total background rate was found to be caused by such intrinsic β/γ -emitters. In the energy range (1-40) keV, the highest activity values of $346 \mu\text{Bq/kg}$ and $93 \mu\text{Bq/kg}$ can be attributed to the isotopes ^{234}Th and ^{227}Ac , respectively.

The continuous Compton background originating from external sources constitutes a negligible activity value of less than 0.03 counts/(kg keV day) [82].

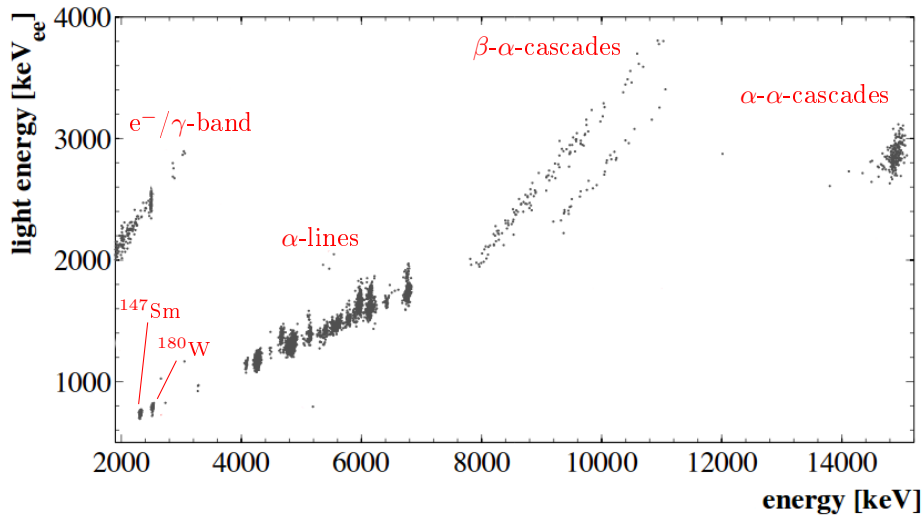


Figure 7.3.: α -decays observed in the detector crystal TUM40 during 29 kg days of its operation in CRESST-II Phase 2. At energies of ~ 2.5 MeV, α -lines due to the decays of ^{147}Sm and ^{180}W are visible. The α -region is dominated by single α -lines in the energy range (4 - 7) MeV originating from decays within the natural decay chains. β - α -cascades and α - α -cascades occur at even higher energies when the cryogenic detector is not able to separate two subsequent decays happening within a time window of $\lesssim 10$ ms. Plot adapted from [82].

The exposure achieved for the CRESST-III Phase 1 data set analyzed in the present work is ~ 2.75 kg days (see section 7.2) for each detector. For a better comparison, the energy spectrum of a partial data set of TUM40 with this exposure is plotted in figure 7.1 (b). Due to the lower statistics, only the K- and L1-lines of ^{179}Ta as well as the copper K_α -line and the 46.5 keV γ -line of ^{210}Pb can clearly be identified in this spectrum.

7.1.2. α -Spectrum

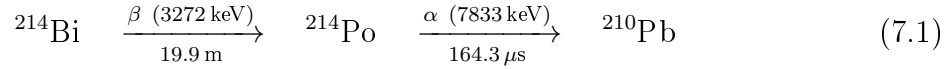
A detailed α -analysis of TUM40 was performed in [82] for a data set with an exposure of 29 kg days. The α -region in the light energy versus energy plane is depicted in figure 7.3. Apart from the high-energy part of the e^-/γ -band extending up to ~ 2.6 MeV, which is the energy of the highest γ -line (^{208}Tl) occurring in the natural decay chains, different α -features are visible in the plot:

Single α -Lines

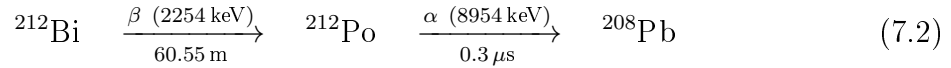
Single α -lines are found at energies between 4 MeV and 7 MeV. These lines originate from α -decays within the natural decay chains (compare figure 1.4). The total α -activity in this region is (3.08 ± 0.04) mBq/kg for TUM40. The two most prominent lines with an activity of ~ 1 mBq/kg each are caused by the isotopes ^{238}U and ^{234}U [82].

Cascade Decays

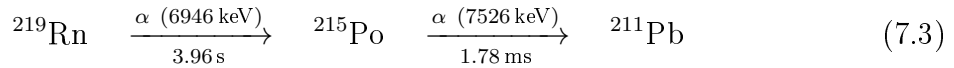
At higher energies above ~ 8 MeV, cascade events are indicated in figure 7.3. If a β - or an α -decay is followed by another α -decay with a half-life below ~ 10 ms, the cryogenic detectors are not able to separate the two pulses. Two such β - α -cascades with involved half-lives of $164.3 \mu\text{s}$ and $0.3 \mu\text{s}$ are the so-called Bi-Po-coincidences



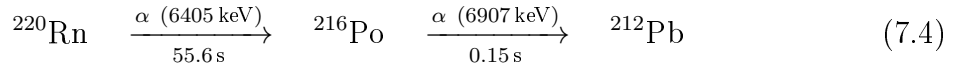
and



The Q-values of the respective decays are given above the arrows, the half-lives below. The summed energy deposited in the crystal is composed of the continuous β -spectrum and of the discrete α -energy. This results in a band which is parallel to the e^-/γ -band starting at 7833 keV (8954 keV) and extending up to 11 105 keV (11 208 keV) in case of the cascade of equation 7.1 (equation 7.2). Furthermore, a superposition of two α -decays (α - α -cascade) can occur in the following cases:



and



The half-life of the ${}^{215}\text{Po}$ decay of equation 7.3 is very short with a value of 1.78 ms and a detection of separated pulses is also here not feasible. The result is a discrete line at an energy of 14 472 keV. In case of the ${}^{220}\text{Rn}$ - ${}^{216}\text{Po}$ -cascade, the involved half-life is 150 ms which is about half of the record length used in CRESST-II Phase 2 (327.68 ms). As a consequence, in most cases pile-up events within the same record window are observed. If the two pulses are close enough to each other, the template fit can not disentangle the two pulse components leading to a discrete detected energy of 13 312 keV. On the other hand, if the pulses of the two decays are separated, only one of them is fitted by the template fit routine and the resulting data point lies in the region of single α -lines. In a few cases, the second pulse can also be lost when it occurs in the dead time after the record. In figure 7.3, no events are observed as ${}^{220}\text{Rn}$ - ${}^{216}\text{Po}$ -cascade.

${}^{147}\text{Sm}$ and ${}^{180}\text{W}$

In the energy range (2-3) MeV, the lines of the two α -decaying isotopes ${}^{147}\text{Sm}$ and ${}^{180}\text{W}$ are dominating. The natural α -decay of ${}^{180}\text{W}$ (isotopic abundance of $\sim 0.1\%$) with a half-life of $T_{\frac{1}{2}} = (1.8 \pm 0.2) \cdot 10^{18}$ and a Q-value of $Q = (2516.4 \pm 1.1 \text{ (stat)} \pm 1.2 \text{ (sys)})$ was first discovered with CRESST CaWO_4 detectors in 2004 [167]. Typical activities observed in TUM-grown as well as in commercial CaWO_4 detector crystals are $\sim 30 \mu\text{Bq/kg}$ [82,158]. ${}^{147}\text{Sm}$, on the other hand, is a rare-earth element being present in (formerly investigated) CaWO_4 crystals to a different extent ($50 \mu\text{Bq/kg}$ - 1 mBq/kg). Only in a few commercial CaWO_4 detector crystals also the α -decays of other rare-earth isotopes such as ${}^{144}\text{Nd}$ or ${}^{152}\text{Gd}$ were observed [158].

module	crystal	m [g]	$t_{\text{live, tot}}^{e/\gamma}$ [h]	$t_{\text{live, stab}}^{e/\gamma}$ [h]	$t_{\text{live, tot}}^{\alpha}$ [h]	$t_{\text{live, stab}}^{\alpha}$ [h]
A	TUM56	23.6	2836.26	2711.96	2578.93	2499.15
B	TUM73-1	24.5	2854.33	2754.23	2596.11	2526.05
D	TUM56	23.6	2812.23	2723.52	2564.54	2520.43
E	TUM73-2	24.5	2844.59	2760.29	2591.02	2545.01

Table 7.1.: Information on the four CRESST-III Phase 1 detector modules investigated in the present work. Included are the respective crystal type and mass as well as the live time of the data set used for the analysis of the e^-/γ -band ($t_{\text{live}}^{e/\gamma}$) and of α -decays (t_{live}^{α}). Due to the application of the stability cut, the total live time is reduced by (3.0-4.5) % (e^-/γ) and by (1.7-3.1) % (α).

7.2. Analyzed CRESST-III Phase 1 Detectors and Data Set

In total, ten detector crystals with a mass of ~ 24 g and a volume of $(20 \times 20 \times 10) \text{ mm}^3$ each are installed in CRESST-III Phase 1 (compare table 2.3). In the present work, the four detector modules A, B, D and E representing the crystals TUM56 and TUM73 have been investigated. The detector modules A and E can be operated completely, i.e. including all iSticks. In case of the modules B and D, two iSticks and one iStick, respectively, are operational. Also in detector module J all included detectors are working. However, periods of high noise conditions, low iStick signals as well as a change in the TES-operation point make an analysis more complicated. As this module also involves a detector crystal of the ingot TUM56, no radiopurity analysis was performed. Still, detector module J has good potential for a future dark matter analysis. Concerning the detector modules C and G, the thermometers of the iSticks or of the light detector did not show a transition to the superconducting state. In case of module I, no detector is operational. Detector modules F and H work in principle, but feature only very small phonon signals.

The list of all files included in the data set used in the present work can be found in table E.1 of appendix E. The analysis of the e^-/γ -band was performed for background data recorded within about five months between October 2016 and March 2017. As the parameters of the iSticks were changed after the first few background files, only data after this change was used for the α -analysis of the present work. The files which are not included in the α -data set are marked in grey in table E.1. In between, single files are excluded due to earthquakes, extremely high noise conditions or failures of the data taking.

For each investigated detector module, information on the mass m of the included CaWO_4 detector crystal as well as on the live time t_{live} are summarized in table 7.1. The detector crystals of modules A and D have a mass of 23.6 g each and both originate from the crystal ingot TUM56 which was produced from the non-purified batch 1 raw materials of MV Laboratories (compare table B.1 in appendix B.5). TUM73-1 and TUM73-2 were cut from the ingot TUM73 (produced from powder batch 2 with appli-

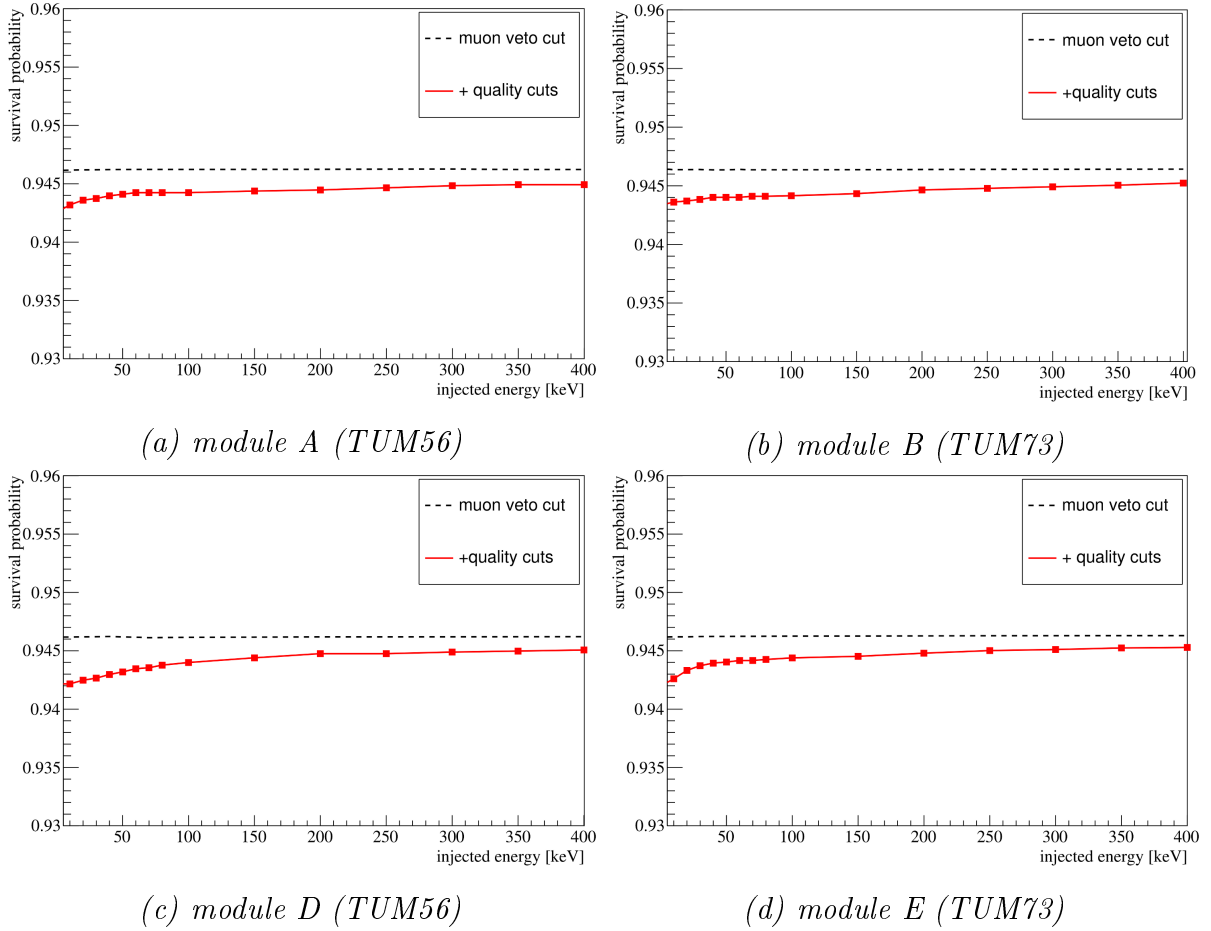


Figure 7.4.: Energy-dependent e^-/γ survival probabilities of the analyzed detector modules A (a), B (b), D (c), and E (d) after the application of the muon veto cut (dashed black line) and of data quality cuts (red). A survival probability of 1 corresponds to the data set after the stability cut. In all detectors, the highest fraction of pulses is removed by the muon veto cut ($\sim 5.4\%$). After having applied not very strict data quality cuts, the red data points mark the simulated events with discrete energies. The values in between are interpolated. A fraction of less than 1% is discarded by the quality cuts with a tiny energy dependence only observed for energies below ~ 100 keV.

cation of version 1 purification, see section 5.3.2) and have a mass of 24.5 g each. They are operated in the detector modules B and E, respectively. The total live time $t_{\text{live, tot}}^{e^-/\gamma}$ of the e^-/γ data set ranges between 2812 h (D) and 2854 h (B). The stability cut (see section 6.4.1) removes a fraction of (3.0-4.5)% resulting in a stable live time $t_{\text{live, stab}}^{e^-/\gamma}$ well above 2700 h for each detector. The removal of a few data files for the α -analysis results in a reduced total live time $t_{\text{live, tot}}^\alpha$ which is slightly below 2600 h for all modules. After the application of a weak stability cut removing a fraction of (1.7-3.1)% of the data, a stable live time $t_{\text{live, stab}}^\alpha$ with a value ranging between 2499 h in case of module A and 2545 h in case of module E is left.

The e^-/γ survival probabilities $\epsilon_{e^-/\gamma}$ of the four investigated detector modules are plotted in figure 7.4. A value of 1 corresponds to the data set after the application of the

stability cut. An energy-independent fraction of $\sim 5.4\%$ is removed by the muon veto cut introduced in section 6.4.6 (dashed black line). In the case of quality cuts (see section 6.4.3), the red data points mark the various energies simulated between 5 keV and 400 keV. The data points are interpolated (solid red lines) yielding the survival probability. The quality cuts applied to the data set of the present work are not very strict which results in a small fraction of less than 1% of valid events discarded in each module. The final survival probabilities after the application of all cuts are approximately constant at values of $\sim 94.5\%$. Only for energies below ~ 100 keV, a tiny decrease is observable towards lower energies.

In case of the α -analysis, a few cuts are applied which remove only pulses with arbitrary or completely different pulse shapes (compare section 6.6). Therefore, the α survival probability ϵ_α is close to 1. A small error might be introduced due to the removal of random coincidences of α -pulses with other particle pulses: The observed rate of particle pulses (excluding test pulses) is on the average ~ 10 MHz for each detector. With typical total α -activities of 5 mBq/kg, the rate for pulses being coincident within the time of the record window (655.36 ms in case of CRESST-III Phase 1) is ~ 0.03 MHz/kg. Assuming the most conservative scenario that all these coincident α -events are not recognized gives a maximal error of $\sim 1\%$.

7.3. e^-/γ Band

The exposure of the e^-/γ data set investigated is ~ 2.75 kg days for each detector. The background spectra in the energy range (5-100) keV are shown in figure 7.5 for the CRESST-III Phase 1 detector modules A (a), B (b), D (c), and E (d). It should be mentioned that the energy is reconstructed here using the ^{57}Co calibration source (see section 6.3). As the energy scale is not linear over the whole range, a deviation of a few percent ($< 5\%$ in case of modules A, D, E and $\sim 10\%$ for module B) is observed at low energies. The different aspects of the spectra are treated in the following sections.

7.3.1. External Radiation

In CRESST-III, each detector module is surrounded by a copper housing with a thickness of 2 mm. This housing efficiently blocks external electrons as well as low-energy γ -radiation. The fraction of radiation entering the housing is negligible for γ -energies below 20 keV and increases to $\sim 1\%$ at 50 keV [159]. External γ -rays with higher energies can contribute to the low-energy spectrum due to Compton scattering. However, this background source was found to be negligible in TUM40 (see section 7.1.1). Assuming a similar behaviour for CRESST-III modules leads to the conclusion that the main background contribution below ~ 50 keV is of module-intrinsic or even of crystal-intrinsic origin.

7.3.2. Background Rates

The background rates calculated for each detector module investigated in the present thesis are listed in the upper part of table 7.2. All rate values obtained in the energy range

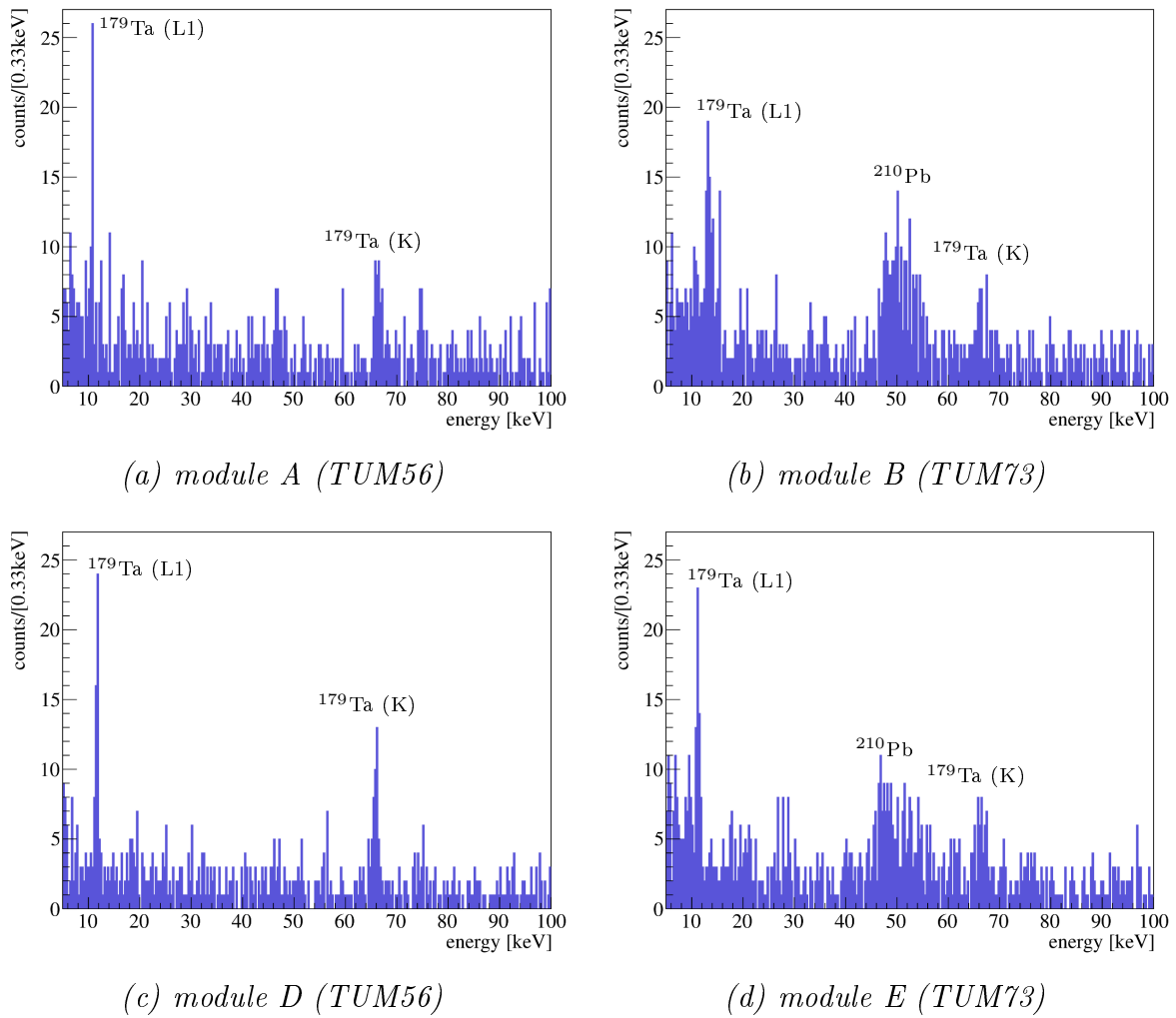


Figure 7.5.: Energy spectra of the CRESST-III Phase 1 detector modules A (a), B (b), D (c), and E (d) with an exposure of ~ 2.75 kg days each. Like in the spectrum of TUM40 in figure 7.1, the ^{179}Ta K- and L1-lines originating from cosmogenic activation are clearly visible. In addition, the modules B and E including crystals of TUM73 feature a pronounced internal ^{210}Pb β -spectrum in contrast to TUM56 crystals operated in modules A and D. As the energy scale is not linear up to 100 keV, the reconstructed energies deviate from the literature values by a few percent ($< 5\%$ for modules A, D, E and $\sim 10\%$ for module B). Calculated rates and activities are listed in table 7.2.

(10-40) keV are comparable. The highest rate of (4.38 ± 0.23) counts/(kg keV day) is found for module B whereas D features the lowest rate of (3.51 ± 0.22) counts/(kg keV day). As the ^{179}Ta L1-line is included in the energy region (10-40) keV, a background rate was also calculated between 30 keV and 40 keV, where no γ -lines are observed. In this range, the rates of all detector modules are compatible with an average value of ~ 2.5 counts/(kg keV day).

module	A (TUM56)	B (TUM73)	D (TUM56)	E (TUM73)
energy range	rate [counts/(kg · keV · day)]			
(10 - 40) keV	4.19 ± 0.24	4.38 ± 0.23	3.51 ± 0.22	3.88 ± 0.22
(30 - 40) keV	2.78 ± 0.33	2.64 ± 0.32	2.30 ± 0.30	2.26 ± 0.29
(46.5 - 63.5) keV	2.66 ± 0.25	5.83 ± 0.36	2.28 ± 0.23	5.57 ± 0.35
origin	activity [$\mu\text{Bq/kg}$]			
^{210}Pb	< 111.35	627.89 ± 94.07	< 119.88	652.46 ± 89.75
^{179}Ta (L1)	149.48 ± 49.62	250.67 ± 101.14	198.03 ± 54.63	150.36 ± 57.07
^{179}Ta (K)	174.18 ± 60.04	146.25 ± 67.61	169.36 ± 64.71	144.74 ± 49.69

Table 7.2.: The upper part of the table shows the rates in different energy regions of the e^-/γ -band determined for the four detector modules A, B, D, and E. In the lower part, several activities are estimated. The L1- and K-lines of ^{179}Ta were fitted by the sum of a Gaussian function and a constant (see figure 7.6) to calculate the activity according to equation 6.1. A corresponding 84 % activity of ^{210}Pb was derived from the different rates in the energy regions (46.5-63.5) keV and (30-40) keV. The detector crystals of TUM73 included in the modules B and E feature an intrinsic contamination with ^{210}Pb with an activity of $\sim 650 \mu\text{Bq/kg}$. In case of modules A and D, only upper limits could be estimated indicating that no visible excess above the background is present there.

7.3.3. Internal ^{210}Pb Contamination

The modules B and E including detector crystals of the crystal ingot TUM73 feature a pronounced distribution of events in the energy range (46.5-63.5) keV (see figures 7.5 (b) and (d)). As explained in section 7.1.1, such a distribution is due to an internal contamination with ^{210}Pb resulting in a β -spectrum starting at the energy of the simultaneous γ -emission at 46.5 keV and extending up to 63.5 keV. In case of the TUM56 detector crystals operated in modules A and D, only a hint for a peak with a much lower rate is visible. To estimate the activity of the internal ^{210}Pb contamination, the count rate in the energy range of the β -spectrum (46.5-63.5) keV is also listed in table 7.2. This rate is increased by more than a factor of two in the TUM73-crystals of modules B and E compared to the detector modules A and D. After having subtracted the rate of the background region (30-40) keV (which is taken as a reference), the count rate can be converted into a ^{210}Pb activity as done in the second part of the table. The result are activities of $(627.89 \pm 94.07) \mu\text{Bq/kg}$ for module B and $(652.46 \pm 89.75) \mu\text{Bq/kg}$ in case of module E. These activities correspond to 84% of the ^{210}Pb -decays. In the remaining 16 %, a β -spectrum distributed between 0 and the Q-value of 63.5 keV should be visible [58] which means that also the total count rate down to zero energy is slightly increased due to ^{210}Pb . Using the simulated spectrum of figure 7.2 (b), it is estimated that 8.9 % of the total ^{210}Pb activity contribute to the background rate in the energy region (10-40) keV. For the calculated total ^{210}Pb activities of $\sim 0.75 \text{ mBq/kg}$ (module B) and $\sim 0.78 \text{ mBq/kg}$ (module E), this corresponds to activity values of $67 \mu\text{Bq/kg}$ and $70 \mu\text{Bq/kg}$, respectively, or to a rate of $\sim 0.2 \text{ counts}/(\text{kg keV day})$.

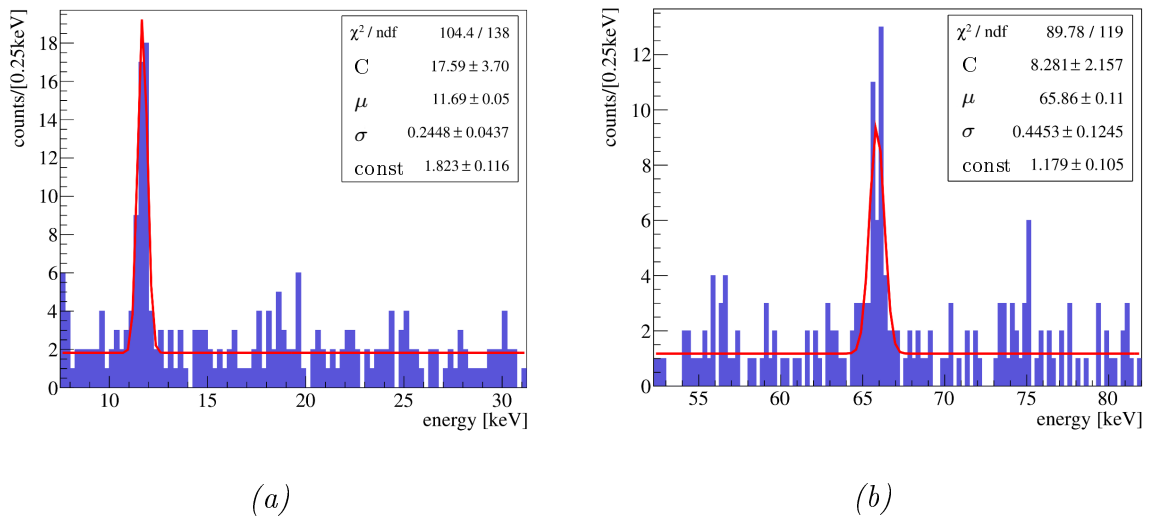


Figure 7.6.: ^{179}Ta L1- (a) and K- (b) lines originating from the cosmogenic activation of tungsten shown for module D. To estimate an activity, each line is fitted by the sum of a constant and of a Gaussian function (red line). The fit parameters including the amplitude C , the mean μ , the width σ and a constant part are also drawn. The resulting activities calculated according to equation 6.1 can be found in table 7.2.

In case of detector modules A and D, a subtraction of the event rate in the region (46.5-63.5) keV from the one in the reference region (30-40) keV leads to negative (not-physical) values. This implies that no hint for an excess above the background determined in the reference region is found. By assuming Gaussian distributions, upper limits of $< 111 \mu\text{Bq/kg}$ (A) and $< 119.88 \mu\text{Bq/kg}$ (D) can be calculated with a confidence level of 95 % for the 84 % activity of ^{210}Pb .

7.3.4. Cosmogenic Activation Lines

Like in the spectrum of TUM40 (figure 7.1), the K- and L1-lines of ^{179}Ta originating from cosmogenic activation are visible in figure 7.5 (a)-(d). Figure 7.6 illustrates exemplarily for module D, how the L1-line (a) and the K-line (b) are fitted by the sum of a constant and a Gaussian function (red line). The fit parameters including the amplitude C , the mean μ , the width σ as well as the constant are also shown together with their statistical errors. The mean values deviate by $\sim 4\%$ and less than 1 % from the literature values of the L1- and K-line, respectively. The deviation is smaller at 65.35 keV since this line is close to the energy value used for calibration. To achieve a better energy reconstruction around 10 keV, a recalibration can be performed with the 11.27 keV-line. The 1σ energy resolution is $\sim 2\%$ for the L1-line and increased to 7 % in case of the K-line at higher energies¹. The constant used in the fit is reduced at higher energies.

The activities are calculated according to equation 6.1 resulting in the values shown in the lower part of table 7.2. Due to the low statistics, the errors are relatively

¹The increased energy resolution at higher energies is not related to phonon properties, but is caused by the truncated template fit.

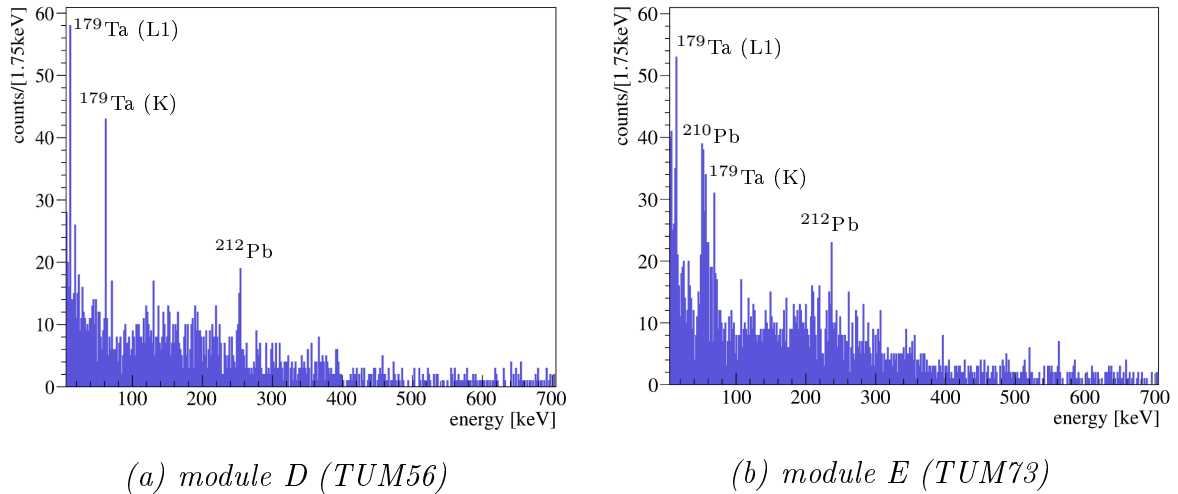


Figure 7.7.: Energy spectra up to 700 keV of the detector modules D (a) and E (b). With the statistics of the data investigated in the present work, only a γ -line at 238.63 keV [58] originating from ^{212}Pb can clearly be identified. In both cases, the energy scale deviates by about 10 % relative to the literature value, as no test pulses are available in this region and as only a linear extrapolation was applied.

large. The calculated L1-activities range between $(149.48 \pm 49.62) \mu\text{Bq/kg}$ (A) and $(250.67 \pm 101.14) \mu\text{Bq/kg}$ (B) which agrees within uncertainties with the values obtained for TUM40 (compare section 7.1.1). The same is valid for the slightly lower activities of the K-line ranging between $(144.74 \pm 49.69) \mu\text{Bq/kg}$ (E) and $(174.18 \pm 60.04) \mu\text{Bq/kg}$ (A). This is reasonable as all powders and crystals were exposed about the same time to cosmic radiation. The capture-ratios L1/K (neglecting L2 which is not separable with this low statistics) are 0.86 ± 0.42 , 1.71 ± 1.27 , 1.17 ± 0.54 and 1.04 ± 0.53 for the four modules A, B, D, and E, respectively. Within the large uncertainties (due to low statistics), the ratios are compatible with the results of [43], with the value of 1.4 ± 0.4 found in [163] and also with the value of 0.63 ± 0.06 published in [164].

7.3.5. Background Spectra up to 700 keV

Above 100 keV, only few features are observed with the statistics of the data investigated in the present work. The spectra of the modules D and E up to 700 keV are exemplarily shown in figure 7.7 (a) and (b) for the two detector crystal types TUM56 and TUM73, respectively. As the calibration is not supported by test pulses in this energy range, (compare section 6.3.2), a linear energy extrapolation was applied. This implies that the calibrated energy can deviate from the real energy. In case of the γ -line at an energy of ~ 240 keV, which is observed in both detector modules and which can be attributed to the decay of the isotope ^{212}Pb , the deviation from the literature value of 238.63 keV [58] is (5-10) %. The scenario of the ^{212}Pb -decay is similar to that of ^{210}Pb : in 82.5 % of the decays, the daughter nucleus is in an excited state and decays to the ground state under emission of γ -radiation with an energy of 238.63 keV. Therefore, in case of an intrinsic contamination the combination of β -spectrum and γ -radiation extending up to

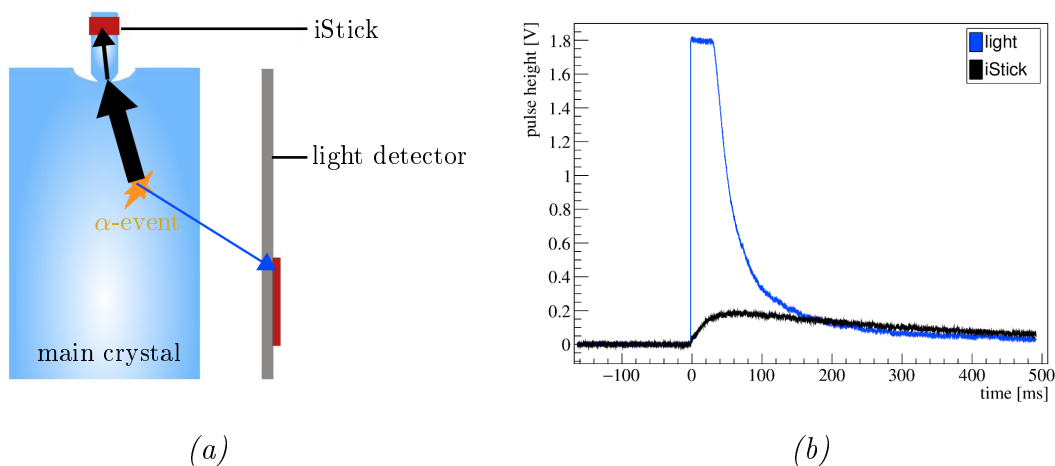


Figure 7.8.: (a) Schematic illustration how an α -event happening in the main CaWO_4 detector crystal produces a phonon signal part of which can be detected as degraded signal in the iStick (black arrows). The simultaneously emitted scintillation light is read out by the light detector (blue arrow). (b) Neglecting the main phonon signal, the resulting event consists of a light pulse (blue) and a degraded iStick pulse (black). Plotting the energy of the light channel versus the energy of the iStick channel results in a separated band containing the α -events.

the β -endpoint of 573.8 keV [58] can be observed. A clear statement in case of the two plots shown in figure 7.7 is difficult. However, detector module E (b) appears to feature a higher distribution in this energy region which could hint towards a contribution of an internal ^{212}Pb -contamination. The calculation of a rate in the energy range between the ^{212}Pb -line and the added β -spectrum with a maximal energy of 335.2 keV confirms the increased background distribution in module E ((0.89 ± 0.03) counts/(kg keV day)) compared to module D ((0.58 ± 0.03) counts/(kg keV day)).

Additional β -decaying isotopes with an endpoint energy below ~ 500 keV seem to contribute in case of both detector modules. Possible candidates are ^{90}Sr with a Q-value of 546.0 keV, ^{234}Th which has in 70.3% of its decays an endpoint energy of 199.08 keV, or ^{231}Th whose β -spectrum (in combination with several γ -lines) extends up to 389.5 keV [58]. Below 100 keV, also the isotope ^{228}Ra with β -spectra up to 45.9 keV could play a role. However, more statistics is necessary for a better investigation of the isotopes involved.

7.4. α -Events

Figure 7.8 (a) illustrates in detail, which signals can be used for the analysis of α -events in CRESST-III Phase 1. An α -decay produces a large phonon signal, part of which crosses to the iStick where it can be detected as degraded signal (black arrows). The simultaneously emitted scintillation light is read out by the light detector (blue arrow). The two resulting pulses in light and iStick channels are shown in figure 7.8 (b). Their fitted amplitudes depend on the energy deposited in the CaWO_4 absorber crystal. Like

module	A (TUM56)	B (TUM73)	D (TUM56)	E (TUM73)
origin	activity [mBq/kg]			
single α -lines, total	2.020 ± 0.098	3.627 ± 0.128	$< 2.998 \pm 0.118$	3.319 ± 0.122
α -cascades, total	0.353 ± 0.041	0.660 ± 0.054		0.682 ± 0.055
$^{147}\text{Sm} + ^{180}\text{W}$	3.436 ± 0.204	0.063 ± 0.017	3.399 ± 0.185	0.071 ± 0.018

Table 7.3.: Total α -activities in the regions of single α -lines and of α -cascades (originating from the natural decay chains) as obtained for the four investigated detector modules A, B, D, and E. Due to the poor resolution of the iStick channel in D ($> 10\%$ at 2.3 MeV), only a combined upper limit is given for both regions there. Also included is the activity of an α -event population around ~ 2.5 MeV. It can be attributed to the decays of ^{147}Sm and ^{180}W as was observed in former work [82, 158]. The reason for the large activity of ~ 3.4 mBq/kg in the TUM56-modules A and D is presently unknown.

in the case of the main crystal, a particle discrimination can be achieved with the help of both signals. In particular, the α -band can be separated from other background events via plotting the energy of the light signal versus the energy of the iStick channel. After the application of the preparation steps to the α -data set (with exposures of ~ 2.5 kg days in each detector) as described in section 6.6, such scatter plots are drawn for the detector modules A and D (TUM56) in figure 7.9 and for the modules B and E (TUM73) in figure 7.10. The energy of the light detector E_L (y-axis) was either determined via a linear extrapolation of the test-pulse energy-calibration (B, E) or was adapted via a prominent α -line (A, D). In case of the iStick channel on the x-axis, the region of single α -lines was identified in order to roughly estimate the energy scale. A more accurate calibration is only feasible when several α -contributions over the whole energy range can be identified.

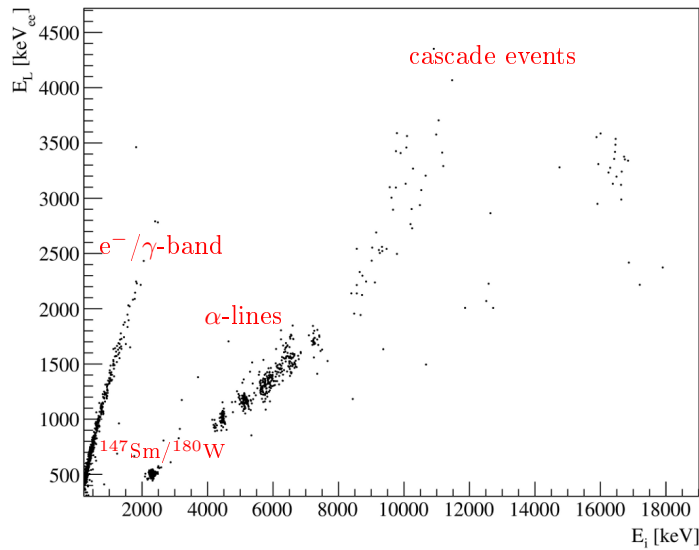
Single α -lines as well as cascade events² as explained in section 7.1.2 are visible in the scatter plots of figures 7.9 and 7.10. Depending on the resolution of the iStick channel, information about the radiopurity can be derived for the different detectors.

7.4.1. Total α -Activities

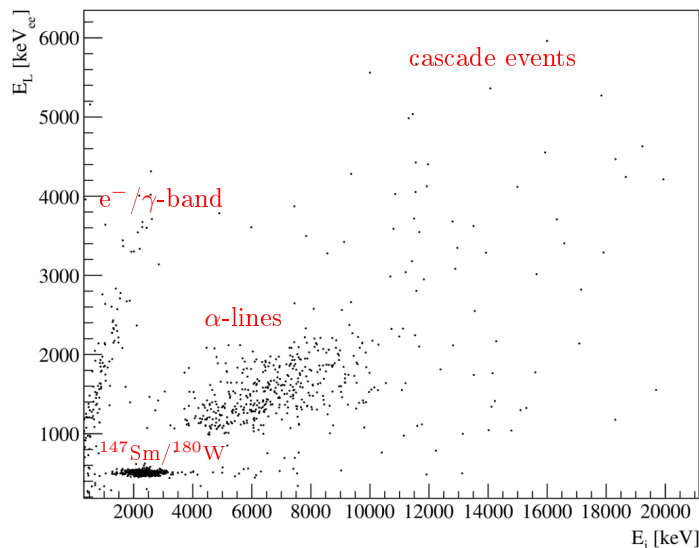
The summed activities of the different α -features described in section 7.1.2 are listed in table 7.3. In case of the detector modules A, B, and E, a total activity of the α -lines was calculated by counting all events in the plotted iStick energy ranges from (4000 - 8000) keV³. A summed activity is given for all cascade events above 8000 keV. Due to the poor resolution observed in module D ($> 10\%$ at 2.3 MeV, probably caused by the fact that only one iStick is working there), only an upper limit is set on the combined activity of single and cascade decays via counting all events above 4000 keV. No selection is

²The distribution of the α - α -cascades is slightly broadened as events with such high energies are difficult to be reconstructed well, especially when effects like pile-up are included.

³Usually, a total α -activity is calculated in the energy range (4 - 7) MeV. Due to deviations in the energy calibration (compared to literature values), single α -lines extend up to ~ 7.5 MeV and cascade events start above 8 MeV in the plots shown in figures 7.9 and 7.10.

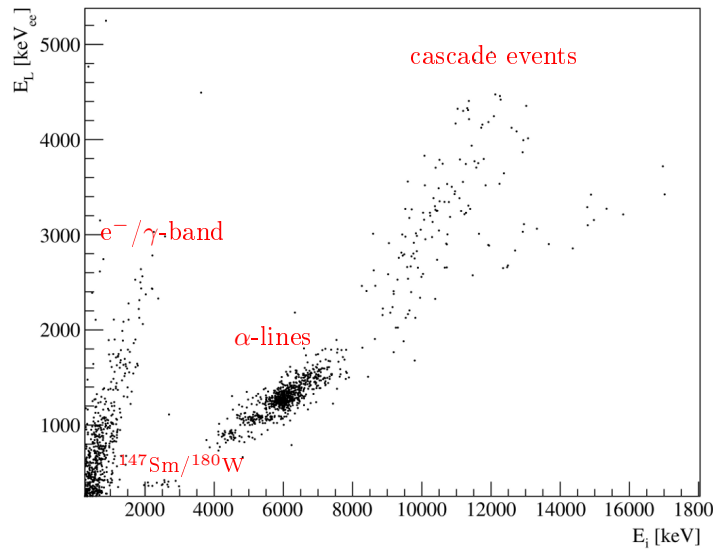


(a) module A (TUM56)

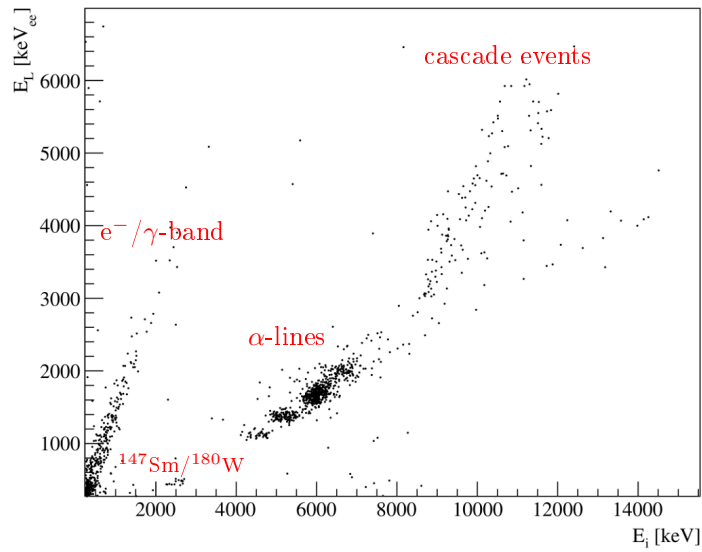


(b) module D (TUM56)

Figure 7.9.: Scatter plots of the α -region in the light energy (E_L) versus *iStick* energy (E_i) plane for the detector modules A (a) and D (b) which include both detector crystals of TUM56. The energy scale in the *iStick* channel is only roughly estimated. The high-energy part of the e^-/γ -band as well as several features in the α -region are visible. Single α -lines originating from the natural decay chains occur at energies between 4 MeV and 8 MeV and are rather well resolved ($\sigma \sim 1\%$) in (a) whereas the resolution is rather poor ($> 10\%$) in (b), probably since only one *iStick* is operable there. Cascade events ($\alpha + \alpha$ or $\beta + \alpha$) are observable at energies higher than 8 MeV. A pronounced line is present at energies slightly above 2 MeV, where events due to the decays of ^{147}Sm and ^{180}W are expected.



(a) module B (TUM73)



(b) module E (TUM73)

Figure 7.10.: Scatter plots of the α -region in the light energy (E_L) versus iStick energy (E_i) plane for the detector modules B (a) and E (b) which include both detector crystals of TUM73. The energy scale in the iStick channel is only roughly estimated. The high-energy part of the e^-/γ -band as well as several features in the α -region are visible. Single α -lines originating from the natural decay chains occur at energies between 4 MeV and 8 MeV, whereas cascade events ($\alpha + \alpha$ or $\beta + \alpha$) are observable at still higher energies. Slightly above 2 MeV, events due to the decays of ^{147}Sm and ^{180}W can be identified.

applied to the light detector as flux quantum losses (compare section 6.4.2) occurred there for a few α -events resulting in wrong template fit and energy reconstruction of the light detector (see, e.g., data points below the main region of the α -lines in figure 7.10 (b)). The lowest total α -activities of (2.020 ± 0.098) mBq/kg (single α -lines) and of (0.353 ± 0.041) mBq/kg (cascade decays) are observed for module A. This result fits well with the upper limit of ~ 3 mBq/kg calculated for the second TUM56-detector crystal of module D. The total α -activities of single lines of the modules B and E including the detector crystals TUM73-1 and TUM73-2 are with values of (3.627 ± 0.128) mBq/kg and (3.319 ± 0.122) mBq/kg almost compatible within the statistical error bars but increased by a factor 1.6-1.8 with respect to detector module A. Like in case of module A, the summed activity of the cascade events is about 20 % of that of the single lines, namely (0.660 ± 0.054) mBq/kg and (0.682 ± 0.055) mBq/kg for modules B and E, respectively. Concerning ^{147}Sm and ^{180}W -lines, a rather high activity of 3.4 mBq/kg (see table 7.3) is present in the two modules A and D whereas activities of (0.063 ± 0.017) mBq/kg and (0.071 ± 0.018) mBq/kg in detector modules B and E are comparable to former results [82, 158].

7.4.2. Single α -Activities

Judging from figures 7.9 and 7.10, the best resolution of $\sim 1\%$ for the α -region in the iStick channel is achieved by detector module A. The corresponding α -spectrum is plotted in figure 7.11. In the lower part of the figure, the literature energies of the various α -decays of the natural decay chains of ^{238}U (green), ^{235}U (blue), and ^{232}Th (red) are drawn. The energy scale of the iStick spectrum was slightly corrected compared to figure 7.9 (a) in order to fit to the energies given in the literature. In this way, despite of the low statistics, the lines caused by the isotopes ^{232}Th , ^{238}U and ^{211}Bi can clearly be identified in the spectrum of figure 7.11. The decays of the isotopes ^{235}U , ^{230}Th , ^{234}U and ^{226}Ra cannot be resolved which results in a superposition of lines at ~ 4.85 MeV. The activities derived for the identified lines can be found in table 7.4. Due to the relatively short half-lives (< 19 days) of several subsequent decays in the ^{235}U chain (compare figure 1.4), ^{211}Bi is in equilibrium with the isotopes ^{207}Tl (β), ^{211}Pb (β), ^{215}Po (α), ^{219}Rn (α), ^{223}Ra (α), ^{227}Th (α), and ^{227}Ac (β). Furthermore, an equilibrium is also present between ^{238}U and the β -decaying isotopes ^{234}Th and ^{234m}Pa . Although the half-life of the subsequent α -decay of ^{234}U is very long, it can be assumed that the fraction of ^{238}U - and ^{234}U -decays is about 1 and not changed during crystal production. This implies a ^{234}U -activity of 0.293 mBq/kg leaving a value of 0.116 mBq/kg for ^{235}U , ^{230}Th , and ^{226}Ra .

Only the iSticks of module A feature a sufficient resolution to separate the single α -lines. In the cases of modules D and B, a determination of single activities is not feasible. A partial separation of a few structures in the region of single α -lines is observed for module E. However, as can be seen in figure 7.10 (b), this separation can be attributed more to the performance of the light detector than to that of the iSticks. A projection of the region containing the single α -lines onto the E_L -axis of figure 7.10 (b) is shown in figure 7.12. The light energy E_L is, hereby, adapted to fit the α -energy scale and is, thus, given in α -equivalent. Still, the correct energy scale might be slightly ($\sim 10\%$) different as no line in the high-energy part of the α -spectrum can clearly be identified.

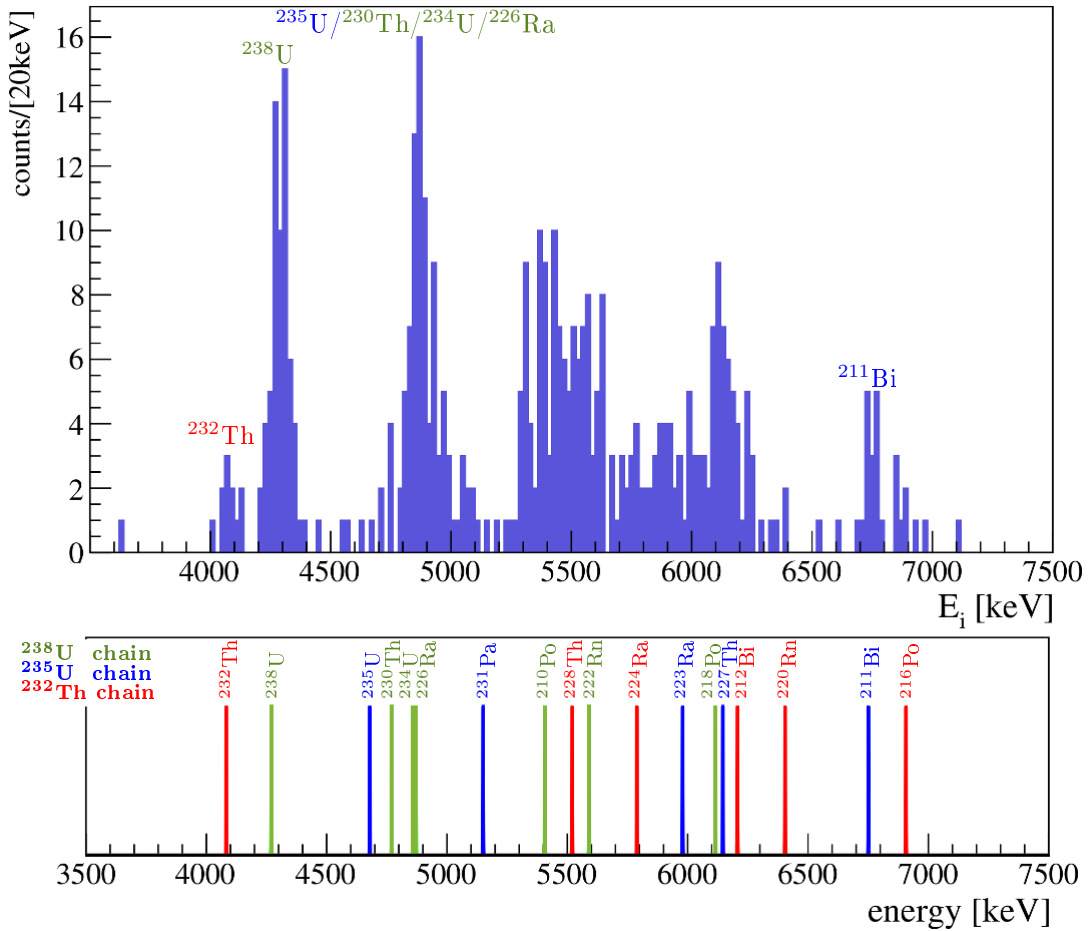


Figure 7.11.: α -spectrum (upper part) as detected in the *iStick* channel of detector module A (TUM56) in the main α -region (3.5-7.5)MeV. Several of the observed lines originating from decays in the natural decay chains of ^{238}U (green), ^{235}U (blue), and ^{232}Th (red) can clearly be identified. The literature values of their energies according to [58] are shown in the lower plot. The energy scale of the spectrum was adapted and fits the expected positions of the different lines. Activities of the identified α -lines (marked in the spectrum) are listed in table 7.4.

Two structures at energies of ~ 4250 keV and at ~ 4850 keV (in the given scale) are well separated and can be attributed to the combined decay lines of $^{232}\text{Th}/^{238}\text{U}$ as well as of $^{235}\text{U}/^{230}\text{Th}/^{234}\text{U}/^{226}\text{Ra}$. Compared to module A, the $^{232}\text{Th}/^{238}\text{U}$ activity is reduced by a factor of ~ 1.9 (see table 7.4). Furthermore, changed contamination ratios are found in module E: whereas the ratio between $^{235}\text{U}/^{230}\text{Th}/^{234}\text{U}/^{226}\text{Ra}$ and $^{232}\text{Th}/^{238}\text{U}$ equals about 1.1 in case of detector module A, it is higher than 3 in case of module E. Lines above 5 MeV contribute $\sim 62\%$ to the total α -activity in module A while this fraction is 75% in module E.

module		A (TUM56)	E (TUM73)
origin	E_{lit} [keV]	activity [mBq/kg]	
^{232}Th	4082.8	0.052 ± 0.023	0.185 ± 0.044
^{238}U	4270	0.293 ± 0.054	
^{235}U	4678.7	0.409 ± 0.068	0.616 ± 0.087
^{230}Th	4770.0		
^{234}U	4858.5		
^{226}Ra	4870.6		
^{211}Bi	6750.5	0.077 ± 0.030	-

Table 7.4.: Activities of several identified single α -lines or superpositions of several decays determined for modules A (TUM56) and E (TUM73). The activity of $^{232}\text{Th}/^{238}\text{U}$ is lower in module E compared to that in module A by a factor of ~ 1.9 whereas the combined activity of ^{235}U , ^{230}Th , ^{234}U , and ^{226}Ra is higher by a factor of ~ 1.5 . Concerning the high-energy part of the α -spectrum, only the ^{211}Bi -line can clearly be identified in detector module A, but no line at all in module E.

7.5. Discussion

Using the results described in the previous sections, the radiopurities of the CaWO_4 crystals TUM40, TUM56, and TUM73 can be compared. Each crystal was produced from a different batch of raw materials supplied by Alfa Aesar [168] (TUM40) and MV Laboratories [121] (batch 1: TUM56, batch 2: TUM73). An additional chemical treatment (version 1 purification) was applied to the CaCO_3 powder used for the production of TUM73 (compare section 5.3.2). Furthermore, two main aspects related to the crystal growth should also be considered: Segregation changes the contamination level within the crystal compared to the initial material by a certain factor, which is the same for each crystal growth (compare section 5.4). However, the radiopurity of the initial material can vary depending upon which material (powder or crystal parts) is melted and on how often the remaining melt is reused. The crystal ingot TUM73 was grown from freshly synthesized CaWO_4 powder filled into a cleaned crucible, whereas the remaining melt was reused several times before the growth processes of TUM40 and TUM56. In between, the required melt level was re-established via adding mainly already crystallized material but also new powder to the crucible.

Table 7.5 summarizes the various measurement results concerning the levels of intrinsic contamination in the crystals TUM40, TUM56, and TUM73. In case of CRESST measurements (upper part of the table), the mean of the activities was taken for detector modules involving CaWO_4 crystals from the same ingot. The values of TUM40 were obtained during its operation in CRESST-II Phase 2 [82]. In order to also allow a comparison with the impurity levels of the different powder batches included, the results of HPGe measurements are listed in the lower part of table 7.5. The activity values of the raw materials of TUM40 and TUM56 have been taken from [120].

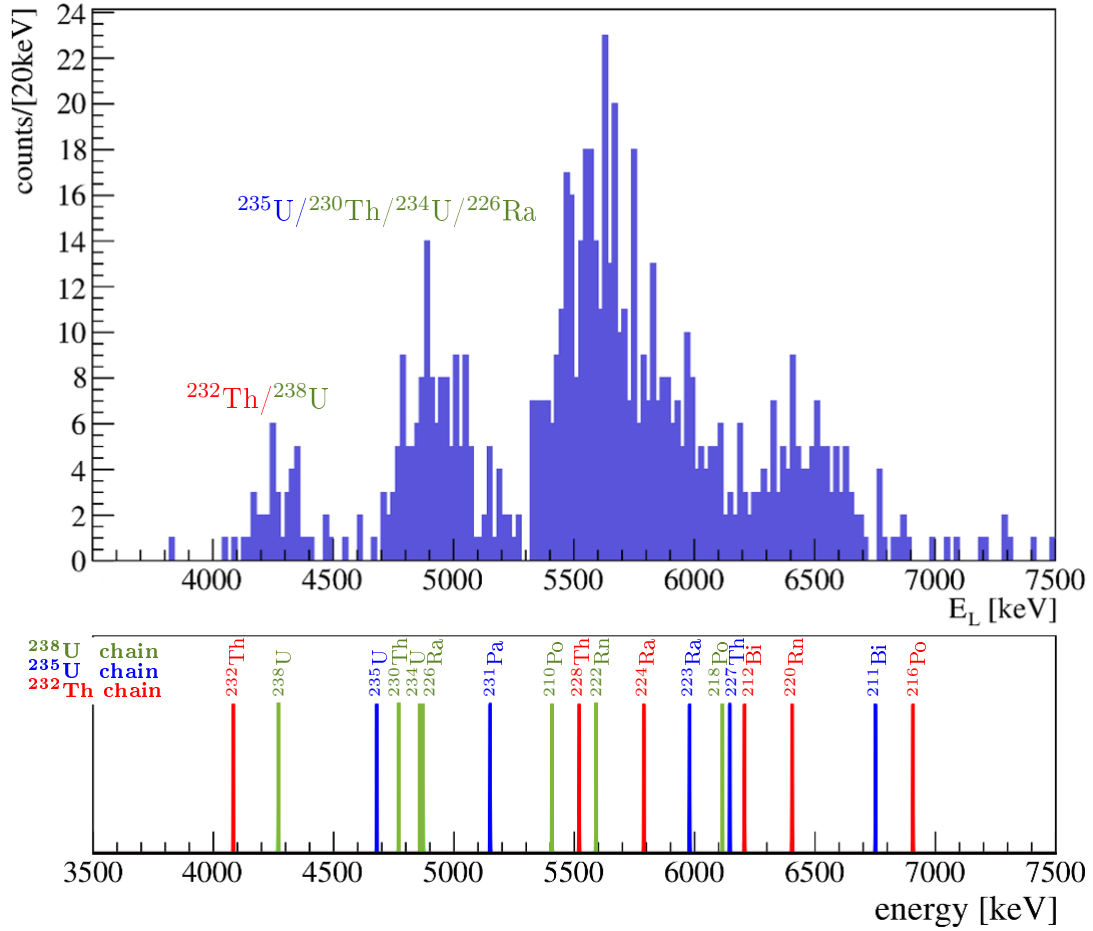


Figure 7.12.: α -spectrum as recorded by the light detector of module E (TUM73). The energy scale was adapted to the main region of single α -lines originating from the natural decay chains and occurring at energies between (3.5-7.5)MeV. The two structures originating from the superpositions of the $^{232}\text{Th}/^{238}\text{U}$ -decays as well as of the $^{235}\text{U}/^{230}\text{Th}/^{234}\text{U}/^{226}\text{Ra}$ -decays can clearly be separated. The corresponding activities calculated for these lines are included in table 7.4.

Comparison of total Contamination Levels

The integrated e^-/γ -rates between 10 keV and 40 keV are (3.26 ± 0.08) counts/(kg keV day) (estimated based on the analysis of [43]), (3.85 ± 0.16) counts/(kg keV day), and (4.13 ± 0.16) counts/(kg keV day) for TUM40, TUM56, and TUM73, respectively. These values translate to integral count rates of (1.13 ± 0.03) mHz/kg in case of TUM40 and to slightly higher values of (1.34 ± 0.06) mHz/kg (TUM56) and of (1.43 ± 0.06) mHz/kg (TUM73) in this energy region. Although the activities of the two CRESST-III Phase 1 crystals TUM56 and TUM73 are compatible within uncertainties, the background level seems to be slightly increased in TUM73. This observation can be explained by an intrinsic ^{210}Pb contamination with a total activity of (0.76 ± 0.08) mBq/kg within this crystal. In the energy range (10-40) keV, the contribution of the ^{210}Pb β -decay is 8.9% of this value, i.e., 0.07 mBq/kg corresponding to a rate of ~ 0.2 counts/(kg keV day). The upper

crystal			TUM40	TUM56	TUM73
material	measurement	isotope	activity [mBq/kg]/rate [mHz/kg]		
CaWO ₄ crystal	CRESST	(10- 40) keV (β , γ)	1.13 ± 0.03	1.34 ± 0.06	1.43 ± 0.06
		²¹⁰ Pb (β)	-	< 0.07	0.76 ± 0.08
		total α (4- 7) MeV	3.08 ± 0.04	2.02 ± 0.10	3.47 ± 0.09
		¹⁴⁷ Sm (α)	0.040 ± 0.004	3.42 ± 0.14	0.07 ± 0.01
		¹⁸⁰ W (α)	0.036 ± 0.009		
		²³² Th (α)	0.009 ± 0.002	0.05 ± 0.02	0.19 ± 0.04
		²³⁸ U (α)	1.01 ± 0.02	0.29 ± 0.05	
		²³⁴ U (α)	1.08 ± 0.03	0.41 ± 0.07	0.62 ± 0.09
		²³⁰ Th (α)	0.06 ± 0.01		
		²²⁶ Ra (α)	0.04 ± 0.01		
		²³⁵ U (α)	0.040 ± 0.004		
		²¹¹ Bi (α)	0.11 ± 0.01	0.08 ± 0.03	-
CaCO ₃ powder	HPGe	²²⁸ Ra	< 27	4.3 ± 1.1	< 3.2
		²²⁸ Th	< 33	6.0 ± 0.6	2.2 ± 0.6
		²³⁸ U	< 260	< 23	47 ± 10
		²²⁶ Ra	26 ± 6	< 0.9	2.5 ± 0.6
		²³⁵ U	-	-	2.2 ± 0.5
		²²⁷ Ac	< 31	< 3.1	5.2 ± 1.2
WO ₃ powder	HPGe	²²⁸ Ra	< 23	< 2.1	< 3.0
		²²⁸ Th	< 6	< 1.6	< 1.7
		²³⁸ U	< 400	< 68	< 40
		²²⁶ Ra	< 10	< 2.2	1.8 ± 0.4
		²³⁵ U	-	-	< 2.0
		²²⁷ Ac	< 36	< 5.6	< 3.2
chemical purification			no	no	CaCO ₃

Table 7.5.: Summary of the various measurement results concerning the levels of intrinsic contamination in the crystals TUM40, TUM56, and TUM73. In the upper part, activities are listed which are derived from a crystal operation in CRESST-II Phase 2 (TUM40) [82] and CRESST-III Phase 1 (TUM56, TUM73) via the investigation of e^-/γ - and α -backgrounds. In the case of an analysis of various detector modules including the same crystal type, the given activity corresponds to the mean of the measured values. For a comparison, also the activities of the respective raw materials CaCO₃ (before purification) and WO₃ measured by means of HPGe spectroscopy are included in the lower part of the table.

limit (95 % C.L.) calculated for the ^{210}Pb activity in TUM56 (compare section 7.3.3) indicates that no or at least a much lower internal contamination with this isotope is present there. In case of TUM40, only a γ -line with an external origin of ^{210}Pb was found.

Also the investigation of α -events leads to the result of a higher total level of impurities in TUM73 compared to TUM56. The total activity of single α -lines of the natural decay chains in the energy range (4- 7) MeV is increased by a factor of ~ 1.7 in case of TUM73 ((3.47 ± 0.09) mBq/kg) with respect to TUM56 ((2.02 ± 0.10) mBq/kg). Compared to the total α -activity of TUM40 of (3.08 ± 0.04) mBq/kg, TUM73 appears to have a slightly higher value whereas the contamination of TUM56 is lower.

The varying (total) contamination levels of the three detector crystals TUM40, TUM56, and TUM73 are likely related to the impurity variations of the different batches of raw materials as indicated by the HPGe measurements of the raw powders (see lower part of table 7.5). For most isotopes, only limits are given which are well above the total α -activity in the crystal making conclusions challenging. In addition, also segregation, chemical purification in case of TUM73 as well as the purity status of the initial melt material affect the measured impurity levels. At least one of these effects appears to successfully reduce the crystal-intrinsic contamination level, as for all crystals the total α -activity is below the summed activities measured via HPGe spectroscopy in the powders.

Still, the varying activities could also be connected to the different handling of the raw materials. The purification applied to the CaCO_3 powder of TUM73 was specifically aimed at the reduction of the thorium and uranium concentrations which does not necessarily lead to a reduced e^-/γ background rate below 100 keV or to a decreased total α -activity. In particular, contaminations can also originate from the WO_3 powder, which was not chemically purified during the production of the crystal ingots TUM40, TUM56 and TUM73. Furthermore, it can not be excluded that the CaCO_3 powder got in contact with materials featuring a higher impurity level during the various purification steps. In this way, a contamination with, e.g., lead could have been introduced. A slightly increased lead concentration was actually found by a ICP-MS measurement of the CaCO_3 powder after purification (compare table 5.5).

Comparison of the Activities of α -emitting Isotopes

A more detailed study of single α -lines gives indications on the isotopes contributing to the total impurity level. Energy depositions at ~ 2.3 MeV can be attributed to the α -decays of ^{147}Sm and ^{180}W . Activities derived for these two isotopes within the detector crystals TUM40 and TUM73 are below 0.1 mBq/kg which is comparable to the results of other commercial and TUM-grown CaWO_4 crystals. In contrast, a strong line with an activity of (3.42 ± 0.14) mBq/kg is present in TUM56. This line can well be fitted by one Gaussian and no hint for a second structure is visible, i.e. it is probably caused by mainly one background component. The only difference during the growth of the crystal ingot TUM56 compared to other crystals was the addition of 1 % WO_3 powder to the CaWO_4 material in order to increase the amount of oxygen present in the melt. However, neither a contamination with ^{147}Sm nor with any other isotope emitting an α -particle in that energy region is known and also the amount of ^{180}W cannot have been increased by

such an amount to lead to an activity in the order of mBq/kg. Thus, the origin of the large population in TUM56 remains unknown. However, as this contamination appears to be responsible for solely one line in the α -region, no problems for the dark matter search within the region of interest below 40 keV are expected.

Concerning α -decays of the natural decay chains, the two main contaminating isotopes in TUM40, namely ^{238}U and ^{234}U with an activity of ~ 1 mBq/kg each, are clearly reduced in TUM56 and TUM73. The reduction factor of ^{238}U is ~ 3.5 in case of TUM56 and at least 5.4 for TUM73. An increased activity of ^{232}Th can be noted for TUM56 compared to TUM40 while the value of ^{211}Bi is comparable in both crystals. Due to the limited resolution and statistics, only a summed activity of ^{235}U , ^{230}Th , ^{234}U , and ^{226}Ra can be calculated for the crystals operated in CRESST-III Phase 2. Compared to TUM40, the contamination with these isotopes is decreased in both crystals TUM56 and TUM73 by a factor of 3 and 2, respectively. Assuming an equal activity of ^{238}U and ^{234}U implies that the main contribution to this superposed line originates from the ^{234}U -decay in TUM56 while it accounts maximally for ~ 0.2 mBq/kg, i.e. a fraction of 1/3 of this line, in TUM73. Already in earlier works, low segregation coefficients were found for the isotope ^{226}Ra which is confirmed by the comparison of the ^{226}Ra -activity in TUM40 ((0.04 ± 0.01) mBq/kg) and the one of the corresponding CaCO_3 powder ((26 ± 6) mBq/kg). Due to this observation, a large contribution of this isotope to the $^{235}\text{U}/^{230}\text{Th}/^{234}\text{U}/^{226}\text{Ra}$ -line is improbable, leaving ^{230}Th and ^{235}U as main contributing isotopes.

Reduced Uranium and Thorium Content in TUM73

Although a clear identification of the contaminating isotopes cannot be achieved for TUM56 and TUM73, the reduced uranium level compared to TUM40 is obvious. Additionally, the content of ^{232}Th and ^{238}U is – despite of a higher total α -activity – further decreased in TUM73 with respect to TUM56 by a factor of ~ 1.9 . For ^{238}U , a huge reduction by at least two orders of magnitude can be found when comparing the activity of the detector crystal TUM73 (< 0.19 mBq/kg) and the one of its raw materials ((47 ± 10) mBq/kg). The segregation coefficient of ^{238}U was determined to be ~ 0.3 in [153] and cannot solely be responsible for the change in activity. The uranium and thorium contents in TUM73 were also measured by means of LA-ICP-MS resulting in a concentration limit of < 0.001 ppb and a value of 0.7 ppb, respectively (compare table 5.6). Based on the long-lived isotopes ^{238}U and ^{232}Th , these values can be transformed to activities of < 0.01 mBq/kg and 2.5 mBq/kg. A ^{232}Th -activity of 2.5 mBq/kg is much too high which means that other isotopes (or molecules with the same mass) must contribute. However, the limit of < 0.01 mBq/kg calculated for ^{238}U agrees with the results achieved within the CRESST-III Phase 1 measurement. In total, the amount of uranium in TUM73 seems to be much lower than the contamination with thorium. This could also imply that the main contribution of the $^{235}\text{U}/^{230}\text{Th}/^{234}\text{U}/^{226}\text{Ra}$ -line is ^{230}Th in case of TUM73. Compared to TUM56, this superposed line has an activity which is increased by a factor of 1.5. The contamination ratios between $(^{235}\text{U} + ^{230}\text{Th} + ^{234}\text{U} + ^{226}\text{Ra})$ and $(^{232}\text{Th} + ^{238}\text{U})$ are, therefore, different in TUM73 (3.3) and TUM56 (1.2) which is a further hint towards changed contributions of contaminating isotopes. All these results together establish a successful removal of uranium and also thorium during the purifica-

tion procedure applied to the CaCO_3 powder of TUM73.

In summary, the detector crystals TUM40 (produced from raw materials of Alfa Aesar without purification), TUM56 (produced from batch 1 of raw materials of MV Laboratories without purification), and TUM73 (produced from batch 2 of raw materials of MV Laboratories with purification of the CaCO_3 powder) were compared with respect to their radiopurity. The e^-/γ background rate in the energy range (10 - 40) keV is – compared to TUM40 – slightly increased in TUM56 and TUM73. In the latter, an intrinsic ^{210}Pb contamination is present. In terms of total α -activities, the highest value is also found for TUM73. However, comparing the combined activity caused by the decays of ^{232}Th and ^{238}U , this contamination is reduced in TUM73. The – in total – higher activity can be attributed to the different batches whereas the reduced activity of these two isotopes gives a strong indication that the purification, which aimed at the removal of thorium and uranium, was successful. Concerning powder purification, these results suggest a cleaning also from other elements than uranium and thorium, in particular a targeted removal of lead. In the second version of the purification procedure (see section 5.3), these requirements have already been taken into account. In order to investigate the final radiopurity achieved, a crystal will be grown from the existing, purified CaWO_4 powder and will be measured and analyzed in the near future.

8. Summary and Conclusions

The present work was performed within the scope of the CRESST experiment which is located in the Gran Sasso underground laboratory LNGS and searches for DM particles via their elastic scattering off the nuclei contained in CaWO_4 target crystals. A particle interaction in such a crystal, which is operated as cryogenic detector at a temperature of ~ 10 mK, produces heat (phonons) as well as scintillation light. To read out both signals, the CaWO_4 crystal and a separate light absorber are each equipped with a sensitive superconducting thermometer in form of a transition edge sensor (TES). All these detector components form a detector module and are enclosed in a reflective and scintillating housing to maximize the light signal as well as to discriminate decays occurring on surfaces.

The main part of the energy deposited by an interaction within the crystal is detected as phonon signal which, therefore, allows a precise energy reconstruction. The light signal, on the other hand, depends on the type of interacting particle and enables a discrimination of e^-/γ - and α -backgrounds from nuclear recoils (i.e. potential DM recoils).

For a successful operation as DM detectors, mainly two properties are crucial for CaWO_4 crystals. An optimized optical quality is required since a high transmittance and light output strengthen the ability for particle discrimination. Furthermore, very low interaction rates are expected for DM particles which means that all kinds of backgrounds have to be suppressed. This requires, in particular, a high radiopurity of the CaWO_4 crystals. The issue of radiopurity is the main topic of the present thesis.

In the past, commercial companies in Russia and the Ukraine supplied the CRESST experiment with CaWO_4 crystals. In order to achieve an improvement of the optical quality and of the radiopurity, it is crucial to have control on the various production steps. Therefore, a Czochralski facility dedicated solely to CaWO_4 crystal growth was installed at the Technische Universität München (TUM) in 2007. The successful crystal production at TUM consists of the synthesis of CaWO_4 powder from selected raw materials of CaCO_3 and WO_3 powders, the CaWO_4 crystal growth as well as post-growth treatments including annealing in pure oxygen atmosphere and cutting into detector crystals.

In the extended physics run CRESST-II Phase 2 lasting for two years from 2013 to 2015, TUM-grown detector crystals were for the first time operated in the experiment. Compared to commercial crystals, the radiopurity was found to be significantly improved by factors of 2-10. Furthermore, a new module design was tested with TUM-grown crystals. Holding the crystals by CaWO_4 sticks (instead of non-scintillating bronze clamps in the conventional design) provides a fully scintillating housing. It was shown in earlier work that surface decays are successfully vetoed in this so-called stick-design.

The crystals operated in CRESST-II Phase 2 featured masses of about (250-300) g and reached energy thresholds down to ~ 300 eV. A low-threshold analysis of the TUM-grown

crystal TUM40 as well as of the commercial crystal "Lise" resulted in a leading sensitivity for DM particle masses below $\sim 2 \text{ GeV}/c^2$. This result motivated the CRESST collaboration to further improve the sensitivity for low-mass DM particles. A reduction of the volume and, thus, of the mass of each detector crystal to $\sim 25 \text{ g}$ leads to a higher phonon density after a particle interaction and makes energy thresholds below 100 eV possible. The concept of holding the crystals by CaWO_4 sticks was adopted with the additional feature that also these sticks are instrumented with a TES (iStick). In this way, degraded events in the main absorber originating from a crosstalk of an interaction in one of the three iSticks can be vetoed. The CRESST group at TUM provided the majority of the ten CaWO_4 detector crystals for CRESST-III Phase 1 which started data taking in summer 2016. Within the frame of the present work, I produced most of these crystals in collaboration with Dr. Andreas Erb.

The optical quality of various CaWO_4 crystals was investigated in the present thesis. A setup was built for visualizing internal stresses based on photoelasticity. In former work, it was observed that TUM-grown crystals feature intrinsic tensions in contrast to commercial crystals. An investigation in dependence on the crystal orientation revealed that only internal stresses perpendicular to the c -axis are present in TUM-grown crystals. As commercial detector crystals were usually not delivered in a c -oriented way, a block-shaped crystal with surfaces parallel and perpendicular to the c -axis was exemplarily cut from the cylindrical Ukrainian crystal "Alexej". The photoelasticity measurements confirmed that internal stresses perpendicular to the c -axis are also visible in this crystal, although less pronounced than in the TUM-grown crystal TUM73-3. The origin of the intrinsic tensions in TUM-grown crystals can be explained by dislocations forming in the crystal lattice already during growth due to radial temperature gradients. Such dislocations cannot be cured via, e.g., the application of an annealing procedure. This has been confirmed in the present thesis.

The transmittance of several crystals was measured with a UV-Vis spectrometer in dependence of the wavelength. For a comparison with the results of earlier work, the attenuation length at 430 nm – the wavelength of the maximal emission intensity of the intrinsic scintillation – is calculated. In general, TUM-grown crystals have attenuation lengths in the order of 100 mm which is comparable to the ones of standard Ukrainian crystals. However, the fact that several Russian crystals have a transmittance which is higher up to one order of magnitude is still unexplained. The transmittance is connected to the (oxygen-) defect density within the CaWO_4 crystals. Via the application of an additional annealing procedure in pure oxygen atmosphere, oxygen-related vacancies and defects can be reduced. It was confirmed in the present thesis that this improves the transmittance significantly. The attenuation length at 430 nm can be increased by a factor of 1.5-3.

The evaporation of a TES onto a crystal, however, leads to a decreased transmittance, probably due to an optically dead layer on the crystal surface caused by the temperatures (up to $600 \text{ }^\circ\text{C}$) applied during the evaporation in vacuum. It was shown that re-polishing the crystals, i.e. removing the uppermost $\sim 5 \mu\text{m}$ of the surface, re-establishes the transmittance reached before the evaporation procedure.

A further improvement of the radiopurity is required for the upcoming experiment CRESST-III Phase 2. The focus of the present thesis lies on the development of methods

to reduce the concentrations of contaminating isotopes within CaWO_4 crystals as well as on the measurements of trace impurities in powder and crystal samples.

A promising approach to improve the radiopurity is the chemical purification of the raw materials. To guarantee the basic requirement of a clean environment, all purification steps were carried out in a dedicated laboratory. In version 1 (2015), a liquid-liquid extraction was applied to the dissolved CaCO_3 powder using the extractant trioctylphosphineoxide (TOPO) which is capable to bind contaminating metals, in particular uranium and thorium isotopes. Measurements by means of inductively coupled plasma mass spectrometry (ICP-MS) of the CaCO_3 powder before and after this treatment show a reduction of the thorium and uranium contamination by a factor of $\gtrsim 7$ and $\gtrsim 35$, respectively. The radiopurity of the crystal TUM73 produced from this purified material was investigated via laser ablation (LA-) ICP-MS. In comparison to TUM69, a crystal grown from the same raw materials without application of any purification, several isotopes feature significantly reduced concentration values in the case of TUM73.

In the second version of the chemical powder purification (2016), also the TOPO solution was cleaned and the whole liquid-liquid extraction was repeated in order to improve the purification efficiency. Furthermore, a new method was developed to produce CaWO_4 powder via a precipitation reaction. A cross-cleaning based on coprecipitation was applied as additional cleaning step to the dissolved CaCO_3 and WO_3 powders. ICP-MS measurements indicate that the concentrations of isotopes like, e.g., ^{23}Na , ^{27}Al , ^{39}K , ^{55}Mn , ^{88}Sr and ^{208}Pb can be reduced in at least one of the two solutions (Ca^{2+} - and WO_4^{2-} -solution).

After the precipitation reaction had been completed, the resulting CaWO_4 powder was cleaned in a washing procedure with ultrapure ammonia solution and water in order to remove further solvable contaminants. In particular, the activity of the isotope ^{40}K was decreased by a factor of two by this procedure. Hints for a successful reduction of the contamination level were also found for other isotopes such as ^{23}Na , ^{24}Mg , ^{27}Al , or ^{88}Sr . In the final CaWO_4 powder, the activities determined by means of high-purity germanium spectroscopy are significantly reduced by factors of at least 2-4, 3 and 5.5 for the isotopes ^{228}Th , ^{238}U and ^{226}Ra , respectively.

The Czochralski process has – due to segregation – also a cleaning effect. Indications for segregation in CaWO_4 crystals were found for ^{228}Th and for ^{226}Ra in earlier work, where the segregation coefficient of the latter isotope was determined to be $\lesssim 0.12$. The knowledge of segregation coefficients of other isotopes would help to estimate the cleaning capability of CaWO_4 crystal growth via the Czochralski method. Therefore, a feasibility study for the determination of the segregation coefficients via cryogenic measurements was performed within the scope of the present work. The basic idea refers to the change of the concentration level within one raw crystal. The simulation included in the study suggests that it is feasible to correctly derive the segregation coefficient when the initial activity is $\gtrsim 10$ mBq/kg or when the segregation coefficient is $\gtrsim 0.5$. The probability for a reliable determination is slightly increased for longer measuring times or for higher fractions of the crystallized mass (i.e. the total mass of the grown crystal ingot). However, a significantly improved result for lower values of the segregation coefficient requires a better knowledge of the initial activity.

In the final part of the present thesis, a radiopurity analysis of a partial CRESST-III

Phase 1 data set was performed for four detector modules. The crystal TUM73, which was produced from purified CaCO_3 powder (version 1), is included in two of these detector modules. For comparison, two detector crystals cut from the ingot TUM56, which was grown from a different non-purified powder batch, were investigated as well. The exposure of each analyzed detector is ~ 2.5 kg days. Investigated regions are the e^-/γ -band up to several 100 keV and α -decays occurring in the MeV energy range. Various data preparation steps including energy reconstruction and data quality cuts are necessary for the calculation of background rates and activities. The total rates of e^-/γ -interactions between 10 keV and 40 keV were determined to be (3.51 ± 0.22) counts/(kg keV day) and (4.19 ± 0.24) counts/(kg keV day) for the TUM56 detector crystals as well as (3.88 ± 0.22) counts/(kg keV day) and (4.38 ± 0.23) counts/(kg keV day) for the TUM73 detector crystals. Averaging the two values of each crystal type, integrated count rates of (1.34 ± 0.06) mHz/kg and (1.43 ± 0.06) mHz/kg can be derived. Both rates are slightly increased compared to the value of (1.13 ± 0.03) mHz/kg calculated for the crystal TUM40 (CRESST-II Phase 2 data). In the crystal TUM73, an internal ^{210}Pb contamination with an activity of ~ 0.76 mBq/kg was found to be present. This contaminating isotope contributes ~ 0.07 mBq/kg in the energy range (10-40) keV.

Due to the relatively low statistics, only the ^{179}Ta K- and L1-lines originating from cosmogenic activation of tungsten in CaWO_4 have additionally been identified in the background spectra. The activities derived for these lines are – within their uncertainties – for all investigated detectors comparable to those determined for TUM-grown crystals installed in the previous CRESST-II Phase 2.

In a completely different energy range of a few MeV, α -interactions within the crystals also reveal information on the intrinsic contamination level. As CRESST-III Phase 1 detectors are optimized for very low thresholds and energy depositions, the phonon signal is highly saturated for α -events in the main absorber. However, new analysis methods were developed in order to use the corresponding crosstalk events within the iSticks and the simultaneous light signal for an α -analysis. The total α -activities determined for the energy range $\sim(4-7)$ MeV are (2.02 ± 0.10) mBq/kg (TUM56) and (3.47 ± 0.09) mBq/kg (TUM73). This result confirms a slightly higher contamination level in TUM73 than in TUM56 detector crystals which can be explained by the different batches of raw materials the two crystals were produced from. Activities of single α -lines can only partially be determined for one detector module of TUM56 and one of TUM73, as the resolution of the degraded iStick signals is limited in most detectors. In both cases, the activities of ^{238}U and ^{234}U are significantly lower with respect to TUM40, in which these two isotopes were the dominant contaminations in the α -region. The reduction factors are 3.5 and at least 5 in the cases of TUM56 and TUM73, respectively. Despite of the higher total α -activity, the contamination with $^{232}\text{Th}/^{238}\text{U}$ is further reduced by a factor of ~ 1.9 in TUM73 compared to TUM56. This result indicates a successful purification concerning uranium and thorium during the liquid-liquid extraction performed for the CaCO_3 powder used for the growth of TUM73.

9. Outlook

Data taking of CRESST-III Phase 1 is planned to be continued at least until the end of the year 2017. Within the collaboration, a dark matter analysis is currently being prepared. Concerning the investigation of the radiopurity, statistics will be increased by a factor of more than two in the final data set compared to the partial data set analyzed in the present work. Applying the developed analysis to the full data set will improve the precision of rate and activity determinations and will also become sensitive to potential contaminations with still lower activities.

The resolution of the degraded α -events is not limited by statistics but by other parameters related to the iSticks, e.g., the force applied to press the sticks onto the main crystal. This implies that it will not be feasible to confirm the hints for a reduced thorium and uranium contamination found in the detector crystals of TUM73, which was produced from cleaned CaCO_3 powder (version 1). Therefore, an additional dedicated measurement of α -events is planned for the near future to finally determine the improvement factor achieved for TUM73 in comparison to a crystal produced from the same batch of raw materials without application of any purification (e.g. TUM69). Such a (cryogenic) measurement can be optimized for high energy depositions by operating detector crystals with higher masses and adapted thermometers. One possibility is to use a NTD (neutron-transmutation-doped) sensor instead of a TES in order to achieve a high-resolution α -spectroscopy.

In the future, the CRESST collaboration aims at installing an increased number of detectors with a further improved radiopurity of the whole experimental setup and, in particular, of the CaWO_4 crystals. With respect to this goal, the radiopurity measurements performed for the CaWO_4 powder precipitated and purified in version 2 yield promising results. In the near future, it is planned to grow a crystal from the first 1.5 kg CaWO_4 powder of version 2 and to investigate its performance as cryogenic detector. In case the achieved radiopurity fulfills the requirements of CRESST-III Phase 2, a larger amount of powder has to be produced via the method presented here. With the personal and technical equipment currently available, only a production rate of ~ 150 g per week is feasible. To enable higher production rates, more manpower as well as better equipment are essential. In particular, for an easier handling of all materials outside the flowbox as well as for an even cleaner environment, the laboratory should completely be converted into a clean room.

Depending on the results of the radiopurity measurements, further improvement steps could be included in the powder production and purification process. In the present work, the focus of the liquid-liquid extraction was set to uranium and thorium isotopes. The extraction efficiency with respect to the removal of further isotopes should be studied for various other chemicals. Other precipitating materials can also be investigated for coprecipitation. However, the drawback is that every additional material getting in

contact with the raw materials also increases the risk of introducing new contaminations. Besides powder purification, the cleaning capability of recrystallization should be further investigated. A determination of the segregation coefficients of different isotopes becomes feasible when a crystal is grown from CaWO_4 material with known contamination level. This could be studied with two materials available: a large powder batch (which is currently stored in the Garching underground laboratory) and a large (broken) raw crystal (TUM61), each with a mass of ~ 1.6 kg. Both were investigated by means of HPGe spectroscopy where the activities of several isotopes were determined. After a crystal ingot has been grown from this powder or from the recrystallized raw crystal TUM61 (which happened recently), another HPGe measurement or a cryogenic measurement can clarify the (new) contamination levels of various isotopes which enables a derivation of the segregation coefficients.

Concerning radiopurity measurements, laser ablation inductively coupled plasma mass spectrometry (LA-ICP-MS) was found to be a suitable method for the insoluble CaWO_4 crystal samples. An investigation of pressed CaWO_4 powder seems to be feasible via this method, as well. However, the instrument at the TUM centre for building materials (CBM) is mainly laid out for samples of building materials where the constraints for radiopurity are much lower. It would be beneficial if an instrument for LA-ICP-MS was installed at an institute where the requirements of low-rate experiments are known, e.g. at LNGS.

Regardless of the purity of the CaWO_4 material, the amount of melt remaining after crystal growth should be kept low. Currently, the fraction of the grown crystal mass compared to the mass of the remaining melt is limited due to the pronounced convex growth boundary. A changed crystallization border might be achieved by an adaption of the growth parameters such as an increased rotation speed, a decreased growth speed or a different crystal geometry. Also the installation of an additional heater at the bottom of the crucible would be beneficial. This, however, is difficult to realize as a stringent temperature monitoring would be necessary to exclude the risk of locally over-heating the crucible. Still, improving the insulation layer at the bottom could already help to increase the yield of the crystallized CaWO_4 material. Furthermore, running the after-heater not only after the growth but already during the whole process can reduce heat losses of the grown crystal part and result in a lower temperature gradient. The effect of this additional heat source on the crystallization border will be investigated in the near future.

Such a changed heating setup with a lower thermal gradient could also affect the optical properties of the crystal ingot in a positive way. The efforts to improve the optical quality of the CaWO_4 crystals further should be continued in order to strengthen the ability of CRESST detectors to discriminate backgrounds down to very low thresholds of ~ 10 eV. Decreasing internal stresses implies not only a potential improvement in light propagation but also a minimized risk of cleavage, especially during cutting the raw ingots and, thus, an increased yield of good detector crystals. For a more quantitative measurement of internal stresses in connection to the growth parameters (e.g. the translation and rotation speeds as well as the cooling rate after the growth), the existing photoelasticity setup should be upgraded by a permanently installed CCD camera. Using a professional software will enable a more sophisticated analysis of the photoelastic fringe patterns. A

calibration of internal stresses could be feasible via applying an increasing external force to a CaWO_4 crystal while observing the behaviour of the isochromatics.

Several commercial crystals supplied by a Russian company feature a significantly higher light output and an attenuation length which is higher by a factor of up to 6 compared to TUM-grown crystals (after two annealing procedures). In order to obtain a better understanding of the amount and origin of actual light losses within a CaWO_4 crystal, a measurement capable of distinguishing between scattering and absorption should be carried out. Such a measurement can provide a more detailed relation between transmittance/absorption and different (post)-growth parameters and conditions. For example, annealing procedures with even lower cool-down rates (e.g. $2^\circ/\text{h}$ instead of $5^\circ/\text{h}$ down to 1200°C) or an extended cool-down rate of $5^\circ\text{C}/\text{h}$ down to 1000°C could be tested with respect to their effects on the transmittance of the CaWO_4 crystals.

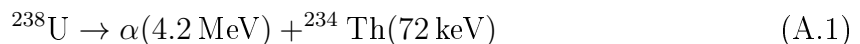
Altogether, there is still significant room for improving the quality of CaWO_4 crystals with respect to their optical properties and radiopurity. However, the CRESST collaboration is well on track to achieve the goals set for upcoming experimental phases. A significantly enhanced intrinsic radiopurity of $10\ \mu\text{Bq}/\text{kg}$ as well as energy thresholds reduced to $\sim 10\ \text{eV}$ will allow to scrutinize dark matter particles in a mass range from $\text{sub-GeV}/c^2$ to $\sim 10\ \text{GeV}/c^2$ down to the interaction cross sections of the neutrino floor. Many interesting results of the CRESST experiment and of the field of dark matter search in general are expected within the near future.

A. Reflective and Scintillating Foil

A CRESST detector module is surrounded by a reflective and scintillating foil as described in section 2.2.5. In the past, the multilayer specular reflecting foil "VM2002" produced by 3M was used, whereas in CRESST-III modules the subsequent "Vikuiti" foil, also manufactured by 3M [169], is implemented. A detailed investigation of the reflectivity of these foils can be found in [170].

The scintillation spectrum of the Vikuiti enhanced specular reflector foil was measured with a fluorescence spectrometer (Cary Eclipse, Agilent Technologies [171]) as shown in figure A.1. The foil was excited by photons with an energy of 4 eV leading to a reflection peak at this energy as well as to a second-order reflex at 2 eV. In between lies the scintillation spectrum. The uncertainty in intensity was determined by averaging over multiple measurements. However, it does not play a role here since the position of the spectrum is the quantity of interest. The spectrum can well be fitted by a double Gaussian fit function (red) with mean values of $\mu_1 = 2.85$ eV and $\mu_2 = 3.04$ eV as well as widths of $\sigma_1 = 0.20$ eV and $\sigma_2 = 0.12$ eV, respectively. This hints towards two scintillation centers inside the foil with slightly shifted mean values. An investigation of the scintillation spectrum of the Vikuiti foil with a different setup was also performed in [148].

The scintillation of a Vikuiti foil when excited by α -particles was investigated in a 7 days test measurement of a CaWO_4 crystal operated as cryogenic detector at the CRESST test-setup at LNGS [77]. A small area (~ 1 mm²) of the lateral crystal surface was covered with ~ 5 μ l of a solution containing ^{238}U atoms. The solution itself dried and left an α -source consisting of ^{238}U particles decaying via



on the crystal surface. It is illustrated in figure A.2 how α -particles produced in this decay can hit the Vikuiti foil surrounding the crystal and induce scintillation light there whereas, at the same time, the ^{234}Th nucleus deposits its energy of 72 keV in the crystal. Due to the high mass of the recoiling ^{234}Th , the light produced by such a nucleus is quenched even more than that of tungsten recoils and can be neglected in the following. Different preparation steps as explained in chapter 6 are applied to the data. This includes several basic data quality cuts, template fits and an energy calibration of phonon and light detector by means of heater pulses as well as of ^{57}Co and ^{241}Am sources. The resulting scatterplot in the LY-energy-plane (compare section 2.2.6) is shown in figure A.3 (a). The black data points mark all events below 300 keV with the e^-/γ -band forming the main population. Highlighted in red are the foil events originating from the α -decay of ^{238}U . They can be separated since their pulse shape is deviating from the standard shape. These foil events form a band starting at the recoil energy of ^{234}Th of 72 keV and extending towards higher energies with a $(1/E)$ -dependency. This behaviour can be explained by α -particles depositing part of their energy inside the

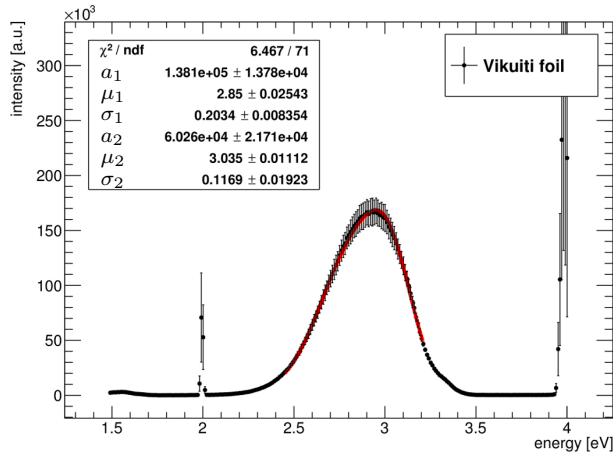


Figure A.1.: Scintillation spectrum of the Vikuiti enhanced specular reflector foil measured with a fluorescence spectrometer (Cary Eclipse, Agilent Technologies) [171]. The foil was excited by photons with an energy of 4 eV leading to a reflection peak at this energy and a second-order reflex at 2 eV. The scintillation spectrum in between can well be described by a double Gaussian fit (red) with mean values at $\mu_1 = 2.85$ eV and $\mu_2 = 3.04$ eV hinting towards two scintillation centers. The uncertainty in intensity was determined by averaging over multiple measurements.

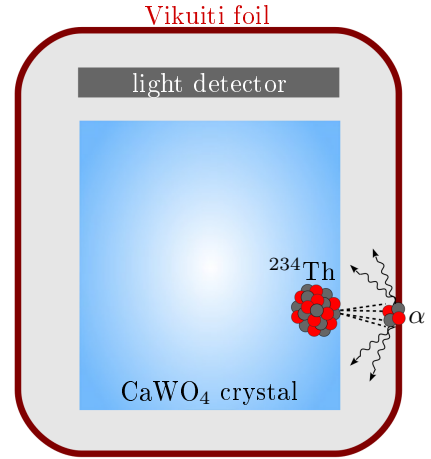


Figure A.2.: Schematic drawing of a CRESST-like detector module operated to investigate the scintillation of the Vikuiti foil. A small area of the CaWO_4 crystal surface is covered by a ^{238}U source which decays into an α -particle and a ^{234}Th nucleus. In case the recoiling nucleus deposits its energy in the crystal and, simultaneously, the α -particle hits the foil, a certain amount of additional scintillation light is absorbed in the light detector.

crystal before hitting the foil which results in a higher phonon energy whereas the amount of scintillation light, on the other hand, remains the same. Several events can also be observed in an extension of this band towards energies lower than 72 keV. In these cases the recoiling nucleus loses part of its energy before entering the crystal. However, also misidentifications at the lowest energies cannot be excluded since it has been observed that the pulse shape discrimination does not work properly any more in this region.

In addition to the electron equivalent energy reconstruction of the light detector, an absolute light energy calibration is feasible as the light detector is equipped with a ^{55}Fe source. Differences in the pulse shapes of ^{55}Fe events and of the foil scintillation signal are considered in an energy correction by the fraction of the integrals over the two pulse shapes. Plotting the absolute light energy $E_{\text{L,abs}}$ (including pulse shape correction) versus the phonon energy E_{Ph} (figure A.3 (b)) confirms that the scintillation light produced by the α -particle hitting the foil stays constant for phonon energies below 300 keV.

The absolute light-energy spectrum of the foil events with $E_{\text{Ph}} < 300$ keV is drawn in figure A.4. The maximum can be found at an energy of ~ 500 eV.

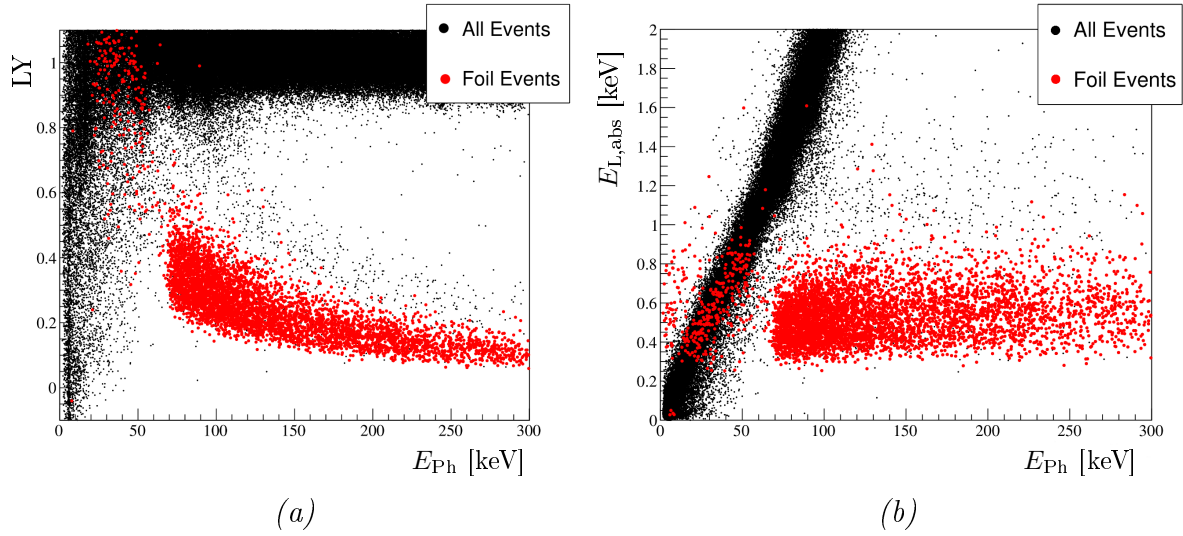


Figure A.3.: Light yield LY (a) and absolute light energy $E_{L,abs}$ (b) plotted versus the phonon energy E_{Ph} . The main population of all events (black) is due to electron recoils. The band shown in red represents foil events where α -particles originating from the decay of a ^{238}U source on the crystal surface hit the surrounding scintillating Vikuiti foil and produce additional scintillation light there. The band starts at 72 keV – the energy of the recoiling nucleus ^{234}Th – and extends towards higher phonon energies when part of the α -energy is deposited in the crystal, as well. The amount of scintillation light produced in the foil does not depend on the energy of the α -particle (b) resulting in a $(1/E)$ -dependency in (a).

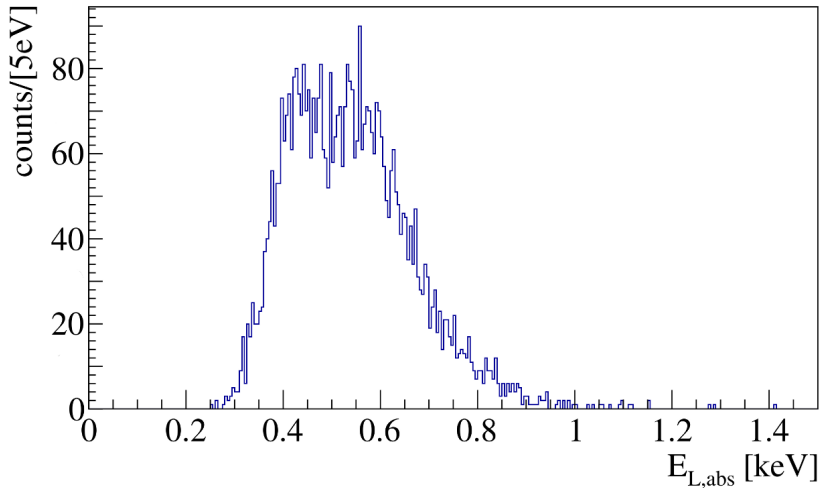


Figure A.4.: Absolute light-energy spectrum of the foil events below a phonon energy of 300 keV identified via pulse shape discrimination. The light energy produced by α -particles hitting the scintillating foil peaks around 500 eV.

B. Additional Aspects of CaWO_4 Crystal Growth

This chapter includes several additional aspects of CaWO_4 crystal growth. The importance of the seed orientation as well as the seed and seed holder geometry is demonstrated in section B.1. An example for growth abortion is given in section B.2. Crystal defects in form of grain boundaries were observed in the crystal ingot TUM77 and are explained in section B.3. Section B.4 describes details of the stone-like CaWO_4 powder, which was produced from the CaCO_3 powder purified in version 1 of the TOPO extraction (compare section 5.3.2) and which was later used for crystal growth of TUM73. Finally, information on all CaWO_4 crystals that were produced in the scope of the present work is summarized in section B.5.

B.1. Seed and Seed Holder Geometry

The orientation of the seed crystal as well as a suitable holding concept are crucial for a successful crystal growth. At TUM, seed crystals are c-oriented to achieve the nearly cylindrical shape of the raw crystal. The picture on the right side of figure B.1 shows how the crystal ingot looks like when the orientation of the seed is tilted by $\sim 15^\circ$. Due to growth anisotropies in the different directions the result is an asymmetric ingot. As an additional factor, also the crystal weight plays a role which finally leads to huge stresses and cracks inside the crystal ingot.

A comparable raw crystal was grown with a holding concept where the seed sits too loosely inside the holder and, therefore, can easily tilt (schematically shown in figure B.1 left). An attempt to fix the seed via a step within the holder was undertaken in figure B.2. However, as no rotational symmetry is given and as crystal and holder material can expand by deviating extents at high temperatures, the outcoming crystal ingot was still slightly asymmetric (figure B.2 right).

The holder to grow reproducibly symmetric crystals with a minimum of internal stresses is shown in figure B.3. A conical seed crystal is clamped into a likewise conical inner form of the holder (left) which guarantees rotational symmetry, also for the raw crystal (right).



Figure B.1.: Seed crystal holding concept where the seed crystal sits too loosely within its holder and can easily be tilted (left). This tilt is comparable to a tilted orientation of the seed crystal. Due to growth anisotropies in the different directions within the crystal, the result is an asymmetric raw crystal (right). As an additional factor, also the crystal weight plays a role which finally leads to huge stresses and cracks inside the crystal ingot.



Figure B.2.: Seed crystal holding concept where the seed crystal is fixed by a step within the holder (left). As this concept is not rotationally symmetric, the resulting raw crystal (right) shows a slight asymmetry.

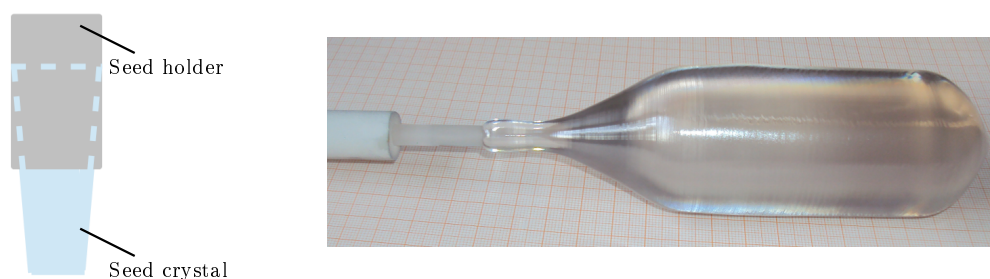


Figure B.3.: Holding concept where a conical seed crystal is clamped into a conical inner form of the holder (left). Due to its rotational symmetry, this concept is suitable to grow reproducibly symmetric crystals with a minimum of internal stresses as shown on the right.

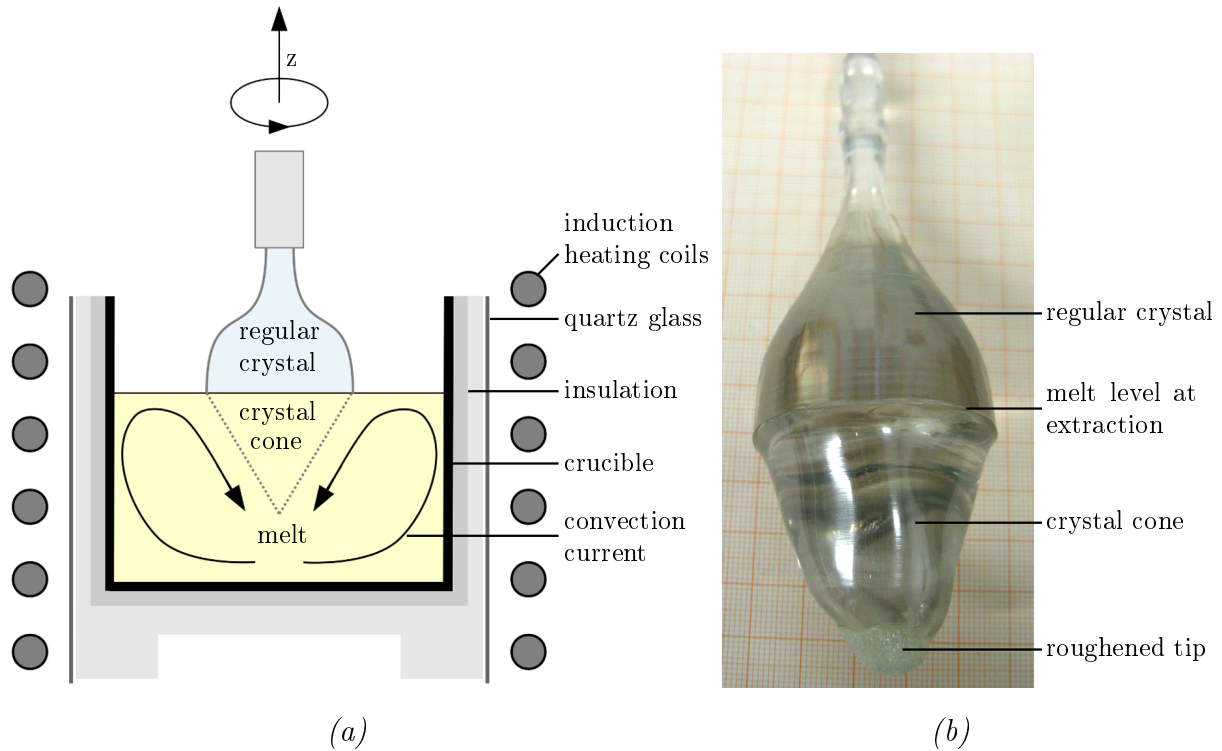


Figure B.4.: Example for the abortion of the growth process. As the crucible is not heated from below, a temperature gradient arises not only from the margins to the center but also in z -direction. (a) shows the resulting convection currents (arrows) and the cone-shaped crystal growth below the melt level. If this crystal touches, e.g., the bottom of the crucible, the growth is aborted. (b) shows a picture of such a crystal that was extracted prematurely due to growth abortion.

B.2. Growth Abortion

As explained in section 3.3, the growth process is automatically aborted when the growth-rate error becomes higher than a certain threshold. This can happen when the grown part of the crystal touches another solid surface which implies that a correct mass calculation is not possible any more. Hereby, the form of the growing crystal plays a role. The shape depends on the temperature distribution which is regulated by heat currents. These include convection currents within the melt (also influenced by the rotation), the heat of crystallization connected to the growth speed, the heat conduction along the crystal as well as the heat exchange between crystal surfaces and the surrounding atmosphere. The temperature field depends also on the position of the crucible inside the induction heating coils which surround the lateral area of the crucible inducing a strong electric field in the thin walls but producing only little heat in the bottom plate. As no additional heating but only insulating material is installed at the bottom, a temperature gradient not only occurs from the margins to the center but also from top to bottom, i.e. the coldest part can be found at the bottom center. Due to the temperature distribution, convection currents as indicated by the arrows in figure B.4 (a) appear within the melt leading to a cone-shaped crystal growth also below the melt level. When this

melt level is too low, it can happen that the tip of the crystal cone touches the bottom of the crucible. This results in a wrong mass calculation leading to the abortion of the growth process as well as to the extraction of the grown crystal ingot. A picture of such a raw crystal is shown in figure B.4 (b). At the bottom, the tip is roughened due to the contact with the bottom of the crucible.

Another effect could occur when not the whole material was melted and when a solid remnant stays at the bottom of the crucible. During the growth process, material also crystallizes there which could at some point touch the grown part of the crystal ingot, as well. Therefore, an overheating by $\sim 100^\circ\text{C}$ as described in section 3.3 is important to avoid any such solid remnants and to assure that all material has melted.

Due to the crystal cone growing below the melt level, it is not feasible to empty the crucible completely via crystal growth only. This has the disadvantage of a considerable material loss. Furthermore, it is more difficult to investigate properties of the crystal ingot which are changing with crystallized mass (e.g. radiopurity changing due to segregation, compare section 5.4). An attempt to vary the height of the crucible within the heating coils did not show any significant effect. A lower temperature gradient could be achieved when the insulation from below is improved or when an additional heater is installed at the bottom. However, a realization of such an additional heater is very challenging as it has to be guaranteed that no position exists where the temperature of the crucible is too high. Also an additional heat source at the top could establish more constant temperature conditions and could – due to suppressed heat losses of the grown crystal ingot – potentially lead to a reduced crystallization below the melt level. For this purpose, the effect of running the after-heater during the whole growth process will be investigated in the near future. Another solution avoiding a change of the heating system of the crucible is the growth of a crystal ingot with a different geometry. As the angle of the cone below the melt level is expected to stay approximately the same, a heavier crystal with less remaining melt can potentially be grown when the diameter is decreased. This, however, was not tested in the present thesis.

B.3. Crystal Defects

During cutting the crystal ingot TUM77, a crystal defect in form of a pronounced grain boundary was observed. Figure B.5 (a) shows a photograph of the lower cylindrical part of this crystal with the line of sight parallel to the c-axis. The green arrow indicates the grain boundary which extends over the whole cross-section. The orientation in each of the two different grains marked as grain 1 and grain 2 was measured by means of a real-time back reflection Laue camera [110]. The corresponding Laue patterns (see section 3.1) are depicted in figure B.5 (b). The arrays of red and black spots are formed by X-rays with certain wavelengths diffracted in case of grain 1 and 2, respectively. The two patterns show a clear shift and tilt which reveals a misorientation between the two grains of the order of about 1° .

The origin of this two-dimensional crystal defect in TUM77 is not clear. In general, grain boundaries can be introduced by small impurities which come in contact with the growing crystal ingot and induce the growth of crystallites with a deviating orientation there. Another possibility is that grain boundaries were already present in the seed

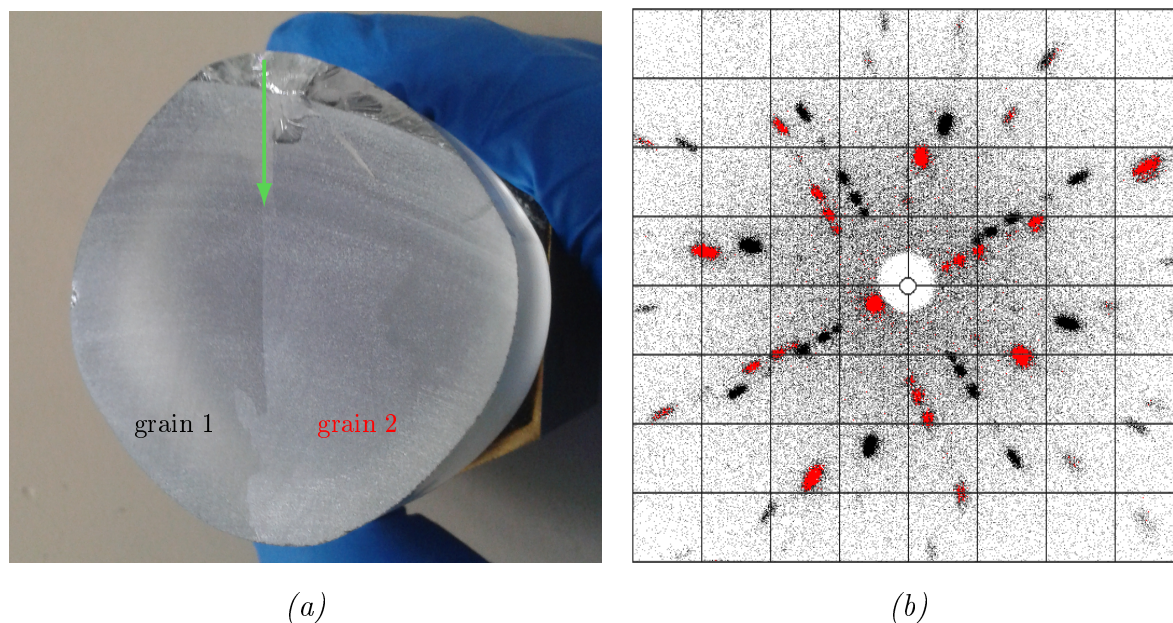


Figure B.5.: (a) shows a grain boundary (indicated by a green arrow) as observed in the cylindrical part of the crystal ingot TUM77. The orientation in both grains was measured by means of a real-time back reflection Laue camera [110]. In the Laue patterns of the two grains (b), a clear shift and tilt is visible between the red and black spots representing diffracted X-rays with certain wavelengths in case of grain 1 and 2, respectively. This implies that a misorientation between the two grains of the order of about 1° is present.

crystal. However, neither impurities are visible in the case of TUM77 nor does the used CaWO_4 seed crystal feature any defects. In any case, the occurrence of such grain boundaries emphasizes the importance of a defect-free well-oriented seed crystal.

B.4. CaWO_4 Powder used for TUM73

In the first version of the CaCO_3 powder purification, a back-transformation to CaCO_3 powder was conducted via a precipitation reaction with Na_2CO_3 (see section 5.3.2). The cleaned CaCO_3 powder was further processed to CaWO_4 via the solid state reaction explained in section 3.2. The result for this chemically treated powder was a stone-like, very hard end product. Two of the in total three CaWO_4 "stones" can be seen in figure B.6. Only after the reaction to CaWO_4 , it was discovered that the material contains a high amount of sodium (and potentially potassium) which could – together with the much finer structure of the cleaned CaCO_3 powder – be an explanation for the hardness of the CaWO_4 material. To apply a procedure which removes the sodium contamination, the stones had to be transformed back into powder. As neither a purely mechanical treatment nor, e.g., soaking in water helped to pulverize the material, the following method was applied: Inside an Al_2O_3 crucible, the stones were heated up to $\sim 600^\circ\text{C}$ and plunged into cold (supra-pure) water. In this way, the material became porous enough to be pulverized with an agate mortar before it was cleaned and used for the growth of TUM73. Although all steps were carefully executed, it cannot be excluded



Figure B.6.: CaWO_4 "stones" after production via the solid state reaction from purified CaCO_3 powder (version 1). To be able to clean the material from sodium and potassium contaminations, the material had to be heated up to $\sim 600^\circ\text{C}$ and plunged into cold (supra-pure) water. This method made the CaWO_4 porous enough to be pulverized with an agate mortar.

that contaminations were introduced during this rather extraordinary treatment.

B.5. Grown Crystal Ingots

Table B.1 lists all crystals that were grown at TUM via the Czochralski method in the scope of the present work. Each crystal can be identified by the acronym "TUM" plus a growth number. Included in table B.1 are the growth date, the crystal mass, the total length, the diameter of the cylindrical part, the growth speed (within the cylindrical part) as well as comments about anomalies or special characteristics. For all these growth processes, raw materials supplied by the company MV Laboratories [121] were used. Crystals with growth numbers between 48 and 68 were grown from a batch of CaCO_3 and WO_3 powders with the lot numbers D0712CAA3 and D0113WB1, respectively, which is denoted as batch 1. Starting from TUM69, the raw materials CaCO_3 and WO_3 with the lot numbers D0812CAA2R and D0714WB1, respectively, were used (batch 2). The corresponding analysis certificates are included in appendix D.

After each growth, new material has to be added as a certain melt level is needed for a successful seeding. However, the contamination of the remaining melt increases with the number of crystal ingots grown from the same material (see section 5.4). To ensure crystal ingots with good radiopurity and optical properties, the remaining melt has to be removed and the crucible has to be cleaned after several growth processes. The table points out in green when this has happened and which material has been used to refill the cleaned/exchanged crucible. It should be mentioned that two rhodium crucibles are available for Czochralski crystal growth. In the beginning of the present work, one of the crucibles had a diameter of 80 mm and, additionally, a larger one with a diameter of 120 mm was existent. It happened two times that the crucible was damaged during a growth process. A local melting of the 80 mm crucible was observed during the growth of

B.5. Grown Crystal Ingots

crystal	date	mass [g]	length [mm]	diameter [mm]	speed [mm/h]	comments
80 mm crucible cleaned and refilled with new CaWO ₄ powder (MV Laboratories, batch 1)						
TUM48	14.03.13	737	130	45.5	12	-
TUM49	19.03.13	737	130	45.5	6	striations
TUM50	05.04.13	737	130	45.5	12	3 % O, pink coloration, inclusions
TUM51	16.04.13	719	130	45.5	12	pink coloration, inclusions
TUM52	25.04.13	734	130	45.5	12	pink coloration, inclusions
80 mm crucible cleaned and refilled with new CaWO ₄ powder (MV Laboratories, batch 1)						
TUM53	28.10.13	370	130	45.5	12	growth unsuccessful, remelted
TUM54	04.11.13	735	130	45.5	12	-
TUM55	11.11.13	739	130	45.5	12	1 % excess WO ₃
TUM56	18.11.13	737	130	45.5	12	1 % excess WO ₃
120 mm crucible installed, filled with new CaWO ₄ powder (MV Laboratories, batch 1)						
TUM57	14.01.14	1849	170	63	12	cracks, remelted
TUM58	06.02.14	1960	170	65	12	growth unsuccessful, remelted
TUM59	18.02.14	-	-	-	-	seed holder broke
80 mm crucible installed, filled with crystal parts of TUM54, TUM57						
TUM60	09.07.14	-	-	-	-	crucible broke
120 mm crucible installed, filled with new CaWO ₄ powder (MV Laboratories, batch 1)						
TUM61	14.05.14	1903	170	65	12	cracks
TUM62	09.07.14	77	140	11	20	production of new seed crystals
TUM63	15.07.14	850	140	45.5	12	cracks, clouds, partially remelted
TUM64	07.09.14	490	105	45.5	2	cracks, asymmetric, remelted
TUM65	29.10.14	490	105	45.5	2	cracks, asymmetric, remelted
TUM66	25.11.14	730	130	45.5	12	slightly asymmetric, clouds
TUM67	04.02.15	730	130	45.5	6	slightly asymmetric
TUM68	26.02.15	730	130	45.5	6	after-heater and crucible broke
80 mm crucible and new after-heater installed, filled with new CaWO ₄ powder (MV Laboratories, batch 2)						
TUM69	19.08.15	355	110	30	12	few clouds
TUM70	03.09.15	355	110	30	12	few clouds
TUM71	10.09.15	370	120	30	12	few clouds
TUM72	21.10.15	370	120	30	12	few clouds
new 80 mm crucible installed, filled with new CaWO ₄ powder (MV Laboratories, batch 2, chemically cleaned)						
TUM73	13.11.15	390	125	30	12	-
TUM74	20.04.16	-	-	-	12	growth aborted
TUM75	27.04.16	-	-	-	12	growth aborted
TUM76	11.10.16	-	-	-	12	growth aborted
TUM77	04.05.17	-	-	-	12	growth aborted, crystal broke
TUM78	07.06.17	-	-	-	12	growth aborted, crystal broke
TUM79	12.07.17	690	130	44	12	cracks
TUM80	26.07.17	690	130	44	12	cracks
80 mm crucible installed, filled with CaWO ₄ crystal TUM61						
TUM81	13.09.17	390	125	30	12	-
TUM82	20.09.17	690	130	44	12	-

Table B.1.: Crystals grown at TUM via the Czochralski method during the present work. Included are the growth date, the crystal mass, the total length as well as diameter and growth speed in the cylindrical part. Anomalies or special features of the growth or crystal characteristics can be found as comments in the last column. A cleaning or an exchange of the crucible is indicated in green. Rows containing crystal ingots which were further processed into detector crystals now installed in CRESST-III Phase 1 are highlighted in light red. For details see text.

TUM60 whereas the 120 mm crucible was severely damaged during the growth of TUM68 due to a melting after-heater coil dripping onto the crucible. After this incident, a second 80 mm crucible was manufactured instead of the one with a diameter of 120 mm.

Several attempts were undertaken to improve the optical properties of the CaWO_4 crystals – in particular with respect to oxygen-related defects. The growth atmosphere, which is usually a mixture of 99 % argon and 1 % oxygen, was enriched with oxygen (in total 3 %) for the production of TUM50. However, a pink coloration of the crystal hints towards an incorporation of rhodium due to oxidation of the crucible material. Although the subsequent two crystals TUM51 and TUM52 were again grown in an atmosphere with only 1 % of oxygen, they featured a pinkish coloration, as well. Only a cleaning of the crucible removed the coloration of the crystals. Another attempt to increase the oxygen content was performed in the growth processes of the crystals TUM55 and TUM56 via adding an excess of 1 % WO_3 powder into the melt. However, the resulting crystals did not show a visible improvement.

Optical properties and also radiopurity might be improved when the growth speed is reduced. To investigate its influence, TUM64 and TUM65 were grown with 2 mm/h instead of the standard speed of 12 mm/h. Unfortunately, the resulting crystals of both growth processes featured cracks and an asymmetric form due to problems with the seed crystal and holder (compare section B.1). After reliable seed holding conditions had been re-established, the test was only repeated with a growth speed of 6 mm/h which did not result in visible effects on the quality of the crystal ingot.

The 80 mm crucible can hold up to ~ 1.5 kg of CaWO_4 material. A higher amount of up to ~ 4.5 kg could be filled into the 120 mm crucible allowing the growth of crystals with higher masses (compared to standard crystals with a mass of maximal ~ 800 g). All attempts to grow raw crystals with a mass of ~ 2 kg (TUM57, TUM58, TUM59, TUM61) were, however, not successful. The cracks observed in these crystal ingots hint towards large internal stresses. Like in case of almost all abortive growth processes, the crystal ingots were usually remelted for the following growth. The last available large crystal ingot (TUM61, with cracks) was recently remelted for recrystallization purposes (compare section 5.4) (growth 81).

In some cases, the growth was aborted by the software which happens when the deviation of the growth rate from the current set point exceeds a certain limit. In the growths of TUM74-TUM78 it was tried to crystallize the main part of the remaining melt, in case of TUM74-TUM76 starting with an already low melt level. However, a crystal cone growing below the melt level was at some point touching the bottom of the crucible (see section B.2) which led to an abortion. In the cases of TUM77 and TUM78, a higher amount of CaWO_4 material was filled into the crucible and the crystal length was reduced. Nevertheless, the growth process was aborted due to the touching crystal cone, however, these times occurring late in the last phases of the growth.

In several crystal ingots, a few clouds and inclusions are visible, particularly in the upper part, in the transition from shoulder to cylinder. These crystal parts can easily be cut away and the remaining cylinder can be used for detector crystal production. The rows in table B.1 containing crystals that are included as detector crystals in CRESST-III Phase 1 are highlighted in light red.

A more detailed list of the growth parameters is included for crystals that were further

parameter	TUM26				TUM68			
crystal mass [g]	337.7				747.6			
crystal length [mm]	105.0				130.0			
covered height [mm]	100.2				119.5			
crucible diameter [mm]	120				120			
R2/R1	0.3				0.3			
angle [deg]	58				68			
growth duration [h]	9.8				18.3			
	seed	shoulder	cylinder	tail	seed	shoulder	cylinder	tail
length [mm]	5	25	60	15	5	55	45	25
diameter [mm]	8	8 → 30	30	30 → 0	6	6 → 45.5	45.5	45.5 → 0
growth speed [mm/h]	20	10	10	15	20	6	6	15
rotation speed [rpm]	15	15	15	10	15	15	15	10
proportional term	5	5	3	4	5	2	1.5	4
integral term	20	30	40	30	20	40	55	40

Table B.2.: Growth parameters of the crystals TUM26 and TUM68 including mass, all geometrical values, speeds and proportional/integral terms. Global parameters are listed in the upper part, parameters changing in the different crystal parts (seed, shoulder, cylinder, and tail) are listed below. The transitions between the values are not abrupt but are happening gradually.

investigated in the present work. Table 3.2 shows the parameters for the raw crystals TUM73 and TUM56 whose CRESST-III detector crystals were analyzed as described in chapter 7. In addition, the optical properties of small crystals cut from the ingots TUM26 and TUM68 were investigated in chapter 4. Therefore, also their growth parameters are listed in a more detailed version in table B.2. TUM26 was grown with a small cylindrical diameter of 30 mm and a total length of 105 mm resulting in a mass of ~ 338 g. TUM68, on the other hand, is another example of a large CaWO_4 crystal with a maximal diameter of 45.5 mm, a crystal length of 130 mm and a total mass of ~ 748 g. Both crystals have a growth speed that is reduced compared to the usual value of 12 mm/h – namely 10 mm/h in the case of TUM26 and 6 mm/h for TUM68 leading to a significantly increased growth duration of 18.3 h in the latter case. All other parameters like the ratio R2/R1 and the angle determining the crystal geometry in the shoulder part (compare figure 3.10 in chapter 3) as well as proportional and integral terms needed for temperature regulation are comparable to that of standard raw crystals.

C. Measurement Methods for Trace Impurities

For the investigation of possible trace impurities in powder samples of CaCO_3 , WO_3 and CaWO_4 as well as in CaWO_4 crystal samples, various methods were tested. A short description of these methods as well as the suitability for the samples of interest can be found in the following.

C.1. γ -Ray Spectroscopy with High-Purity Germanium (HPGe) Detectors

Most radioactive isotopes produce γ -rays with discrete energies corresponding to the typical energy levels in their nuclei. γ -ray emissions of a sample can be detected with a spectroscopy system. The measured γ -ray energy spectrum is then used to identify the kind and amount of different isotopes present in the sample. Suitable for the detection of γ -rays of up to a few MeV are semiconductor-based instruments like germanium detectors. When ionizing γ -radiation strikes the semiconducting detector material, electrons and holes are formed. The quantity of electrons raised from valence to conducting band is, hereby, proportional to the energy of the incident photon. Via application of an electric field, electrons and holes move to the respective contacts producing a voltage signal. To suppress thermal excitation of valence electrons, such detectors have to be cooled with liquid nitrogen.

Very high resolutions in γ -ray spectroscopy are achieved by high-purity germanium (HPGe) detectors. A high purity of the germanium single crystal is a precondition for the sensitivity, otherwise impurities in the crystal can trap electrons and holes ruining the performance of the detector. With a sophisticated shielding and underground operation, low-level γ -spectroscopy with HPGe detectors can reach a sensitivity down to $\sim 10 \mu\text{Bq/kg}$ [142, 145, 172]. No restrictions on the kind of sample are given.

C.2. Neutron Activation Analysis (NAA)

Neutron activation analysis (NAA) describes the irradiation of a sample with thermal neutrons and the observation of subsequent decays of activated isotopes. The capturing of thermal neutrons by the various isotopes is, hereby, determined by their neutron-capture cross section.

In the case the activated isotopes emit γ -rays, HPGe detectors can again be used for the measurement. Compared to γ -ray spectroscopy without any activation, the sensitivity for several isotopes (e.g. ^{40}K) can significantly be enhanced. Due to their artificial

production, the γ -energies of the decaying nuclei do not match the γ -energies of natural radioactive isotopes which means that the background is comparably low [172].

For irradiation of samples, a thermal neutron source like, e.g., the Heinz-Maier-Leibnitz scientific neutron source FRM II in Garching is needed. An attempt to analyse a small amount (order of mg) of irradiated CaWO_4 powder was not successful. Although this small sample was irradiated at the position with the lowest flux¹ with the shortest possible irradiation time of less than one minute, the resulting activity of the sample was much too high for NAA. In other words, due to the large neutron-capture cross-section of, especially, ^{187}W and due to a half-life of the produced nucleus that is longer than for the isotopes of interest, NAA does not seem to be an appropriate investigation method for samples containing tungsten.

C.3. Atomic Absorption Spectroscopy (AAS)

Atomic absorption spectroscopy (AAS) is based on the absorption of energy by valence electrons of ground state atoms lifting them to a higher energy level (excited state). For resonant transitions, each element needs a specific energy to be excited. The total amount of radiation with a certain wavelength absorbed depends (amongst other factors) on the number of atoms of the element with corresponding excitation energy present in the sample.

For atomic absorption analysis, a sample is brought into solution (via dissolving or melting) in order to be presented to the spectrometer. The sample is turned into an aerosol and fed into a flame leading to a dissociation into ground state atoms (atomization). The radiation of a lamp is passed through the flame and is absorbed by the atoms to be analyzed. By measuring the radiation before and after absorption, the concentration of the analyzed atoms can be derived from the absorbed amount of radiation.

Atomic absorption is a comparative technique which is able to detect a large number of different elements down to concentrations in the range of ppm. Traces within the blank solution, i.e. the solution with all contents except for the sample to be analyzed, have to be measured and subtracted from the actual measurement. Furthermore, suitable standard reference materials of known compositions have to be available for calibration and for checking the analytical procedures [145].

As samples are processed as solutions, this method is not suitable for measuring absolute concentrations of hardly soluble substances like CaWO_4 powder and crystals.

C.4. Inductively Coupled Plasma Mass Spectrometry (ICP-MS)

In general, mass spectrometry is an analytic technique by which chemical substances are identified by the sorting of gaseous ions in electric and magnetic fields based on their mass-to-charge ratios. One possibility to generate ions is an electrodeless source with

¹At FRM II, samples can be transported to a couple of different positions in the direct vicinity of the reactor core via a pneumatic delivery facility.

high temperature as realized with an inductively coupled high-frequency plasma (ICP). The ICP is sustained in a torch where a flow of argon gas is introduced and seeded with free electrons. These electrons are accelerated with the applied high frequency and collide with argon atoms which leads to a partial ionization. With a suitable frequency and gas flow, a stable plasma with temperatures in the order of 10 000 K is formed. The sample which shall be investigated with inductively coupled plasma mass spectrometry (ICP-MS) is brought into solution with an internal standard usually consisting of deionized water and nitric or hydrochloric acid. It is nebulized in order to be introduced as wet aerosol into the central part of the ICP torch with argon carrier gas. There, the molecules contained in the sample evaporate and break apart. The constituent atoms are ionized and extracted into the mass spectrometer for separation and quantification. ICP-MS offers the possibility of a rapid and flexible multi-element determination of concentrations down to the ppq (10^{-15}) range. The concentration of low-background isotopes cannot be measured when they have a mass that interferes with the mass of molecules contained in the components of the instrument itself. Also here, certified reference materials such as single or multi-element reference standards are required for calibration. The accuracy of a quantitative measurement depends on the precision of the standards employed. Unfortunately, such reference standards with known compositions do often not exist for the materials of interest allowing only an investigation in a semi-quantitative mode [145].

As the preparation of samples includes dissolving and diluting in water and nitric or hydrochloric acid, absolute concentration values can only be achieved for solvable samples and not for materials like CaWO_4 .

C.5. Laser Ablation Inductively Coupled Plasma Mass Spectrometry (LA-ICP-MS)

An alternative to the standard ICP-MS method, which is also suitable for solid samples, is laser ablation inductively coupled plasma mass spectrometry (LA-ICP-MS). Instead of generating an aerosol as in case of standard ICP-MS, sample material is ablated with a pulsed UV laser and passed into the plasma [145]. From this point on, the identical procedure as for ICP-MS described in section C.4 is applied. As a dissolution of materials is not necessary, this method should also be suitable for (polished) CaWO_4 crystals and for pressed CaWO_4 powder samples.

C.6. Accelerator Mass Spectrometry (AMS)


Accelerator mass spectrometry (AMS) [173, 174] has – in comparison to other forms of mass spectrometry – the advantage of being able to separate rare isotopes from an abundant neighbouring mass. In an ion source, negative ions are sputtered off the sample of interest. These ions are extracted and cross a 90° injector magnet before entering a tandem accelerator. By means of a stripper foil, electrons are removed from the ions converting them into positively charged ions of different charge stages. In this way, all

molecular background can be suppressed. Another 90° magnet as well as Wien velocity filters are applied for a further mass and charge separation. The detection system (e.g. a time-of-flight spectrometer) finally allows the discrimination of mass and energy. However, also AMS depends on the comparison to a standard with known concentration. The feasibility of measuring CaWO_4 samples by means of AMS is currently being investigated at TUM [175].

D. Analysis Certificates

In this part the analysis certificates of all the materials and chemicals used in the present thesis are included. In case of each of the two raw powders CaCO_3 and WO_3 , two different batches supplied by the company MV Laboratories [121] were used in the present work for the production of CaWO_4 crystals. The analysis certificates of batch 1 and 2 of the WO_3 powder with the lot numbers D0113WB1 and D0714WB1 are included in figures D.1 and D.2, respectively. The purity of the WO_3 powder is 99.995% and the upper limit for the total metallic impurities was determined to be 10.46 ppm and 11.8 ppm, respectively. The CaCO_3 powder batches 1 and 2 with the lot numbers D0712CAA3 and D0812CAA2R are certificated in figures D.3 and D.4, respectively. The purity of 99.999% corresponds to a total metallic contamination of 3.2 ppm and 4.3 ppm, respectively. Batch 1 of both powders was used to produce CaWO_4 crystal ingots with growth numbers ranging between 48 and 68. Starting from TUM69, crystal ingots were grown from CaWO_4 powder produced from the second powder batches.

The certificate of analysis for the TOPO powder used for purification via the extraction method was delivered by the company Alfa Aesar [168]. The purity determined by a gas chromatographic (gc) analysis is 99.5% (see figure D.5). The supplier for the other chemicals needed for powder purification and production via the precipitation method is the company Carl Roth [176]. Exemplary certificates of analysis for NH_3 in supra and ultra quality, HNO_3 in supra quality as well as ultrapure H_2O are shown in figures D.6, D.7, D.8 and D.9, respectively. In these certificates, the maximum specification values for the corresponding quality as well as the actual values measured for the respective batch are listed.



MV LABORATORIES, INC.
A SUBSIDIARY OF SEASTAR CHEMICALS INC.
843 ROUTE 12 WEST, SUITE B17, FRENCHTOWN, NJ 08825
Phone: 908-788-6908 - Fax: 908-788-1746
www.mvlaboratories.com

Certificate of Analysis

Product: **Tungsten Oxide**
 Part Number: **MPWxBx6Z45**
 Purity¹: **99.995%**
 Lot Number: **D0113WB1**
 Certification Date: **February 6, 2013**
 Formula: **WO₃**
 Form: **Yellow powder**
 C.A.S. Number: **1314-35-8**

Actual lot analysis:
 Assay: 79.3% W
 Trace Impurities:

Ag	< 0.05	Cs	< 5	La	< 0.05	Pr	< 0.05	Te	< 0.1
Al	0.07	Cu	< 0.1	Li	< 0.05	Pt	< 0.5	Th	< 0.005
As	1.8	Dy	< 0.05	Lu	< 0.05	Rb	< 0.05	Ti	0.04
B	2.7	Er	< 0.05	Mg	< 0.05	Re	< 1	Tl	< 0.05
Ba	< 0.05	Eu	< 0.5	Mn	< 0.1	Rh	< 0.5	Tm	< 0.05
Be	< 0.01	Fe	0.44	Mo	< 1	Ru	< 0.5	U	< 0.005
Bi	< 0.01	Ga	< 0.1	Na	1.2	Sb	0.14	V	3.8
Ca	< 0.5	Gd	< 0.05	Nb	0.08	Sc	< 0.01	Y	< 0.05
Cd	< 0.5	Ge	< 0.5	Nd	< 0.05	Sm	< 0.05	Yb	< 0.05
Ce	< 0.05	Hf	< 0.05	Ni	< 0.1	Sn	< 0.5	Zn	< 0.1
Co	< 0.05	Ho	< 0.05	Pb	< 0.05	Sr	< 0.05	Zr	< 0.05
Cr	0.19	K	< 0.5	Pd	< 0.05	Tb	< 0.05		

Total Metallic Impurities (TMI) determined: 10.46ppm

¹ Purity is based on the measured trace impurities listed. For example, a Grade of 99.999% is defined as the total measured impurities are no greater than 10ppm. MV Laboratories, inc. lists all analytes where there is quantitative analytical certainty. Elemental impurities are determined by one or more of the following techniques ICP-OES, HR-ICP-MS, GD-MS, & AA. Values above the limit of quantitation are reported in ppm. Values below the limit of quantitation are reported as less than(<) the limit of quantitation in ppm.

All trace impurity values in ppm, unless otherwise noted.
 Impurities determined by GD-MS, unless otherwise noted. * Impurities determined by ICP-OES.



 Michael Stecker
 Senior Analytical Chemist
 MV Laboratories, Inc.

Figure D.1.: Certificate of analysis for WO₃ powder (batch 1 used in the present work) with a purity of 99.995 % delivered by the company MV Laboratories.

Certificate of Analysis

Product: Tungsten(VI) Oxide
 Part Number: MPWxBx6Z45
 Purity¹: 99.995%
 Lot Number: D0714WB1
 Certification Date: July 28, 2014
 Formula: WO₃
 Form: Yellow to lime-green powder
 C.A.S. Number: 1314-35-8

Actual lot analysis:

Assay: 79.3% W

Trace Impurities:

Ag	< 0.5	Cs	< 0.5	K	< 5	Pd	< 0.5	Tb	< 0.05
Al	< 1	Cu	< 0.5	La	< 0.5	Pr	< 0.05	Te	< 0.5
As	0.8	Dy	< 0.05	Li	< 0.1	Pt	< 0.5	Th	< 0.005
B	2	Er	< 1	Lu	< 0.05	Rb	< 0.5	Ti	< 0.5
Ba	< 0.5	Eu	< 0.5	Mg	< 0.5	Re	3	Tl	< 0.05
Be	< 0.5	Fe	< 1	Mn	< 0.5	Rh	< 0.5	Tm	< 0.05
Bi	< 0.5	Ga	< 2	Mo	2	Ru	< 0.5	U	< 0.005
Ca	< 1	Gd	< 0.05	Na	< 5	Sb	< 0.1	V	4
Cd	< 0.1	Ge	< 0.05	Nb	< 0.5	Sc	< 0.1	Y	< 0.1
Ce	< 0.1	Hf	< 1	Nd	< 0.05	Sm	< 0.05	Yb	< 0.05
Co	< 0.5	Ho	< 0.05	Ni	< 0.5	Sr	< 0.5	Zn	< 1
Cr	< 10	In	< 1	Pb	< 0.1	Ta	< 0.5	Zr	< 0.1

Total Metallic Impurities (TMI) determined: 11.8ppm

¹ Purity is based on the measured trace impurities listed. For example, a Grade of 99.999% is defined as the total measured impurities are no greater than 10ppm. MV Laboratories, inc. lists all analytes where there is quantitative analytical certainty. Elemental impurities are determined by one or more of the following techniques ICP-OES, HR-ICP-MS, GD-MS, & AA. Values above the limit of quantitation are reported in ppm. Values below the limit of quantitation are reported as less than(<) the limit of quantitation in ppm.


All trace impurity values in ppm, unless otherwise noted.

Impurities determined by GD-MS, unless otherwise noted. * Impurities determined by ICP-OES.



Michael Stecker
 Senior Analytical Chemist
 MV Laboratories, Inc.

Figure D.2.: Certificate of analysis for WO₃ powder (batch 2 used in the present work) with a purity of 99.995% delivered by the company MV Laboratories.



MV LABORATORIES, INC.
A SUBSIDIARY OF SEASTAR CHEMICALS INC.
843 ROUTE 12 WEST, SUITE B17, FRENCHTOWN, NJ 08825
Phone: 908-788-6508 - Fax: 908-788-1746
www.mvlaboratories.com

Certificate of Analysis

Product: Calcium Carbonate
 Part Number: MPCaHx2Z50
 Purity¹: 99.999%
 Lot Number: D0712CAA3
 Certification Date: August 2, 2012
 Formula: CaCO₃
 Form: White powder
 C.A.S. Number: 471-34-1

Actual lot analysis:

Assay: 39.6% Ca

Trace Impurities:

Ag	< 0.3	Cu	< 0.4	K	< 0.6	Pt	< 1	Tl	< 0.6
Al	< 0.6	Dy	< 0.8	La	< 0.3	Re	< 0.4	Tm	< 0.7
As	< 1	Er	< 0.9	Lu	< 0.1	Rh	< 1	V	< 0.3
Au	< 1	Eu	< 0.2	Mg	< 0.2	Ru	< 1	W	< 2
Ba	< 0.3	Fe	0.6	Mn	< 0.1	Sc	< 0.1	Y	< 0.3
Be	< 0.1	Ga	< 2	Mo	< 0.2	Sn	< 0.3	Yb	< 0.2
Bi	< 2	Gd	< 1	Na	< 1	Sr	0.8	Zn	< 0.2
Cd	0.8	Ge	< 1	Nb	< 0.6	Ta	< 1	Zr	< 0.3
Ce	< 2	Hf	< 0.7	Ni	< 0.2	Tb	< 1		
Co	< 0.2	Ho	< 1	Pb	< 0.5	Te	< 2		
Cr	0.4	Ir	< 0.7	Pd	< 1	Ti	0.6		

Total Metallic Impurities (TMI) determined: 3.2ppm

¹ Purity is based on the measured trace impurities listed. For example, a Grade of 99.999% is defined as the total measured impurities are no greater than 10ppm. MV Laboratories, Inc. lists all analytes where there is quantitative analytical certainty. Elemental impurities are determined by one or more of the following techniques ICP-OES, HR-ICP-MS, GD-MS, & AA. Values above the limit of quantitation are reported in ppm. Values below the limit of quantitation are reported as less than(<) the limit of quantitation in ppm.

All trace impurity values in ppm, unless otherwise noted.
 Impurities determined by ICP-OES, unless otherwise noted. * Impurities determined by AA.



 Michael Stecker
 Senior Analytical Chemist
 MV Laboratories, Inc.

Figure D.3.: Certificate of analysis for CaCO₃ powder (batch 1 used in the present work) with a purity of 99.999 % delivered by the company MV Laboratories.

Certificate of Analysis

Product: Calcium Carbonate, low Strontium
 Part Number: C2CaHx2Z50
 Purity¹: 99.999%
 Lot Number: D0812CAA2R
 Certification Date: August 16, 2012
 Formula: CaCO₃
 Form: White powder
 C.A.S. Number: 471-34-1

Actual lot analysis:

Assay: 41.0% Ca

Trace Impurities:

Ag	< 0.3	Cu	< 0.4	K	< 0.4	Pt	< 1	Tl	< 0.7
Al	< 0.5	Dy	< 0.8	La	< 0.3	Re	< 0.4	Tm	< 0.7
As	< 2	Er	< 0.9	Lu	< 0.2	Rh	< 1	V	< 0.3
Au	< 1	Eu	< 0.2	Mg	< 0.3	Ru	< 1	W	< 2
Ba	< 0.3	Fe	3	Mn	0.1	Sc	< 0.1	Y	< 0.1
Be	< 0.1	Ga	< 2	Mo	< 0.2	Sn	< 0.3	Yb	< 0.1
Bi	< 2	Gd	< 1	Na	< 1	Sr	1.2	Zn	< 0.2
Cd	< 0.1	Ge	< 1	Nb	< 0.6	Ta	< 1	Zr	< 0.3
Ce	< 2	Hf	< 0.7	Ni	< 0.2	Tb	< 1		
Co	< 0.2	Ho	< 1	Pb	< 0.5	Tc	< 2		
Cr	< 0.4	Ir	< 0.7	Pd	< 1	Ti	< 0.2		

Total Metallic Impurities (TMI) determined: 4.3ppm

¹ Purity is based on the measured trace impurities listed. For example, a Grade of 99.999% is defined as the total measured impurities are no greater than 10ppm. MV Laboratories, Inc. lists all analytes where there is quantitative analytical certainty. Elemental impurities are determined by one or more of the following techniques ICP-OES, HR-ICP-MS, GD-MS, & AA. Values above the limit of quantitation are reported in ppm. Values below the limit of quantitation are reported as less than(<) the limit of quantitation in ppm.

All trace impurity values in ppm, unless otherwise noted.

Impurities determined by ICP-OES, unless otherwise noted. * Impurities determined by AA.



Michael Stecker
 Senior Analytical Chemist
 MV Laboratories, Inc.

Figure D.4.: Certificate of analysis for CaCO₃ powder (batch 2 used in the present work) with a purity of 99.999 % delivered by the company MV Laboratories.

Alfa Aesar

Certificate of analysis

Product No.: A11062
Product: Tri-n-octylphosphine oxide, 98%
Lot No.: 10171483

Appearance: White fused solid
Melting Point: 53.0-55.3°C
Assay (GC): 99.5%

This document has been electronically generated and does not require a signature.

Order our products online www.alfa.com

ThermoFisher
SCIENTIFIC

Figure D.5.: Certificate of analysis for TOPO powder with an assay purity of 99.5 % supplied by Alfa Aesar [168].

Analysenzertifikat

CERTIFICATE OF ANALYSIS



Art.Nr. / PRODUCT NO.: HN56
 Produkt / PRODUCT: Ammoniaklösung Supra-Qualität
 ROTIPURAN® Supra, 20%
 Ammonia Solution
 Charge / LOT NUMBER: 7116041
 Dichte / DENSITY: D 0,92 g/ml
 Molekulargewicht / MOLECULAR WEIGHT: NH₃ - M 17,03 g/mol
 Lagertemperatur / STORAGE TEMPERATURE: 15°C - 25°C.
 MHD / EXPIRY DATE: 05/05/2019 Druckdatum / DATE PRINTED: 05/05/2016

Gehalt/Assay(NH ₃ , w/w): 20 - 22%		Actual Value: 22%			
MaximumSpecification/ Garantieanalyse	Actual Values/ Chargenwerte	MaximumSpecification/ Garantieanalyse	Actual Values/ Chargenwerte	MaximumSpecification/ Garantieanalyse	Actual Values/ Chargenwerte
Farbe	≤ 10 APHA	<10 APHA		Molybdän (Mo)	≤ 0.5 ppb
Chlorid (Cl)	≤ 0.00005 %	<0.00005%		Natrium (Na)	≤ 1 ppb
Phosphat (PO ₄ ³⁻)	≤ 0.000001 %	<0.000001%		Neodym (Nd)	≤ 0.1 ppb
Sulfat (SO ₄ ²⁻)	≤ 0.0001 %	<0.0001%		Nickel (Ni)	≤ 0.5 ppb
Aluminium (Al)	≤ 1 ppb	<0.2 ppb		Niob (Nb)	≤ 0.1 ppb
Antimon (Sb)	≤ 0.5 ppb	<0.1 ppb		Palladium (Pd)	Nur Informationen
Arsen (As)	≤ 1 ppb	<0.1 ppb		Platin (Pt)	Nur Informationen
Barium (Ba)	≤ 0.1 ppb	<0.1 ppb		Praseodym (Pr)	≤ 0.1 ppb
Beryllium (Be)	≤ 0.1 ppb	<0.1 ppb		Quecksilber (Hg)	≤ 0.2 ppb
Blei (Pb)	≤ 0.1 ppb	<0.1 ppb		Rhenium (Re)	Nur Informationen
Cadmium (Cd)	≤ 0.5 ppb	<0.1 ppb		Rhodium (Rh)	≤ 0.5 ppb
Calcium (Ca)	≤ 1 ppb	<0.5 ppb		Rubidium (Rb)	≤ 0.1 ppb
Cäsium (Cs)	≤ 0.1 ppb	<0.1 ppb		Ruthenium (Ru)	Nur Informationen
Cer (Ce)	≤ 0.1 ppb	<0.1 ppb		Samarium (Sm)	≤ 0.1 ppb
Chrom (Cr)	≤ 0.5 ppb	<0.1 ppb		Scandium (Sc)	≤ 0.1 ppb
Dysprosium (Dy)	≤ 0.1 ppb	<0.1 ppb		Selen (Se)	≤ 1 ppb
Eisen (Fe)	≤ 1 ppb	<0.5 ppb		Silber (Ag)	≤ 0.5 ppb
Erbium (Er)	≤ 0.1 ppb	<0.1 ppb		Strontium (Sr)	≤ 0.1 ppb
Europium (Eu)	≤ 0.1 ppb	<0.1 ppb		Tellur (Te)	≤ 0.1 ppb
Gadolinium (Gd)	≤ 0.1 ppb	<0.1 ppb		Terbium (Tb)	≤ 0.1 ppb
Gallium (Ga)	≤ 0.1 ppb	<0.1 ppb		Thallium (Tl)	≤ 0.1 ppb
Germanium (Ge)	≤ 0.1 ppb	<0.1 ppb		Thorium (Th)	≤ 0.1 ppb
Gold (Au)	≤ 0.5 ppb	<0.1 ppb		Thulium (Tm)	≤ 0.1 ppb
Hafnium (Hf)	Nur Informationen	<0.5 ppb		Titan (Ti)	≤ 0.5 ppb
Holmium (Ho)	≤ 0.1 ppb	<0.1 ppb		Uran (U)	≤ 0.1 ppb
Indium (In)	≤ 0.1 ppb	<0.1 ppb		Vanadium (V)	≤ 0.5 ppb
Kalium (K)	≤ 1 ppb	<0.2 ppb		Wismut (Bi)	≤ 0.1 ppb
Kobalt (Co)	≤ 0.5 ppb	<0.1 ppb		Wolfram (W)	≤ 0.1 ppb
Kupfer (Cu)	≤ 0.5 ppb	<0.5 ppb		Ytterbium (Yb)	≤ 0.1 ppb
Lanthan (La)	≤ 0.1 ppb	<0.1 ppb		Yttrium (Y)	≤ 0.1 ppb
Lithium (Li)	≤ 0.1 ppb	<0.1 ppb		Zink (Zn)	≤ 0.5 ppb
Lutetium (Lu)	≤ 0.1 ppb	<0.1 ppb		Zinn (Sn)	≤ 0.5 ppb
Magnesium (Mg)	≤ 1 ppb	<0.2 ppb		Zirkonium (Zr)	≤ 0.1 ppb
Mangan (Mn)	≤ 0.5 ppb	<0.2 ppb			

Die Elementkonzentration entspricht zum Zeitpunkt der Konfektionierung. / Element concentrations are at the point of bottling.
 Die Konzentration einiger Elemente, insbesondere von Al, Ca, Fe, Na, & Zn kann sich während der Lagerung in Polyethylenflaschen erhöhen. / Concentrations of some elements in particular, Al, Ca, Fe, Na, & Zn will increase due to storage in polyethylene bottles.
 Unsere Produkte sind für Laborzwecke geprüft. / Our products are tested for laboratory use only.
 Carl Roth GmbH + Co. KG
 Qualitätskontrolle/Quality Control
 Dieses Dokument wurde automatisch erstellt und ist ohne Unterschrift gültig. / This document is computer printout and has therefore not been signed by hand.

Carl Roth GmbH + Co. KG
 Schoemperlenstraße 3-5
 76185 Karlsruhe
 Telefon 0721/5606-0
 Telefax 0721/5606-149
 E-Mail: info@carlroth.de

Die Firma ist eine Kommanditgesellschaft mit Sitz in Karlsruhe, Reg. Gericht Mannheim HRB 100055. Persönlich haftende Gesellschafterin ist die Firma Roth Chemie GmbH mit Sitz in Karlsruhe, Reg. Gericht Mannheim HRB 100428.
 Vorsitzender des Aufsichtsrats: Eberhard Gaul
 Geschäftsführer: Dr. Alfred Wagner und Lothar Haidmann



Figure D.6.: Certificate of analysis for NH₃ solution in supra quality from the supplier Carl Roth [176].

Analysenzertifikat

CERTIFICATE OF ANALYSIS



Art.Nr. / PRODUCT NO.: HN66
 Produkt / PRODUCT: **Ammoniaklösung Ultra-Qualität**
 ROTIPURAN® Ultra, 20%
 Ammonia Solution
 Charge / LOT NUMBER: **7214100**
 Dichte / DENSITY: D 0,92 g/ml
 Molekulargewicht / MOLECULAR WEIGHT: NH₃ - M 17,03 g/mol
 Lagertemperatur / STORAGE TEMPERATURE: 15°C - 25°C.
 MHD / EXPIRY DATE: **05/11/2017** Druckdatum / DATE PRINTED: **05/11/2014**

Gehalt / Assay (NH ₃ , w/w): 20 - 22%		Actual Value: 21%			
Maximum Specification / Garantieanalyse	Actual Values / Chargenwerte	Maximum Specification / Garantieanalyse	Actual Values / Chargenwerte		
Aluminium (Al)	≤ 20 ppt	< 5 ppt	Neodym (Nd)	≤ 10 ppt	< 0.01 ppt
Antimon (Sb)	≤ 10 ppt	< 0.01 ppt	Nickel (Ni)	≤ 10 ppt	< 0.5 ppt
Arsen (As)	≤ 10 ppt	< 1 ppt	Niob (Nb)	≤ 10 ppt	< 0.01 ppt
Barium (Ba)	≤ 10 ppt	< 0.05 ppt	Palladium (Pd)	Nur Informationen	< 1 ppt
Beryllium (Be)	≤ 10 ppt	< 0.01 ppt	Platin (Pt)	Nur Informationen	< 1 ppt
Blei (Pb)	≤ 10 ppt	< 0.05 ppt	Praseodym (Pr)	≤ 10 ppt	< 0.01 ppt
Cadmium (Cd)	≤ 10 ppt	< 0.01 ppt	Quecksilber (Hg)	≤ 200 ppt	< 100 ppt
Calcium (Ca)	≤ 10 ppt	< 5 ppt	Rhenium (Re)	Nur Informationen	< 1 ppt
Cäsium (Cs)	≤ 10 ppt	< 0.01 ppt	Rhodium (Rh)	≤ 10 ppt	< 0.01 ppt
Cer (Ce)	≤ 10 ppt	< 0.01 ppt	Rubidium (Rb)	≤ 10 ppt	< 0.01 ppt
Chrom (Cr)	≤ 10 ppt	< 0.05 ppt	Ruthenium (Ru)	Nur Informationen	< 1 ppt
Dysprosium (Dy)	≤ 10 ppt	< 0.01 ppt	Samarium (Sm)	≤ 10 ppt	< 0.01 ppt
Eisen (Fe)	≤ 10 ppt	< 0.5 ppt	Scandium (Sc)	≤ 10 ppt	< 0.1 ppt
Erbium (Er)	≤ 10 ppt	< 0.01 ppt	Selen (Se)	Nur Informationen	< 10 ppt
Europium (Eu)	≤ 10 ppt	< 0.01 ppt	Silber (Ag)	≤ 10 ppt	< 0.01 ppt
Gadolinium (Gd)	≤ 10 ppt	< 0.01 ppt	Strontium (Sr)	≤ 10 ppt	< 0.05 ppt
Gallium (Ga)	≤ 10 ppt	< 0.01 ppt	Tellur (Te)	≤ 10 ppt	< 0.05 ppt
Germanium (Ge)	≤ 10 ppt	< 0.01 ppt	Terbium (Tb)	≤ 10 ppt	< 0.01 ppt
Gold (Au)	≤ 10 ppt	< 1 ppt	Thallium (Tl)	≤ 10 ppt	< 0.01 ppt
Hafnium (Hf)	Nur Informationen	< 0.01 ppt	Thorium (Th)	≤ 10 ppt	< 0.01 ppt
Holmium (Ho)	≤ 10 ppt	< 0.01 ppt	Thulium (Tm)	≤ 10 ppt	< 0.01 ppt
Indium (In)	≤ 10 ppt	< 0.01 ppt	Titan (Ti)	≤ 10 ppt	< 0.1 ppt
Kalium (K)	≤ 10 ppt	< 1 ppt	Uran (U)	≤ 10 ppt	< 0.01 ppt
Kobalt (Co)	≤ 10 ppt	< 0.05 ppt	Vanadium (V)	≤ 10 ppt	< 0.5 ppt
Kupfer (Cu)	≤ 10 ppt	< 0.1 ppt	Wismut (Bi)	≤ 10 ppt	< 0.01 ppt
Lanthan (La)	≤ 10 ppt	< 0.01 ppt	Wolfram (W)	≤ 10 ppt	< 0.05 ppt
Lithium (Li)	≤ 10 ppt	< 0.01 ppt	Ytterbium (Yb)	≤ 10 ppt	< 0.01 ppt
Lutetium (Lu)	≤ 10 ppt	< 0.01 ppt	Yttrium (Y)	≤ 10 ppt	< 0.01 ppt
Magnesium (Mg)	≤ 10 ppt	< 0.5 ppt	Zink (Zn)	≤ 10 ppt	< 0.5 ppt
Mangan (Mn)	≤ 10 ppt	< 0.05 ppt	Zinn (Sn)	≤ 10 ppt	< 0.05 ppt
Molybdän (Mo)	≤ 10 ppt	< 0.05 ppt	Zirkonium (Zr)	≤ 10 ppt	< 0.01 ppt
Natrium (Na)	≤ 20 ppt	< 10 ppt			

Unsere Produkte sind für Laborzwecke geprüft. / Our products are tested for laboratory use only.

Carl Roth GmbH + Co. KG
 Qualitätskontrolle/Quality Control

Dieses Dokument wurde maschinell erstellt und ist ohne Unterschrift gültig. / This document is computer printout and has therefore not been signed by hand.

Carl Roth GmbH + Co. KG
 Schoemperlenstraße 3-5
 76185 Karlsruhe
 Telefon 0721/5606-0
 Telefax 0721/5606-149
 E-Mail: info@carlroth.de

Die Firma ist eine Kommanditgesellschaft mit Sitz in Karlsruhe, Reg. Gericht
 Mannheim HRA 100055. Persönlich haftende Gesellschafterin ist die Firma Roth
 Chemie GmbH mit Sitz in Karlsruhe, Reg. Gericht Mannheim HRB 100428.
 Vorsitzender des Aufsichtsrats: Eberhard Gaul
 Geschäftsführer: Dr. Alfred Wagner und Lothar Haidmann



Figure D.7.: Certificate of analysis for NH₃ solution in ultra quality delivered by Carl Roth [176].

Analysenzertifikat

CERTIFICATE OF ANALYSIS



Art.Nr. / PRODUCT NO.: HN50
 Produkt / PRODUCT: **Salpetersäure Supra-Qualität**
 ROTIPURAN® Supra, 69%
 Nitric acid
 Charge / LOT NUMBER: **1115090**
 Dichte / DENSITY: D 1,41 g/ml
 Molekulargewicht / MOLECULAR WEIGHT: HNO₃ - M 63,01 g/mol
 Lagertemperatur / STORAGE TEMPERATURE: 15°C - 25°C.
MHD / EXPIRY DATE: 14/10/2017 **Druckdatum / DATE PRINTED: 14/10/2015**

Gehalt / Assay (HNO ₃ , w/w): 67 - 69%		Actual Value: 69%	
Maximum Specification / Garantieranalyse	Actual Values / Chargenwerte	Maximum Specification / Garantieranalyse	Actual Values / Chargenwerte
Farbe ≤ 10 APHA	< 7 APHA	Molybdän (Mo) ≤ 0.1 ppb	< 0.1 ppb
Chlorid (Cl) ≤ 0.00002 %	< 0.00002%	Natrium (Na) ≤ 1 ppb	< 0.3 ppb
Gesamtschwefel (S) ≤ 0.00003 %	< 0.00003%	Neodym (Nd) ≤ 0.1 ppb	< 0.1 ppb
Aluminium (Al) ≤ 1 ppb	< 0.5 ppb	Nickel (Ni) ≤ 0.5 ppb	< 0.5 ppb
Antimon (Sb) ≤ 0.5 ppb	< 0.1 ppb	Niob (Nb) ≤ 0.1 ppb	< 0.1 ppb
Arsen (As) ≤ 0.5 ppb	< 0.1 ppb	Palladium (Pd) ≤ 0.5 ppb	< 0.1 ppb
Barium (Ba) ≤ 0.1 ppb	< 0.1 ppb	Platin (Pt) ≤ 0.5 ppb	< 0.1 ppb
Beryllium (Be) ≤ 0.1 ppb	< 0.1 ppb	Praseodym (Pr) ≤ 0.1 ppb	< 0.1 ppb
Blei (Pb) ≤ 0.1 ppb	< 0.1 ppb	Quecksilber (Hg) ≤ 0.1 ppb	< 0.02 ppb
Bor (B) ≤ 1 ppb	< 0.5 ppb	Rhenium (Re) ≤ 0.1 ppb	< 0.1 ppb
Cadmium (Cd) ≤ 0.5 ppb	< 0.1 ppb	Rhodium (Rh) ≤ 0.5 ppb	< 0.1 ppb
Calcium (Ca) ≤ 1 ppb	< 0.5 ppb	Rubidium (Rb) ≤ 0.1 ppb	< 0.1 ppb
Cäsium (Cs) ≤ 0.1 ppb	< 0.1 ppb	Ruthenium (Ru) ≤ 0.5 ppb	< 0.1 ppb
Cer (Ce) ≤ 0.1 ppb	< 0.1 ppb	Samarium (Sm) ≤ 0.1 ppb	< 0.1 ppb
Chrom (Cr) ≤ 1 ppb	< 0.5 ppb	Scandium (Sc) ≤ 0.1 ppb	< 0.1 ppb
Dysprosium (Dy) ≤ 0.1 ppb	< 0.1 ppb	Selen (Se) ≤ 1 ppb	< 0.1 ppb
Eisen (Fe) ≤ 1 ppb	< 0.5 ppb	Silber (Ag) ≤ 0.1 ppb	< 0.1 ppb
Erbium (Er) ≤ 0.1 ppb	< 0.1 ppb	Strontium (Sr) ≤ 0.1 ppb	< 0.1 ppb
Europium (Eu) ≤ 0.1 ppb	< 0.1 ppb	Tantal (Ta) Nur Informationen	< 0.1 ppb
Gadolinium (Gd) ≤ 0.1 ppb	< 0.1 ppb	Tellur (Te) ≤ 0.1 ppb	< 0.1 ppb
Gallium (Ga) ≤ 0.1 ppb	< 0.1 ppb	Terbium (Tb) ≤ 0.1 ppb	< 0.1 ppb
Germanium (Ge) ≤ 0.1 ppb	< 0.1 ppb	Thallium (Tl) ≤ 0.1 ppb	< 0.1 ppb
Gold (Au) ≤ 0.1 ppb	< 0.1 ppb	Thorium (Th) ≤ 0.1 ppb	< 0.1 ppb
Hafnium (Hf) ≤ 0.1 ppb	< 0.1 ppb	Thulium (Tm) ≤ 0.1 ppb	< 0.1 ppb
Holmium (Ho) ≤ 0.1 ppb	< 0.1 ppb	Titan (Ti) ≤ 0.5 ppb	< 0.1 ppb
Indium (In) ≤ 0.1 ppb	< 0.1 ppb	Uran (U) ≤ 0.1 ppb	< 0.1 ppb
Kalium (K) ≤ 1 ppb	< 0.2 ppb	Vanadium (V) ≤ 0.5 ppb	< 0.1 ppb
Kobalt (Co) ≤ 0.5 ppb	< 0.1 ppb	Wismut (Bi) ≤ 0.1 ppb	< 0.1 ppb
Kupfer (Cu) ≤ 0.5 ppb	< 0.2 ppb	Wolfram (W) ≤ 0.1 ppb	< 0.1 ppb
Lanthan (La) ≤ 0.1 ppb	< 0.1 ppb	Ytterbium (Yb) ≤ 0.1 ppb	< 0.1 ppb
Lithium (Li) ≤ 0.1 ppb	< 0.1 ppb	Yttrium (Y) ≤ 0.1 ppb	< 0.1 ppb
Lutetium (Lu) ≤ 0.1 ppb	< 0.1 ppb	Zink (Zn) ≤ 0.5 ppb	< 0.2 ppb
Magnesium (Mg) ≤ 1 ppb	< 0.2 ppb	Zinn (Sn) ≤ 0.5 ppb	< 0.1 ppb
Mangan (Mn) ≤ 0.1 ppb	< 0.1 ppb	Zirkonium (Zr) ≤ 0.1 ppb	< 0.1 ppb

Die Elementkonzentration entspricht zum Zeitpunkt der Konfektionierung. / Element concentrations are at the point of bottling.
 Die Konzentration einiger Elemente, insbesondere von Ca, Si, K, Na, B, Al, Mg & Mn kann sich während der Lagerung in Glasflaschen erhöhen. / Concentrations of some elements in particular, Ca, Si, K, Na, B, Al, Mg & Mn will increase due to storage in glass bottles.
 Unsere Produkte sind für Laborzwecke geprüft. / Our products are tested for laboratory use only.
 Carl Roth GmbH + Co. KG
 Qualitätskontrolle/Quality Control
 Dieses Dokument wurde maschinell erstellt und ist ohne Unterschrift gültig. / This document is computer printout and has therefore not been signed by hand.

Carl Roth GmbH + Co. KG Telefon 0721/5606-0
 Schoemperlenstraße 3-5 Telefax 0721/5606-149
 76185 Karlsruhe E-Mail: info@carlroth.de

Die Firma ist eine Kommanditgesellschaft mit Sitz in Karlsruhe, Reg. Gericht Mannheim HRA 100055. Persönlich haftende Gesellschafterin ist die Firma Roth Chemie GmbH mit Sitz in Karlsruhe, Reg. Gericht Mannheim HRB 100428.
 Vorsitzender des Aufsichtsrats: Eberhard Gaul
 Geschäftsführer: Dr. Alfred Wagner und Lothar Haidmann



Figure D.8.: Certificate of analysis for HNO₃ solution in supra quality supplied by Carl Roth [176].

Analysenzertifikat

CERTIFICATE OF ANALYSIS



Art.Nr. / PRODUCT NO.:

HN68

Produkt / PRODUCT:

Wasser Ultra-Qualität

ROTIPURAN® Ultra

Water

Charge / LOT NUMBER:

9216010

Dichte / DENSITY:

D 1,00 g/ml

Molekulargewicht / MOLECULAR WEIGHT:

H₂O - M 18,02 g/mol

Lagertemperatur / STORAGE TEMPERATURE:

15°C - 25°C

MHD / EXPIRY DATE: 29/01/2019

Druckdatum / DATE PRINTED: 29/01/2016

Maximum Specification / Garantieanalyse	Actual Values / Chargenwerte	Maximum Specification / Garantieanalyse	Actual Values / Chargenwerte
Farbe	≤ 10 APHA	Mangan (Mn)	≤ 10 ppt
Chlorid (Cl ⁻)	≤ 1 ppb	Molybdän (Mo)	≤ 10 ppt
Phosphat (PO ₄ ³⁻)	≤ 1 ppb	Natrium (Na)	≤ 10 ppt
Sulfat (SO ₄ ²⁻)	≤ 1 ppb	Neodym (Nd)	≤ 1 ppt
Aluminium (Al)	≤ 20 ppt	Nickel (Ni)	≤ 10 ppt
Antimon (Sb)	≤ 10 ppt	Niob (Nb)	≤ 10 ppt
Arsen (As)	≤ 10 ppt	Palladium (Pd)	≤ 10 ppt
Barium (Ba)	≤ 10 ppt	Platin (Pt)	≤ 10 ppt
Beryllium (Be)	≤ 10 ppt	Praseodym (Pr)	≤ 10 ppt
Blei (Pb)	≤ 10 ppt	Quecksilber (Hg)	≤ 20 ppt
Bor (B)	≤ 20 ppt	Rhenium (Re)	≤ 10 ppt
Cadmium (Cd)	≤ 10 ppt	Rhodium (Rh)	≤ 10 ppt
Calcium (Ca)	≤ 10 ppt	Rubidium (Rb)	≤ 10 ppt
Cäsium (Cs)	≤ 10 ppt	Ruthenium (Ru)	≤ 10 ppt
Cer (Ce)	≤ 10 ppt	Samarium (Sm)	≤ 10 ppt
Chrom (Cr)	≤ 10 ppt	Scandium (Sc)	≤ 10 ppt
Dysprosium (Dy)	≤ 1 ppt	Selen (Se)	≤ 50 ppt
Eisen (Fe)	≤ 10 ppt	Silber (Ag)	≤ 10 ppt
Erbium (Er)	≤ 1 ppt	Strontium (Sr)	≤ 10 ppt
Europium (Eu)	≤ 1 ppt	Tantal (Ta)	≤ 10 ppt
Gadolinium (Gd)	≤ 1 ppt	Tellur (Te)	≤ 1 ppt
Gallium (Ga)	≤ 10 ppt	Terbium (Tb)	≤ 10 ppt
Germanium (Ge)	≤ 10 ppt	Thallium (Tl)	≤ 10 ppt
Gold (Au)	≤ 10 ppt	Thorium (Th)	≤ 1 ppt
Hafnium (Hf)	≤ 1 ppt	Thulium (Tm)	≤ 10 ppt
Holmium (Ho)	≤ 1 ppt	Titan (Ti)	≤ 10 ppt
Indium (In)	≤ 1 ppt	Uran (U)	≤ 1 ppt
Kalium (K)	≤ 10 ppt	Vanadium (V)	≤ 10 ppt
Kobalt (Co)	≤ 10 ppt	Wismut (Bi)	≤ 10 ppt
Kupfer (Cu)	≤ 10 ppt	Wolfram (W)	≤ 10 ppt
Lanthan (La)	≤ 1 ppt	Ytterbium (Yb)	≤ 10 ppt
Lithium (Li)	≤ 10 ppt	Yttrium (Y)	≤ 1 ppt
Lutetium (Lu)	≤ 1 ppt	Zink (Zn)	≤ 10 ppt
Magnesium (Mg)	≤ 10 ppt	Zinn (Sn)	≤ 10 ppt
		Zirkonium (Zr)	≤ 10 ppt

Unsere Produkte sind für Laborzwecke geprüft. / Our products are tested for laboratory use only.

Carl Roth GmbH + Co. KG

Qualitätskontrolle/Quality Control

Dieses Dokument wurde maschinell erstellt und ist ohne Unterschrift gültig. / This document is computer printout and has therefore not been signed by hand.

Carl Roth GmbH + Co. KG
Schoemperlenstraße 3-5
76185 Karlsruhe

Telefon 0721/5606-0
Telefax 0721/5606-149
E-Mail: info@carlroth.de

Die Firma ist eine Kommanditgesellschaft mit Sitz in Karlsruhe, Reg. Gericht
Mannheim HRA 100055. Persönlich haftende Gesellschafterin ist die Firma Roth
Chemie GmbH mit Sitz in Karlsruhe, Reg. Gericht Mannheim HRB 100428.
Vorsitzender des Aufsichtsrats: Eberhard Gaul
Geschäftsführer: Dr. Alfred Wagner und Lothar Haidmann



Figure D.9.: Certificate of analysis for ultrapure H₂O delivered by the company Carl Roth [176].

E. Analysis and Cut Parameters

In the present work, a partial data set of CRESST-III Phase 1 lasting from October 2016 until March 2017 was analyzed (see chapters 6 and 7). CRESST data taking has to be interrupted every ~ 50 h due to cryostat maintenance and a new measurement file is started afterwards. Background data is denoted as bg plus the corresponding file number. The list of files included for the analysis of e^-/γ -events in the present work can be found in table E.1. The files bg_004 - bg_015 marked in grey are excluded from the analysis of α -events as the operation parameters of the iSticks were not stable before file bg_018. In between the listed filenames, several files are excluded when data taking was somehow corrupted or when the detectors were severely disturbed (e.g., due to earthquakes or extremely high noise conditions).

Several preparation steps as described in chapter 6 are applied to the data of the four analyzed detector modules A, B, D, and E. Table E.2 summarizes the truncation limits of the truncated template fit of particle pulses (PP) and test pulses (TP) for each phonon (PH) and light (L) detector. Furthermore, the CPE factors determined for the energy calibration are included. In a first step, the CPE factors were calculated from the 63.3 keV line of a ^{57}Co calibration. In the background data set, the energy scale was cross-checked with the 11.27 keV line originating from cosmogenic activation and – in case of a deviation – corrected for the phonon detectors.

After the template fit and the energy calibration, a series of data quality cuts is applied to the various detectors for the investigation of e^-/γ -events. To guarantee stable operation conditions, a stable range of the control pulse (CP) height has to be defined for the stability cut. Afterwards, cuts on the parameters right-left baseline (RLB), peak position (PP), peak position-peak onset (PPO), delta voltage/RMS (DV) as well as on the FWHM of the baseline (FWHMB) are performed to remove invalid event classes. Several cuts are only applied to the phonon detectors as these cuts would discard potential signal events in the light detector. In order to discriminate interactions occurring directly in the iStick, the iStick channel i is used for a cut on its pulse height. All cut ranges of the valid events kept for the e^-/γ -analysis are listed in table E.3 for the investigated detectors.

Concerning the α -analysis, the cut limits applied to the detectors of modules A, B, D, and E are summarized in table E.4. Compared to the analysis of the e^-/γ -band, much higher values were chosen for the stable range of control pulses since it was observed that a non-proportionally high fraction of α -events is removed otherwise. As all channels involved in an α -event (phonon, light, and iStick) feature a clear signal, cuts are applied to negative values of the parameter PPO indicating arbitrary pulse shapes. To select crosstalk events in the iStick, events that are first triggered by the iStick are discarded. Furthermore, a cut on the rise time (10 - 50) % of iStick pulses in the α -region allows a removal of interface events as described in section 6.6.

bg_004	bg_021	bg_033	bg_045	bg_056	bg_068	bg_082	bg_104
bg_005	bg_022	bg_034	bg_046	bg_057	bg_069	bg_083	bg_105
bg_006	bg_024	bg_035	bg_047	bg_058	bg_072	bg_092	bg_106
bg_007	bg_025	bg_036	bg_048	bg_059	bg_073	bg_093	bg_107
bg_009	bg_026	bg_037	bg_049	bg_060	bg_074	bg_094	bg_108
bg_010	bg_027	bg_039	bg_050	bg_061	bg_076	bg_095	bg_109
bg_012	bg_028	bg_040	bg_051	bg_062	bg_077	bg_099	
bg_013	bg_029	bg_041	bg_052	bg_063	bg_078	bg_100	
bg_015	bg_030	bg_042	bg_053	bg_064	bg_079	bg_101	
bg_018	bg_031	bg_043	bg_054	bg_065	bg_080	bg_102	
bg_020	bg_032	bg_044	bg_055	bg_067	bg_081	bg_103	

Table E.1.: List of all CRESST-III Phase 1 background (bg) files used for the analysis of the e^-/γ -band. The filenames bg_004 - bg_015 (grey) are excluded for the α -analysis as the operation parameters of the *iSticks* were not stable before file bg_018.

detector	truncation limit for PP [V]	truncation limit for TP [V]	CPE-factor @ 63.3 keV [keV/V]	CPE-factor @ 11.27 keV [keV/V]
A-PH	2	2	8.03	8.49
A-L	1.3	0.2	7.82	-
B-PH	1.5	1.5	11.75	9.86
B-L	0.3	0.15	12.35	-
D-PH	1.5	1	10.61	10.25
D-L	0.5	0.5	8.69	-
E-PH	1.3	1.2	14.39	14.32
E-L	0.2	0.05	13.33	-

Table E.2.: Truncation limits used for the template fit of the particle pulses (PP) and the test pulses (TP). Furthermore, also the CPE-factors calculated for the energy calibration of all phonon (PH) and light (L) detectors in the analyzed modules A, B, D, and E are included. The CPE factor @ 63.3 keV was determined from the calibration with the ^{57}Co source. In the background data, the energy scale was cross-checked or slightly corrected using the 11.27 keV γ -line originating from cosmogenic activation.

detector	control pulse range CP [V]	Right - Left-Baseline RLB [V]	Peak Position PP [ms]	Peak Position - Peak Onset PPO [ms]	Delta Voltage/RMS DV	FWHM Baseline FWHMB [V]	Pulse Height PH [V]
A-PH	$4.3563 < CP < 4.6437$	$-0.5 < RLB < 2$	$120 < PP < 300$	$0 < PPO$	$-10 < DV$	$FWHMB < 0.5$	-
A-L	$1.3712 < CP < 1.4288$	$-0.2 < RLB < 0.2$	-	-	$-10 < DV$	-	-
A-i	-	-	-	-	-	-	PH < 0.08
B-PH	$4.1012 < CP < 4.8988$	$-0.5 < RLB < 2$	$120 < PP < 300$	$0 < PPO$	$-8 < DV$	$FWHMB < 0.5$	-
B-L	$0.9340 < CP < 0.9660$	$-0.1 < RLB < 0.1$	-	-	$-8 < DV$	-	-
B-i	-	-	-	-	-	-	PH < 0.1
D-PH	$4.4682 < CP < 4.6318$	$-0.3 < RLB < 1$	$140 < PP < 300$	$0 < PPO$	$-12 < DV$	$FWHMB < 0.2$	-
D-L	$1.6279 < CP < 1.7721$	$-0.1 < RLB < 0.2$	-	-	$-8 < DV$	-	-
D-i	-	-	-	-	-	-	PH < 0.04
E-PH	$2.8368 < CP < 3.1632$	$-0.5 < RLB < 1$	$140 < PP < 300$	$0 < PPO$	$-10 < DV$	$FWHMB < 0.2$	-
E-L	$0.3445 < CP < 0.3555$	$-0.02 < RLB < 0.02$	-	-	$-10 < DV$	-	-
E-i	-	-	-	-	-	-	PH < 0.2

Table E.3.: Limits of the various cuts applied to the CRESST-III Phase 1 detectors of modules A, B, D, and E for the analysis of the e^-/γ -band. Several cuts are only applied to the phonon detector PH, as potential signal events could be removed in the light detector L. The *iStick* channel *i* is only used for a cut on the pulse height for discrimination of interactions happening in the *iStick* itself.

detector	control pulse range CP [V]	Peak Position - Peak Onset PPO [ms]	Trigger Delay TD [ms]	Rise Time (10 - 50) % RT [ms]
A-PH	$3.6 < \text{CP} < 5.4$	$0 < \text{PPO}$	-	-
A-L	$1.2 < \text{CP} < 1.6$	$0 < \text{PPO}$	-	-
A-i	-	$0 < \text{PPO}$	$0.01 < \text{TD}$	$6 < \text{RT}$
B-PH	$2.1 < \text{CP} < 6.9$	$0 < \text{PPO}$	-	-
B-L	$0.85 < \text{CP} < 1.05$	$0 < \text{PPO}$	-	-
B-i	-	$0 < \text{PPO}$	$0.01 < \text{TD}$	$3 < \text{RT}$
D-PH	$4.05 < \text{CP} < 5.05$	$0 < \text{PPO}$	-	-
D-L	$1.3 < \text{CP} < 2.1$	$0 < \text{PPO}$	-	-
D-i	-	$0 < \text{PPO}$	$0.01 < \text{TD}$	-
E-PH	$2 < \text{CP} < 4$	$0 < \text{PPO}$	-	-
E-L	$0.32 < \text{CP} < 0.38$	$0 < \text{PPO}$	-	-
E-i	-	$0 < \text{PPO}$	$0.01 < \text{TD}$	$2 < \text{RT}$

Table E.4.: Limits of the cuts applied to the CRESST-III Phase 1 detectors of modules A, B, D, and E for the analysis of the α -events. Compared to table E.3, much higher values were chosen for the stable range of control pulses as it was observed that too high a fraction of α -events is cut otherwise. Negative values of the parameter PPO indicate an arbitrary pulse shape and are removed for all three detectors (phonon PH, light L, iStick i) as in case of α -events a clear signal is expected in each of them. To select crosstalk events in the iStick, events that are first triggered by the iStick are discarded. A cut on the rise time of iStick pulses in the α -region allows a removal of interface events as described in section 6.6.

Bibliography

- [1] J. C. Kapteyn, *First Attempt at a Theory of the Arrangement and Motion of the Sidereal System*, The Astrophysical Journal **55** 302 (1922).
- [2] F. Zwicky, *Die Rotverschiebung von extragalaktischen Nebeln*, Helvetica Physica Acta **6** 110 (1933).
- [3] V. C. Rubin et al., *Rotational properties of 21 Sc galaxies with a large range of luminosities and radii, from NGC 4605 ($R = 4$ kpc) to UGC 2885 ($R = 122$ kpc)*, The Astrophysical Journal **238** 471 (1980).
- [4] C. Tortora et al., *Dark matter and alternative recipes for the missing mass*, Journal of Physics Conference Series **354** 012021 (2012).
- [5] E. Corbelli et al., *The extended rotation curve and the dark matter halo of M33*, Monthly Notices of the Royal Astronomical Society **311** 441 (2000).
- [6] A. Einstein, *Lens-Like Action of a Star by the Deviation of Light in the Gravitational Field*, Science **84** 506 (1936).
- [7] M. Markevitch et al., *Direct Constraints on the Dark Matter Self-Interaction Cross Section from the Merging Galaxy Cluster 1E 0657–56*, The Astrophysical Journal **606** 819 (2004).
- [8] A. A. Penzias et al., *A Measurement of Excess Antenna Temperature at 4080 Mc/s*, The Astrophysical Journal **142** 419 (1965).
- [9] E. Komatsu et al., *Seven-year Wilkinson Microwave Anisotropy Probe (WMAP) Observations: Cosmological Interpretation*, The Astrophysical Journal Supplement Series **192** 18 (2011).
- [10] R. Adam et al., *Planck 2015 results - I. Overview of products and scientific results*, Astronomy&Astrophysics **594** A1 (2016).
- [11] P. A. R. Ade et al., *Planck 2015 results - XIII. Cosmological parameters*, Astronomy&Astrophysics **594** A13 (2016).
- [12] G. Bertone et al., *Particle dark matter: evidence, candidates and constraints*, Physics Reports **405** 279 (2005).
- [13] A. Klypin et al., *MultiDark simulations: the story of dark matter halo concentrations and density profiles*, Monthly Notices of the Royal Astronomical Society **457** 4340 (2016).

- [14] D. G. York et al., *The Sloan Digital Sky Survey: Technical Summary*, The Astrophysical Journal **120** 1579 (2000).
- [15] C. S. Frenk et al., *Dark matter and cosmic structure*, Annalen der Physik **524** 507 (2012).
- [16] R. Genzel et al., *Strongly baryon-dominated disk galaxies at the peak of galaxy formation ten billion years ago*, Nature **543** 397 (2017).
- [17] S. Adhikari et al., *Splashback in accreting dark matter halos*, Journal of Cosmology and Astroparticle Physics **2014** 019 (2014).
- [18] E. Baxter et al., *The Halo Boundary of Galaxy Clusters in the SDSS*, The Astrophysical Journal **841** 18 (2017).
- [19] C. Alcock et al., *The MACHO Project: Microlensing Results from 5.7 Years of Large Magellanic Cloud Observations*, The Astrophysical Journal **542** 281 (2000).
- [20] B. P. Abbott et al., *GW151226: Observation of Gravitational Waves from a 22-Solar-Mass Binary Black Hole Coalescence*, Physical Review Letters **116** 241103 (2016).
- [21] S. Bird et al., *Did LIGO Detect Dark Matter?*, Physical Review Letters **116** 201301 (2016).
- [22] S. Calchi Novati et al., *Microlensing towards the SMC: a new analysis of OGLE and EROS results*, Monthly Notices of the Royal Astronomical Society **435** 1582 (2013).
- [23] E. Mediavilla et al., *Limits on the Mass and Abundance of Primordial Black Holes from Quasar Gravitational Microlensing*, The Astrophysical Journal Letters **836** L18 (2017).
- [24] T. D. Brandt, *Constraints on MACHO Dark Matter from Compact Stellar Systems in Ultra-faint Dwarf Galaxies*, The Astrophysical Journal Letters **824** L31 (2016).
- [25] J. L. Feng, *Dark Matter Candidates from Particle Physics and Methods of Detection*, Annual Review of Astronomy and Astrophysics **48** 495 (2010).
- [26] G. Jungman et al., *Supersymmetric dark matter*, Physics Reports **267** 195 (1996).
- [27] B. W. Lee et al., *Cosmological Lower Bound on Heavy-Neutrino Masses*, Physical Review Letters **39** 165 (1977).
- [28] K. Petraki et al., *Review of Asymmetric Dark Matter*, International Journal of Modern Physics A **28** 1330028 (2013).
- [29] J. L. Feng et al., *Dark-Matter Particles without Weak-Scale Masses or Weak Interactions*, Physical Review Letters **101** 231301 (2008).

-
- [30] B. S. Acharya et al., *Lightest Visible-Sector Supersymmetric Particle is Likely to be Unstable*, Physical Review Letters **117** 181802 (2016).
- [31] R. T. D’Agnolo et al., *Light Dark Matter from Forbidden Channels*, Physical Review Letters **115** 061301 (2015).
- [32] J. Cline et al., *Enabling Forbidden Dark Matter*, arXiv:1702.07716 [hep-ph] (2017).
- [33] Y. Hochberg et al., *Mechanism for Thermal Relic Dark Matter of Strongly Interacting Massive Particles*, Physical Review Letters **113** 171301 (2014).
- [34] G. Aad et al., *Search for new phenomena in final states with an energetic jet and large missing transverse momentum in pp collisions at $\sqrt{s} = 8$ TeV with the ATLAS detector*, The European Physical Journal C **75** 299 (2015).
- [35] V. Khachatryan et al., *Search for new phenomena in monophoton final states in proton–proton collisions at $\sqrt{s} = 8$ TeV*, Physics Letters B **755** 102 (2016).
- [36] J. M. Gaskins, *A review of indirect searches for particle dark matter*, Contemporary Physics **57** 496 (2016).
- [37] R. Caputo et al., *Search for gamma-ray emission from dark matter annihilation in the Small Magellanic Cloud with the Fermi Large Area Telescope*, Physical Review D **93** 062004 (2016).
- [38] M. G. Aartsen et al., *All-flavour search for neutrinos from dark matter annihilations in the Milky Way with IceCube/DeepCore*, The European Physical Journal C **76** 531 (2016).
- [39] M. Aguilar et al., *Precision Measurement of the Proton Flux in Primary Cosmic Rays from Rigidity 1 GV to 1.8 TV with the Alpha Magnetic Spectrometer on the International Space Station*, Physical Review Letters **114** 171103 (2015).
- [40] L. Accardo et al., *High Statistics Measurement of the Positron Fraction in Primary Cosmic Rays of 0.5–500 GeV with the Alpha Magnetic Spectrometer on the International Space Station*, Physical Review Letters **113** 121101 (2014).
- [41] J. Bovy et al., *On the Local Dark Matter Density*, The Astrophysical Journal **756** 89 (2012).
- [42] M. Pato et al., *Dynamical constraints on the dark matter distribution in the Milky Way*, Journal of Cosmology and Astroparticle Physics **2015** 001 (2015).
- [43] A. J. Zöller, *Artificial Neural Network Based Pulse-Shape Analysis for Cryogenic Detectors Operated in CRESST-II*, Dissertation, Technische Universität München (2016).
- [44] J. M. Schmaler, *The CRESST Dark Matter Search - New Analysis Methods and Recent Results*, Dissertation, Technische Universität München (2010).

- [45] F. Reindl, *Exploring Light Dark Matter With CRESST-II Low-Threshold Detectors*, Dissertation, Technische Universität München, München (2016).
- [46] D. S. Akerib et al., *Results from a Search for Dark Matter in the Complete LUX Exposure*, Physical Review Letters **118** 021303 (2017).
- [47] X. Cui et al., *Dark Matter Results From 54-Ton-Day Exposure of PandaX-II Experiment*, arXiv:1708.06917 [astro-ph.CO] (2017).
- [48] E. Aprile et al., *Dark Matter Results from 225 Live Days of XENON100 Data*, Physical Review Letters **109** 181301 (2012).
- [49] E. Aprile et al., *First Dark Matter Search Results from the XENON1T Experiment*, arXiv:1705.06655 [astro-ph.CO] (2017).
- [50] P. Agnes et al., *First results from the DarkSide-50 dark matter experiment at Laboratori Nazionali del Gran Sasso*, Physics Letters B **743** 456 (2015).
- [51] M. Kuźniak et al., *DEAP-3600 Dark Matter Search*, Nuclear and Particle Physics Proceedings **273–275** 340 , 37th International Conference on High Energy Physics (ICHEP) (2016).
- [52] P.-A. Amaudruz et al., *First results from the DEAP-3600 dark matter search with argon at SNOLAB*, arXiv:1707.08042 [astro-ph.CO] (2017).
- [53] E. Aprile et al., *Physics reach of the XENON1T dark matter experiment*, Journal of Cosmology and Astroparticle Physics **2016** 027 (2016).
- [54] E. Armengaud et al., *Constraints on low-mass WIMPs from the EDELWEISS-III dark matter search*, Journal of Cosmology and Astroparticle Physics **2016** 019 (2016).
- [55] R. Agnese et al., *Search for Low-Mass Weakly Interacting Massive Particles with SuperCDMS*, Physical Review Letters **112** 241302 (2014).
- [56] R. Bernabei et al., *Final model independent result of DAMA/LIBRA-phase1*, The European Physical Journal C **73** 2648 (2013).
- [57] K. H. Lieser, *Nuclear and Radiochemistry: Radioactive Decay*, 29–46, Wiley-VCH Verlag GmbH (2007).
- [58] Lund/LBNL Nuclear Data Search, *Table of Radioactive Isotopes*, <http://nucleardata.nuclear.lu.se/toi/>, accessed: 07/09/2017 (Version 2.0, February 1999).
- [59] T. K. Gaisser et al., *Cosmic rays and particle physics*, Cambridge University Press, 2nd edition (2016).
- [60] V. F. Hess, *Über Beobachtungen der durchdringenden Strahlung bei sieben Freiballonfahrten*, Physikalische Zeitschrift **13** 1084 (1912).

-
- [61] LNGS, *Laboratori Nazionali del Gran Sasso*, <https://www.lngs.infn.it/en/>, accessed: 07/09/2017.
- [62] G. Bellini et al., *Cosmic-muon flux and annual modulation in Borexino at 3800 m water-equivalent depth*, *Journal of Cosmology and Astroparticle Physics* **2012** 015 (2012).
- [63] V. A. Kudryavtsev et al., *Neutron- and muon-induced background in underground physics experiments*, *The European Physical Journal A* **36** 171 (2008).
- [64] P. Belli et al., *Deep underground neutron flux measurement with large BF_3 counters*, *Il Nuovo Cimento A (1965-1970)* **101** 959 (1989).
- [65] H. Wulandari et al., *Neutron flux at the Gran Sasso underground laboratory revisited*, *Astroparticle Physics* **22** 313 (2004).
- [66] M. Haffke et al., *Background measurements in the Gran Sasso Underground Laboratory*, *Nuclear Instruments and Methods in Physics Research Section A: Accelerators, Spectrometers, Detectors and Associated Equipment* **643** 36 (2011).
- [67] F. Pobell, *Matter and Methods at Low Temperatures*, Springer, 3rd edition (2007).
- [68] A. Münster et al., *Cryogenic detectors for dark matter search and neutrinoless double beta decay*, *Nuclear Instruments and Methods in Physics Research Section A: Accelerators, Spectrometers, Detectors and Associated Equipment* **845** 387 , proceedings of the Vienna Conference on Instrumentation 2016 (2017).
- [69] F. Pröbst et al., *Model for cryogenic particle detectors with superconducting phase transition thermometers*, *Journal of Low Temperature Physics* **100** 69 (1995).
- [70] R. Strauss et al., *A prototype detector for the CRESST-III low-mass dark matter search*, *Nuclear Instruments and Methods in Physics Research Section A: Accelerators, Spectrometers, Detectors and Associated Equipment* **845** 414 , proceedings of the Vienna Conference on Instrumentation 2016 (2017).
- [71] A. Tanzke, *Low-Threshold Detectors for Low-Mass Direct Dark Matter Search with CRESST-III*, Dissertation, Technische Universität München (2017).
- [72] N. Ferreiro Iachellini, *in preparation*, Dissertation, Ludwig-Maximilians-Universität München.
- [73] G. Angloher et al., *Results from 730 kg days of the CRESST-II Dark Matter search*, *The European Physical Journal C* **72** 1971 (2012).
- [74] R. Strauss et al., *Energy-dependent light quenching in $CaWO_4$ crystals at mK temperatures*, *The European Physical Journal C* **74** 2957 (2014).
- [75] C. Bruhn, *Production and Characterization of Scintillating $CaWO_4$ Single Crystals for Rare Event Searches*, Master's Thesis, Technische Universität München (2015).

- [76] C. Oppenheimer, *Development, production and characterization of high-purity CaWO_4 crystals for the CRESST-experiment*, Master's Thesis, Technische Universität München (2016).
- [77] K. J. Schäffner, *Study of Backgrounds in the CRESST Dark Matter Search*, Dissertation, Technische Universität München (2013).
- [78] M. Kuźniak et al., *Surface roughness interpretation of 730 kg days CRESST-II results*, *Astroparticle Physics* **36** 77 (2012).
- [79] K. Alfonso et al., *Search for Neutrinoless Double-Beta Decay of ^{130}Te with CUORE-0*, *Physical Review Letters* **115** 102502 (2015).
- [80] R. Strauss et al., *A detector module with highly efficient surface-alpha event rejection operated in CRESST-II Phase 2*, *The European Physical Journal C* **75** 352 (2015).
- [81] G. Angloher et al., *Performance of a CRESST-II Detector Module with True 4π -veto*, arXiv:1708.01581 [astro-ph.IM] (2017).
- [82] R. Strauss et al., *Beta/gamma and alpha backgrounds in CRESST-II Phase 2*, *Journal of Cosmology and Astroparticle Physics* **2015** 030 (2015).
- [83] A. Münster et al., *Radiopurity of CaWO_4 crystals for direct dark matter search with CRESST and EURECA*, *Journal of Cosmology and Astroparticle Physics* **2014** 018 (2014).
- [84] S. Yellin, *Finding an upper limit in the presence of an unknown background*, *Physical Review D* **66** 032005 (2002).
- [85] G. Angloher et al., *Results on low mass WIMPs using an upgraded CRESST-II detector*, *The European Physical Journal C* **74** 3184 (2014).
- [86] G. Angloher et al., *Results on light dark matter particles with a low-threshold CRESST-II detector*, *The European Physical Journal C* **76** 25 (2016).
- [87] D. S. Akerib et al., *First Results from the LUX Dark Matter Experiment at the Sanford Underground Research Facility*, *Physical Review Letters* **112** 091303 (2014).
- [88] X. Xiao et al., *Low-mass dark matter search results from full exposure of the PandaX-I experiment*, *Physical Review D* **92** 052004 (2015).
- [89] Q. Yue et al., *Limits on light weakly interacting massive particles from the CDEX-1 experiment with a p-type point-contact germanium detector at the China Jinping Underground Laboratory*, *Physical Review D* **90** 091701 (2014).
- [90] R. Agnese et al., *New Results from the Search for Low-Mass Weakly Interacting Massive Particles with the CDMS Low Ionization Threshold Experiment*, *Physical Review Letters* **116** 071301 (2016).

-
- [91] R. Agnese et al., *Silicon Detector Dark Matter Results from the Final Exposure of CDMS II*, Physical Review Letters **111** 251301 (2013).
- [92] C. E. Aalseth et al., *CoGeNT: A search for low-mass dark matter using p-type point contact germanium detectors*, Physical Review D **88** 012002 (2013).
- [93] E. Armengaud et al., *Search for low-mass WIMPs with EDELWEISS-II heat-and-ionization detectors*, Physical Review D **86** 051701 (2012).
- [94] J. Barreto et al., *Direct search for low mass dark matter particles with CCDs*, Physics Letters B **711** 264 (2012).
- [95] A. Brown et al., *Extending the CRESST-II commissioning run limits to lower masses*, Physical Review D **85** 021301 (2012).
- [96] A. Gütlein et al., *Impact of coherent neutrino nucleus scattering on direct dark matter searches based on CaWO_4 crystals*, Astroparticle Physics **69** 44 (2015).
- [97] G. Angloher et al., *Limits on Momentum-Dependent Asymmetric Dark Matter with CRESST-II*, Physical Review Letters **117** 021303 (2016).
- [98] G. Angloher et al., *Dark-photon search using data from CRESST-II Phase 2*, The European Physical Journal C **77** 299 (2017).
- [99] G. Angloher et al., *Probing low WIMP masses with the next generation of CRESST detector*, arXiv:1503.08065 [astro-ph.IM] (2015).
- [100] J. Rothe, *Achieving Low Thresholds: Cryogenic Detectors for Low-Mass Dark Matter Searches*, Master's Thesis, Ludwig-Maximilians-Universität München (2016).
- [101] M. Wüstrich, *in preparation*, Dissertation, Technische Universität München.
- [102] *General Physics Institute*, 38 Vavilov Str., 119991 Moscow, Russia, <http://www.gpi.ru/eng/index.php>.
- [103] D. Akimov et al., *Observation of coherent elastic neutrino-nucleus scattering*, Science (2017).
- [104] R. Strauss et al., *The ν -cleus experiment: a gram-scale fiducial-volume cryogenic detector for the first detection of coherent neutrino-nucleus scattering*, The European Physical Journal C **77** 506 (2017).
- [105] R. Strauss et al., *Gram-scale cryogenic calorimeters for rare-event searches*, Physical Review D **96** 022009 (2017).
- [106] *Scientific Research Company Karat*, str.Stryiska 202, 79031 Lviv, Ukraine, <http://en.carat.electron.ua/>.
- [107] A. Erb et al., *Growth of high-purity scintillating CaWO_4 single crystals for the low-temperature direct dark matter search experiments CRESST-II and EURECA*, CrystEngComm **15** 2301 (2013).

- [108] mindat database of minerals, localities and mineral photographs, *Scheelite*, <http://www.mindat.org/min-3560.html>, accessed: 07/09/2017.
- [109] D. Meschede, *Gerthsen Physik*, Springer, 25th edition (2015).
- [110] A. Erb, *Crystal Orientation the Real Time Way*, <http://www.lauecamera.com/indexengl.htm>, accessed: 07/09/2017.
- [111] W. Haynes, *Handbook of chemistry and physics*, CRC Press, 95th edition (2014-2015).
- [112] M. Sivers et al., *Influence of annealing on the optical and scintillation properties of CaWO₄ single crystals*, *Optical Materials* **34** 1843 (2012).
- [113] M. Moszyński et al., *Characterization of CaWO₄ scintillator at room and liquid nitrogen temperatures*, *Nuclear Instruments and Methods in Physics Research Section A: Accelerators, Spectrometers, Detectors and Associated Equipment* **553** 578 (2005).
- [114] V. B. Mikhailik et al., *One- and two-photon excited luminescence and band-gap assignment in CaWO₄*, *Physical Review B* **69** 205110 (2004).
- [115] M. v. Sivers et al., *Low-temperature scintillation properties of CaWO₄ crystals for rare-event searches*, *Journal of Applied Physics* **118** 164505 (2015).
- [116] V. B. Mikhailik et al., *Scintillation studies of CaWO₄ in the millikelvin temperature range*, *Physical Review B* **75** 184308 (2007).
- [117] M. von Sivers, *Optimizing Detectors for Dark Matter Search*, Diploma Thesis, Technische Universität München (2010).
- [118] S. Baccaro et al., *Effect of La Doping on Calcium Tungstate (CaWO₄) Crystals Radiation Hardness*, *Physica Status Solidi Applied Research* **178** 799 (2000).
- [119] M. Kobayashi et al., *Significant improvement of PbWO₄ scintillating crystals by doping with trivalent ions*, *Nuclear Instruments and Methods in Physics Research Section A: Accelerators, Spectrometers, Detectors and Associated Equipment* **434** 412 (1999).
- [120] M. von Sivers, *Scintillating CaWO₄ Crystals for the Direct Dark Matter Search Experiments CRESST and EURECA*, Dissertation, Technische Universität München (2014).
- [121] *MV Laboratories, Inc.*, 843 Route 12 West, Frenchtown NJ 08825, USA, not existing any more since autumn 2014.
- [122] M. Hofmann et al., *Low-background gamma-ray spectrometry in the Garching underground laboratory*, *AIP Conference Proceedings* **1549** 38 (2013).

-
- [123] K. Nassau et al., *Preparation of Large Calcium-Tungstate Crystals Containing Paramagnetic Ions for Maser Applications*, Journal of Applied Physics **31** 1508 (1960).
- [124] K. Nassau et al., *Calcium Tungstate: Czochralski Growth, Perfection, and Substitution*, Journal of Applied Physics **33** 3064 (1962).
- [125] *Cyberstar*, Parc Sud Galaxie 1, rue des Tropiques, BP 344, 38435 Echirolles, Cedex, France, <http://www.cyberstar.fr/>.
- [126] A. Erb, private communication (2017).
- [127] H. Mehrer, *Diffusion in Solids*, Springer (2007).
- [128] S. Roth, *The Potential of Neganov-Luke Amplified Cryogenic Light Detectors and the Scintillation-Light Quenching Mechanism in CaWO₄ Single Crystals in the Context of the Dark Matter Search Experiment CRESST-II*, Dissertation, Technische Universität München (2013).
- [129] J. W. Dally et al., *Experimental stress analysis*, McGRAW-HILL, 3rd edition (1991).
- [130] J. F. Doyle et al., *Manual on Experimental Stress Analysis*, Society for Experimental Mechanics (1989).
- [131] W. Demtröder, *Experimentalphysik 2 - Elektrizität und Optik*, Springer, 3rd edition (2004).
- [132] J. Ninkovic, *Investigation of CaWO₄ Crystals for Simultaneous Phonon-Light Detection in the CRESST Dark Matter Search*, Dissertation, Technische Universität München (2005).
- [133] D. Wulff-Molder, Korth Kristalle GmbH, private communication (2017).
- [134] *PerkinElmer*, <http://www.perkinelmer.com/>, accessed: 07/09/2017.
- [135] W. L. Bond, *Measurement of the Refractive Indices of Several Crystals*, Journal of Applied Physics **36** 1674 (1965).
- [136] M. Bass et al., *Handbook of Optics, Volume II*, McGRAW-HILL, 2nd edition (1995).
- [137] Hamamatsu, *Photomultiplier Tubes – Basics and Applications*, Hamamatsu Photonics K.K., 3rd edition (2007).
- [138] M. Stanger, private communication (2017).
- [139] S. Roth et al., *Thermal detector model for cryogenic composite detectors for the dark matter experiments CRESST and EURECA*, Journal of Physics: Conference Series **136** 042085 (2008).

- [140] LSC, *Laboratorio Subterráneo de Canfranc*, <http://www.lsc-canfranc.es/en/>, accessed: 07/09/2017.
- [141] A. Bettini, *The Canfranc Underground Laboratory (LSC)*, *The European Physical Journal Plus* **127** 112 (2012).
- [142] G. Heusser et al., *Low-level germanium gamma-ray spectrometry at the $\mu\text{Bq/kg}$ level and future developments towards higher sensitivity*, *Radioactivity in the Environment* **8** 495 (2006).
- [143] TUM, *Centre for Building Materials (CBM)*, <https://www.cbm.bgu.tum.de/index.php?id=5&L=1>, accessed: 07/09/2017.
- [144] K. H. Lieser, *Nuclear and Radiochemistry: Production of Radionuclides and Labeled Compounds*, 239–263, Wiley-VCH Verlag GmbH (2007).
- [145] Z. B. Alfassi, *Determination of Trace Elements*, VCH Verlagsgesellschaft mbH (1994).
- [146] P. Patnaik, *Dean's Analytical Chemistry Handbook*, McGRAW-HILL, 2nd edition (2004).
- [147] J. C. White et al., *Separations by Solvent Extraction With Tri-n-octylphosphine Oxide*, The National Academies Press (1961).
- [148] R. Hampf, *Study of the Scintillation Properties of CaWO_4 -Crystals with Laser Induced Two-Photon Excitation*, Master's Thesis, Technische Universität München (2017).
- [149] V. Morgalyuk, private communication (2017).
- [150] J. Katz et al., *The chemistry of the actinide elements*, volume 1, Springer, 2nd edition (1986).
- [151] H. H. Trinh Thi, private communication (2017).
- [152] K.-T. Wilke et al., *Kristallzüchtung*, VEB Deutscher Verlag der Wissenschaften (1990).
- [153] F. A. Danevich et al., *Effect of recrystallisation on the radioactive contamination of CaWO_4 crystal scintillators*, *Nuclear Instruments and Methods in Physics Research A: Accelerators, Spectrometers, Detectors and Associated Equipment* **631** 44 (2011).
- [154] A. Zöller, private communication (2017).
- [155] R. McGowan, *Data Analysis and Results of the Upgraded CRESST Dark Matter Search*, Dissertation, University of Oxford (2008).
- [156] A. Brown, *Analysis and Modelling for CRESST-II*, Dissertation, University of Oxford (2011).

-
- [157] R. Brun et al., *ROOT: An object oriented data analysis framework*, Nuclear Instruments and Methods in Physics Research Section A: Accelerators, Spectrometers, Detectors and Associated Equipment **A389** 81 (1997).
- [158] A. Münster, *Absolute α -Radioactivity Determination of Scintillating CaWO_4 Crystals for Direct Dark Matter Search*, Diploma Thesis, Technische Universität München (2013).
- [159] National Institute of Standards and Technology (NIST), *X-Ray Mass Attenuation Coefficients*, <https://www.nist.gov/pml/x-ray-mass-attenuation-coefficients>, accessed: 07/09/2017.
- [160] C. de Boor, *A Practical Guide to Splines (Applied Mathematical Sciences)*, Springer (1994).
- [161] F. Petricca, *Dark Matter Search with Cryogenic Phonon-Light Detectors*, Dissertation, Ludwig-Maximilians-Universität München (2005).
- [162] F. Reindl, *Analysis of CRESST Dark Matter Search Data*, Diploma Thesis, Technische Universität München (2011).
- [163] A. Bisi et al., *Orbital electron capture in ^{179}Ta* , Il Nuovo Cimento (1955-1965) **4** 307 (1956).
- [164] R. C. Jopson et al., *L to K Ratios in the Electron Capture Decay of W^{181} and Ta^{179}* , Physical Review **124** 157 (1961).
- [165] *Institut f. Hochenergiephysik der Österreichischen Akademie der Wissenschaften*, A-1050 Vienna, Austria.
- [166] *Atomintitut, Vienna University of Technology*, A-1020 Vienna, Austria.
- [167] C. Cozzini et al., *Detection of the natural α decay of tungsten*, Physical Review C **70** 064606 (2004).
- [168] *Alfa Aesar, Thermo Fischer Scientific*, <https://www.alfa.com/en/>, accessed: 07/09/2017.
- [169] *3M Deutschland GmbH*, <http://www.3mdeutschland.de>, accessed: 07/09/2017.
- [170] A. Langenkämper, *Investigation of reflective and scintillating foils and Neganov-Trofimov-Luke amplified cryogenic light detectors for the CRESST experiment*, Master's Thesis, Technische Universität München (2016).
- [171] *Agilent Technologies*, <http://www.agilent.com/home>, accessed: 07/09/2017.
- [172] T. Mannel, *Low-level radioactivity techniques for the neutrino-oscillation experiment Double Chooz*, Master's Thesis, Technische Universität München (2013).

- [173] N. Famulok et al., *Ultrasensitive detection method for primordial nuclides in copper with Accelerator Mass Spectrometry*, Nuclear Instruments and Methods in Physics Research Section B: Beam Interactions with Materials and Atoms **361** 193 , the Thirteenth Accelerator Mass Spectrometry Conference (2015).
- [174] L. K. Fifield et al., *Accelerator mass spectrometry with the 14UD accelerator at the Australian National University*, Nuclear Instruments and Methods in Physics Research B: Beam Interactions with Materials and Atoms **268** 858 (2010).
- [175] A. Kinast, *in preparation*, Master's Thesis, Technische Universität München.
- [176] *Carl Roth GmbH + Co. KG*, <https://www.carlroth.com/en/en>, accessed: 07/09/2017.

Acknowledgements

Ich möchte mich bei allen Personen bedanken, die zum erfolgreichen Abschluss dieser Arbeit beigetragen haben. Zunächst ein großes Dankeschön an Prof. Stefan Schönerert und Prof. Lothar Oberauer für die Möglichkeit meine Doktorarbeit am Lehrstuhl E15 zu machen. Danke für die vielen Erfahrungen, die ich sammeln konnte, und für die bereitwillige Unterstützung in den letzten Jahren! Auch bei Dr. Jean-Come Lanfranchi möchte ich mich für die engagierte Betreuung in der ersten Zeit meiner Arbeit bedanken. Danke für die Organisation des Workshops auf Korsika, er zählt definitiv zu meinen Höhepunkten während meiner Zeit bei E15.

Großer Dank gilt Dr. Walter Potzel. Du hattest immer ein offenes Ohr und die Diskussionen mit dir waren aufgrund deines enormen physikalischen Verständnisses und deiner großen Erfahrung stets sehr hilfreich. Vielen Dank, dass du deine Freizeit für das intensive Korrekturlesen meiner Arbeit geopfert hast!

Bei Prof. Andreas Erb möchte ich mich für die gute Zusammenarbeit im Kristalllabor bei der Herstellung von CaWO_4 Kristallen bedanken. Danke für all deine Hilfe, ich konnte viel von deinen Erfahrungen profitieren. Bedanken möchte ich mich auch bei Michael Stanger für die Bearbeitung vieler CaWO_4 Kristalle sowie für deine guten Ideen für weitere Tests und Versuche. Mein Dank geht außerdem an die restlichen Mitarbeiter des Kristalllabors, deren Hilfsbereitschaft ich des Öfteren in Anspruch genommen habe. Bei Dr. Hong Hanh Trinh Thi möchte ich mich für die gute Zusammenarbeit und für das unvergleichliche Engagement bedanken, das du in unsere Pulverproduktion gesteckt hast. Abgesehen davon zählen die Einblicke in die vietnamesische Küche zu meinen kulinarischen Höhepunkten der letzten Jahre! Dankeschön auch an Vasily Morgalyuk, der seinen Urlaub geopfert hat um uns bei der Entwicklung einer Prozedur für die Pulverreinigung zu helfen.

Ein besonderer Dank gilt auch Prof. Andreas Ulrich. Vor allem deine Hilfe bei der Untersuchung der optischen Eigenschaften der Kristalle war und ist für mich sehr wertvoll. Eine wesentliche Rolle für die Erstellung dieser Arbeit hat Dr. Andreas Zöller gespielt. Danke, Andi, für all deine Hilfe, für die vielen Diskussionen und den hilfreichen Input, für all deine guten Ideen, für die Hilfestellung beim Programmieren, sowie für das Korrekturlesen meiner Arbeit. Und das alles ohne "trotz Allem" ;-). An dieser Stelle möchte ich mich auch bei meinen weiteren Korrekturlesern Dr. Anja Tanzke, Alexander Langenkämper, Birgit Neumair und Dr. Michael Willers bedanken. Danke, Mike, für deine Hilfe, vor allem auch bezüglich Detektorbau und Server-Problemen.

Auch bei meinen Masterand(inn)en Cecilia Bruhn, Corbinian Oppenheimer, Angelina Kinast und Erik Lindner möchte ich mich bedanken. Danke Cecilia, für die gemeinsamen Nachtschichten im Kristalllabor (an dieser Stelle auch ein Dankeschön an Hans Steiger). Danke Corbinian und Angie für euer engagiertes Mitwirken bei der Pulverproduktion – ohne euch wäre das nicht machbar gewesen.

Dr. Dominikus Hellgartner hat mir in meiner Anfangszeit vor allem bei Programmierungs- und Softwarefragen einige Male weiter geholfen – vielen Dank dafür! Danke auch an Andrea Lazzaro für die Zeit, die du für HPGe Messungen unserer Samples im UGL investiert hast.

Bei unseren Sekretärinnen/Team-Assistentinnen, insbesondere bei Maria Bremberger und bei Sabine Kaps, möchte ich mich für die Unterstützung in organisatorischen, verwaltungstechnischen und finanziellen Angelegenheiten bedanken. Wie wichtig ihr für den Lehrstuhl wart, ist uns besonders in den Übergangsphasen mit unbesetztem Sekretariat vor Augen geführt worden. Danke an Hermann Hagn für die bereitwillige Hilfe bei elektronischen Fragen sowie an Norbert Gärtner und an die Mitarbeiter unserer E15 Werkstatt, die mich bei einigen Aufgaben tatkräftig unterstützt haben.

I am sorry that I do not list the names of all persons that somehow played a role for my thesis. I want to thank the whole group at E15, in particular the cryo-group, for the pleasant working atmosphere. My thesis would not exist in this form without the discussions with you all and without your permanent help and support. I also enjoyed our non-university activities (dinners, skiing, sliding, hiking etc.) very much!

I want to thank my CRESST-colleagues for fruitful discussions, nice meetings and for all the hours you worked at home or at Gran Sasso to keep the experiment successfully running. Ein großes Dankeschön geht hierbei an Dr. Franz Pröbst. Dein immenses Wissen über sämtliche Aspekte von CRESST und darüber hinaus war immer enorm wertvoll für mich. Thanks to Dr. Federica Petricca for all your help and support, in particular with respect to the ICP-MS measurements at LNGS. Dankeschön an Dr. Raimund Strauß für die gute Zusammenarbeit beim Einbau der Detektoren für CRESST-III Phase 1 sowie für deine guten Tips und Korrekturvorschläge für meine Arbeit. Für hilfreiche Diskussionen rund um die Analyse (ich bin ja am Ende doch irgendwie zurückgekehrt ;-)) möchte ich mich vor allem bei Dr. Achim Gütlein, Philipp Bauer und Dr. Florian Reindl bedanken. Für weitere Kristall-Messungen habe ich außerdem Hilfe von Marc Wüstrich und Dieter Hauff erhalten, danke dafür! Ein großer Dank gilt definitiv auch Dr. Karoline Schäffner für sämtliche Unterstützung am Gran Sasso sowohl bei meinen Schichten als auch am Testkryostat. Schon als kleine pecorella habe ich dich für deine Begeisterung und dein Engagement in Forschungsfragen bewundert ;-)

I want to thank Stefano Nisi and the chemistry laboratory at LNGS for the ICP-MS measurements you performed for us. Thanks also to Matthias Laubenstein at LNGS as well as to Jorge Puimedon and his team at LSC for HPGe spectroscopy of our powder samples.

Vorrei ringraziare Marco Guetti per tutto l'aiuto con CRESST e il liquefattore! Grazie a la famiglia d'Archivio per i momenti bellissimi! Durante ogni shift al Gran Sasso, mi sono piacute molto le sere passate nel albergo (soprattutto le cene ;-)) e anche le gite che abbiamo fatto insieme.

Zu guter Letzt dürfen natürlich auch meine Freunde und vor allem meine Familie hier nicht fehlen. Ihr habt mir so manche hilfreiche Ablenkung geboten und konntet mich auch in frustrierenden Situationen wieder aufbauen. Danke, dass ihr immer für mich da wart und seid!

